LEVEL (12)

AXIAL FLOW ROTOR UNSTEADY PERFORMANCE

E. P. Bruce

DTIC
SELECTED
FEB 27 1980
C

Technical Memorandum
File No. TM 79-149
14 August 1979
Contract No. N00024-79-C-6043

Copy No. 8

The Pennsylvania State University
APPLIED RESEARCH LABORATORY
Post Office Box 30
State College, PA 16801

Approved for Public Release
Distribution Unlimited

NAVY DEPARTMENT

NAVAL SEA SYSTEMS COMMAND

80 2 25 058

REPORT DOCUMENTATION PAGE	READ INSTRUCTIONS BEFORE COMPLETING FORM

1. REPORT NUMBER	2. GOVT ACCESSION NO.	3. RECIPIENT'S CATALOG NUMBER
TM 79-149		

4. TITLE (and Subtitle)	5. TYPE OF REPORT & PERIOD COVERED
AXIAL FLOW ROTOR UNSTEADY PERFORMANCE	Technical memo,
	6. PERFORMING ORG. REPORT NUMBER

7. AUTHOR(s)	8. CONTRACT OR GRANT NUMBER(s)
E. P. Bruce	N00024-79-C-6043

9. PERFORMING ORGANIZATION NAME AND ADDRESS	10. PROGRAM ELEMENT, PROJECT, TASK AREA & WORK UNIT NUMBERS
Applied Research Laboratory Post Office Box 30 State College, PA 16801	14 Aug 79

11. CONTROLLING OFFICE NAME AND ADDRESS	12. REPORT DATE
Naval Sea Systems Command Washington, DC 20362 (code NSEA 63R3)	08/14/79
	13. NUMBER OF PAGES
	224

14. MONITORING AGENCY NAME & ADDRESS(if different from Controlling Office)	15. SECURITY CLASS. (of this report)
ARL/PSU/TM-79-149	UNCLASSIFIED
	15a. DECLASSIFICATION/DOWNGRADING SCHEDULE

16. DISTRIBUTION STATEMENT (of this Report)

Approved for public release. Distribution unlimited Per NAVSEA Code 63R3.

256

17. DISTRIBUTION STATEMENT (of the abstract entered in Block 20, if different from Report)

18. SUPPLEMENTARY NOTES

19. KEY WORDS (Continue on reverse side if necessary and identify by block number)

axial flow, turbomachinery, rotor, blade, unsteady response, lift force, pitching moment, theoretical model

20. ABSTRACT (Continue on reverse side if necessary and identify by block number)

Two problems facing designers of axial flow turbomachines at present are requirements for operation with increased efficiency and reduced radiated noise. To meet these requirements, it is necessary to have detailed information on the influence of geometrical and operating characteristics of blade rows on their unsteady response to distortions in the inflow velocity field. Unsteady response as defined here refers to the unsteady lift force and pitching moment generated on a rigid (i.e., nonvibrating) blade operating in a nonuniform, inviscid, incompressible flow. The unsteady pressure upon which the unsteady

DD FORM 1473 EDITION OF 1 NOV 65 IS OBSOLETE

force and moment depends is also responsible for generation of part of the radiated acoustic or noise field. In this study, the objective was to investigate unsteady response. Thus, the acoustic problem was not treated in detail. However, a brief discussion is presented which shows how the results can be applied to define the related acoustic source field.

In this study, an existing two-dimensional, nonviscous theory which employed a simplified vortex model in conjunction with the assumptions of thin airfoil theory to define cascade unsteady lift was modified and extended to include an expression for unsteady pitching moment. Computed theoretical results were compared with measured values of unsteady lift force and pitching moment coefficients and their phase angles and with the unsteady center-of-pressure position. The measured quantities were defined in a series of experiments conducted in a large axial flow fan test facility. Specially designed screens were employed to produce a variety of rotor inlet flows having a sinusoidally varying axial velocity component. Uncambered rotor response during operation in these harmonically varying inflows was determined by employing a strain-gaged sensing element on one rotor blade. The cascade stagger angle and space-to-chord ratio and the flow properties, mean incidence angle and reduced frequency, were varied in the program. The results show that, in general, the theory tends to overpredict the magnitude of the force and moment coefficients, that good agreement exists between the majority of the measured and predicted phase angle data, and that the validity of the theory in its present form should be restricted to values of reduced frequency greater than 0.8. The theory was also employed to define the effects of reduced frequency, mean incidence angle, space-to-chord ratio, stagger angle, and maximum camber on the magnitude of the force and moment coefficients. This analysis defined reduced frequency regions where mean incidence, camber or a combination of both can be employed to reduce the magnitude of these coefficients.

The fact that the theory tends to overpredict the force and moment coefficient magnitude was attributed to known real fluid effects. They are attenuation of the distortion velocity as it approaches and passes through the rotor and the effects of fluid viscosity on the blade wakes. Recommendations are made for incorporation of these factors into the theoretical model and for future experimental efforts. The recommended experimental effort is directed toward obtaining data at higher values of reduced frequency for the uncambered rotor and for obtaining data over the full reduced frequency range for a rotor having cambered blades.

ABSTRACT

Two problems facing designers of axial flow turbomachines at pre-
sent are requirements for operation with increased efficiency and
reduced radiated noise. To meet these requirements, it is necessary to
have detailed information on the influence of geometrical and operating
characteristics of blade rows on their unsteady response to distortions
in the inflow velocity field. Unsteady response as defined here refers
to the unsteady lift force and pitching moment generated on a rigid
(i.e., nonvibrating) blade operating in a nonuniform, inviscid, incom-
pressible flow. The unsteady pressure upon which the unsteady force
and moment depends is also responsible for generation of part of the
radiated acoustic or noise field. In this study, the objective was to
investigate unsteady response. Thus, the acoustic problem was not
treated in detail. However, a brief discussion is presented which
shows how the results can be applied to define the related acoustic
source field.

In this study, an existing two-dimensional, nonviscous theory
which employed a simplified vortex model in conjunction with the
assumptions of thin airfoil theory to define cascade unsteady lift was
modified and extended to include an expression for unsteady pitching
moment. Computed theoretical results were compared with measured
values of unsteady lift force and pitching moment coefficients and
their phase angles and with the unsteady center-of-pressure position.
The measured quantities were defined in a series of experiments

conducted in a large axial flow fan test facility. Specially designed screens were employed to produce a variety of rotor inlet flows having a sinusoidally varying axial velocity component. Uncambered rotor response during operation in these harmonically varying inflows was determined by employing a strain-gaged sensing element on one rotor blade. The cascade stagger angle and space-to-chord ratio and the flow properties, mean incidence angle and reduced frequency, were varied in the program. The results show that, in general, the theory tends to overpredict the magnitude of the force and moment coefficients, that good agreement exists between the majority of the measured and predicted phase angle data, and that the validity of the theory in its present form should be restricted to values of reduced frequency greater than 0.8. The theory was also employed to define the effects of reduced frequency, mean incidence angle, space-to-chord ratio, stagger angle, and maximum camber on the magnitude of the force and moment coefficients. This analysis defined reduced frequency regions where mean incidence, camber, or a combination of both can be employed to reduce the magnitude of these coefficients.

The fact that the theory tends to overpredict the force and moment coefficient magnitude was attributed to known real fluid effects. They are attenuation of the distortion velocity as it approaches and passes through the rotor and the effects of fluid viscosity on the blade wakes. Recommendations are made for incorporation of these factors into the theoretical model and for future experimental efforts. The recommended experimental effort is directed toward obtaining data at higher values of reduced frequency for the uncambered rotor and for obtaining data

over the full reduced frequency range for a rotor having cambered blades.

TABLE OF CONTENTS

LIST OF FIGURES

Number	Title	Page

Number	Title	Page

LIST OF TABLES

LIST OF SYMBOLS

Symbol	Definition

a cascade parameter, $a = \dfrac{Ce^{-i\xi}}{2S}$

A cascade influence function,

$$A = \frac{e^{in\tau}(n\cos\xi)}{\left[\dfrac{x_n - x_p}{S} + n\sin\xi\right]^2 + [n\cos\xi]^2}$$

A_1, A_2, A_3, A_4 integrals in Henderson's analysis

b cascade parameter, $b = \dfrac{Ce^{i\xi}}{2S}$

B cascade influence function,

$$B = \frac{e^{in\tau}\left[\dfrac{x_n - x_p}{S} + n\sin\xi\right]}{\left[\dfrac{x_n - x_p}{S} + n\sin\xi\right]^2 + [n\cos\xi]^2}$$

$B(\omega, x_c^+, S/C, \xi)$ cascade pitching moment function

B_1 cascade wake integral, $B_1 = \displaystyle\int_1^\infty \frac{e^{-i\omega\lambda^+}}{\sqrt{g_\lambda^2 - 1}}\, d\lambda^+$

Symbol	Definition

B_2 cascade wake integral, $B_2 = \int_1^\infty \dfrac{e^{-i\omega\lambda^+}}{\sqrt{h_\lambda^2 - 1}} d\lambda^+$

c grid loss coefficient

C blade chord

C_1 cascade function, $C_1 = \sqrt{\dfrac{g_c + 1}{g_c - 1}}$

C_2 cascade function, $C_2 = \sqrt{\dfrac{h_c + 1}{h_c - 1}}$

$C(\omega)$ Theodorsen's isolated airfoil lift function

$\tilde{C}_L$ unsteady lift force coefficient, $\dfrac{\tilde{L}}{(2\pi)\frac{1}{2}\rho W_m \hat{w}_d C e^{i\nu t}}$

$\tilde{C}_M$ unsteady pitching moment coefficient, $\dfrac{\tilde{M}}{(2\pi)\frac{1}{2}\rho W_m \hat{w}_d C^2 e^{i\nu t}}$

$\tilde{C}_N$ unsteady normal force coefficient, $\dfrac{\tilde{N}}{(2\pi)\frac{1}{2}\rho W_m \hat{w}_d C e^{i\nu t}}$

d positive number less than one or grid wire diameter

Symbol	Definition

D_1

cascade wake integral,

$$D_1 = \int\limits_1^\infty \left[\sqrt{\frac{g_\lambda + 1}{g_\lambda - 1}} - 1 \right] e^{-i\omega\lambda^+} d\lambda^+$$

D_2

cascade wake integral,

$$D_2 = \int\limits_1^\infty \left[\sqrt{\frac{h_\lambda + 1}{h_\lambda - 1}} - 1 \right] e^{-i\omega\lambda^+} d\lambda^+$$

E_j

Fourier coefficient amplitude

E_1

cascade function, $E_1 = \sqrt{g_c^2 - 1} - g_c - \sqrt{g_1^2 - 1} + g_1$

E_2

cascade function, $E_2 = \sqrt{h_c^2 - 1} - h_c - \sqrt{h_1^2 - 1} + h_1$

f

frequency

$F(\chi)$

cascade function, $F(\chi) = \dfrac{e^{in\tau}}{\chi + n}$

F_1

cascade function, $F_1 = g_c(g_c - \sqrt{g_c^2 - 1})$

$- g_1(g_1 - \sqrt{g_1^2 - 1})$

F_2

cascade function, $F_2 = h_c(h_c - \sqrt{h_c^2 - 1})$

$- h_1(h_1 - \sqrt{h_1^2 - 1})$

Symbol	Definition

g_c — cascade blade function, $g_c = x_c^+ + \dfrac{n}{ia}$

g_n — cascade function, $g_n = x_n^+ + \dfrac{n}{ia}$

g_λ — cascade wake function, $g_\lambda = \lambda^+ + \dfrac{n}{ia}$

g_1 — cascade wake function evaluated at $\lambda^+ = 1$,

$g_1 = 1 + \dfrac{n}{ia}$

G — wake vorticity constant of proportionality

$G(\omega, x_c^+, S/C, \xi)$ — cascade lift force function

G_1 — cascade function, $G_1 = C_1 + C_2 - 2 - i\omega e^{i\omega}(D_1 + D_2)$

G_2 — cascade function, $G_2 = C_1 + C_2 - 2 - i\omega e^{i\omega}(B_1 + B_2)$

h_c — cascade blade function, $h_c = x_c^+ - \dfrac{n}{ib}$

h_n — cascade function, $h_n = x_n^+ - \dfrac{n}{ib}$

h_λ — cascade wake function, $h_\lambda = \lambda^+ - \dfrac{n}{ib}$

h_1 — cascade wake function evaluated at $\lambda^+ = 1$,

$h_1 = 1 - \dfrac{n}{ib}$

Symbol	Definition
$H_n^{(2)}(\omega)$	Hankel function of the second kind of order n
i	rotor inlet incidence angle or the imaginary unit
j	dummy variable
$J_n(\theta)$	Bessel function of the first kind of order n
k	dummy variable or constant of proportionality
K	grid resistance coefficient, $K = \dfrac{\Delta P}{\frac{1}{2}\rho V^2}$
K_1	cascade function, $K_1 = i\omega e^{-i\omega}\left[F_1 + F_2\right]$ $+ 2e^{-i\omega}\left[g_c(C_1 - 1) - C_1 + h_c(C_2 - 1) - C_2\right]$
K_{min}	support grid resistance coefficient
ΔK	increment in grid resistance coefficient due to overlay segment
ℓ	disturbance wavelength or stator blade-to-blade spacing
L	lift force
m	summation index or spacing between wires in a square mesh grid
M	pitching moment about the leading edge, positive for increasing incidence

Symbol	Definition
n	cascade blade number
N	number of cycles of velocity variation per circumference or normal force
p	pressure
Δp	pressure difference, $\Delta p = P_{(-)} - P_{(+)}$
P	function in Söhngen inversion formula
ΔP	total pressure loss
q	net chordwise velocity, $q = W_m + u_d$
Q	function in Söhngen inversion formula
r	radial distance
R	sensor output-to-input signal amplitude ratio
Re	grid Reynolds number, $Re = \dfrac{Vd}{(1 - s)\nu}$
s	grid solidity, the ratio of blocked area to total area, $s = 2\left[\dfrac{d}{m}\right] - \left[\dfrac{d}{m}\right]^2$
S	rotor blade-to-blade spacing
t	time
δt	small increment of time

Symbol	Definition
u	velocity in the direction parallel to the blade chord (chordwise)
U	rotor blade rotational velocity
v	velocity in the direction normal to the blade chord (transverse)
V	circumferential mean rotor inlet or stator exit absolute velocity
$V(\eta)$	local rotor inlet absolute velocity
w	disturbance velocity magnitude
W	rotor relative velocity
W_1	circumferential mean rotor inlet relative velocity
W_2	circumferential mean rotor exit relative velocity
x	rotor blade chordwise coordinate
y	rotor blade transverse coordinate
y_{max}	rotor blade maximum camber
z	cascade function, $z = \dfrac{x_n - x_p}{S}$
α	stator exit absolute flow angle measured from the axial direction

Symbol	Definition
β	rotor relative flow angle measured from the axial direction
γ	vorticity
Γ	circulation
Δ	cascade circulation parameter, $\Delta = \dfrac{\overline{\Gamma}_o e^{i\omega}}{C}$
ϵ	distance velocity flow angle measured from the y-direction
ζ	angle between the radial direction and the y-direction
η	circumferential position
θ	generalized reduced frequency, $\theta = \dfrac{\mu C}{2W_m}$
$\Theta(\chi)$	cascade function, $\Theta(\chi) = e^{-i\xi}F(\chi) + e^{i\xi}\overline{F(\chi)}$
λ	dummy wake variable
$\Lambda(\sigma,j)$	function in the solution to the integral $\displaystyle\int_{-1}^{\sigma} \sqrt{\dfrac{1-k}{1+k}}\,\dfrac{dk}{j-k}$, $\Lambda(\sigma,j) = 2\tan^{-1}\left[\sqrt{\left[\dfrac{1-\sigma}{1+\sigma}\right]\left[\dfrac{j+1}{j-1}\right]}\right] - \pi$
μ	generalized complex frequency

Symbol	Definition

ν frequency with which waves pass a point on the blade, $\nu = \dfrac{2\pi U}{\ell}$, or fluid kinematic viscosity

ξ rotor blade stagger angle measured from the axial direction

ρ fluid mass density

σ arbitrary point on the blade or standard deviation of a set of measured values

τ blade-to-blade phase angle, $\tau = -\dfrac{2\pi S}{\ell}$

ϕ supplement to the angles α_m and ξ or phase angle

$\Phi(\chi)$ cascade function, $\Phi(\chi) = e^{-i\xi}F(\chi) - e^{i\xi}F(\bar{\chi})$

χ cascade function, $\chi = ize^{-iz}$

ψ grid resistance coefficient parameter, $\psi = (1 + K)^{1/2}$

ψ_o grid minimum resistance coefficient parameter, $\psi_o = (1 + K_{min})^{1/2}$

Ψ grid resistance parameter, $\Psi = \dfrac{1 + 6\psi_o^3}{6\psi_o^2} + \dfrac{w_d(1 + \psi_o^3)^{2/3}}{1.02V(1 + \psi_o)}$

Symbol	Definition

ω

reduced frequency, $\omega = \dfrac{\nu C}{2W_m}$

$\Omega(\sigma,j)$

function in the solution to the integral

$$\oint_{-1}^{\infty} \sqrt{\frac{1-k}{1+k}} \frac{dk}{j-k} \, , \ \Omega(\sigma,j) =$$

$$\frac{1}{2} \ln \left[\frac{1 - \sigma j + \sqrt{1 - j^2}\,\sqrt{1 - \sigma^2}}{1 - \sigma j - \sqrt{1 - j^2}\,\sqrt{1 - \sigma^2}} \right]$$

Subscript

C	blade quarter-chord point
C.P.	center-of-pressure
d	disturbance
F	related to the lift or normal force
i	induced
I	imaginary part of a complex quantity
j	related to the jth Fourier component
m	circumferential mean value
M	related to the pitching moment
n	rotor blade number $n = 0, \pm1, \pm2, \pm3, \ldots$

Symbol	Definition
o,o	quantity evaluated at zero mean incidence and zero camber
p	point on the reference (n = 0) blade
R	real part of a complex quantity
s	steady or time-independent
u	unsteady or time-dependent
w	wake
λ	arbitrary point in the wake
0, 1, 2, ...	specific rotor blade number
(+)	pressure side of blade
(−)	suction side of blade

Superscript

+	quantity expressed in nondimensional coordinate system
−	amplitude of a harmonic function of time or mean value of a set of measured values
=	complex conjugate
^	amplitude of a harmonic function of position and time
∿	unsteady or time-dependent

ACKNOWLEDGMENTS

With sincere appreciation, the author collectively acknowledges the guidance and support of his advisor, Professor J. J. Eisenhuth; the other members of the doctoral committee; and of the many people associated with the Fluids Engineering Unit of the Applied Research Laboratory who contributed to this study. Special recognition must be given to Professor R. E. Henderson for many helpful suggestions regarding development of the theoretical model, to Professor G. B. Gurney for assistance with mechanical and electrical problems as they arose during operation of the test facility, and to Mr. R. F. Davis for programming of the theoretical solution.

CHAPTER 1

INTRODUCTION

Two of the most pressing problems facing axial flow turbomachinery

design teams at present are associated with requirements for operation

with increased efficiency and decreased radiated noise. To meet these

requirements, it is necessary to have detailed information on the influ-

ence of geometrical and operating characteristics of blade rows on their

unsteady response to distortions in the inflow velocity field. Unsteady

response as defined here refers to the unsteady lift force and pitching

moment generated on a rigid (i.e., nonvibrating) blade operating in a

nonuniform, inviscid, incompressible flow. The unsteady pressure upon

which the unsteady force and moment depends is also responsible for

generation of part of the radiated acoustic or noise field. In this

study, the objective was to investigate unsteady response. Thus, the

acoustic problem was not treated in detail. However, a brief discus-

sion is presented herein which shows how the results of this study can

be applied to define the related acoustic source field.

Historically, the best known and most widely used method for pre-

dicting the unsteady response of a turbomachine blade is a result of

the work of Kemp and Sears [1, 2]. This method is based on an

adaptation of earlier work by von Kármán and Sears [3] and Sears [4]

which defines the fluctuating lift and moment on an uncambered

flat-plate isolated airfoil subjected to a small sinusoidal velocity

disturbance in the direction normal to the chord. Kemp [5] called

attention to the relation between Sears' result for the transverse sinusoidal gust and Theodorsen's [6] result for an oscillating airfoil. Later, Meyer [7] undertook a detailed study of the pressure and velocity fluctuations on a flat plate. His equation for the pressure perturbation agreed with Küssner's [8] result for a sinusoidal "snaking" airfoil. Yeh and Eisenhuth [9] predicted theoretically the unsteady pressure distributions on a blade as a result of interaction with periodic wakes shed by an upstream blade row. They also compared their predictions with the results of a series of cavitation experiments. More recently, Horlock [10] obtained a solution for the response of an isolated airfoil at small mean angles of incidence subjected to small sinusoidal velocity perturbations parallel to the chord. He combined his results with those of Sears to treat the case of a generalized disturbance. Horlock [11] and Naumann and Yeh [12] considered the effects of camber and Naumann and Yeh produced a series of design charts which define the variation of unsteady lift as a function of blade camber and stagger angle. Holmes [13] extended these results by solving the generalized disturbance case for the pressure distribution and the pitching moment.

Even with these developments, analyses of this type are of questionable validity for treatment of the flow in a real turbomachine since they do not account for the effect on a given blade of fluctuations occurring on other blades of the same blade row. This cascade effect could exert a strong influence on the results, particularly for blade rows with close blade-to-blade spacing and high values of stagger angle.

Several authors, for example, Whitehead [14], Mani [15], Schorr and Reddy [16], and Smith [17], in a continuation of Whitehead's work, have developed analytical models which account for the unsteady effects of the entire blade row. However, these methods specify the response only for a cascade of uncambered flat-plate blades at zero mean incidence angle. For efficient design work, it is necessary to specify how the fluctuating forces and moments vary, in both magnitude and phase, with variations in blade geometry and operating conditions.

In recently published results, Henderson [18] has solved the unsteady cascade lift problem when postulated in this frame of reference. He obtained agreement between theoretically and experimentally determined rotor response inferred from analysis of the time-mean total pressure change across the rotor. He concluded that the contribution of neighboring blades in the blade row to the unsteady lift on the reference blade was significant and that, as a result, representation of the unsteady response of a turbomachine blade by isolated airfoil analyses, however well refined, was not valid.

The rigid blade, or blade response, analyses of the type previously discussed have counterparts in vibrating blade, or flutter, analyses. Two-dimensional, incompressible, inviscid flow solutions to this problem have been presented by Whitehead [14] and by Hanamura [19]. As noted previously, Whitehead's solution applies to cascades with uncambered blades operating at zero mean incidence angle. Hanamura's solution is more general in that it applies to cascades having thin circular arc blades with arbitrary amounts of camber operating at a series of arbitrary mean incidence angles. In his report, Hanamura presented a large body of theoretical and experimental results on the flutter

characteristics of cascades having flexure and torsion degress of free-
dom. These results are presented for a wide range of variation in cam-
ber, stagger angle, space-to-chord ratio, incidence, and the blade
elastic properties.

The theoretical developments and analyses of the present study
employ Henderson's theoretical model as a basis. Chapter 2 contains
the details of the derivation due to Henderson which leads to an
expression for cascade unsteady lift force and the extension of this
derivation to include an expression for cascade unsteady pitching
moment. The derivation presented in Chapter 2 differs in certain areas
from Henderson's derivation. These differences are discussed in detail
in Appendix A. Chapter 3 contains a description of the experimental
apparatus employed in obtaining, for the first time, direct measurements
of the unsteady normal force and pitching moment acting on a rotor blade
that is operating in nonuniform inflow. Chapter 4 presents a comparison
of the theoretically predicted and experimentally determined performance
parameters and concludes with a brief discussion of possible causes for
the discrepancies. Included in Chapter 4 are theoretical predictions
based on the Whitehead-Smith model and on the theoretical model devel-
oped in Chapter 2. The two models differ in two fundamental respects.
First, in the model developed in Chapter 2, the reference blade, the
blade whose unsteady lift force and pitching moment is to be determined,
is represented by a continuous distribution of bound vorticity and the
bound vorticity on all neighboring blades is lumped at the quarter-chord
point. In the Whitehead-Smith model, each blade in the cascade is
represented by an odd number of equally spaced bound vortices. In each
model, the strength of the bound vortices varies continuously, thus

giving rise to wakes containing continuous distributions of free vor-
ticity. Second, in the model developed herein, the solution employs
integration over an arbitrary neighboring blade and its wake followed
by summation over all blades, whereas the Whitehead-Smith model employs
the same operations in the reverse order. The effects of this second
difference appear in the manner in which the predicted force and moment
coefficients vary with reduced frequency in the neighborhood of reduced
frequencies corresponding to flow conditions for which the blade-to-
blade spacing is equal to the wavelength of the inflow distortion or to
a multiple of this wavelength. At these critical reduced frequencies
the theory developed herein predicts significant changes in the level
of the coefficients. The experimental results, in a number of cases,
undergo similar level changes at the same critical values of reduced
frequency. These abrupt changes in level in the variation of the coef-
ficients with reduced frequency are not predicted by the Whitehead-Smith
theory. The only major cascade physical parameter included in the
theory that was not varied in the experimental program was blade camber.
This deficiency is overcome in the analytical results presented in
Chapter 5. This chapter contains theoretical results which define the
effects of changes in cascade physical parameters and operating
conditions on cascade response for a range of conditions beyond those
covered in the experimental program.

The manner in which the unsteady results obtained in this study
can be applied to the problem of isolated rotor noise generation is
quite straightforward. Rotor-alone noise generation is a problem that
has been studied extensively because of the many and varied uses for
rotors in fluid systems in homes, farms, commercial buildings, industry,

and all phases of transportation. The literature is much too extensive
to permit a thorough review here; however, a few key references should
serve as a starting point.

One of the earliest studies of multibladed rotor, or propeller,
radiated noise was conducted by Gutin [20] who replaced the periodic
forces by acoustic dipoles. More recently, Tyler and Sofrin [21]
reviewed this problem and also presented a solution for the case of a
rotor located in a cylindrical duct. A thorough review of the entire
problem area was recently presented by House [22]. He states that, in
subsonic, incompressible, aerodynamic noise problems, both monopole and
dipole source mechanisms can exist but that it has been demonstrated
that the really important aspects arise from sources of the dipole
type.

An acoustic analysis employing the unsteady force results obtained
in this study should be restricted to apply to cases for which the
wavelength of the radiated sound is much greater than the chord length
of the blade. For these cases, the blade acts, from an acoustic stand-
point, as a compact dipole source. Then the magnitude of the acoustic
pressure at a distant point is proportional to the product of the fre-
quency times the magnitude of the unsteady force times the directivity
index (a cosine dependence) divided by the product of the distance from
the source to the distant point times the speed of sound in the fluid
medium. Thus, an equivalent acoustic dipole can be defined to represent
the unsteady force acting on any radial increment of a reference blade.
The dipole should be located at the blade center-of-pressure position
and aligned with its major axis normal to the blade chord line. By
representing the reference blade as a finite number of equal height

radial increments, a radial distribution of equivalent acoustic dipoles would result. The equivalent acoustic source distribution for the entire rotor could then be defined by specifying the acoustic pressure magnitude on the remaining blades by use of the blade-to-blade phase relationship. This equivalent acoustic source distribution would then represent the unsteady lift forces acting on the rotor.

A listing of the major tasks that were completed in this study is presented below for the experimental, theoretical, and analytical areas. They are:

(1) Experimental

    (a) Designed, assembled, and conducted shakedown testing of the Axial Flow Research Fan facility.

    (b) Designed, fabricated, and calibrated the disturbance-generating wire grids.

    (c) Designed, fabricated, instrumented, and statically and dynamically calibrated the unsteady force and moment sensor.

    (d) Developed a working data acquisition and reduction system.

    (e) Conducted tests to determine unsteady cascade response.

(2) Theoretical

    (a) Rederived Henderson's solution for unsteady cascade lift and improved the derivation by:

        (1) Solving certain integrals that previously had been computed numerically,

(2) Included a term dependent upon mean incidence
and camber that previously had been ignored,
and

(3) Rigorously defined the region of validity of
the theoretical model.

(b) Derived the equation for the unsteady cascade
pitching moment.

(3) Analytical

(a) Defined the over-all effects of cascade stagger angle,
space-to-chord ratio, mean incidence, camber, and
reduced frequency on cascade unsteady response.

Conclusions and recommendations for the direction of future theoretical
and experimental work are presented as Chapter 6.

CHAPTER 2

DERIVATION OF THE THEORETICAL MODEL

2.1 Introduction

This analysis was originally intended to consist of an extention
of Henderson's [18] analysis of the fluctuating lift on an axial flow
rotor by derivation of the expression for the fluctuating pitching
moment. However, in reviewing Henderson's derivation, a number of
errors were detected and corrected. Thus, the results presented in the
following sections of this chapter contain a complete derivation of a
revised equation for the fluctuating lift as well as the derivation of
the desired expression for the fluctuating pitching moment. The com-
plete statement of the analysis presented herein necessarily repeats
much of Henderson's work. A discussion of the differences that exist
in the two analyses is presented in Appendix A.

2.2 Flow Model and Basic Assumptions

The problem under consideration is the interaction of an isolate.
axial flow rotor with a spatially varying periodic incompressible inlet
flow. In order to permit a two-dimensional treatment, it is necessary
to assume that the flow proceeds through the rotor along concentric
cylindrical surfaces. Any chosen cylindrical stream surface or section
through the rotor may then be developed into a plane, as shown in Figure
1. The resulting representation is called an infinite cascade of
blades. Its geometric parameters are stagger angle ξ, blade-to-blade
spacing S, chord length C, and maximum camber y_{max}.
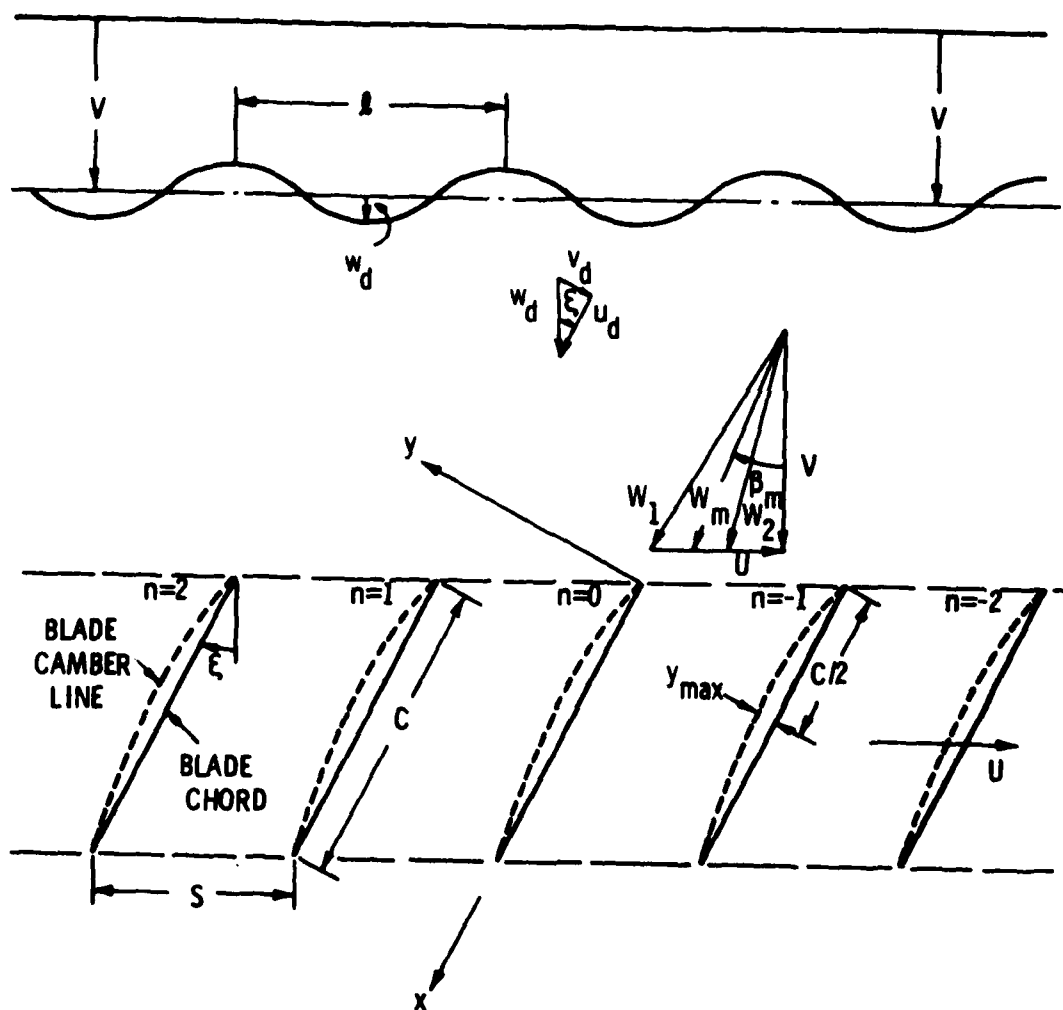
Figure 1.   Two-Dimensional Cascade of Cambered Airfoils
Moving Through a Disturbance Flow Field.

The disturbance flow shown in Figure 1 represents a special case in which the rotor inlet absolute velocity is axial in direction and varies sinusoidally, with wavelength ℓ, in the direction of motion of the blades. This sinusoidal representation is appropriate since any periodic inflow can be decomposed by Fourier analysis into a related series of harmonic waves of this type. Such a purely axial inflow could be generated by the presence of support struts which produce no mean tangential flow.

Throughout this analysis, the disturbance flow properties characterize this flow as it exists prior to its interaction with the rotor, i.e., far upstream. In Figure 1, the circumferential mean rotor inlet absolute velocity V represents the velocity with which fluid is transported through the machine. The far upstream disturbance flow field is fixed relative to solid boundaries, and the rotor blade row moves through the flow field with a constant rotational velocity U. The circumferential mean velocities, relative to the blades at the inlet and exit, are shown as W_1 and W_2 along with the mean relative velocity W_m which is displaced from the axial direction by the angle β_m. The disturbance velocity amplitude w_d is positive in the direction of positive V. Components of w_d perpendicular and parallel to the blade chord are v_d and u_d, respectively.

Based on the circulation theory of airfoils, each blade in a cascade is represented by a vortex sheet, i.e., by a system of vortex lines with a continuous distribution of vorticity. Since the total circulation around each blade is variable, because of the nonuniformity of the inflow and the effects of neighboring blades, each blade leaves a wake composed of continuously distributed vortex lines behind itself.

This is the concept upon which this analysis is based; however, a modification to this model, shown in Figure 2, is employed herein which greatly simplifies the mathematical treatment. This modification affects only the vortex distribution on the blades. It is suggested by the results of Tanabe and Horlock [23], who analyzed the steady lift in a cascade. They represented the reference blade (n = 0 in Figure 2), the blade whose lift they evaluated, by vortex lines distributed continuously along the blade chord and concentrated the vorticity on the adjacent blades (n = ±1, ±2, etc., in Figure 2) in a vortex line located at the quarter-chord point. This simplified model produced results in excellent agreement with an exact analysis by Weinig [24] except at very low values of space-to-chord ratio, $S/C < 0.5$, and high values of stagger angle, $\xi > 60^{\circ}$.

The mathematical analysis presented in the remainder of this chapter follows the procedure utilized by Bisplinghoff et al. [25] for the case of an isolated airfoil. Bisplinghoff et al.'s analysis, in turn, draws heavily on results presented earlier by Reissner [26]. In the present case, the treatment is more complex due to the presence of the additional blades in the cascade. Additional assumptions which are required in isolated airfoil theory also apply in this cascade analysis. They are:

(1)   the flow is nonviscous;

(2)   the blades may be represented by thin slightly cambered airfoils at small mean angles of incidence;

(3)   the disturbance velocities, v_d and u_d, are small in comparison with the mean relative velocity W_m;
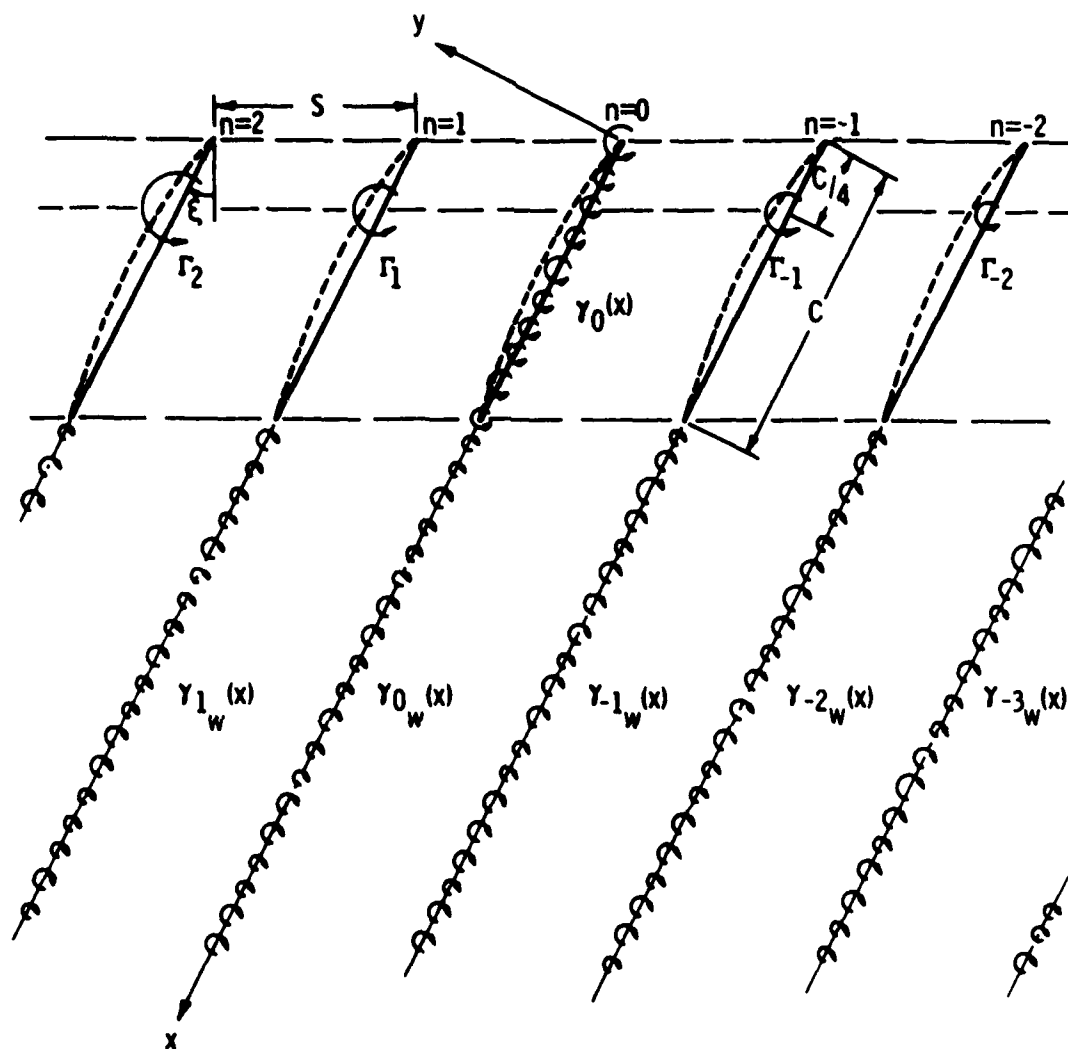
Figure 2. Vortex Representation of a Cascade Operating in Unsteady Flow.

(4) the shed or trailing vorticity is transported away from the blades in the direction of the blade chord with the mean relative velocity W_m;

(5) a blade induces no chordwise velocity upon itself; and

(6) all flow quantities representing the unsteadiness vary as harmonic functions with respect to time.

2.3 Unsteady Induced Velocities

Consider the general situation illustrated in Figure 3. Let the $n = +2$ blade represent any neighboring blade. From the Biot-Savart law, the velocity dw_{i_o} induced at a point x_p on the reference ($n = 0$) blade due to an element of positive circulation $\gamma_n dx$ located at the point x_n on the nth blade is

$$dw_{i_o}(x_p) = \frac{\gamma_n(x_n)dx}{2\pi r} \quad .$$

For positive circulation, dw_{i_o} is positive as shown. The components of dw_{i_o} parallel to the x- and y-axes are

$$du_{i_o}(x_p) = -dw_{i_o}(x_p)\cos\zeta$$

and

$$dv_{i_o}(x_p) = dw_{i_o}(x_p)\sin\zeta \quad ,$$

respectively. With the relations

$$\cos\zeta = \frac{nS\cos\xi}{r} \quad ,$$
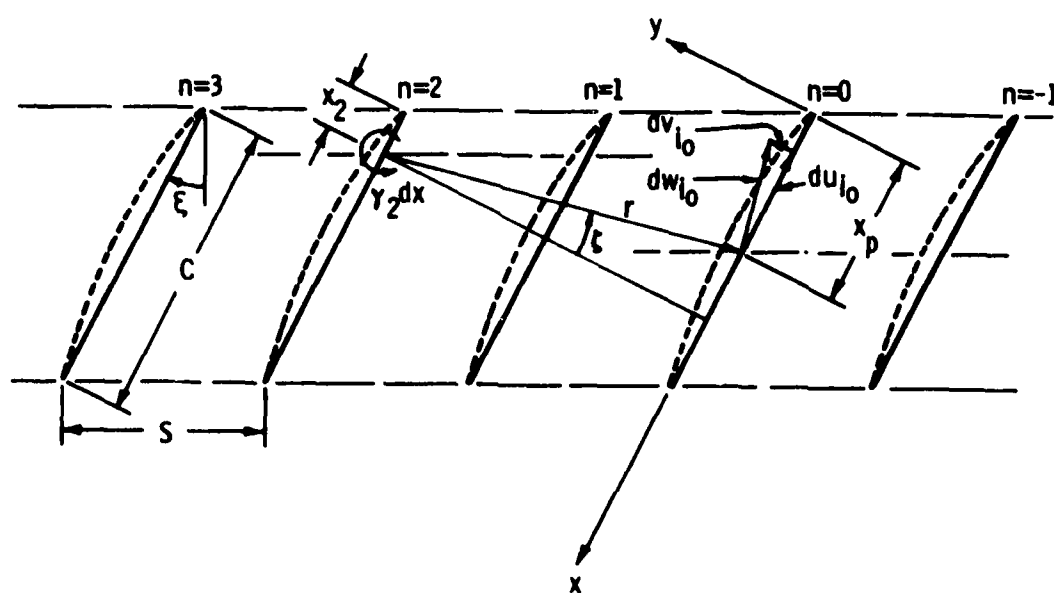
Figure 3. Incremental Velocity Induced at a Point on the
Reference Blade by an Element of Bound
Circulation on a Neighboring Blade.

$$\sin\zeta = \frac{x_n - x_p + nSsin\xi}{r} \quad ,$$

and

$$r = \left[(nScos\xi)^2 + (x_n - x_p + nSsin\xi)^2\right]^{1/2} \quad ,$$

it follows that

$$du_{i_o}(x_p) = -\frac{1}{2\pi} \frac{\gamma_n(x_n)nScos\xi dx}{(nScos\xi)^2 + (x_n - x_p + nSsin\xi)^2} \tag{1a}$$

and

$$dv_{i_o}(x_p) = \frac{1}{2\pi} \frac{\gamma_n(x_n)(x_n - x_p + nSsin\xi)dx}{(nScos\xi)^2 + (x_n - x_p + nSsin\xi)^2} \quad . \tag{1b}$$

Since the distorted inflow is periodic, the vorticity at a given distance from the leading edge of each blade in the cascade must have the same amplitude γ_o. In addition, a constant blade-to-blade phase difference must exist which is given by

$$\tau = -\frac{2\pi S}{\ell} \quad ,$$

where τ is negative since the vorticity variation on a given blade leads the variation on the blade that follows [i.e., the variation on the nth blade leads the variation on the $(n + 1)^{th}$ blade]. Therefore,

$$\gamma_n(x_n) = \gamma_o(x)e^{in\tau} \quad .$$

Utilizing the assumption that unsteady quantities vary harmonically with time,

$$\gamma_n(x_n) = \bar{\gamma}_0(x)e^{i(\nu t + n\tau)} \quad ,$$

$$du_{1_0}(x_p) = d\bar{u}_{1_0}(x_p)e^{i\nu t} \quad ,$$

and

$$dv_{1_0}(x_p) = d\bar{v}_{1_0}(x_p)e^{i\nu t} \quad ,$$

where ν, the frequency with which waves pass a point on the blade, is

$$\nu = \frac{2\pi U}{\ell}$$

and the overbar denotes the presence of a phase angle in the quantity involved. With these results, Equations (1) may be written as

$$d\bar{u}_{1_0}(x_p) = -\frac{1}{2\pi} \frac{\bar{\gamma}_0(x)e^{in\tau}nS\cos\xi\,dx}{(nS\cos\xi)^2 + (x_n - x_p + nS\sin\xi)^2} \tag{2a}$$

and

$$d\bar{v}_{1_0}(x_p) = \frac{1}{2\pi} \frac{\bar{\gamma}_0(x)e^{in\tau}(x_n - x_p + nS\sin\xi)\,dx}{(nS\cos\xi)^2 + (x_n - x_p + nS\sin\xi)^2} \quad . \tag{2b}$$

The $e^{i\nu t}$ term has been cancelled since it appears on both sides of these relations; however, its presence is implied.

Equations (2) express the incremental velocity induced at a point x_p on the reference blade by an element of circulation located at the point x_n on the nth blade. When integrated from the leading edge $(x = 0)$ to $x = \infty$ in the wake, they yield the total velocity induced at x_p due to the flow over the nth blade. However, before integrating, it is necessary to relate the free vorticity in the wake to the bound vorticity on the blade.

Consider an element of free vorticity in the wake of the reference blade of strength $\gamma_{o_w} = \bar{\gamma}_{o_w} e^{i\nu t}$ which is being transported away from the blade with velocity W_m along the positive x-axis. Then, at any location $(x,0)$ downstream of the blade, if G is a constant to be determined,

$$\gamma_{o_w} = \bar{\gamma}_{o_w} e^{i\nu t} = G e^{i\nu(t - \frac{x}{W_m})} \quad . \tag{3}$$

In general, the total circulation on the reference blade Γ_o can be expressed as

$$\Gamma_o = \bar{\Gamma}_o e^{i\nu t}$$

and, at any instant in time,

$$\Gamma_o = \int_o^C \gamma_o dx \quad .$$

In an interval of time δt, the total circulation on the blade changes its strength by

$$\frac{d\Gamma_o}{dt}\delta t = \frac{d}{dt}(\overline{\Gamma}_o e^{i\nu t})\delta t = i\nu\overline{\Gamma}_o e^{i\nu t}\delta t \quad .$$

This change in total circulation results in the production of an element of wake circulation which is shed at $x = C$ and moves downstream a distance $W_m \delta t$ in the time δt. By Kelvin's circulation theorem, this circulation is equal in magnitude and opposite in sign to the change in circulation on the blade. Therefore, from Equation (3), since

$$d\Gamma_o = -\gamma_{o_w} dx = -\gamma_{o_w} W_m \delta t \quad ,$$

it follows that

$$\gamma_{o_w} = -\frac{d\Gamma_o}{W_m \delta t} = -\frac{i\nu\overline{\Gamma}_o e^{i\nu t}}{W_m} = Ge^{i\nu(t - \frac{C}{W_m})} \quad .$$

From this,

$$G = -\frac{i\nu\overline{\Gamma}_o}{W_m}e^{i\nu C/W_m}$$

and then

$$\gamma_{o_w} = -\frac{i\nu\overline{\Gamma}_o}{W_m}e^{i\nu\left[t - \frac{(x - C)}{W_m}\right]} \quad . \tag{4}$$

Now, rewrite Equations (2) in the form

$$d\overline{u}_{1_o}(x_p) = -\frac{1}{2\pi S}\overline{\gamma}_o(x)Adx \tag{5a}$$

and

$$d\bar{v}_{i_0}(x_p) = \frac{1}{2\pi S} \bar{\gamma}_0(x) B dx \quad , \tag{5b}$$

where

$$A = \frac{e^{in\tau} n\cos\xi}{\left[\frac{x_n - x_p}{S} + n\sin\xi\right]^2 + \left[n\cos\xi\right]^2}$$

and

$$B = \frac{e^{in\tau}\left[\frac{x_n - x_p}{S} + n\sin\xi\right]}{\left[\frac{x_n - x_p}{S} + n\sin\xi\right]^2 + \left[n\cos\xi\right]^2} \quad .$$

The total velocity induced in the chordwise direction at the point x_p on the reference blade due to the flow over the nth blade is

$$\bar{u}_{i_0}(x_p) = \int_0^\infty d\bar{u}_{i_0}$$

and, from Equation (5a),

$$\bar{u}_{i_0}(x_p) = -\frac{1}{2\pi S}\int_0^\infty \bar{\gamma}_0(x) A dx = -\frac{1}{2\pi S}\int_0^C \bar{\gamma}_0(x) A dx - \frac{1}{2\pi S}\int_C^\infty \bar{\gamma}_{0_w}(x) A dx \quad .$$

From Appendix B, $A = \frac{1}{2}\Theta(\chi)$, so $\bar{u}_{i_0}(x_p)$ becomes

$$\bar{u}_{i_0}(x_p) = -\frac{1}{4\pi S}\int_0^C \bar{\gamma}_0(x)\Theta(\chi) dx - \frac{1}{4\pi S}\int_C^\infty \bar{\gamma}_{0_w}(x)\Theta(\chi) dx \quad .$$

Consider the first integral in this expression. If the bound vorticity on the nth blade is concentrated at the point x_c, then $\Theta(x_c) \neq f(x)$, and this term can be taken outside of the integral sign. Then, this integral becomes

$$\int_o^C \bar{\gamma}_o(x)\Theta(\chi)dx = \Theta(x_c) \int_o^C \bar{\gamma}_o(x)dx = \Theta(x_c)\bar{\Gamma}_o \quad .$$

Now consider the second integral. With the wake vorticity distribution given by Equation (4),

$$\int_C^\infty \bar{\gamma}_{o_w}(x)\Theta(\chi)dx = - \frac{i\nu\bar{\Gamma}_o}{W_m} \int_C^\infty e^{i\nu(\frac{C - x}{W_m})}\Theta(\chi)dx$$

$$= - \frac{i\nu\bar{\Gamma}_o}{W_m} \int_C^\infty e^{i\omega}e^{i\nu(\frac{C - 2x}{2W_m})}\Theta(\chi)dx \quad ,$$

where the reduced frequency $\omega = \frac{\nu C}{2W_m}$. By defining $\Delta = \frac{\bar{\Gamma}_o e^{i\omega}}{C}$, this can be written as

$$\int_C^\infty \bar{\gamma}_{o_w}(x)\Theta(\chi)dx = -2i\omega\Delta \int_C^\infty e^{-i\omega(\frac{2x}{C} - 1)}\Theta(\chi)dx \quad .$$

With a transformation of coordinates to a nondimensionalized system whose origin is located at the mid-chord point on the reference blade defined by

$$x^+ = \frac{2x}{C} - 1 \quad , \quad y^+ = \frac{2y}{C} \quad ,$$

the wake integral becomes

$$\int_C^\infty \overline{\gamma}_{o_w}(x)\Theta(\chi)dx = -iC\omega\Delta \int_1^\infty e^{-i\omega x^+}\Theta(\chi^+)dx^+ \quad .$$

Note that in the nondimensional coordinate system, the leading edge of the reference blade is located at the point (-1,0) and the trailing edge is located at the point (1,0). Thus, the total velocity induced in the chordwise direction at a point x_p^+ on the reference blade by the flow over the nth blade can be expressed as

$$\overline{u}_{i_o}(x_p^+) = -\frac{\overline{\Gamma}_o\Theta(x_c^+)}{4\pi S} + \frac{i\omega\Delta}{4\pi}\left[\frac{C}{S}\right]\int_1^\infty e^{-i\omega\lambda^+}\Theta(\chi_\lambda^+)d\lambda^+ \quad , \tag{6}$$

where λ^+ is a dummy variable of integration running only in the wake.

Now, consider the total velocity induced normal to the chord at the point x_p on the reference blade by the flow over the nth blade. By analogy with the development above,

$$\overline{v}_{i_o}(x_p) = \int_o^\infty d\overline{v}_{i_o} \quad .$$

From Equation (5b),

$$\bar{v}_{i_0}(x_p) = \frac{1}{2\pi S}\int_0^\infty \bar{\gamma}_0(x)B\,dx = \frac{1}{2\pi S}\int_0^C \bar{\gamma}_0(x)B\,dx + \frac{1}{2\pi S}\int_C^\infty \bar{\gamma}_{0_w}(x)B\,dx \quad.$$

From Appendix B, $B = -\frac{1}{2i}\Phi(\chi)$, so

$$\bar{v}_{i_0}(x_p) = -\frac{1}{4\pi iS}\int_0^C \bar{\gamma}_0(x)\Phi(\chi)\,dx - \frac{1}{4\pi iS}\int_C^\infty \bar{\gamma}_{0_w}(x)\Phi(\chi)\,dx \quad.$$

Since the bound vorticity on all blades except the reference blade is concentrated at the point x_c, $\Phi(\chi_c) \neq f(x)$ and the first integral in this expression becomes

$$\int_0^C \bar{\gamma}_0(x)\Phi(\chi)\,dx = \Phi(\chi_c)\int_0^C \bar{\gamma}_0(x)\,dx = \Phi(\chi_c)\bar{\Gamma}_0 \quad.$$

By employing the wake vorticity distribution, Equation (4), the second integral can be written as

$$\int_C^\infty \bar{\gamma}_{0_w}(x)\Phi(\chi)\,dx = -\frac{i\nu\bar{\Gamma}_0}{W_m}\int_C^\infty e^{i\nu(\frac{C-x}{W_m})}\Phi(\chi)\,dx$$

$$= -iC\omega\Delta\int_1^\infty e^{-i\omega x^+}\Phi(\chi^+)\,dx^+ \quad.$$

Thus, the total velocity induced in the direction normal to the chord at the point x_p^+ on the reference blade due to the flow over the nth blade is

$$\bar{v}_{i_o}(x_p^+) = -\frac{\bar{\Gamma}_o \phi(x_c^+)}{4\pi i S} + \frac{\omega\Delta}{4\pi}\left[\frac{C}{S}\right]\int_1^\infty e^{-i\omega\lambda^+}\phi(x_\lambda^+)d\lambda^+ \quad . \tag{7}$$

The total velocity induced at the point x_p^+ by all of the blades can be found by taking the summation of Equations (6) and (7) from n = −∞ to n = +∞. For the chordwise velocity component, the result is

$$\bar{u}_{i_o}(x_p^+) = -\frac{\bar{\Gamma}_o}{4\pi S}\left[\sum_{-\infty}^{-1}+\sum_1^\infty\right]\Theta(x_c^+)$$

$$+ \frac{i\omega\Delta}{4\pi}\left[\frac{C}{S}\right]\left[\sum_{-\infty}^{-1}+\sum_1^\infty\right]\int_1^\infty e^{-i\omega\lambda^+}\Theta(x_\lambda^+)d\lambda^+ \quad , \tag{8}$$

where, within the framework of thin airfoil theory, it has been assumed that the reference (n = 0) blade induces no chordwise velocity upon itself.

The transverse velocity component is given by

$$\bar{v}_{i_o}(x_p^+) = -\frac{\bar{\Gamma}_o}{4\pi i S}\left[\sum_{-\infty}^{-1} + \sum_{1}^{\infty}\right]\phi(x_c^+)$$

$$+ \frac{\omega\Delta}{4\pi}\left[\frac{C}{S}\right]\left[\sum_{-\infty}^{-1} + \sum_{1}^{\infty}\right]\int_1^\infty e^{-i\omega\lambda^+}\phi(x_\lambda^+)d\lambda^+$$

$$+ \frac{1}{2\pi S}\int_o^\infty \bar{\gamma}_o(x_o)B_o dx_o \quad , \tag{9}$$

where the last term represents the effect of the reference blade. Note that the vorticity distribution on the reference blade $\bar{\gamma}_o(x_o)$ is a continuous function of x_o.

The last term in Equation (9) can be rearranged by utilizing Equation (4) and the fact that $B_o = \dfrac{S}{x_o - x_p}$. Employing the procedures used previously leads to

$$\frac{1}{2\pi S}\int_o^\infty \bar{\gamma}_o(x_o)B_o dx_o = \frac{1}{2\pi S}\int_o^C \bar{\gamma}_o(x_o)B_o dx_o + \frac{1}{2\pi S}\int_C^\infty \bar{\gamma}_{o_w}(x_o)B_o dx_o$$

$$= \frac{1}{2\pi}\oint_o^C \frac{\bar{\gamma}_o(x_o)}{x_o - x_p}dx_o - \frac{i\nu\bar{\Gamma}_o}{2\pi W_m}\int_C^\infty \frac{e^{i\frac{\nu}{W_m}(C - \lambda_o)}}{\lambda_o - x_p}d\lambda_o$$

$$= \frac{1}{2\pi} \int\limits_{-1}^{1} \frac{\bar{\gamma}_o(x_o^+)dx_o^+}{x_o^+ - x_p^+} + \frac{\omega\Delta}{i\pi} \int\limits_{1}^{\infty} \frac{e^{-i\omega\lambda_o^+}}{\lambda_o^+ - x_p^+}d\lambda_o^+ \quad ,$$

where the Cauchy principal value is required for the airfoil integral.
Substituting this result into Equation (9) leads to the desired relation

$$\bar{v}_{i_o}(x_p^+) = \frac{1}{2\pi} \int\limits_{-1}^{1} \frac{\bar{\gamma}_o(x_o^+)dx_o^+}{x_o^+ - x_p^+} + \frac{\omega\Delta}{i\pi} \int\limits_{1}^{\infty} \frac{e^{-i\omega\lambda^+}d\lambda^+}{\lambda^+ - x_p^+} - \frac{\bar{\Gamma}_o}{4\pi i S} \left[\sum_{-\infty}^{-1} + \sum_{1}^{\infty} \right] \Phi(x_c^+)$$

$$+ \frac{\omega\Delta}{4\pi} \left[\frac{C}{S} \right] \left[\sum_{-\infty}^{-1} + \sum_{1}^{\infty} \right] \int\limits_{1}^{\infty} e^{-i\omega\lambda^+} \Phi(x_\lambda^+)d\lambda^+ \quad , \qquad (10)$$

where λ_o^+ has been set equal to λ^+ since λ^+ varies from 1 to ∞ for all
values of n. If the terms containing the summations are neglected in
Equation (10), the remaining two terms are identical to the results
presented by Bisplinghoff et al. [25] for an isolated airfoil.

2.4 Unsteady Vorticity Distribution

Definition of the unsteady response of a cascade of blades sub-
jected to a periodic perturbation in inlet velocity requires an evalua-
tion of the vorticity distribution $\bar{\gamma}_o(x_p^+)$ on the reference blade. The
basis for solution of Equation (10) for $\bar{\gamma}_o(x_p^+)$ is the inversion formula
by Söhngen [27] which states that, for any two functions P and Q of
engineering interest, the unique solution of the integral equation

$$P(x_p^+) = -\frac{1}{2\pi} \oint_{-1}^{1} \frac{Q(x_o^+)}{x_o^+ - x_p^+} dx_o^+ \quad,$$

for which $Q(1)$ is finite or zero, is

$$Q(x_p^+) = -\frac{2}{\pi} \sqrt{\frac{1 - x_p^+}{1 + x_p^+}} \oint_{-1}^{1} \sqrt{\frac{1 + x_o^+}{1 - x_o^+}} \frac{P(x_o^+)}{x_p^+ - x_o^+} dx_o^+ \quad.$$

The functions P and Q must be continuous, except possibly for a finite number of finite discontinuities and/or a finite number of integrable singularities. An integrable singularity at $x_o^+ = x_p^+$ is one which, in the neighborhood of this point, can be shown to behave like $\dfrac{1}{(x_p^+ - x_o^+)^d}$, where d is a positive number less than one.

By rewriting Equation (10) as

$$-\frac{1}{2\pi} \oint_{-1}^{1} \frac{\gamma_o(x_o^+) dx_o^+}{x_o^+ - x_p^+} = \bar{v}_{i_o}(x_p^+) + \frac{\omega\Delta}{i\pi} \int_{1}^{\infty} \frac{e^{-i\omega\lambda^+} d\lambda^+}{\lambda^+ - x_p^+}$$

$$-\frac{\bar{\Gamma}_o}{4\pi i S} \left[\sum_{-\infty}^{-1} + \sum_{1}^{\infty} \right] \phi(\chi_c^+)$$

$$+\frac{\omega\Delta}{4\pi} \left[\frac{C}{S} \right] \left[\sum_{-\infty}^{-1} + \sum_{1}^{\infty} \right] \int_{1}^{\infty} e^{-i\omega\lambda^+} \phi(\chi_\lambda^+) d\lambda^+$$

and temporarily regarding Δ (i.e., $\bar{\Gamma}_o$) as a known quantity, application of the inversion formula leads to

$$\bar{\gamma}_o(x_p^+) = \frac{2}{\pi}\sqrt{\frac{1-x_p^+}{1+x_p^+}} \oint_{-1}^{1} \sqrt{\frac{1+x_o^+}{1-x_o^+}} \frac{\bar{v}_{i_o}(x_o^+)}{x_p^+ - x_o^+} dx_o^+$$

$$- \frac{2\omega\Delta}{i\pi^2}\sqrt{\frac{1-x_p^+}{1+x_p^+}} \oint_{-1}^{1} \sqrt{\frac{1+x_o^+}{1-x_o^+}} \int_{1}^{\infty} \frac{e^{-i\omega\lambda^+}d\lambda^+}{(\lambda^+ - x_o^+)(x_p^+ - x_o^+)} dx_o^+$$

$$+ \frac{2}{\pi}\sqrt{\frac{1-x_p^+}{1+x_p^+}} \oint_{-1}^{1} \sqrt{\frac{1+x_o^+}{1-x_o^+}}$$

$$\cdot \left[\frac{\bar{\Gamma}_o}{4\pi i S} \left[\sum_{-\infty}^{-1} + \sum_{1}^{\infty} \right] \phi(\chi_c^+) \right] \frac{dx_o^+}{x_p^+ - x_o^+}$$

$$- \frac{2}{\pi}\sqrt{\frac{1-x_p^+}{1+x_p^+}} \oint_{-1}^{1} \sqrt{\frac{1+x_o^+}{1-x_o^+}} \left[\frac{\omega\Delta}{4\pi}\left[\frac{C}{S}\right] \left[\sum_{-\infty}^{-1} + \sum_{1}^{\infty} \right] \right.$$

$$\left. \cdot \int_{1}^{\infty} e^{-i\omega\lambda^+}\phi(\chi_\lambda^+)d\lambda^+ \right] \frac{dx_o^+}{x_p^+ - x_o^+} \quad ,$$

where the $\left[\sum_{-\infty}^{-1} + \sum_{1}^{\infty} \right]$ operation has been placed outside of the integral sign since the same result can be obtained by considering the reference

blade and integrating along the nth blade after which the summation is carried out.

Note that only the induced velocity $\bar{v}_{i_o}(x_o^+)$ appears in this expression. The velocity $\bar{v}_{i_o}(x_o^+)$ will eventually be specified through boundary conditions on the reference blade. The influence of $\bar{u}_{i_o}(x_o^+)$ has been neglected since, as is shown by Tanabe and Horlock [23], its contribution is of a higher order.

By interchanging the order of integration in the second and fourth terms on the right-hand side, dropping the subscript zero in the quantities x_o^+ and $\bar{v}_{i_o}$ and introducing expressions for $\Phi(\chi_c^+)$ and $\Phi(\chi_\lambda^+)$ from Appendix B, $\bar{\gamma}_o(x_p^+)$ can be written as

$$
\bar{\gamma}_o(x_p^+) = \frac{2}{\pi} \sqrt{\frac{1 - x_p^+}{1 + x_p^+}} \oint_{-1}^{1} \sqrt{\frac{1 + x^+}{1 - x^+}} \frac{\bar{v}_i(x^+)}{x_p^+ - x^+} dx^+
$$

$$
- \frac{2\omega\Delta}{i\pi^2} \sqrt{\frac{1 - x_p^+}{1 + x_p^+}} \int_{-1}^{1} \sqrt{\frac{1 + x^+}{1 - x^+}} \int_{1}^{\infty} \frac{e^{-i\omega\lambda^+} d\lambda^+}{(\lambda^+ - x^+)(x_p^+ - x^+)} dx^+
$$

$$
- \frac{\bar{\Gamma}_o}{\pi^2 C} \sqrt{\frac{1 - x_p^+}{1 + x_p^+}} \oint_{-1}^{1} \sqrt{\frac{1 + x^+}{1 - x^+}} \left[\sum_{-\infty}^{-1} + \sum_{1}^{\infty} \right]
$$

$$
\cdot \left[e^{in\tau} \left[\frac{1}{g_c - x^+} + \frac{1}{h_c - x^+} \right] \right] \frac{dx^+}{x_p^+ - x^+}
$$

$$-\frac{\omega\Delta}{i\pi^2}\sqrt{\frac{1-x_p^+}{1+x_p^+}}\oint_{-1}^{1}\sqrt{\frac{1+x^+}{1-x^+}}\left[\sum_{-\infty}^{-1}+\sum_{1}^{\infty}\right]$$

$$\cdot\left[e^{in\tau}\int_{1}^{\infty}e^{-i\omega\lambda^+}\left[\frac{1}{g_\lambda-x^+}+\frac{1}{h_\lambda-x^+}\right]d\lambda^+\right]\frac{dx^+}{x_p^+-x^+}\quad.$$

where $g_c = x_c^+ + \frac{n}{ia}$, $g_\lambda = \lambda^+ + \frac{n}{ia}$, $h_c = x_c^+ - \frac{n}{ib}$, and $h_\lambda = \lambda^+ - \frac{n}{ib}$. The quantities g_c and h_c define the position of the concentrated bound vorticies on the neighboring blades, while g_λ and h_λ define the position of elements of shed (or wake) vorticity.

The products of the form $(k - x^+)^{-1}(x_p^+ - x^+)^{-1}$ which appear in the second and fourth terms of the right-hand side of this expression can be rewritten as

$$\left[\frac{1}{k-x^+}\right]\left[\frac{1}{x_p^+-x^+}\right] = \frac{1}{k-x_p^+}\left[\frac{1}{x_p^+-x^+}-\frac{1}{k-x^+}\right]\quad.$$

Use of this relation in the expression for $\bar{\gamma}_o(x_p^+)$ leads to

$$\bar{\gamma}_o(x_p^+) = \frac{2}{\pi}\sqrt{\frac{1-x_p^+}{1+x_p^+}}\oint_{-1}^{1}\sqrt{\frac{1+x^+}{1-x^+}}\frac{\bar{v}_i(x^+)}{x_p^+-x^+}dx^+$$

$$-\frac{2\omega\Delta}{i\pi^2}\sqrt{\frac{1-x_p^+}{1+x_p^+}}\int_{1}^{\infty}\frac{e^{-i\omega\lambda^+}}{\lambda^+-x_p^+}\left[\oint_{-1}^{1}\sqrt{\frac{1+x^+}{1-x^+}}\frac{dx^+}{x_p^+-x^+}\right.$$

$$- \int_{-1}^{1} \sqrt{\frac{1 + x^+}{1 - x^+}} \frac{dx^+}{\lambda^+ - x^+} \Bigg] d\lambda^+ - \frac{\overline{\Gamma}_o}{\pi^2 C} \sqrt{\frac{1 - x_p^+}{1 + x_p^+}} \left[\sum_{-\infty}^{-1} + \sum_{1}^{\infty} \right]$$

$$\cdot \, e^{in\tau} \left\{ \frac{1}{g_c - x_p^+} \left[\oint_{-1}^{1} \sqrt{\frac{1 + x^+}{1 - x^+}} \frac{dx^+}{x_p^+ - x^+} \right. \right.$$

$$\left. - \int_{-1}^{1} \sqrt{\frac{1 + x^+}{1 - x^+}} \frac{dx^+}{g_c - x^+} \right]$$

$$+ \frac{1}{h_c - x_p^+} \left[\oint_{-1}^{1} \sqrt{\frac{1 + x^+}{1 - x^+}} \frac{dx^+}{x_p^+ - x^+} \right.$$

$$\left. \left. - \int_{-1}^{1} \sqrt{\frac{1 + x^+}{1 - x^+}} \frac{dx^+}{h_c - x^+} \right] \right\}$$

$$- \frac{\omega \Delta}{i\pi^2} \sqrt{\frac{1 - x_p^+}{1 + x_p^+}} \left[\sum_{-\infty}^{-1} + \sum_{1}^{\infty} \right] e^{in\tau} \int_{1}^{\infty} e^{-i\omega\lambda^+}$$

$$\cdot \left\{ \frac{1}{g_\lambda - x_p^+} \left[\oint_{-1}^{1} \sqrt{\frac{1 + x^+}{1 - x^+}} \frac{dx^+}{x_p^+ - x^+} \right. \right.$$

$$- \int_{-1}^{1} \sqrt{\frac{1 + x^+}{1 - x^+}} \frac{dx^+}{g_\lambda - x^+} \Bigg]$$

$$+ \frac{1}{h_\lambda - x_p^+} \Bigg[\oint_{-1}^{1} \sqrt{\frac{1 + x^+}{1 - x^+}} \frac{dx^+}{x_p^+ - x^+}$$

$$- \int_{-1}^{1} \sqrt{\frac{1 + x^+}{1 - x^+}} \frac{dx^+}{h_\lambda - x^+} \Bigg] \Bigg\} d\lambda^+ \quad . \tag{11}$$

Equation (11) is the basic equation defining $\bar{\gamma}_o(x_p^+)$. The next step in the solution for $\bar{\gamma}_o(x_p^+)$ requires evaluation of the ten integrals with respect to the variable x^+ in the last terms on the right-hand side. The value to be assigned to these integrals depends upon whether the magnitude of the individual quantities x_p^+, λ^+, g_c, h_c, g_λ, and h_λ is greater than or less than one. It is clear that $|x_p^+|^2 \leq 1$ since x_p^+ represents a point on the reference blade. It is also clear that $|\lambda^+|^2 > 1$ since λ^+ represents a point in the wake of the reference blade. In Appendix C, an analysis is presented which shows that the magnitude of the remaining quantities (g_c, h_c, g_λ, and h_λ) is greater than one for values of the cascade parameters space-to-chord ratio (S/C) and stagger angle (ξ) of interest. In fact, the boundary defined on a plot of (S/C) versus $\sin\xi$ by setting $|g_c|^2 = |h_c|^2 = 1$ and $|g_\lambda|^2 = |h_\lambda|^2 = 1$ establishes the limiting values of the cascade parameters for which this theoretical model is valid (see Appendix C).

Replacing the ten integrals discussed above by appropriate values, obtained from Equations (1) and (2) of Appendix D, and simplifying yields the following expression for the reference blade vorticity distribution:

$$\bar{\gamma}_o(x_p^+) = \frac{2}{\pi} \sqrt{\frac{1 - x_p^+}{1 + x_p^+}} \int_{-1}^{1} \sqrt{\frac{1 + x^+}{1 - x^+}} \frac{\bar{v}_1(x^+)}{x_p^+ - x^+} dx^+$$

$$- \frac{2i\omega\Delta}{\pi} \sqrt{\frac{1 - x_p^+}{1 + x_p^+}} \int_{1}^{\infty} \sqrt{\frac{\lambda^+ + 1}{\lambda^+ - 1}} \frac{e^{-i\omega\lambda^+}}{\lambda^+ - x_p^+} d\lambda^+$$

$$+ \frac{\bar{\Gamma}_o}{\pi C} \sqrt{\frac{1 - x_p^+}{1 + x_p^+}} \left[\sum_{-\infty}^{-1} + \sum_{1}^{\infty} \right]$$

$$\cdot e^{in\tau} \left[\frac{1}{g_c - x_p^+} \sqrt{\frac{g_c + 1}{g_c - 1}} + \frac{1}{h_c - x_p^+} \sqrt{\frac{h_c + 1}{h_c - 1}} \right]$$

$$- \frac{i\omega\Delta}{\pi} \sqrt{\frac{1 - x_p^+}{1 + x_p^+}} \left[\sum_{-\infty}^{-1} + \sum_{1}^{\infty} \right]$$

$$\cdot e^{in\tau} \left[\int_{1}^{\infty} \sqrt{\frac{g_\lambda + 1}{g_\lambda - 1}} \frac{e^{-i\omega\lambda^+}}{g_\lambda - x_p^+} d\lambda^+ \right.$$

$$+ \int_1^\infty \sqrt{\frac{h_\lambda + 1}{h_\lambda - 1}} \; \frac{e^{-i\omega\lambda^+}}{h_\lambda - x_p^+} d\lambda^+ \Bigg] \quad . \tag{12}$$

In this quation, the first two terms on the right-hand side represent the vorticity distribution on an isolated airfoil.

The total circulation on the reference blade $\overline{\Gamma}_o$ is given by

$$\overline{\Gamma}_o = \int_0^C \overline{\gamma}_o(x_p) dx_p \quad .$$

With $x_p = \frac{C}{2}(x_p^+ + 1)$ and $dx_p = \frac{C}{2}dx_p^+$, the relation for $\overline{\Gamma}_o$ becomes

$$\frac{2\overline{\Gamma}_o}{C} = \int_{-1}^1 \overline{\gamma}_o(x_p^+) dx_p^+ \quad .$$

Substituting Equation (12) into this relation and bringing the summations outside of the integrals as was done previously leads to

$$\frac{2\overline{\Gamma}_o}{C} = \frac{2}{\pi} \int_{-1}^1 \sqrt{\frac{1 + x^+}{1 - x^+}} \left[\int_{-1}^1 \sqrt{\frac{1 - x_p^+}{1 + x_p^+}} \frac{dx_p^+}{x_p^+ - x^+} \right] \overline{v}_1(x^+) dx^+$$

$$- \frac{2i\omega\Delta}{\pi} \int_1^\infty \sqrt{\frac{\lambda^+ + 1}{\lambda^+ - 1}} \left[\int_{-1}^1 \sqrt{\frac{1 - x_p^+}{1 + x_p^+}} \frac{dx_p^+}{\lambda^+ - x_p^+} \right] e^{-i\omega\lambda^+} d\lambda^+$$

$$+ \frac{\overline{\Gamma}_o}{\pi C} \left[\sum_{-\infty}^{-1} + \sum_{1}^{\infty} \right] e^{in\tau} \left\{ \sqrt{\frac{g_c + 1}{g_c - 1}} \left[\int_{-1}^{1} \sqrt{\frac{1 - x_p^+}{1 + x_p^+}} \frac{dx_p^+}{g_c - x_p^+} \right] \right.$$

$$\left. + \sqrt{\frac{h_c + 1}{h_c - 1}} \left[\int_{-1}^{1} \sqrt{\frac{1 - x_p^+}{1 + x_p^+}} \frac{dx_p^+}{h_c - x_p^+} \right] \right\}$$

$$- \frac{i\omega\Delta}{\pi} \left[\sum_{-\infty}^{-1} + \sum_{1}^{\infty} \right] e^{in\tau} \left\{ \int_{1}^{\infty} \sqrt{\frac{g_\lambda + 1}{g_\lambda - 1}} \right.$$

$$\cdot \left[\int_{-1}^{1} \sqrt{\frac{1 - x_p^+}{1 + x_p^+}} \frac{dx_p^+}{g_\lambda - x_p^+} \right] e^{-i\omega\lambda^+} d\lambda^+$$

$$\left. + \int_{1}^{\infty} \sqrt{\frac{h_\lambda + 1}{h_\lambda - 1}} \left[\int_{-1}^{1} \sqrt{\frac{1 - x_p^+}{1 + x_p^+}} \frac{dx_p^+}{h_\lambda - x_p^+} \right] e^{-i\omega\lambda^+} d\lambda^+ \right\} \quad .$$

The values of the integrals with respect to the variable x_p^+ on the right-hand side of this expression are given by Equations (3) and (4) of Appendix D. Substituting these values into the above expression, utilizing the relation $\Delta = \dfrac{\overline{\Gamma}_o e^{i\omega}}{C}$, and simplifying produces

$$\frac{2\bar{\Gamma}_o}{C} = -2 \int\limits_1^1 \sqrt{\frac{1 + x^+}{1 - x^+}}\, \bar{v}_i(x^+)dx^+$$

$$+ \frac{\bar{\Gamma}_o}{C} \left\{ \left[\sum_{-\infty}^{-1} + \sum_1^\infty \right] e^{in\tau} \left[\sqrt{\frac{g_c + 1}{g_c - 1}} + \sqrt{\frac{h_c + 1}{h_c - 1}} - 2 \right] \right.$$

$$- 2i\omega e^{i\omega} \int\limits_1^\infty \left[\sqrt{\frac{\lambda^+ + 1}{\lambda^+ - 1}} - 1 \right] e^{-i\omega\lambda^+} d\lambda^+$$

$$- i\omega e^{i\omega} \left[\sum_{-\infty}^{-1} + \sum_1^\infty \right] e^{in\tau} \left[\int\limits_1^\infty \left[\sqrt{\frac{g_\lambda + 1}{g_\lambda - 1}} - 1 \right] e^{-i\omega\lambda^+} d\lambda^+ \right.$$

$$\left. \left. + \int\limits_1^\infty \left[\sqrt{\frac{h_\lambda + 1}{h_\lambda - 1}} - 1 \right] e^{-i\omega\lambda^+} d\lambda^+ \right] \right\} \quad . \tag{13}$$

The value of the integral with respect to the variable λ^+ in the middle term inside the large bracket on the right-hand side of Equation (13) is given as Equation (5) in Appendix D. Substituting this value into the above expression, introducing the notation

$$C_1 = \sqrt{\frac{g_c + 1}{g_c - 1}} \quad ,$$

$$C_2 = \sqrt{\frac{h_c + 1}{h_c - 1}} \quad ,$$

$$D_1 = \int_1^\infty \left[\sqrt{\frac{g_\lambda + 1}{g_\lambda - 1}} - 1 \right] e^{-i\omega\lambda^+} d\lambda^+ \quad ,$$

and

$$D_2 = \int_1^\infty \left[\sqrt{\frac{h_\lambda + 1}{h_\lambda - 1}} - 1 \right] e^{-i\omega\lambda^+} d\lambda^+ \quad ,$$

and collecting terms yields the following expression for the total circulation on the reference blade:

$$\bar{\Gamma}_o = \frac{2C \int_{-1}^1 \sqrt{\frac{1 + x^+}{1 - x^+}} \, \bar{v}_1(x^+) dx^+}{i\pi\omega e^{i\omega}\left[H_1^{(2)}(\omega) + iH_0^{(2)}(\omega)\right] + \left[\sum_{-\infty}^{-1} + \sum_1^\infty\right] \left[e^{in\tau}(G_1)\right]} \tag{14}$$

where $G_1 = \left[C_1 + C_2 - 2 - i\omega e^{i\omega}(D_1 + D_2)\right]$. In Equation (14), the numerator and the first term of the denominator represent the circulation magnitude on an isolated airfoil.

2.5 Unsteady Pressure Distribution

The unsteady distribution of the pressure difference across the reference blade can be determined by application of the equation of motion in the chordwise direction

$$\left(\frac{\partial}{\partial t} + q\frac{\partial}{\partial x}\right)(q_{(-)} - q_{(+)}) = -\frac{1}{\rho}\frac{\partial}{\partial x}(p_{(-)} - p_{(+)}) = -\frac{1}{\rho}\frac{\partial}{\partial x}(\Delta p) \quad .$$

where $q = W_m + u_d$ is the net chordwise velocity along the airfoil, and the subscripts (-) and (+) refer to the suction and pressure surfaces of the blade, respectively. The velocities $q_{(-)}$ and $q_{(+)}$ can be written as

$$q_{(-)} = W_m + u_d + \frac{\gamma_o}{2}$$

and

$$q_{(+)} = W_m + u_d - \frac{\gamma_o}{2} \quad ,$$

where u_d is the disturbance velocity in the chordwise direction (see Figure 1) and $\frac{\gamma_o}{2}$ is the velocity induced by the vorticity distribution γ_o which represents the reference blade. Thus, the equation of motion can be written as

$$\left[\frac{\partial}{\partial t} + (W_m + u_d)\frac{\partial}{\partial x} \right] \gamma_o = - \frac{1}{\rho} \frac{\partial}{\partial x}(\Delta p) \quad .$$

Integration of this expression from the leading edge of the blade to any location σ yields the pressure difference at σ in terms of the vorticity distribution as

$$-\Delta p(\sigma) = \rho(W_m + u_d)\gamma_o(\sigma) + \rho\frac{\partial}{\partial t} \int_o^\sigma \gamma_o(k)dk \quad ,$$

where k is a dummy integration variable. The vorticity distribution $\gamma_o(\sigma)$ is now assumed to consist of the sum of a steady part $\gamma_{o_s}(\sigma)$ and an unsteady part $\gamma_{o_u}(\sigma)$, i.e.,

$$\gamma_0(\sigma) = \gamma_{0_s}(\sigma) + \gamma_{0_u}(\sigma) \quad .$$

In keeping with the assumptions of linearized unsteady flow theory, $\gamma_{0_u}(\sigma)$ is considered to be small in comparison with $\gamma_{0_s}(\sigma)$. Substituting this expression for $\gamma_0(\sigma)$ into the equation for the unsteady pressure difference leads to

$$-\Delta p(\sigma) = \rho W_m \gamma_0(\sigma) + \rho u_d \gamma_{0_s}(\sigma) + \rho \frac{\partial}{\partial t} \int_0^\sigma \gamma_0(k) dk \quad ,$$

where, since u_d is also considered to be small in comparison with W_m, the term containing the product $u_d \gamma_{0_u}(\sigma)$ has been dropped. In the non-dimensional coordinate system, this relation can be written as

$$- \frac{\Delta p(\sigma^+)}{\rho W_m} = \gamma_0(\sigma^+) + \left[\frac{u_d}{W_m} \right] \gamma_{0_s}(\sigma^+) + \left[\frac{C}{2 W_m} \right] \frac{\partial}{\partial t} \int_0^{\sigma^+} \gamma_0(k^+) dk^+ \quad .$$

Assuming, as has been done throughout this analysis, that all quantities associated with the flow vary harmonically with time,

$$\Delta p(\sigma^+) = \overline{\Delta p}(\sigma^+) e^{i\nu t} \quad ,$$

$$\gamma_0(\sigma^+) = \overline{\gamma_0}(\sigma^+) e^{i\nu t} \quad ,$$

and

$$u_d = \overline{u}_d e^{i\nu t} \quad .$$

Substituting these relations into the expression for the unsteady pressure difference leads to

$$-\frac{\overline{\Delta p}(\sigma^+)}{\rho W_m} = \overline{\gamma}_0(\sigma^+) + \left[\frac{\overline{u}_d}{W_m}\right] \gamma_{0_s}(\sigma^+) + i\omega \int_{-1}^{\sigma^+} \overline{\gamma}_0(k^+)dk^+ \quad . \qquad (15)$$

The last term on the right-hand side of Equation (15) requires integrating the expression for $\overline{\gamma}_0(k^+)$ given as Equation (12) between the limits -1 and σ^+. This integration is performed by moving the summations outside of the integral sign, reversing the order of integration in the first, second, and fourth terms, employing Equations (6) and (7) of Appendix D, and collecting terms. The result is

$$\int_{-1}^{\sigma^+} \overline{\gamma}_0(k^+)dk^+ = -\frac{2}{\pi} \int_{-1}^{1} \left[\sqrt{\frac{1+x^+}{1-x^+}} \left[\frac{\pi}{2} + \sin^{-1}\sigma^+\right] \right.$$

$$\left. + \Omega(\sigma^+,x^+) \right] \overline{v}_i(x^+)dx^+$$

$$-\frac{2i\omega\Delta}{\pi} \int_{1}^{\infty} \left[\sqrt{\frac{\lambda^+ + 1}{\lambda^+ - 1}} \left[\frac{\pi}{2} + \sin^{-1}\sigma^+\right] \right.$$

$$\left. + \Lambda(\sigma^+,\lambda^+) \right] e^{-i\omega\lambda^+}d\lambda^+ + \frac{\overline{\Gamma}_0}{\pi C} \left[\sum_{-\infty}^{-1} + \sum_{1}^{\infty}\right]$$

$$\cdot\ e^{in\tau}\left[\ \left[\ \frac{\pi}{2}+\sin^{-1}\sigma^{+}\right]\ \left[\ \sqrt{\frac{g_{c}+1}{g_{c}-1}}+\sqrt{\frac{h_{c}+1}{h_{c}-1}}\ \right]\right.$$

$$\left. +\ \Lambda(\sigma^{+},g_{c})+\Lambda(\sigma^{+},h_{c})\ \right]-\frac{i\omega\Delta}{\pi}\left[\ \sum_{-\infty}^{-1}+\sum_{1}^{\infty}\ \right]$$

$$\cdot\ e^{in\tau}\left[\ \int_{1}^{\infty}\left[\ \sqrt{\frac{g_{\lambda}+1}{g_{\lambda}-1}}\left[\ \frac{\pi}{2}+\sin^{-1}\sigma^{+}\right]\right.\right.$$

$$\left. +\ \Lambda(\sigma^{+},g_{\lambda})\ \right]\ e^{-i\omega\lambda^{+}}d\lambda^{+}$$

$$+\int_{1}^{\infty}\left[\ \sqrt{\frac{h_{\lambda}+1}{h_{\lambda}-1}}\left[\ \frac{\pi}{2}+\sin^{-1}\sigma^{+}\right]\right.$$

$$\left.\left. +\ \Lambda(\sigma^{+},h_{\lambda})\ \right]\ e^{-i\omega\lambda^{+}}d\lambda^{+}\ \right]\ .$$

As noted by Bisplinghoff et al. [25], this expression can be simplified by subtracting from it the product of the quantity $\frac{1}{\pi}(\frac{\pi}{2}+\sin^{-1}\sigma^{+})$ and Equation (13). The result is

$$\int_{-1}^{\sigma^{+}}\overline{\gamma}_{o}(k^{+})dk^{+}=-\frac{2}{\pi}\int_{-1}^{1}\Omega(\sigma^{+},x^{+})\overline{v}_{i}(x^{+})dx^{+}-\frac{2i\omega\Delta}{\pi}\int_{1}^{\infty}\left[\ \Lambda(\sigma^{+},\lambda^{+})\right.$$

$$+ \left[\frac{\pi}{2} + \sin^{-1}\sigma^+ \right] \right] e^{-i\omega\lambda^+} d\lambda^+ + \frac{\Delta e^{-i\omega}}{\pi} \left[\sum_{-\infty}^{-1} + \sum_{1}^{\infty} \right]$$

$$\cdot e^{in\tau} \left[\Lambda(\sigma^+, g_c) + \Lambda(\sigma^+, h_c) + 2 \left[\frac{\pi}{2} + \sin^{-1}\sigma^+ \right] \right]$$

$$- \frac{i\omega\Delta}{\pi} \left[\sum_{-\infty}^{-1} + \sum_{1}^{\infty} \right] e^{in\tau} \left[\int_{1}^{\infty} \left[\Lambda(\sigma^+, g_\lambda) \right. \right.$$

$$\left. + \left[\frac{\pi}{2} + \sin^{-1}\sigma^+ \right] \right] e^{-i\omega\lambda^+} d\lambda^+$$

$$\left. + \int_{1}^{\infty} \left[\Lambda(\sigma^+, h_\lambda) + \left[\frac{\pi}{2} + \sin^{-1}\sigma^+ \right] \right] e^{-i\omega\lambda^+} d\lambda^+ \right]$$

$$+ \frac{2\overline{\Gamma}_o}{\pi C} \left[\frac{\pi}{2} + \sin^{-1}\sigma^+ \right] \quad .$$

Values for the three integrals with respect to the variable λ^+ in the second and fourth terms on the right-hand side of this expression are given by Equations (8) and (9) of Appendix D. After substituting appropriate values for these integrals and collecting terms, the result is

$$\int_{-1}^{\sigma^+} \overline{\gamma}_o(k^+)dk^+ = -\frac{2}{\pi} \int_{-1}^{1} \Omega(\sigma^+, x^+)\overline{v}_1(x^+)dx^+ - \frac{2\Delta}{\pi} \int_{1}^{\infty} \frac{\partial\Lambda(\sigma^+, \lambda^+)}{\partial\lambda^+} e^{-i\omega\lambda^+} d\lambda^+$$

$$+ \frac{\Delta e^{-i\omega}}{\pi} \left[\sum_{-\infty}^{-1} + \sum_{1}^{\infty} \right] e^{in\tau} [\Lambda(\sigma^+, g_c) + \Lambda(\sigma^+, h_c)$$

$$- \Lambda(\sigma^+, g_1) - \Lambda(\sigma^+, h_1)] - \frac{\Delta}{\pi} \left[\sum_{-\infty}^{-1} + \sum_{1}^{\infty} \right]$$

$$\cdot e^{in\tau} \left[\int_1^{\infty} \frac{\partial \Lambda(\sigma^+, g_\lambda)}{\partial g_\lambda} e^{-i\omega \lambda^+} d\lambda^+ \right.$$

$$\left. + \int_1^{\infty} \frac{\partial \Lambda(\sigma^+, h_\lambda)}{\partial h_\lambda} e^{-i\omega \lambda^+} d\lambda^+ \right] . \tag{16}$$

The first two terms on the right-hand side of this expression agree with the result presented by Bisplinghoff et al. [25] for an isolated airfoil. Now, if j is temporarily permitted to represent λ^+, g_λ, or h_λ, the relation

$$\frac{\partial \Lambda(\sigma^+, j)}{\partial j} = \sqrt{\frac{1 - \sigma^+}{1 + \sigma^+}} \left[\frac{1}{\sqrt{j^2 - 1}} + \sqrt{\frac{j + 1}{j - 1}} \frac{1}{\sigma^+ - j} \right]$$

can be applied in evaluating the three integrals on the right-hand side of the above expression. This leads to

$$\int_{-1}^{\sigma^+} \bar{\gamma}_o(k^+) dk^+ = - \frac{2}{\pi} \int_{-1}^{1} \Omega(\sigma^+, x^+) \bar{v}_1(x^+) dx^+$$

$$- \frac{2\Delta}{\pi} \int_{1}^{\infty} \left[\sqrt{\frac{1 - \sigma^+}{1 + \sigma^+}} \left[\frac{1}{\sqrt{\lambda^{+2} - 1}} \right. \right.$$

$$+ \left. \left. \sqrt{\frac{\lambda^+ + 1}{\lambda^+ - 1}} \frac{1}{\sigma^+ - \lambda^+} \right] \right] e^{-i\omega\lambda^+} d\lambda^+$$

$$+ \frac{\Delta e^{-i\omega}}{\pi} \left[\sum_{-\infty}^{-1} + \sum_{1}^{\infty} \right] e^{in\tau} [\Lambda(\sigma^+, g_c)$$

$$+ \Lambda(\sigma^+, h_c) - \Lambda(\sigma^+, g_1) - \Lambda(\sigma^+, h_1)]$$

$$- \frac{\Delta}{\pi} \left[\sum_{-\infty}^{-1} + \sum_{1}^{\infty} \right] e^{in\tau} \left\{ \int_{1}^{\infty} \left[\sqrt{\frac{1 - \sigma^+}{1 + \sigma^+}} \left[\frac{1}{\sqrt{g_\lambda^2 - 1}} \right. \right. \right.$$

$$+ \left. \left. \sqrt{\frac{g_\lambda + 1}{g_\lambda - 1}} \frac{1}{\sigma^+ - g_\lambda} \right] \right] e^{-i\omega\lambda^+} d\lambda^+$$

$$+ \int_{1}^{\infty} \left[\sqrt{\frac{1 - \sigma^+}{1 + \sigma^+}} \left[\frac{1}{\sqrt{h_\lambda^2 - 1}} \right. \right.$$

$$+ \left. \left. \sqrt{\frac{h_\lambda + 1}{h_\lambda - 1}} \frac{1}{\sigma^+ - h_\lambda} \right] \right] e^{-i\omega\lambda^+} d\lambda^+ \right\} \quad . \tag{17}$$

By substituting Equations (12) and (17) into Equation (15), employing Equation (10) of Appendix D, collecting terms, and introducing the notation

$$B_1 = \int\limits_1^\infty \frac{e^{-i\omega\lambda^+}}{\sqrt{g_\lambda^2 - 1}} d\lambda^+$$

and

$$B_2 = \int\limits_1^\infty \frac{e^{-i\omega\lambda^+}}{\sqrt{h_\lambda^2 - 1}} d\lambda^+ \quad ,$$

the unsteady distribution of the pressure difference across the reference blade is given by

$$-\frac{\overline{\Delta p}(\sigma^+)}{\rho W_m} = \left[\frac{\overline{u}_d}{W_m}\right] \gamma_{o_s}(\sigma^+) + \frac{2}{\pi} \sqrt{\frac{1 - \sigma^+}{1 + \sigma^+}} \int\limits_{-1}^{1} \sqrt{\frac{1 + x^+}{1 - x^+}} \frac{\overline{v}_1(x^+)}{\sigma^+ - x^+} dx^+$$

$$- \frac{2i\omega}{\pi} \int\limits_{-1}^{1} \Omega(\sigma^+, x^+) \overline{v}_1(x^+) dx^+$$

$$- \omega \Delta H_o^{(2)}(\omega) \sqrt{\frac{1 - \sigma^+}{1 + \sigma^+}} + \frac{i\omega\Delta e^{-i\omega}}{\pi} \left[\sum\limits_{-\infty}^{-1} + \sum\limits_{1}^{\infty}\right]$$

$$\cdot e^{in\tau}\left[\Lambda(\sigma^+, g_c) + \Lambda(\sigma^+, h_c) - \Lambda(\sigma^+, g_1) - \Lambda(\sigma^+, h_1)\right]$$

$$+ \frac{\Delta e^{-i\omega}}{\pi} \sqrt{\frac{1 - \sigma^+}{1 + \sigma^+}} \left[\sum_{-\infty}^{-1} + \sum_{1}^{\infty} \right]$$

$$\cdot e^{in\tau} \left[\frac{C_1}{g_c - \sigma^+} + \frac{C_2}{h_c - \sigma^+} - i\omega e^{i\omega}(B_1 + B_2) \right] \quad . \quad (18)$$

2.6 Unsteady Lift Force

The unsteady lift on a blade, in this case the reference (n = 0) blade, in a cascade can now be determined. The basic equation is

$$\tilde{L} = \int_0^C \left[-\Delta p(\sigma) \right] d\sigma \quad ,$$

and with $\sigma = \frac{C}{2}(\sigma^+ + 1)$,

$$\tilde{L} = \frac{C}{2} \int_{-1}^{1} \left[-\Delta p(\sigma^+) \right] d\sigma^+ \quad .$$

Then, the unsteady lift coefficient can be expressed as

$$\tilde{C}_L = \frac{1}{2\pi \hat{w}_d} \int_{-1}^{1} \left[- \frac{\overline{\Delta p(\sigma^+)}}{\rho W_m} \right] d\sigma^+ \quad . \tag{19}$$

By substituting Equation (18) into Equation (19), reversing the order of integration in the second and third terms on the right-hand side, moving the summations outside of the integral signs, employing Equations (3), (4), and (11) of Appendix D, and collecting terms, the result is

$$\hat{C}_L = \frac{1}{2\pi W_m \hat{w}_d} \int_{-1}^{1} \bar{u}_d \gamma_{o_s}(x^+)dx^+ - \frac{1}{\pi \hat{w}_d} \int_{-1}^{1} \sqrt{\frac{1+x^+}{1-x^+}} \bar{v}_i(x^+)dx^+$$

$$- \frac{i\omega}{\pi^2 \hat{w}_d} \int_{-1}^{1} \bar{v}_i(x^+) \left[\int_{-1}^{1} \Omega(\sigma^+,x^+)d\sigma^+ \right] dx^+ - \frac{\omega \Delta H_o^{(2)}(\omega)}{2\hat{w}_d}$$

$$+ \frac{i\omega \Delta e^{-i\omega}}{2\pi^2 \hat{w}_d} \left[\sum_{-\infty}^{-1} + \sum_{1}^{\infty} \right] e^{in\tau} \left[\int_{-1}^{1} \Lambda(\sigma^+,g_c)d\sigma^+ \right.$$

$$+ \int_{-1}^{1} \Lambda(\sigma^+,h_c)d\sigma^+ - \int_{-1}^{1} \Lambda(\sigma^+,g_1)d\sigma^+$$

$$\left. - \int_{-1}^{1} \Lambda(\sigma^+,h_1)d\sigma^+ \right] + \frac{\Delta e^{-i\omega}}{2\pi \hat{w}_d} \left[\sum_{-\infty}^{-1} + \sum_{1}^{\infty} \right]$$

$$\cdot e^{in\tau} [C_1 + C_2 - 2 - i\omega e^{i\omega}(B_1 + B_2)] \quad .$$

Integration by parts can be employed with the aid of Equations (12) and (13) of Appendix D to evaluate the remaining five integrals on the right-hand side with respect to the variable σ^+. Values for these integrals are presented as Equations (14) and (15) of Appendix D. Substituting the appropriate values into the above expression leads to

$$\hat{C}_L = \frac{1}{2\pi W_m \hat{w}_d} \int_{-1}^{1} \bar{u}_d \gamma_{o_s}(x^+)dx^+ - \frac{1}{\pi \hat{w}_d} \int_{-1}^{1} \sqrt{\frac{1 + x^+}{1 - x^+}} \bar{v}_i(x^+)dx^+$$

$$- \frac{i\omega}{\pi \hat{w}_d} \int_{-1}^{1} \sqrt{1 - (x^+)^2} \bar{v}_i(x^+)dx^+ - \frac{i\omega\Delta e^{-i\omega}}{2\pi \hat{w}_d} \left[\sum_{-\infty}^{-1} + \sum_{1}^{\infty} \right]$$

$$\cdot e^{in\tau} \left[\sqrt{\frac{g_c - 1}{g_c + 1}} - g_c + g_c \sqrt{\frac{g_c - 1}{g_c + 1}} + \sqrt{\frac{h_c - 1}{h_c + 1}} \right.$$

$$- h_c + h_c \sqrt{\frac{h_c - 1}{h_c + 1}} - \sqrt{\frac{g_1 - 1}{g_1 + 1}} + g_1 - g_1 \sqrt{\frac{g_1 - 1}{g_1 + 1}}$$

$$\left. - \sqrt{\frac{h_1 - 1}{h_1 + 1}} + h_1 - h_1 \sqrt{\frac{h_1 - 1}{h_1 + 1}} \right]$$

$$- \frac{\omega\Delta H_o^{(2)}(\omega)}{2\hat{w}_d} + \frac{\Delta e^{-i\omega}}{2\pi \hat{w}_d} \left[\sum_{-\infty}^{-1} + \sum_{1}^{\infty} \right]$$

$$\cdot e^{in\tau} [C_1 + C_2 - 2 - i\omega e^{i\omega}(B_1 + B_2)] \quad . \tag{20}$$

By employing Equation (14) and the relation $\bar{\Gamma}_o = \Delta C e^{-i\omega}$ defined earlier, the above expression for unsteady lift coefficient becomes

$$\hat{C}_L = \frac{1}{2\pi W_m \hat{w}_d} \int_{-1}^{1} \bar{u}_d \gamma_{o_s}(x^+)dx^+ - \frac{G(\omega, x_c^+, S/C, \xi)}{\pi \hat{w}_d} \int_{-1}^{1} \sqrt{\frac{1 + x^+}{1 - x^+}} \bar{v}_i(x^+)dx^+$$

$$- \frac{i\omega}{\pi \hat{w}_d} \int_{-1}^{1} \sqrt{1 - (x^+)^2} \; \overline{v}_1(x^+)dx^+ \quad , \tag{21}$$

where the function

$$G(\omega, x_c^+, S/C, \xi) =$$

$$1 + \frac{\pi\omega H_o^{(2)}(\omega) + \left[\sum_{-\infty}^{-1} + \sum_{1}^{\infty}\right] e^{in\tau}\left[i\omega e^{-i\omega}[E_1 + E_2] - e^{-i\omega}(G_2)\right]}{i\pi\omega\left[H_1^{(2)}(\omega) + iH_o^{(2)}(\omega)\right] + \left[\sum_{-\infty}^{-1} + \sum_{1}^{\infty}\right] e^{in\tau}\left[e^{-i\omega}(G_1)\right]} \tag{22}$$

with

$$E_1 = \sqrt{g_c^2 - 1} - g_c - \sqrt{g_1^2 - 1} + g_1 \quad ,$$

$$E_2 = \sqrt{h_c^2 - 1} - h_c - \sqrt{h_1^2 - 1} + h_1 \quad ,$$

and

$$G_2 = C_1 + C_2 - 2 - i\omega e^{i\omega}(B_1 + B_2) \quad .$$

This function is the cascade equivalent of the Theodorsen [6] function

$$C(\omega) = \frac{H_1^{(2)}(\omega)}{H_1^{(2)}(\omega) + iH_o^{(2)}(\omega)}$$

which appears in the expression for the unsteady lift on an oscillating
isolated airfoil. For the case of very large blade spacing (i.e., $S \to \infty$)
the terms containing the summations in Equation (22) approach zero, and,
in the limit,

$$G(\omega, x_c^+, \infty, \xi) = C(\omega)$$

as shown in Appendix E.

The analysis of the unsteady lift now requires development of
expressions for the quantities $\bar{v}_i(x^+)$, $\bar{u}_d$, and $\gamma_{o_s}(x^+)$, the only remain-
ing unknowns in Equation (21)

To specify $\bar{v}_i(x^+)$, the velocity induced normal to the chord of the
reference blade, a boundary condition is introduced which states that
the total flow (mean flow plus disturbances plus any induced flow) at
each point on the blade must be tangent to the blade camber line at
that point. Thus, the general condition

$$\frac{dy^+}{dx^+} = \frac{W_m \sin i_m + v_d + v_i}{W_m \cos i_m + u_d + u_i}$$

applies, where y^+ is the nondimensional camber line coordinate, i_m is
the mean incidence angle, and the subscripts d and i denote disturbance
and induced velocities, respectively. By assuming that i_m is small,
this expression reduces to

$$\frac{dy^+}{dx^+} = \frac{W_m i_m + v_d + v_i}{W_m + u_d + u_i} \quad .$$

Henderson [18] concludes, based upon the results of Tanabe and Horlock [23], that the induced velocity in the chordwise direction, u_i, can be neglected. Thus, the boundary condition can be reduced to the expression

$$\frac{dy^+}{dx^+} = \frac{W_m i_m + v_d + v_i}{W_m + u_d} \quad .$$ (23)

The induced velocity normal to the chord, v_i, is composed of a steady part, v_{i_s}, and an unsteady part, v_{i_u} (i.e., $v_i = v_{i_s} + v_{i_u}$). Thus, the steady flow boundary condition is

$$\frac{dy^+}{dx^+} = \frac{W_m i_m + v_{i_s}}{W_m} \quad .$$ (24)

From Equation (23),

$$v_i = (W_m + u_d)\frac{dy^+}{dx^+} - W_m i_m - v_d$$

and, from Equation (24),

$$v_{i_s} = W_m \frac{dy^+}{dx^+} - W_m i_m \quad .$$

Therefore, since $v_{i_u} = v_i - v_{i_s}$,

$$v_{i_u} = u_d \frac{dy^+}{dx^+} - v_d$$ (25)

expresses the unsteady flow boundary condition.

The equation for a symmetrical parabolic arc camber line is

$$y^+ = y^+_{max}\left[1 - (x^+)^2\right] \quad , \tag{26}$$

where y^+_{max} is the nondimensional maximum camber. Thus, the slope of
the camber line is

$$\frac{dy^+}{dx^+} = -2y^+_{max}x^+ \quad .$$

Substitution of this expression into the equations for the induced
velocities leads to

$$v_i = -2y^+_{max}(W_m + u_d)x^+ - W_m i_m - v_d \quad , \tag{27a}$$

$$v_{i_s} = -2y^+_{max}W_m x^+ - W_m i_m \quad , \tag{27b}$$

and

$$v_{i_u} = -2y^+_{max}u_d x^+ - v_d \quad . \tag{27c}$$

Throughout this analysis, the assumption that all fluctuating
quantities vary harmonically with time has been repeatedly applied.
Thus, the disturbance velocities, v_d and u_d, which are functions of
x^+ and t, can be expressed as

$$u_d(x^+,t) = \bar{u}_d(x^+)e^{i\nu t} = \hat{u}_d e^{i(\nu t - \frac{\mu x^+}{W_m})}$$

and

$$v_d(x^+, t) = \bar{v}_d(x^+)e^{i\nu t} = \hat{v}_d e^{i(\nu t - \frac{\mu x^+}{W_m})} \quad .$$

These are expressions for a general harmonic disturbance. When $\nu \neq \mu$, they are applicable to the case analyzed by Kemp [5] and by Kemp and Sears [1] of rotor interaction with wakes shed by an upstream stator. When $\nu = \mu$, the form of the dependence upon x^+ and t is identical to that employed by Sears [4], Kemp and Sears [2], Horlock [10], Naumann and Yeh [12], Whitehead [14], and Bisplinghoff et al. [25]. The parameter μ defines the behavior of the disturbance as it moves downstream through the cascade. For example, if μ is expressed as a complex quantity, $\mu_R + i\mu_I$, then:

(1) if $\mu_I = 0$, the disturbance maximum amplitude is independent of x^+;

(2) if $\mu_I < 0$, the disturbance maximum amplitude decays exponentially with x^+;

(3) if $\mu_R = \nu$, the disturbance is convected and moves in the x^+ direction with the constant velocity W_m;

(4) if $\mu_R \neq \nu$, the disturbance moves in the x^+ direction with a constant velocity different than W_m.

By defining a second reduced frequency, $\theta \equiv \frac{\mu C}{2W_m}$, and noting that, in the nondimensional coordinate system $C = 2$, the expressions for u_d and v_d become

$$u_d(x^+, t) = \hat{u}_d e^{i(\nu t - \theta x^+)} \tag{28a}$$

and

$$v_d(x^+,t) = \hat{v}_d e^{i(\nu t - \theta x^+)} \quad . \tag{28b}$$

Note that, when $\mu_R = \nu$ and $\mu_I = 0$ (i.e., when $\mu \equiv \nu$), $\theta = \omega$, the reduced frequency defined earlier in this analysis.

Substitution of Equations (28) into Equation (27c) defines the following expression for the normal component of the unsteady induced velocity:

$$v_{i_u}(x^+,t) = -(2y_{max}^+ x^+ \hat{u}_d + \hat{v}_d) e^{i(\nu t - \theta x^+)} \quad .$$

This expression can also be written as

$$v_{i_u}(x^+,t) = \bar{v}_i(x^+) e^{i\nu t} \quad .$$

where

$$\bar{v}_i(x^+) = -(2y_{max}^+ x^+ \hat{u}_d + \hat{v}_d) e^{-i\theta x^+} \quad . \tag{29}$$

The rotor inflow velocity field shown in Figure 1 is a special case in which the mean velocity and the disturbance velocity are axial in direction. This case was chosen deliberately to avoid unnecessary complications. In the paragraphs that follow, a more general inflow velocity field will be presented and expressions for the associated normal and chordwise disturbance velocities, v_d and u_d, will be developed.

Consider the situation depicted in Figure 4. This figure illustrates the effect of a stationary upstream blade row on the flow entering a rotor blade row. The flow entering the stator is assumed to be
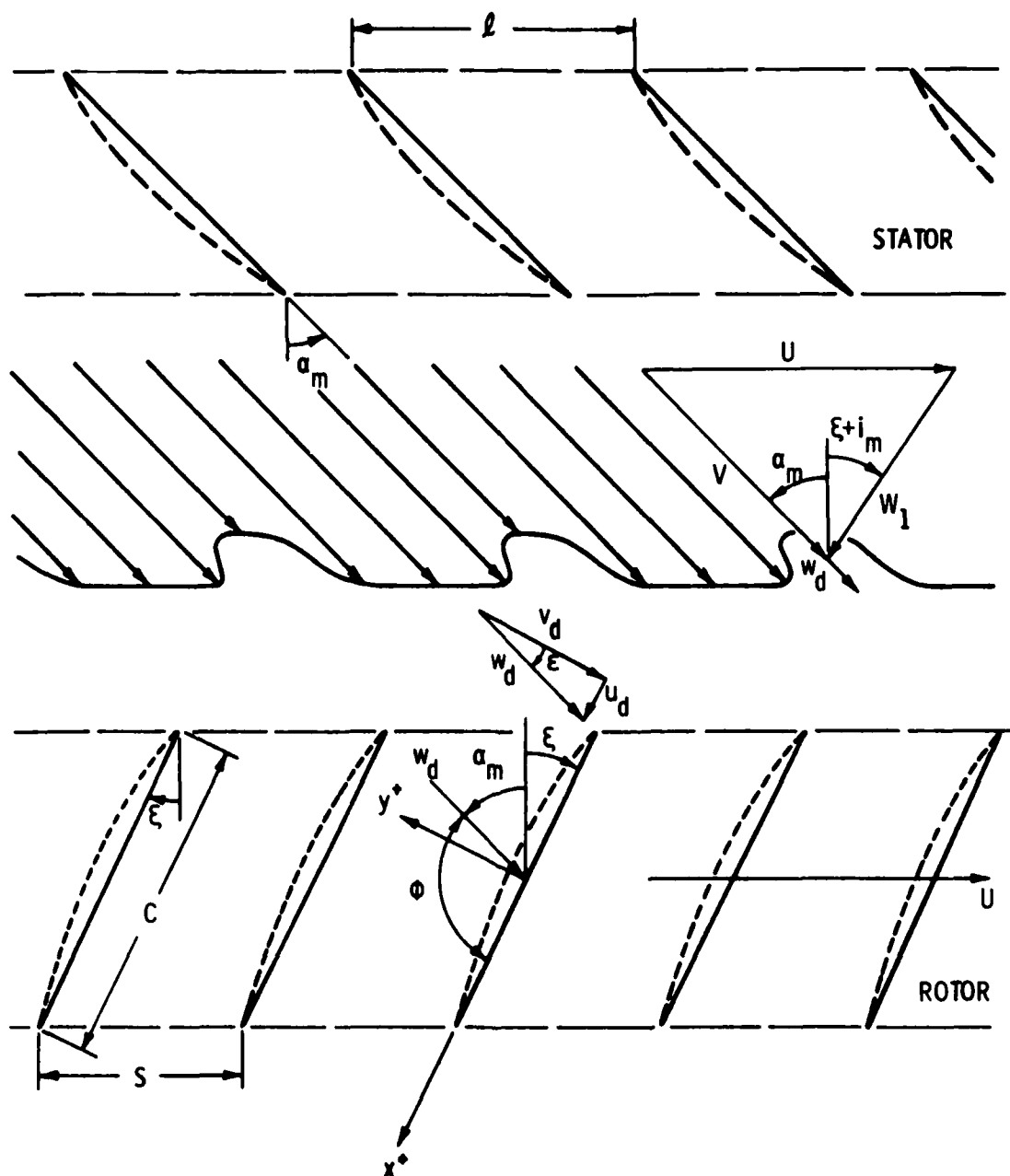
Figure 4. General Rotor Inlet Disturbance Flow Field.

uniform. The angle α_m represents the mean swirl of the flow leaving the stator blade row. This flow contains wakes shed by the stator blades with a spacing equal to ℓ, the stator blade-to-blade spacing. The velocity which characterizes the stator wake deficit, w_d, represents a fluctuation about the stator exit mean absolute velocity V. The mean inlet velocity relative to the rotor, W_1, is determined by V and the rotor rotational velocity U. Its direction differs from the direction of the rotor blade chord by the angle i_m.

The stator exit flow shown in Figure 4 can be represented, for analysis purposes, by a Fourier series. Such a representation would contain a number of harmonics, each of which would contribute to the fluctuating pressures, forces, and moments acting on the rotor blades. No generality in the development or application of this theoretical model is lost if the stator exit flow is assumed to consist of a mean flow, characterized by the velocity V, and one harmonic of the disturbance flow, w_d.

The components of the disturbance flow normal to and parallel to the rotor blade chord are

$$v_d = -w_d \cos\varepsilon$$

and

$$u_d = w_d \sin\varepsilon \quad ,$$

where the positive direction for w_d is taken as the direction of the mean absolute flow approaching the rotor (consistent between Figures 1 and 4) and the negative sign arises because of the relation between the

positive direction for w_d and the orientation of the (x^+, y^+) axis system on the reference rotor blade. As shown in Figure 4, $\phi = 180^\circ - \alpha_m - \xi$ and $\varepsilon + \alpha_m + \xi = 90^\circ$. Thus, $\varepsilon = \phi - 90^\circ$, and the disturbance flow velocity components can be written as

$$v_d = -w_d \sin\phi \tag{30a}$$

and

$$u_d = -w_d \cos\phi \quad . \tag{30b}$$

Note that, if $\alpha_m = 0$, the disturbance flow field of Figure 1 is regained, $\phi = 180^\circ - \xi$, and

$$v_d = -w_d \sin\xi$$

and

$$u_d = w_d \cos\xi \quad .$$

Relative to the moving rotor blades, the disturbance velocity is harmonic with respect to time. Thus, it can be written as

$$w_d = \bar{w}_d e^{i\nu t} = \hat{w}_d e^{i(\nu t - \theta x^+)} \quad . \tag{31}$$

After substituting Equations (28) and (31) into Equations (30), Equation (29) may be written as

$$\bar{v}_i(x^+) = \hat{w}_d (2y_{max}^+ x^+ \cos\phi + \sin\phi) e^{-i\theta x^+} \quad . \tag{32}$$

This is the general expression for the velocity induced normal to the chord of the reference blade.

The form for the chordwise disturbance velocity required in the solution of Equation (21) can be obtained by noting that $u_d = \bar{u}_d e^{i\nu t}$ and inserting this relation and Equation (31) into Equation (30b). The result is

$$\bar{u}_d = -\dot{w}_d e^{-i\theta x^+} \cos\phi \quad . \tag{33}$$

The steady vorticity distribution, $\gamma_{o_s}(x^+)$, can be obtained from Equation (12) evaluated with $\omega = 0$. Thus,

$$\gamma_{o_s}(x^+) = \frac{2}{\pi} \sqrt{\frac{1 - x^+}{1 + x^+}} \int_{-1}^{1} \sqrt{\frac{1 + k}{1 - k}} \frac{v_{i_s}(k)}{x^+ - k} dk$$

$$+ \frac{\Gamma_{o_s}}{\pi C} \sqrt{\frac{1 - x^+}{1 + x^+}} \left[\sum_{-\infty}^{-1} + \sum_{1}^{\infty} \right] \left[\frac{C_1}{g_c - x^+} + \frac{C_2}{h_c - x^+} \right] \quad ,$$

where k is a dummy integration variable and use has been made of the fact that, if $\omega = 0$, $\nu = 0$; if $\nu = 0$, $\ell = \infty$; and, if $\ell = \infty$, $\tau = 0$, and then $e^{in\tau} = 1$. The steady circulation distribution, Γ_{o_s}, can be evaluated from Equation (13) with $\omega = 0$. Thus,

$$\frac{\Gamma_{o_s}}{\pi C} = - \frac{\displaystyle\int_{-1}^{1} \sqrt{\frac{1+k}{1-k}} v_{i_s}(k)\,dk}{\pi - \frac{\pi}{2}\left[\displaystyle\sum_{-\infty}^{-1} + \sum_{1}^{\infty}\right][C_1 + C_2 - 2]} .$$

Substitution of this relation into the expression for $\gamma_{o_s}(x^+)$ and col-
lecting terms leads to

$$\gamma_{o_s}(x^+) = \frac{2}{\pi}\sqrt{\frac{1-x^+}{1+x^+}} \int_{-1}^{1} \sqrt{\frac{1+k}{1-k}} \left\{ \frac{1}{x^+ - k} \right.$$

$$\left. - \frac{\left[\displaystyle\sum_{-\infty}^{-1} + \sum_{1}^{\infty}\right]\left[\dfrac{C_1}{g_c - x^+} + \dfrac{C_2}{h_c - x^+}\right]}{2 - \left[\displaystyle\sum_{-\infty}^{-1} + \sum_{1}^{\infty}\right][C_1 + C_2 - 2]} \right\} v_{i_s}(k)\,dk .$$

This expression can be simplified by noting that

$$G(o, x_c^+, S/C, \xi)$$

$$= \lim_{\omega \to 0} G(\omega, x_c^+, S/C, \xi)$$

$$= \lim_{\omega \to 0} \left\{ \frac{i\pi\omega H_1^{(2)}(\omega)}{i\pi\omega\left[H_1^{(2)}(\omega) + iH_0^{(2)}(\omega)\right] + \left[\displaystyle\sum_{-\infty}^{-1} + \sum_1^{\infty}\right][C_1 + C_2 - 2]} \right\}$$

$$= \frac{2}{2 - \left[\displaystyle\sum_{-\infty}^{-1} + \sum_1^{\infty}\right][C_1 + C_2 - 2]} \tag{34}$$

since $\lim\limits_{\omega \to 0} \omega H_0^{(2)}(\omega) = 0$ and $\lim\limits_{\omega \to 0} \omega H_1^{(2)}(\omega) = \frac{2i}{\pi}$. Thus, $\gamma_{o_s}(x^+)$ can be expressed as

$$\gamma_{o_s}(x^+) = \frac{2}{\pi} \sqrt{\frac{1 - x^+}{1 + x^+}} \oint_{-1}^{1} \sqrt{\frac{1 + k}{1 - k}} \left[\frac{1}{x^+ - k} - \frac{G(o, x_c^+, S/C, \xi)}{2} \right.$$

$$\left. \cdot \left[\sum_{-\infty}^{-1} + \sum_1^{\infty}\right]\left[\frac{C_1}{g_c - x^+} + \frac{C_2}{h_c - x^+}\right] \right] v_{i_s}(k)dk \quad .$$

The steady velocity induced normal to the chord, $v_{i_s}(x^+)$, is given by Equation (27b). Substituting Equation (27b) into the expression for $\gamma_{o_s}(x^+)$ and collecting terms leads to the relation

$$\gamma_{o_s}(x^+) = -\frac{2W_m}{\pi} \left\{ 2y_{max}^+ \left[\oint_{-1}^{1} \frac{kdk}{\sqrt{1 - k^2}\,(x^+ - k)} \right. \right.$$

$$+ \oint_{-1}^{1} \frac{k^2 dk}{\sqrt{1 - k^2} \, (x^+ - k)} \Bigg] + i_m \Bigg[\oint_{-1}^{1} \frac{dk}{\sqrt{1 - k^2} \, (x^+ - k)}$$

$$+ \oint_{-1}^{1} \frac{k dk}{\sqrt{1 - k^2} \, (x^+ - k)} \Bigg] - \frac{G(o, x_c^+, S/C, \xi)}{2}$$

$$\cdot \Bigg[2 y_{max}^+ \int_{-1}^{1} \sqrt{\frac{1 + k}{1 - k}} k dk + i_m \int_{-1}^{1} \sqrt{\frac{1 + k}{1 - k}} dk \Bigg]$$

$$\cdot \Bigg[\sum_{-\infty}^{-1} + \sum_{1}^{\infty} \Bigg] \Bigg[\frac{C_1}{g_c - x^+} + \frac{C_2}{h_c - x^+} \Bigg] \Bigg\} \quad .$$

Values for the integrals with respect to the variable k on the right-hand side of this expression are given by Equations (16) through (20) of Appendix D. Substituting these values into the above expression and collecting terms yields

$$\gamma_{o_s}(x^+) = W_m \sqrt{\frac{1 - x^+}{1 + x^+}} \Bigg[4 y_{max}^+ (1 + x^+) + 2 i_m$$

$$+ (i_m + y_{max}^+) G(o, x_c^+, S/C, \xi) \Bigg[\sum_{-\infty}^{-1} + \sum_{1}^{\infty} \Bigg]$$

$$\cdot \left[\frac{C_1}{g_c - x^+} + \frac{C_2}{h_c - x^+} \right] \right]$$

(35)

The desired expression for the unsteady lift can now be derived by substitution of the expressions for $\bar{v}_1(x^+)$, $\bar{u}_d(x^+)$, and $\gamma_{o_s}(x^+)$ given by Equations (32), (33), and (35) into Equation (21). This leads to the following relation for the unsteady lift coefficient:

$$\mathcal{C}_L = - \frac{\cos\phi}{2\pi} \left\{ \left[4y^+_{max} + 2i_m \right] \left[\int_{-1}^{1} \sqrt{\frac{1 - x^+}{1 + x^+}} e^{-i\theta x^+} dx^+ \right] \right.$$

$$+ 4y^+_{max} \left[\int_{-1}^{1} \sqrt{\frac{1 - x^+}{1 + x^+}} x^+ e^{-i\theta x^+} dx^+ \right]$$

$$+ \left[i_m + y^+_{max} \right] G(o, x^+_c, S/C, \xi) \left[\sum_{-\infty}^{-1} + \sum_{1}^{\infty} \right]$$

$$\cdot \left\{ C_1 \left[\int_{-1}^{1} \sqrt{\frac{1 - x^+}{1 + x^+}} \frac{e^{-i\theta x^+}}{g_c - x^+} dx^+ \right] \right.$$

$$+ C_2 \left[\int_{-1}^{1} \sqrt{\frac{1 - x^+}{1 + x^+}} \frac{e^{-i\theta x^+}}{h_c - x^+} dx^+ \right] \right\} \right\}$$

$$+ 4y^+_{max} G(\omega, x^+_c, S/C, \xi) \left[\int_{-1}^{1} \sqrt{\frac{1 + x^+}{1 - x^+}} x^+ e^{-i\theta x^+} dx \right]$$

$$+ 4i y^+_{max} \left[\int_{-1}^{1} \sqrt{1 - (x^+)^2} \; x^+ e^{-i\theta x^+} dx^+ \right] \Biggr\}$$

$$- \frac{\sin\phi}{\pi} \left\{ G(\omega, x^+_c, S/C, \xi) \left[\int_{-1}^{1} \sqrt{\frac{1 + x^+}{1 - x^+}} e^{-i\theta x^+} dx^+ \right] \right.$$

$$+ i\omega \left[\int_{-1}^{1} \sqrt{1 - (x^+)^2} \; e^{-i\theta x^+} dx^+ \right] \Biggr\} \quad .$$

Values for the integrals on the right-hand side of this expression are
given in Equations (21) through (27) of Appendix D. Substituting appro-
priate values for the integrals and collecting terms in the resulting
expression leads to the following equation for the unsteady lift coef-
ficient for a blade in a cascade of symmetrical parabolic arc blades
operating at a nonzero mean angle of incidence in a velocity field that
contains both transverse and chordwise disturbance velocities:

$$\tilde{C}_L = - \cos\phi \left\{ y^+_{max} \left[\left[1 + \frac{2\omega}{\theta} \right] J_2(\theta) + J_0(\theta) \right. \right.$$

$$+ G(\omega, x^+_c, S/C, \xi) \left[J_0(\theta) - J_2(\theta) - 2i J_1(\theta) \right] \Biggr]$$

$$+ \frac{(y_{max}^{+} + i_m)}{2} G(o, x_c^{+}, S/C, \xi) \left[\sum_{-\infty}^{-1} + \sum_{1}^{\infty} \right] \left[[C_1 + C_2 - 2] J_o(\theta) \right.$$

$$\left. -2 \sum_{m=1}^{\infty} (i)^{-m} J_m(\theta) \left[[g_c - \sqrt{g_c^2 - 1}]^m + [h_c - \sqrt{h_c^2 - 1}]^m \right] \right]$$

$$+ i_m \left[J_o(\theta) + i J_1(\theta) \right] \Bigg\} - \sin\phi \Bigg\{ G(\omega, x_c^{+}, S/C, \xi) \left[J_o(\theta) - i J_1(\theta) \right]$$

$$+ \left[\frac{i\omega}{\theta} \right] J_1(\theta) \Bigg\} \quad . \tag{36}$$

In Appendix E, it is shown that, for very large values of blade spacing (i.e., $S \to \infty$), Equation (36) reduces to the isolated airfoil result obtained by Horlock [11].

2.7 Unsteady Pitching Moment

The basic equation for the unsteady pitching moment about an axis through the mid-chord position, positive for leading-edge up rotation, is

$$M = - \int_{o}^{C} \left[p_{(+)}(\sigma) - p_{(-)}(\sigma) \right] \left[\sigma - \frac{C}{2} \right] d\sigma \quad .$$

As defined previously,

$$\sigma = \frac{C}{2}(\sigma^+ + 1)$$

so

$$d\sigma = (\frac{C}{2})d\sigma^+$$

and then

$$\hat{M} = \frac{C^2}{4} \int_{-1}^{1} \Delta p(\sigma^+)\sigma^+ d\sigma^+$$

in the nondimensional coordinate system. From this,

$$\hat{C}_M = -\frac{1}{4\pi\hat{w}_d} \int_{-1}^{1} \left[-\frac{\overline{\Delta p}(\sigma^+)}{\rho W_m} \right] \sigma^+ d\sigma^+ \quad . \tag{37}$$

By substituting Equation (18) into Equation (37), reversing the order
of integration in the second and third terms on the right-hand side,
moving the summations outside of the integral signs, employing Equations
(22), (28), and (29) of Appendix D, and collecting terms, the result is

$$\hat{C}_M = -\frac{1}{4\pi W_m \hat{w}_d} \int_{-1}^{1} \overline{u}_d \gamma_{o_s}(x^+)x^+ dx^+ - \frac{1}{2\pi\hat{w}_d} \int_{-1}^{1} \sqrt{1 - (x^+)^2}\ \overline{v}_i(x^+) dx^+$$

$$+ \frac{i\omega}{2\pi^2\hat{w}_d} \int_{-1}^{1} \overline{v}_i(x^+) \left[\int_{-1}^{1} \Omega(\sigma^+, x^+)\sigma^+ d\sigma^+ \right] dx^+ - \frac{\omega\Delta H_o^{(2)}(\omega)}{8\hat{w}_d}$$

$$- \frac{i\omega\Delta e^{-i\omega}}{4\pi^2 \hat{w}_d} \left[\sum_{-\infty}^{-1} + \sum_{1}^{\infty} \right] e^{in\tau} \left[\int_{-1}^{1} \Lambda(\sigma^+, g_c)\sigma^+ d\sigma^+ \right.$$

$$\left. + \int_{-1}^{1} \Lambda(\sigma^+, h_c)\sigma^+ d\sigma^+ - \int_{-1}^{1} \Lambda(\sigma^+, g_1)\sigma^+ d\sigma^+ - \int_{-1}^{1} \Lambda(\sigma^+, h_1)\sigma^+ d\sigma^+ \right]$$

$$- \frac{\Delta e^{-i\omega}}{4\pi \hat{w}_d} \left[\sum_{-\infty}^{-1} + \sum_{1}^{\infty} \right] e^{in\tau} \left[g_c(C_1 - 1) - C_1 + h_c(C_2 - 1) - C_2 \right.$$

$$\left. + \frac{i\omega e^{i\omega}}{2}(B_1 + B_2) \right] \quad .$$

Integration by parts can be employed with the aid of Equations (30) and
(31) of Appendix D to evaluate the remaining five integrals on the
right-hand side with respect to the variable σ^+. Values for these
integrals are presented as Equations (32) and (33) of Appendix D.
Substituting the appropriate values into the above expression leads to

$$\overset{\text{?}}{C}_M = - \frac{1}{4\pi W_m \hat{w}_d} \int_{-1}^{1} \bar{u}_d \gamma_{o_s}(x^+) x^+ dx^+ - \frac{1}{2\pi \hat{w}_d} \int_{-1}^{1} \sqrt{1 - (x^+)^2} \, \bar{v}_1(x^+) dx^+$$

$$+ \frac{i\omega}{4\pi \hat{w}_d} \int_{-1}^{1} x^+ \sqrt{1 - (x^+)^2} \, \bar{v}_1(x^+) dx^+ - \frac{\omega \Delta H_o^{(2)}(\omega)}{8\hat{w}_d}$$

$$- \frac{i\omega\Delta e^{-i\omega}}{8\pi\hat{w}_d} \left[\sum_{-\infty}^{-1} + \sum_{1}^{\infty} \right] e^{in\tau}[g_c^2 - g_c \sqrt{g_c^2 - 1}$$

$$+ h_c^2 - h_c \sqrt{h_c^2 - 1} - g_1^2 + g_1 \sqrt{g_1^2 - 1} - h_1^2 + h_1 \sqrt{h_1^2 - 1}]$$

$$- \frac{\Delta e^{-i\omega}}{4\pi\hat{w}_d} \left[\sum_{-\infty}^{-1} + \sum_{1}^{\infty} \right] e^{in\tau} \left[g_c(C_1 - 1) - C_1 + h_c(C_2 - 1) - C_2 \right.$$

$$\left. + \frac{i\omega e^{i\omega}}{2}(B_1 + B_2) \right] \quad .$$

By employing Equation (14) and the relation $\overline{\Gamma}_o = \Delta C e^{-i\omega}$, as was done in the unsteady lift analysis, the above expression for the unsteady pitching moment coefficient becomes

$$\mathcal{C}_M = - \frac{1}{4\pi W_m \hat{w}_d} \int_{-1}^{1} \overline{u}_d \gamma_{o_s}(x^+) x^+ dx^+ - \frac{1}{2\pi\hat{w}_d} \int_{-1}^{1} \sqrt{1 - (x^+)^2} \, \overline{v}_i(x^+) dx^+$$

$$+ \frac{i\omega}{4\pi\hat{w}_d} \int_{-1}^{1} \sqrt{1 - (x^+)^2} \, \overline{v}_i(x^+) x^+ dx^+$$

$$- \frac{B(\omega, x_c^+, S/C, \xi)}{4\pi\hat{w}_d} \int_{-1}^{1} \sqrt{\frac{1 + x^+}{1 - x^+}} \, \overline{v}_i(x^+) dx^+ \quad , \tag{38}$$

where the function

$$B(\omega, x_c^+, S/C, \xi)$$

$$= \frac{\pi\omega H_o^{(2)}(\omega) + \left[\sum_{-\infty}^{-1} + \sum_{1}^{\infty}\right] e^{in\tau}\left[K_1 + i\omega[B_1 + B_2]\right]}{i\pi\omega\left[H_1^{(2)}(\omega) + iH_o^{(2)}(\omega)\right] + \left[\sum_{-\infty}^{-1} + \sum_{1}^{\infty}\right]\left[e^{in\tau}e^{-i\omega}(G_1)\right]} \quad, \quad (39)$$

with

$$K_1 = i\omega e^{-i\omega}\left[F_1 + F_2\right] + 2e^{-i\omega}\left[g_c(C_1 - 1) - C_1 + h_c(C_2 - 1) - C_2\right] \quad,$$

$$F_1 = g_c\left[g_c - \sqrt{g_c^2 - 1}\right] - g_1\left[g_1 - \sqrt{g_1^2 - 1}\right]$$

and

$$F_2 = h_c\left[h_c - \sqrt{h_c^2 - 1}\right] - h_1\left[h_1 - \sqrt{h_1^2 - 1}\right] \quad.$$

The function $B(\omega, x_c^+, S/C, \xi)$ represents the cascade effect on the unsteady pitching moment coefficient. An analysis is presented in Appendix F which shows that, for very large values of blade spacing (i.e., $S \to \infty$), the terms containing the summations in Equation (39) approach zero. In the limit, when $S = \infty$,

$$B(\omega, x_c^+, \infty, \xi) = C(\omega) - 1 \quad.$$

The final expression for the unsteady pitching moment can now be derived by substituting the expressions for $\bar{v}_1(x^+)$, $\bar{u}_d(x^+)$, and $\gamma_{o_s}(x^+)$,

developed in the unsteady lift analysis section and given by Equations (32), (33), and (35), into Equation (38). This leads to the expression

$$
\tilde{C}_M = \frac{\cos\phi}{4\pi} \left[2i_m \int_{-1}^{1} \sqrt{\frac{1-x^+}{1+x^+}} x^+ e^{-i\theta x^+} dx^+ \right.
$$

$$
+ 2i\omega y_{max}^+ \int_{-1}^{1} \sqrt{1-(x^+)^2} \, (x^+)^2 e^{-i\theta x^+} dx^+
$$

$$
+ \left[i_m + y_{max}^+ \right] G(o, x_c^+, S/C, \xi) \left[\sum_{-\infty}^{-1} + \sum_{1}^{\infty} \right]
$$

$$
\cdot \left[C_1 \int_{-1}^{1} \sqrt{\frac{1-x^+}{1+x^+}} \frac{x^+ e^{-i\theta x^+}}{g_c - x^+} dx^+ \right.
$$

$$
\left. + C_2 \int_{-1}^{1} \sqrt{\frac{1-x^+}{1+x^+}} \frac{x^+ e^{-i\theta x^+}}{h_c - x^+} dx^+ \right]
$$

$$
\left. - 2B(\omega, x_c^+, S/C, \xi) y_{max}^+ \int_{-1}^{1} \sqrt{\frac{1+x^+}{1-x^+}} x^+ e^{-i\theta x^+} dx^+ \right]
$$

$$
+ \frac{\sin\phi}{4\pi} \left[2 \int_{-1}^{1} \sqrt{1-(x^+)^2} \, e^{-i\theta x^+} dx^+ \right.
$$

$$+ i\omega \int_{-1}^{1} \sqrt{1 - (x^{+})^{2}} \; x^{+} e^{-i\theta x^{+}} dx^{+}$$

$$- 2B(\omega, x_{c}^{+}, S/C, \xi) \int_{-1}^{1} \sqrt{\frac{1 + x^{+}}{1 - x^{+}}} e^{-i\theta x^{+}} dx^{+} \Bigg] \quad .$$

Values for the integrals on the right-hand side of this expression are given as Equations (22), (24) through (27), (34), and (35) of Appendix D. Substituting appropriate values for the integrals and collecting terms in the resulting expression leads to the expression

$$\overset{\curvearrowright}{C}_{M} = \frac{\cos\phi}{4} \left[-i_{m} J_{o}(\theta) + 2i \left[\left[\frac{\omega}{\theta} \right] y_{max}^{+} - i_{m} \right] J_{1}(\theta) \right.$$

$$+ \left[i_{m} - \frac{6i\omega y_{max}^{+}}{(\theta)^{2}} \right] J_{2}(\theta)$$

$$+ \left[i_{m} + y_{max}^{+} \right] G(o, x_{c}^{+}, S/C, \xi) \left[\sum_{-\infty}^{-1} + \sum_{1}^{\infty} \right]$$

$$\cdot \left[\left[g_{c}(C_{1} - 1) - C_{1} + h_{c}(C_{2} - 1) - C_{2} \right] J_{o}(\theta) - i(C_{1} + C_{2}) J_{1}(\theta) \right.$$
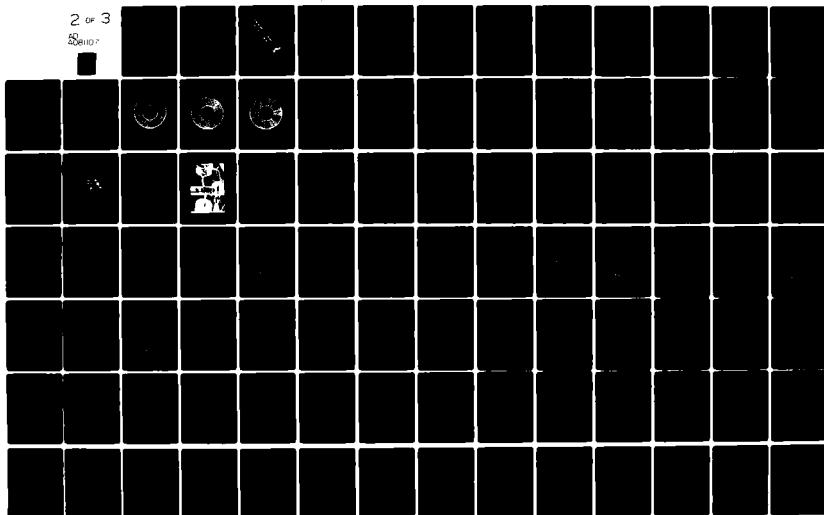
$$- 2 \left[g_c \sum_{m=1}^{\infty} (i)^{-m} (g_c - \sqrt{g_c^2 - 1})^m \right.$$

$$\left. + h_c \sum_{m=1}^{\infty} (i)^{-m} (h_c - \sqrt{h_c^2 - 1})^m \right] J_m(\theta) \right]$$

$$- y_{max}^+ B(\omega, x_c^+, S/C, \xi) \left[J_o(\theta) - 2i J_1(\theta) - J_2(\theta) \right] \right]$$

$$- \frac{\sin\phi}{4} \left[\left[\frac{2}{\theta} \right] J_1(\theta) - \left[\frac{\omega}{\theta} \right] J_2(\theta) \right.$$

$$\left. + B(\omega, x_c^+, S/C, \xi) \left[J_o(\theta) - i J_1(\theta) \right] \right] \quad . \tag{40}$$

This is the equation for the unsteady pitching moment coefficient for a blade in a cascade of symmetrical parabolic arc blades operating at a nonzero mean angle of incidence in a velocity field that contains both transverse and chordwise disturbance velocities. Its value for the limiting case of infinite spacing between adjacent blades provides a check on its validity, since, for this case, the isolated airfoil result obtained by Holmes [13] should be obtained. An analysis presented in Appendix G shows that Equation (40) reduces to Holmes' result in the limit.

CHAPTER 3

EXPERIMENTAL APPARATUS, DATA ACQUISITION,
AND DATA ANALYSIS

3.1 Introduction

The facility described in this chapter was designed specifically
to provide a capability for research on the response of axial flow
turbomachinery blade rows to subsonic, incompressible, unsteady inlet
flows. It is called the Axial Flow Research Fan. It is located in the
Garfield Thomas Water Tunnel Building of the Applied Research
Laboratory. A detailed description of the facility and related data
acquisition and reduction techniques has been presented by Bruce [28].
The data obtained using this facility are presented in a later chapter
where they are compared with theoretical predictions. An analysis of
the experimental error associated with the data is presented in Appendix
H.

3.2 The Axial Flow Research Fan

The facility is shown schematically in Figure 5. It is 18.8 ft
long and consists of an annular flow passage bounded at one end by a
bellmouth inlet and at the other end by an exhaust throttle. It has a
hub radius of 4.750 in. and a hub-to-tip radius ratio of 0.442, and it
operates in the stagnation pressure ratio range from 1.0 to 1.1. The
facility can be operated with mean axial velocities up to 110 ft/sec
with test rotor tip speeds up to 320 ft/sec. The forward region, from
the inlet to a point just upstream of the test rotor drive motor, is

THROTTLE

14.9 in.

35.0 in.

AUXILIARY FAN

AFT SUPPORT STRUTS

SILENCER AND
TEST ROTOR
DRIVE SYSTEM

81.2 in.

TEST ROTOR

FORWARD SUPPORT STRUTS

DISTURBANCE-GENERATING WIRE GRID

HUB RADIUS = 4.75 in.
CASING INSIDE RADIUS = 10.75 in.

TEST SECTION
AUTOMATED FOR
FLOW-FIELD
SURVEYS

37.3 in.

DISTURBANCE-
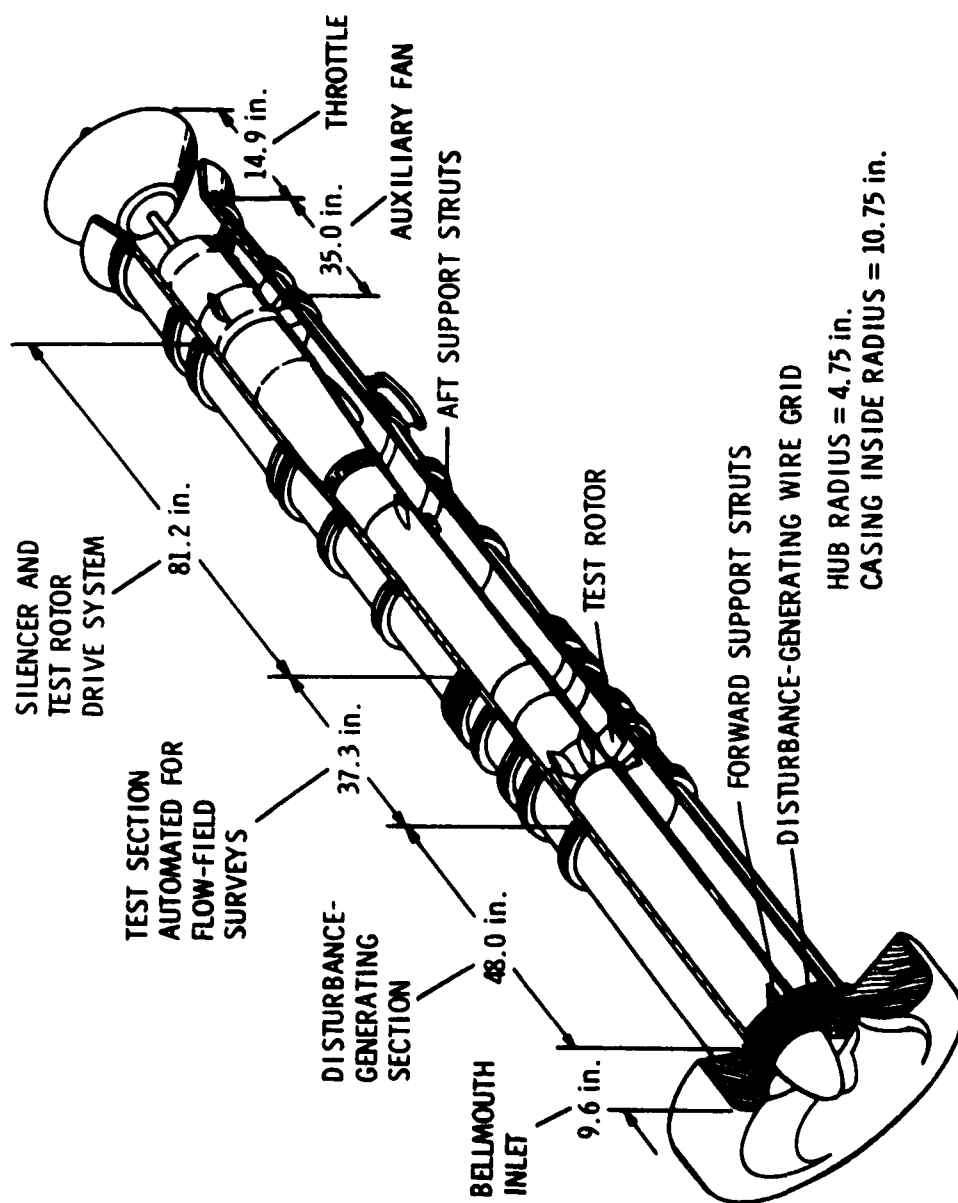GENERATING
SECTION

48.0 in.

BELLMOUTH
INLET

9.6 in.

Figure 5. Axial Flow Research Fan Schematic.

bounded by a 9.500-in. diameter cylindrical hub surface and a 21.500-in. inside diameter cylindrical outer casing. These surfaces are tapered to slightly larger diameters near the downstream end to permit housing the 20 HP test rotor drive motor inside the hub and to permit mating with the auxiliary fan outer casing. The auxiliary fan delivers 15,000 ft^3 of air per minute at a pressure of 3.5 in. of water gage at its nominal operating point. The auxilary fan drive motor and the test rotor drive motor speed can be adjusted independently at values up to 56.7 revolutions per second.

The 48.0-in. long segment located just downstream of the bellmouth inlet is the disturbance-generating section. This long flow path was required to permit the development of distorted flow fields, generated by placing specially tailored wire grids at selected positions within the cylindrical annulus, into a desired pattern at the test rotor inlet.

The section immediately downstream of the disturbance-generating section houses the test rotor-stator stage. The outer casing of the part of this section forward of the stator housing is supported by two large bearings and is free to rotate about the facility centerline. Rotation of this outer casing segment can be controlled automatically in preselected increments from a minimum step of 0.0125° to a maximum step in excess of 360°. This feature permits controlled rotation of casing mounted flow surveying probes in the circumferential direction.

The facility contains split outer casing and hub sections, both upstream of and downstream of the stator. By interchanging split sections of different lengths, it is possible to move the stator blade row relative to the rotor blade row. Rotor-stator axial spacing can be varied by this means from 3 in. to 12 in.

The hardware components downstream of the stator position are a 14-channel coin-silver slip-ring unit, the test rotor drive motor, the auxiliary fan, and the throttle. The motors and throttle were intentionally located at a downstream distance large enough to permit insertion of a silencer between the stator and the noise-generating drive motors. A silencer was available, but it was not required for this research program.

3.3 Disturbance-Generating Wire Grids

A fluid stream passing through a grid experiences a loss in total pressure ΔP. This pressure drop can be described by a dimensionless resistance coefficient K based on the upstream fluid properties as

$$K = \frac{\Delta P}{\frac{1}{2}\rho V^2} \quad .$$

A number of investigators, including Weighardt [29], have shown that grid geometry and resistance coefficient can be related by an equation of the form

$$K = \frac{cs}{(1 - s)^2} \quad . \tag{41}$$

where s is the grid solidity and c is a loss coefficient which is a function of Reynolds number Re based on grid wire diameter d and the interstitial velocity through the grid $\frac{V}{(1 - s)}$. Grid solidity is defined as the ratio of blocked area to total area. For a square mesh grid composed of wires of diameter d with wire center-to-center spacing m, grid solidity is given by

$$S = 2(\frac{d}{m}) - (\frac{d}{m})^2 \quad .$$

Cornell [30] analyzed grid resistance data for Re $\leq$ 20,000 and found,
for square mesh wire grids, that c initially decreased with increasing
Reynolds number, then leveled off at about 0.80 in the range 600 < Re <
4000, and then rose gradually to a value of 1.00 at Re $\approx$ 15,000.

In fabricating disturbance-generating grids for use in this
research program, a grid overlay technique was used; i.e., segments of
wire grid having different mesh sizes and wire diameters were placed
side-by-side in a prescribed pattern over a single support grid of low
resistance coefficient. McCarthy [31] has reported the results of a
series of experiments for an arrangement of this type. His experiments
covered the Reynolds number range from 600 to 5000 based on the overlay
grid geometry. He found that the combined resistance coefficient was
accurately predicted by adding the individual resistance coefficients
of the support and overlay grids as predicted using Equation (41) with
c = 0.78. His experiments were conducted in a water tunnel using a
support grid with a solidity of 0.267. The measured combined resistance
coefficients varied from 0.8 to 17.00.

McCarthy also developed an analytical solution for the steady,
moderately sheared, three-dimensional flow past wire grids of arbitrary
resistance distribution placed normal to the axis of a duct of arbitrary
but constant cross-section. His formulation represents an extension of
the work of Owen and Zienkiewicz [32] and Elder [33] which applies for
weakly sheared, two-dimensional flow past wire grids.

In this research program, the desired mid-span rotor inlet flow
field consists of a spatially fixed axial velocity V(η) that is

independent of radial position and varies sinusoidally in the circum-
ferential direction. Thus, $V(\eta)$ may be expressed as

$$V(\eta) = V\left[1 + (\frac{w_d}{V})\sin(N\eta)\right] \quad , \tag{42}$$

where η is circumferential position, V is circumferential mean rotor
inlet absolute velocity, w_d is disturbance velocity, and N is number of
cycles of velocity variation per circumference. In terms of $V(\eta)$ and
V, McCarthy's solution has the form

$$\frac{V(\eta)}{V} = 1 - \frac{1.02(1 + \psi)}{(1 + \psi^3)^{2/3}}(\frac{1 + 6\psi^3}{6\psi^2} - \psi) \quad . \tag{43}$$

Substitution of Equation (42) into Equation (43) leads to the expres-
sion

$$(\frac{w_d}{V})\sin N\eta = \frac{1.02(1 + \psi)}{(1 + \psi^3)^{2/3}}(\psi - \frac{1 + 6\psi^3}{6\psi^2}) \quad , \tag{44}$$

where

$$\psi = (1 + K)^{1/2} \quad ,$$

$$\psi = \frac{1 + 6\psi_o^3}{6\psi_o^2} + \frac{w_d(1 + \psi_o^3)^{2/3}}{1.02V(1 + \psi_o)} \quad ,$$

and

$$\psi_o = (1 + K_{min})^{1/2} \quad .$$

At any circumferential position, the grid resistance coefficient can be expressed as

$$K = K_{min} + \Delta K \quad ,$$

where K_{min} is associated with the large wire diameter, large wire spacing grid used to provide structural support for the grid assembly and ΔK is the increment in resistance coefficient associated with the overlay grid. Note that both K and ΔK are functions of η and that, for selected values of K_{min}, $(\frac{w_d}{V})$, and N, Equation (44) defines the variation of K with circumferential position η.

The support grid used in the grids fabricated for this research program was made of brass with d = 0.135 in., m = 1.015 in., s = 0.248, and K_{min} = 0.343. Results obtained by solving Equation (44) with K_{min} = 0.343, N = 1, and $(\frac{w_d}{V})$ = 0.05, 0.10, 0.15, and 0.20 are shown in Figure 6. For all values of $(\frac{w_d}{V})$, the circumferential variation of resistance coefficient is characterized by a peak at η = 270° that is sharper than the valley at η = 90°. This occurs because the flow in the vicinity of the screen tends to curve away from the region of high resistance coefficient and toward the region of low resistance coefficient.

The design information presented in Figure 6 with $(\frac{w_d}{V})$ = 0.20 was the basis for fabrication of the grids used in this research program. The required variation of K with η for grids having values of N other than N = 1 was obtained by replotting the data from Figure 6 with η replaced by $\frac{\eta}{N}$. Grids were fabricated for values of N of 1, 2, 4, 5, 6, 9, 12, and 15; however, due to hardware frequency response limitations, the 9-, 12-, and 15-cycle grids were not used in the research program. A detailed description of the design and evaluation of all of the grids
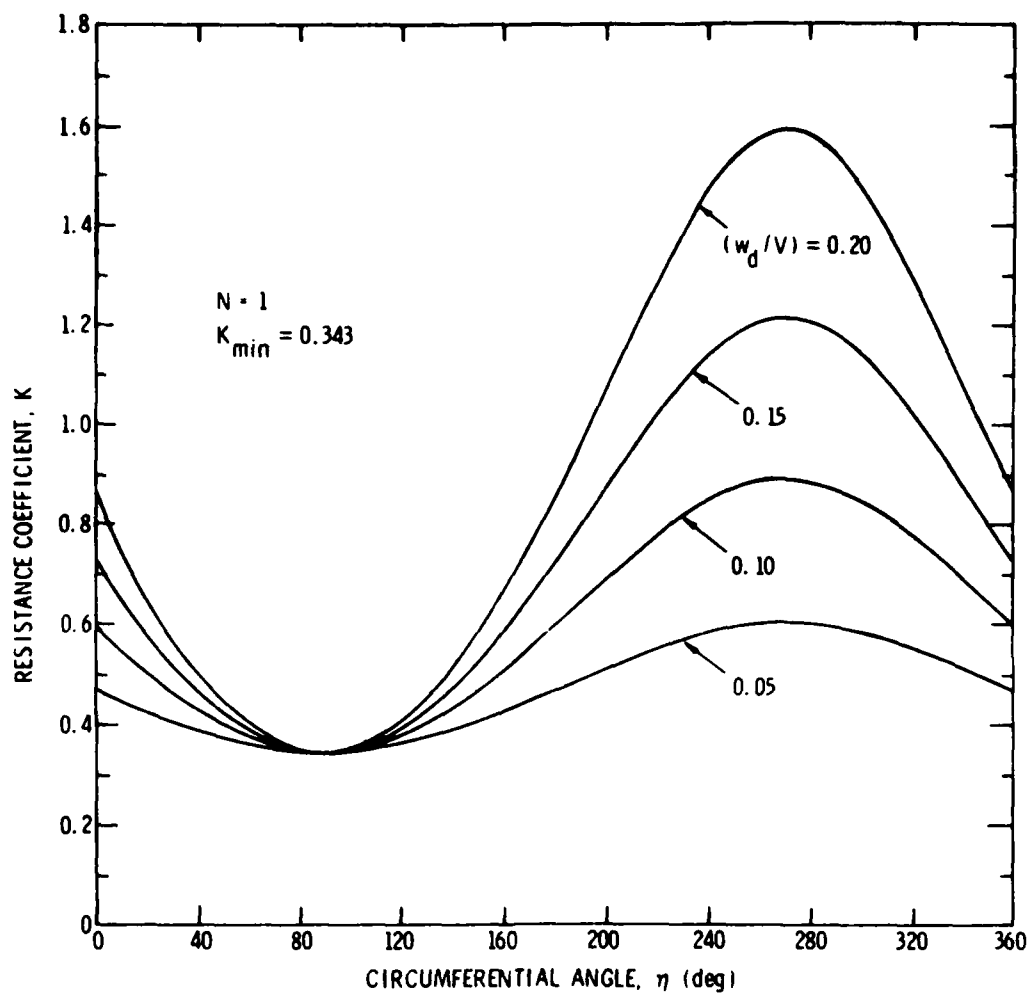
Figure 6. Theoretical Variation of Grid Resistance
Coefficient.

has been presented by Bruce [34]. The following paragraphs summarize this effort with respect to the 1-, 2-, 4-, 5-, and 6-cycle grids.

Fabrication of grids with $(\frac{w_d}{V})$ = 0.20 and K_{min} = 0.343 using McCarthy's single overlay technique required the use of overlay grid segments covering the range $0 < \Delta K < 1.248$. A summary of the characteristics of grids that were available for this purpose is presented in Table 1. As shown in Table 1, the design required definition of the angular extent of segments having combined resistance coefficients of 0.343, 0.484, 0.569, etc., to provide an approximate representation of the design variation of resistance coefficient.

Overlay segment characteristics employed in fabrication of the 1-cycle grid are presented in Figure 7. Identical overlay segment combinations were employed in fabricating the 2- and 4-cycle grids and in fabricating the 5- and 6-cycle grids. These combinations are shown in Figures 8 and 9 for the 2- and 6-cycle grids, respectively. Pictures of the 1-, 2-, and 6-cycle grids are shown as Figures 10, 11, and 12. The overlay setments were positioned on the support grid with the aid of a full-scale drawing and were attached using fine wire. All of the overlay segments were rugged enough to withstand damage during normal handling except for the ΔK = 0.226 setments used in the 2- and 4- cycle grids. These segments were fragile, thus necessitating extra precautions.

Nondimensionalized results of measurements of the mid-span rotor inlet velocity profiles generated by three of the grids are presented in Figures 13, 14, and 15. For these measurements, the grids were placed on the upstream side of the inlet support struts, and the rotor blade row was replaced by a smooth hub. Thus, the results represent

TABLE 1

CHARACTERISTICS OF GRID COMBINATIONS

Grid Material	Overlay Grid Characteristics				Combined Resistance Coefficient of Support and Overlay Grids ($K_{min} + \Delta K$)
	Spacing Between Centers (m) Inches	Wire Diameter (d) Inches	Grid Solidity (s)	Resistance Coefficient (ΔK)	
Stainless Steel	0.500	0.0350	0.135	0.141	0.484
Stainless Steel	0.100	0.0100	0.190	0.226	0.569
Stainless Steel	0.167	0.0230	0.257	0.363	0.706
Stainless Steel	0.250	0.0350	0.260	0.370	0.713
Stainless Steel	0.100	0.0200	0.360	0.685	1.028
Stainless Steel	0.125	0.0280	0.398	0.858	1.201
Stainless Steel	0.083	0.0200	0.422	0.986	1.329
Brass	0.050	0.0135	0.467	1.283	1.626
Bronze	0.100	0.2800	0.482	1.403	1.746
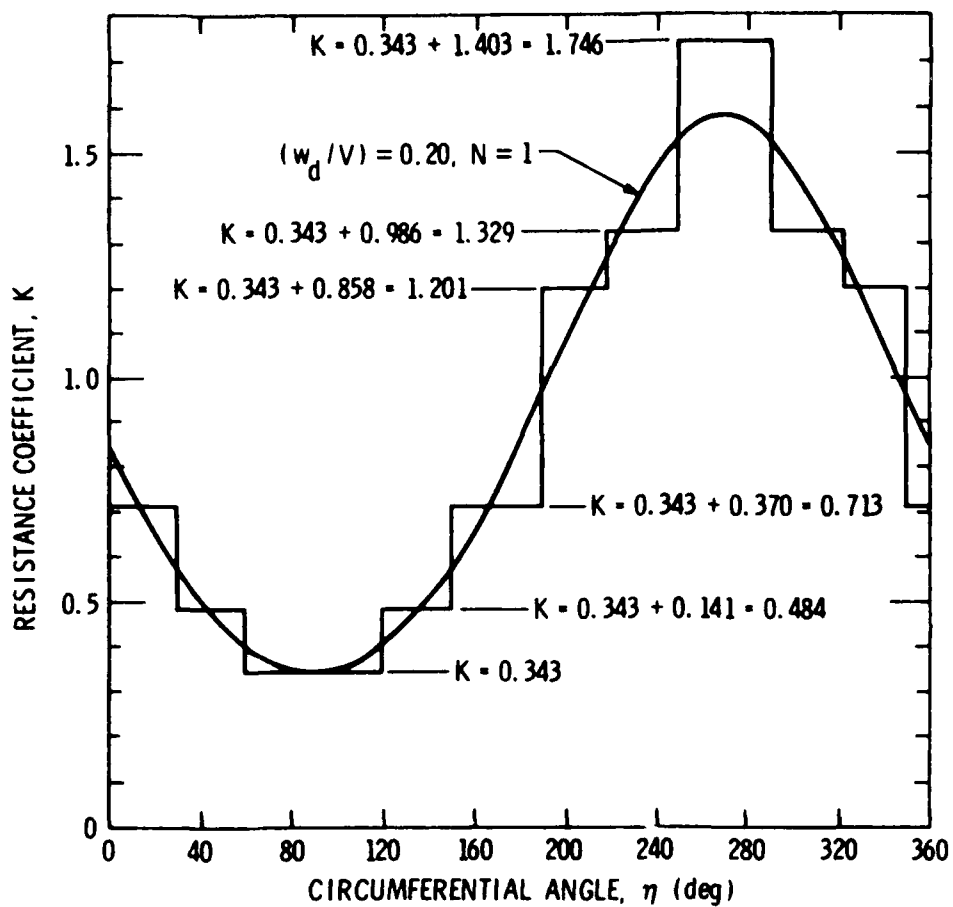
Figure 7. One-Cycle Grid Overlay Segment
Characteristics.
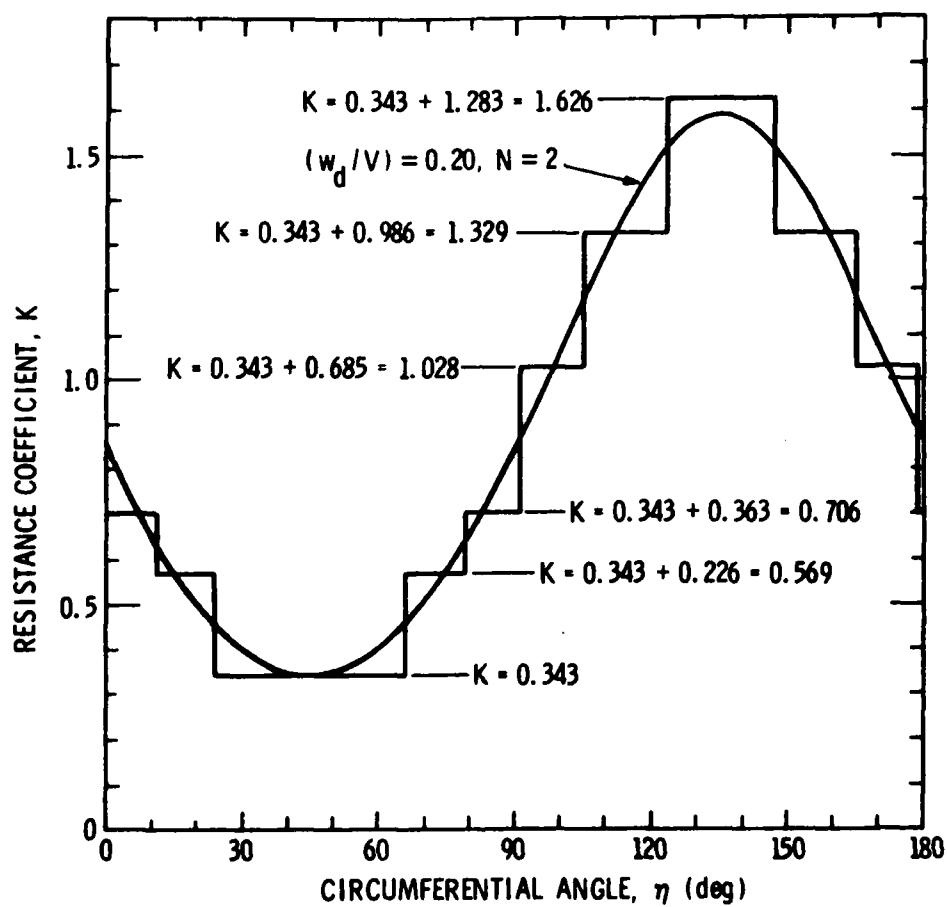
Figure 8. Two-Cycle Grid Overlay Segment
Characteristics.
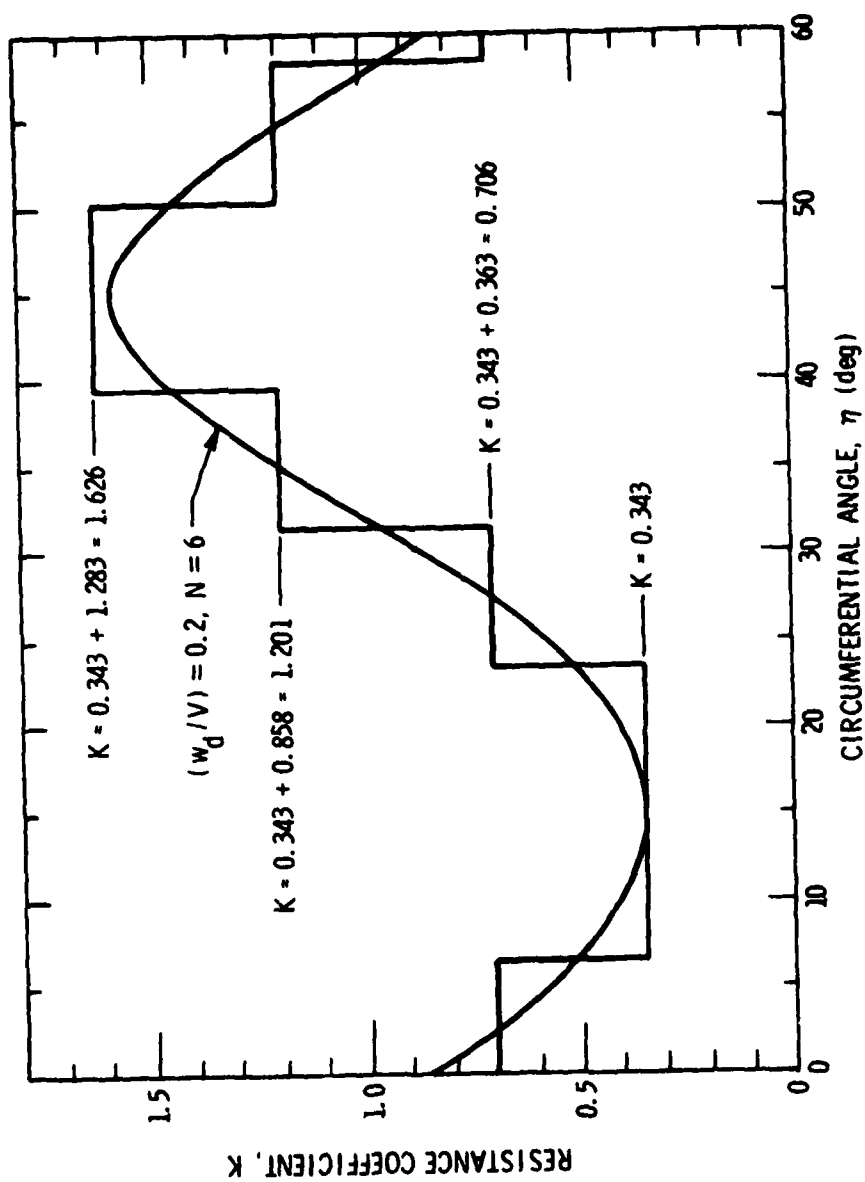
Figure 9. Six-Cycle Grid Overlay Segment Characteristics.
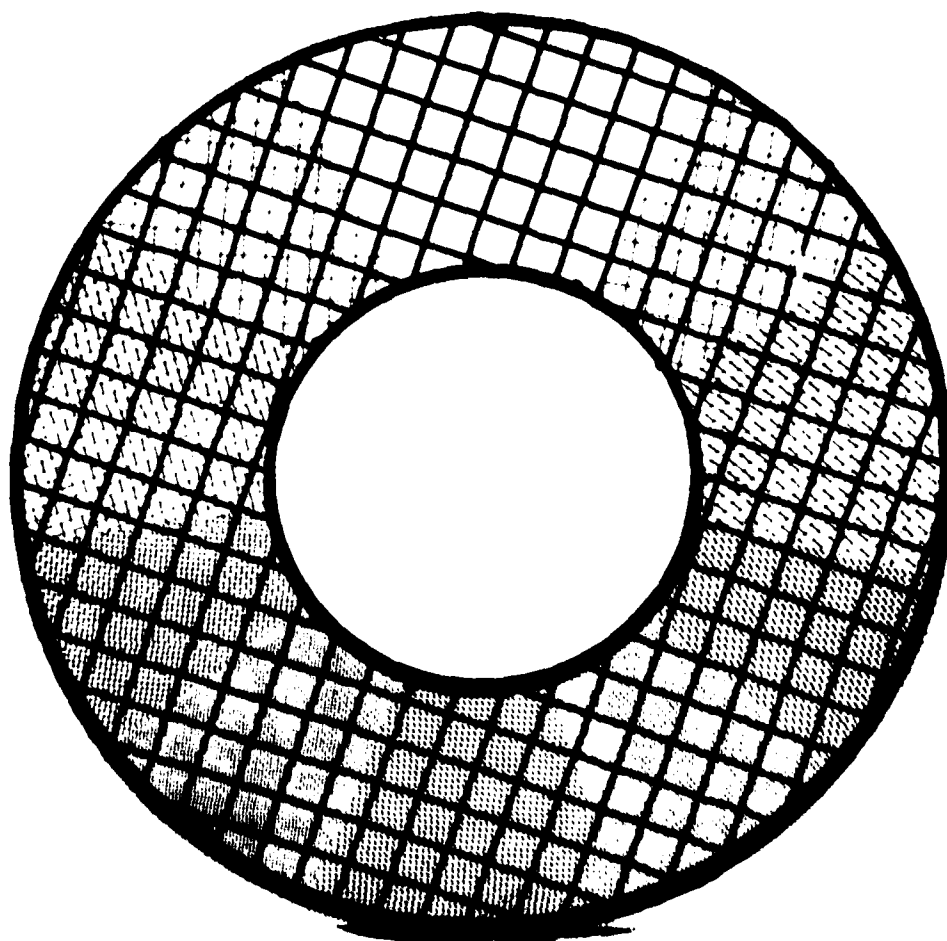
Figure 10. Picture of One-Cycle Grid
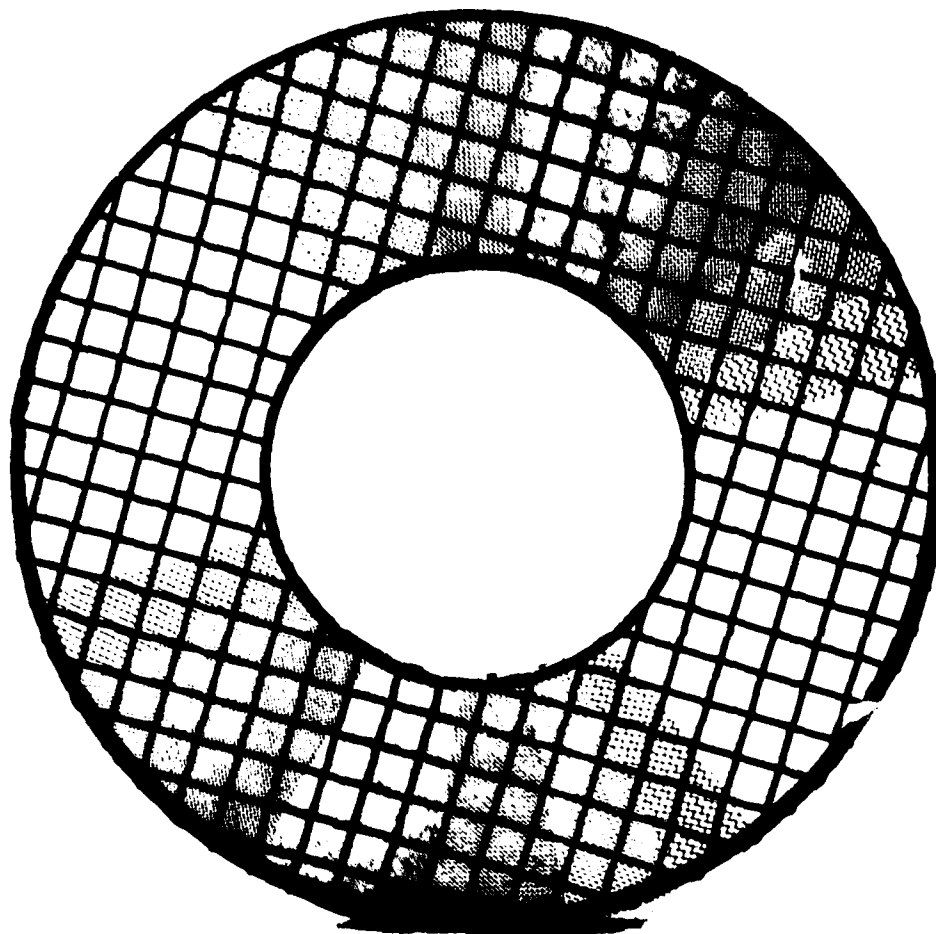
Figure 11. Picture of Two-Cycle Grid.
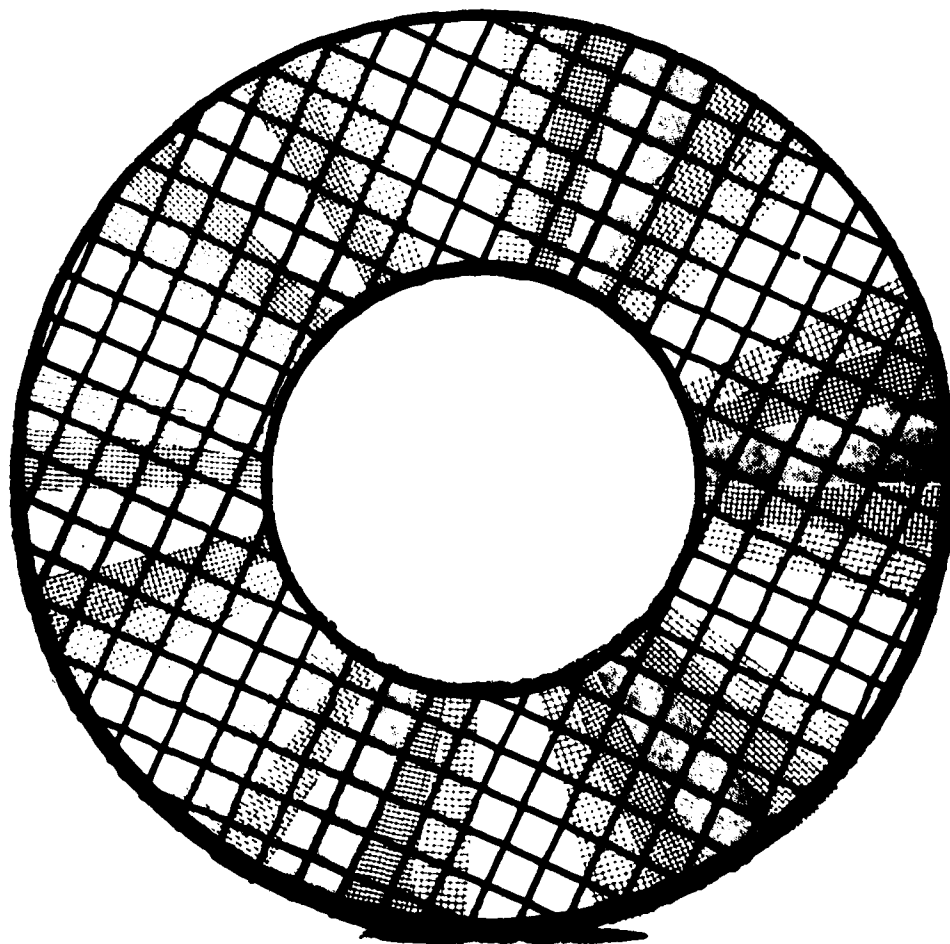
Figure 12.   Picture of Six-Cycle Grid.
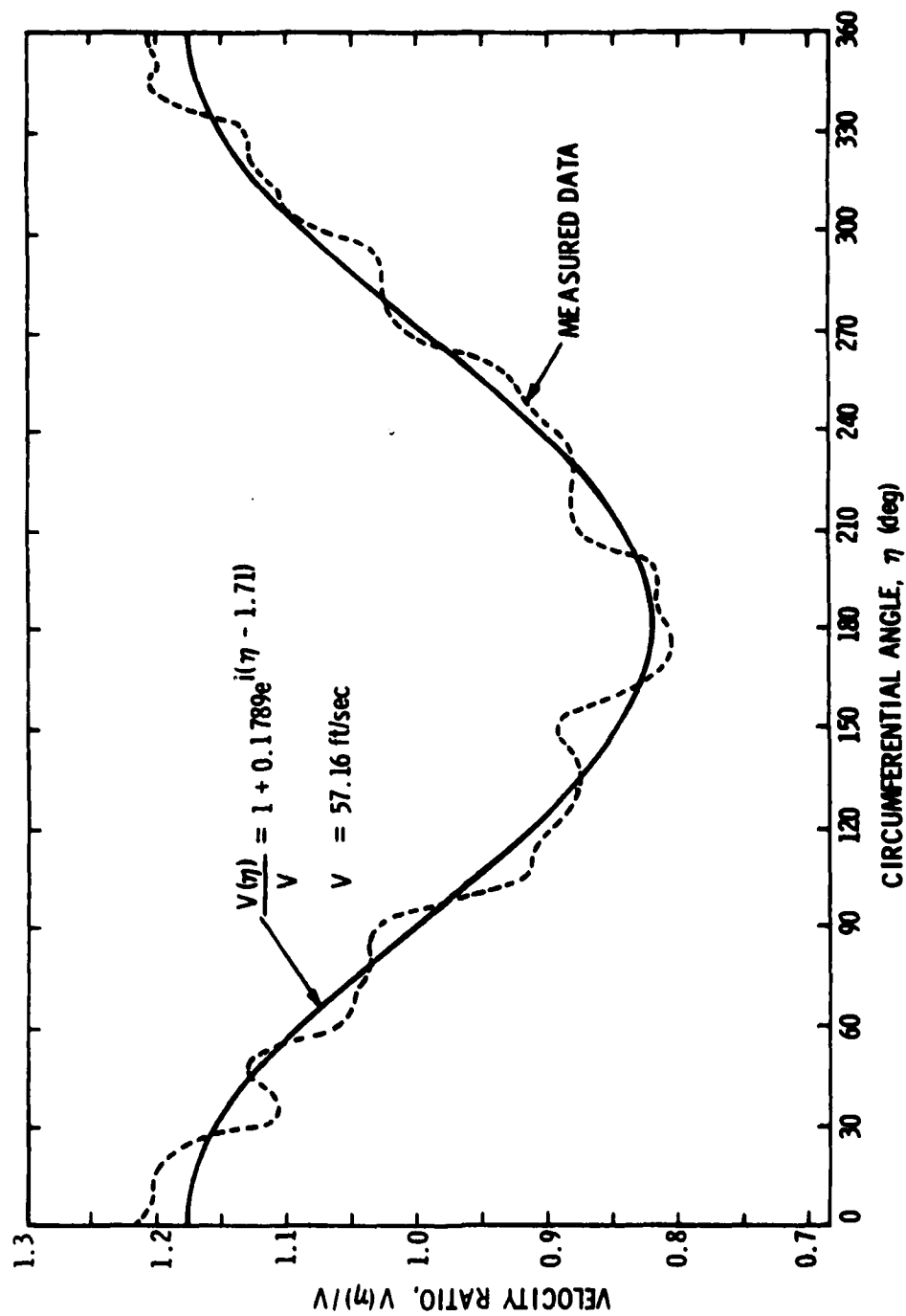
Figure 13. One-Cycle Grid Rotor Inlet Velocity Profile.

89

$$\frac{V(\eta)}{V} = 1 + 0.2092e^{i(2\eta + 18.05)}$$

$\overline{V} = 64.98$ ft/sec

MEASURED DATA

CIRCUMFERENTIAL ANGLE, η (deg)

VELOCITY RATIO, $V(\eta)/\overline{V}$
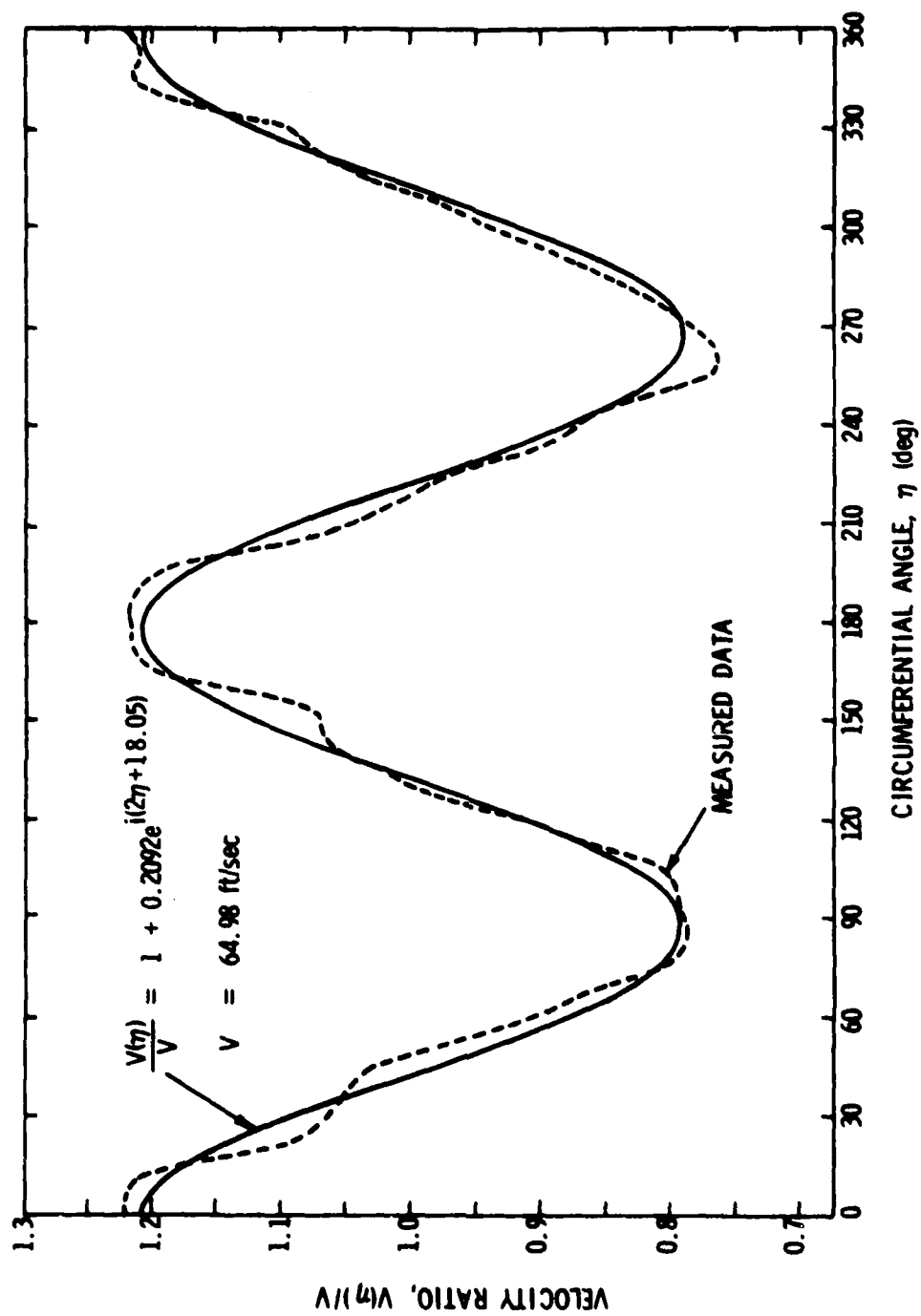
Figure 14. Two-Cycle Grid Rotor Inlet Velocity Profile.
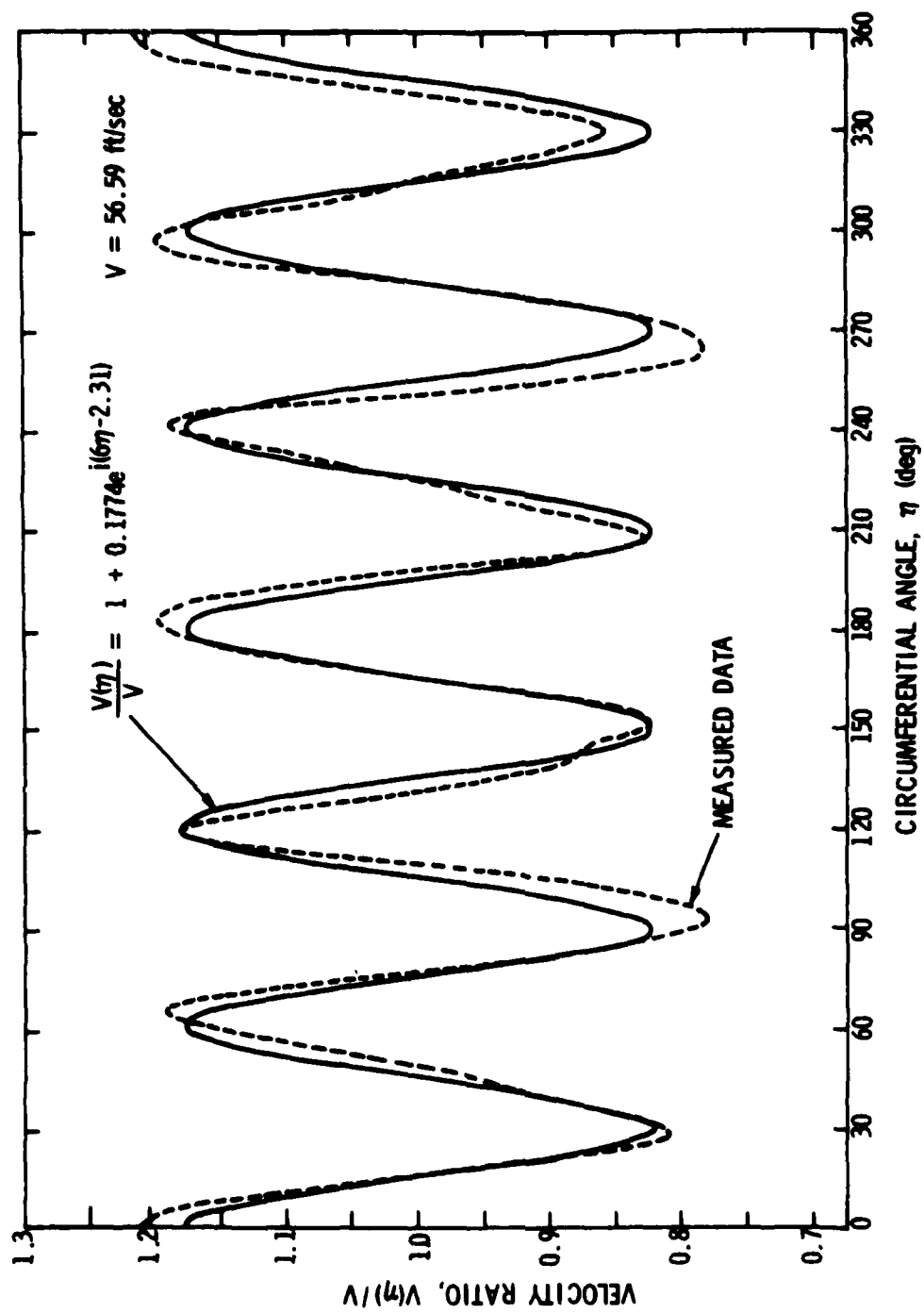
Figure 15. Six-Cycle Grid Rotor Inlet Velocity Profile.

$$\frac{V(\eta)}{V} = 1 + 0.1774e^{i(6\eta - 2.31)}$$

V = 56.59 ft/sec

MEASURED DATA

CIRCUMFERENTIAL ANGLE, η (deg)

VELOCITY RATIO, V(η)/V

the flow field that, for analytical purposes, would exist far upstream
of the rotor. The profiles are based on measured values of mid-span
total pressure taken at 2° increments over the full circumference and
combined with the measured value of the wall static pressure. The
results shown are typical of those obtained for each of the grids over
a range of values of the circumferential mean absolute velocity V. The
solid line shown on these figures represents the variation as given by
the fundamental harmonic obtained from Fourier analysis of the data,
where

$$\frac{V(n)}{V} = \frac{E_o}{2} + \sum_{j=1}^{\infty} E_j e^{i(jn + \phi_j)} \quad .$$

Additional characteristics of the velocity profiles obtained from
Fourier analysis are shown in Figures 16, 17, and 18. If the design
variation of the velocity profile had been obtained, each of these plots
would contain a single line with magnitude 0.20 at the harmonic number
corresponding to the fundamental. In each of the figures, the magnitude
of the fundamental is close to the desired value of 0.20, and the magni-
tudes of other high harmonics are approximately an order of magnitude
below this value. These results show that McCarthy's solution is ade-
quate for the design of grids of this type.

In the report describing the details of the design and evaluation
of all of the wire grids, Bruce [34] shows that the rotor inlet velocity
profile magnitude is dependent upon the value of the circumferential
mean absolute velocity V and the distance from the grid to the rotor
inlet. These dependencies are due to the effects of Reynolds number
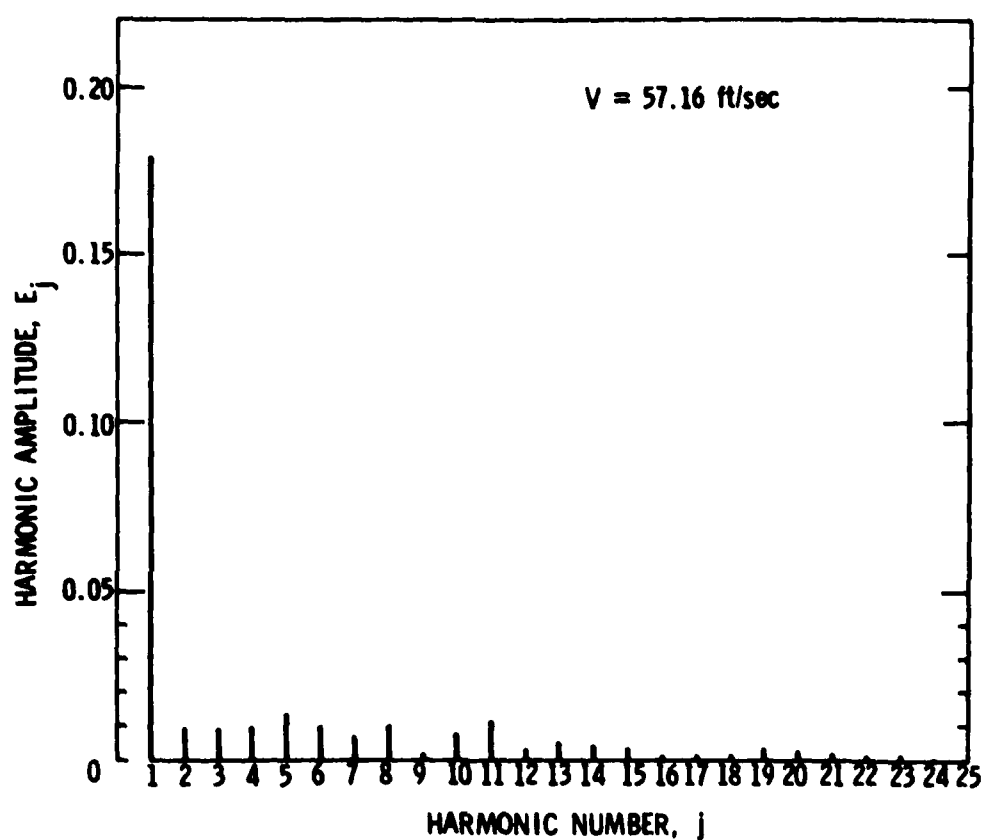
Figure 16. One-Cycle Grid Rotor Inlet Velocity Profile
Fourier Coefficient Magnitude Distribution.
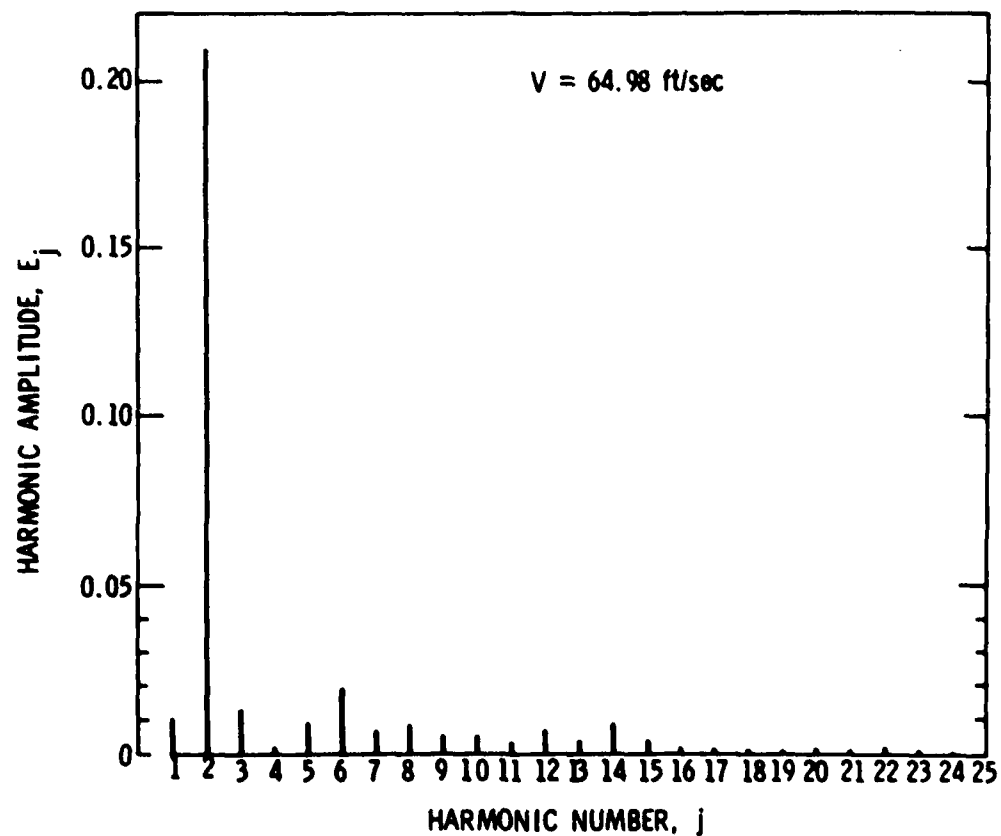
Figure 17. Two-Cycle Grid Rotor Inlet Velocity Profile
Fourier Coefficient Magnitude Distribution.
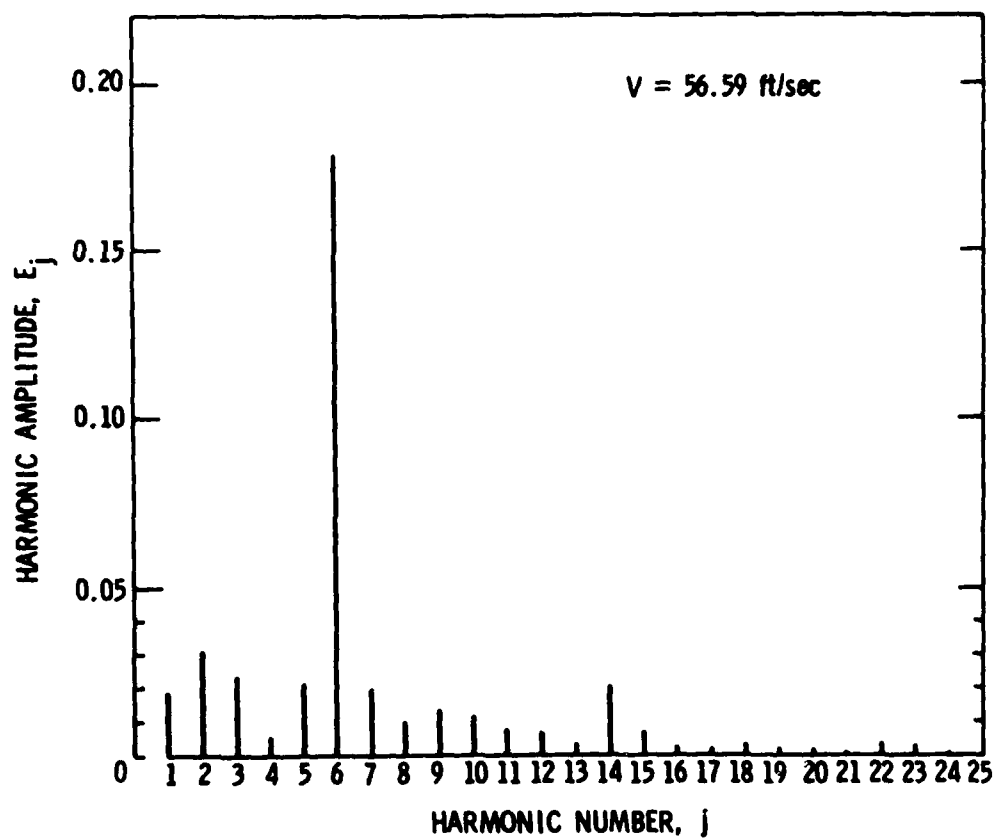
Figure 18.   Six-Cycle Grid Rotor Inlet Velocity Profile
Fourier Coefficient Magnitude Distribution.

and turbulent mixing, respectively. The Reynolds number dependence is slight and is in general agreement with the results of Cornell [30]. Turbulent mixing has an increasingly severe detrimental effect on the velocity profile magnitude as the number of cycles of velocity variation per circumference increases. This brings the regions of maximum and minimum velocity closer together and results in more rapid mixing.

The grid performance characteristics required for reduction of the data obtained in the research program are presented in Table 2. Since all of the grids produce velocity profiles dominated by a single harmonic, the contributions due to all other harmonics were neglected in data analysis.

3.4 Test Rotor

The rotor employed in this program is unique in that it operates with no pressure rise at its uniform inflow design condition. This feature permits investigation of unsteady flow effects in the absence of steady rotor forces and moments.

The rotor design is based on the relation

$$\xi = \beta_m = \tan^{-1}(\frac{U}{V}) \quad ,$$

with $\xi = 45^\circ$ at mid-span (i.e., at $r = 7.75$ in.). The blades have an uncambered 10% thick C1 profile as described by Howell [35], a chord of 6.00 in., a span of 5.90 in., and are made of aluminum. The rotor can be assembled with 2, 3, 4, 6, or 12 blades. Thus, configurations with mid-span space-to-chord ratios, S/C, of 4.058, 2.705, 2.029, 1.353, or 0.676 can be evaluated. Values of S/C of 2.029, 1.353, and 0.676 were included in this program.

TABLE 2

GRID PERFORMANCE CHARACTERISTICS

Number of Cycles of Velocity Variation per Circumference (N)	Circumferential Mean Rotor Inlet Absolute Velocity (V) ft/sec	Fundamental Harmonic Number (j)	Magnitude of Fundamental Harmonic (Ej)	Phase Angle of Fundamental Harmonic (ϕ_j) deg
1	43.82	1	0.1812	180.66
2	43.82	2	0.2041	88.62
4	43.82	4	0.2291	45.23
6	43.82	6	0.1741	30.63
1	56.83	1	0.1780	181.66
2	56.83	2	0.2083	88.65
4	56.83	4	0.2217	45.14
5	56.83	5	0.1873	35.81
6	56.83	6	0.1716	30.59
1	66.72	1	0.1736	181.66
2	66.72	2	0.2000	88.65
4	66.72	4	0.2226	45.14
6	66.72	6	0.1768	30.59

When the rotor is operating at a selected condition, the mean axial velocity is controlled by the auxiliary fan. The test rotor is driven by a separate 20 HP motor--hence, control of test rotor speed is independent of auxiliary fan speed. Starting from design conditions and increasing test rotor speed while making minor adjustments to auxiliary fan speed to maintain a constant value of mean axial velocity permits operating the test rotor at preselected positive mean incidence angles.

As noted above, the design stagger angle at the mid-span radius was 45°. The rotor was also assembled for testing in this program with mid-span stagger angles of 35° and 55°. Operation at these stagger angle settings, or at positive mean incidence angles as described above, has the disadvantage of introducing three-dimensional flow effects into the data.

3.5 System for Measuring Unsteady Normal Force and Pitching Moment

A system was developed and used in this program to measure rotor blade mid-span section unsteady normal force and pitching moment. The major features of this system are depicted in Figure 19. They are:

(1) A 1.00-in. span instrumented segment is cantilevered from the blade hub at the mid-chord position by means of a beam which contains a force cube and a torque tube. The center section of the blade segment is located at the blade mid-span radius. Miniature, commercially available strain gages are bonded to the force cube and torque tube.
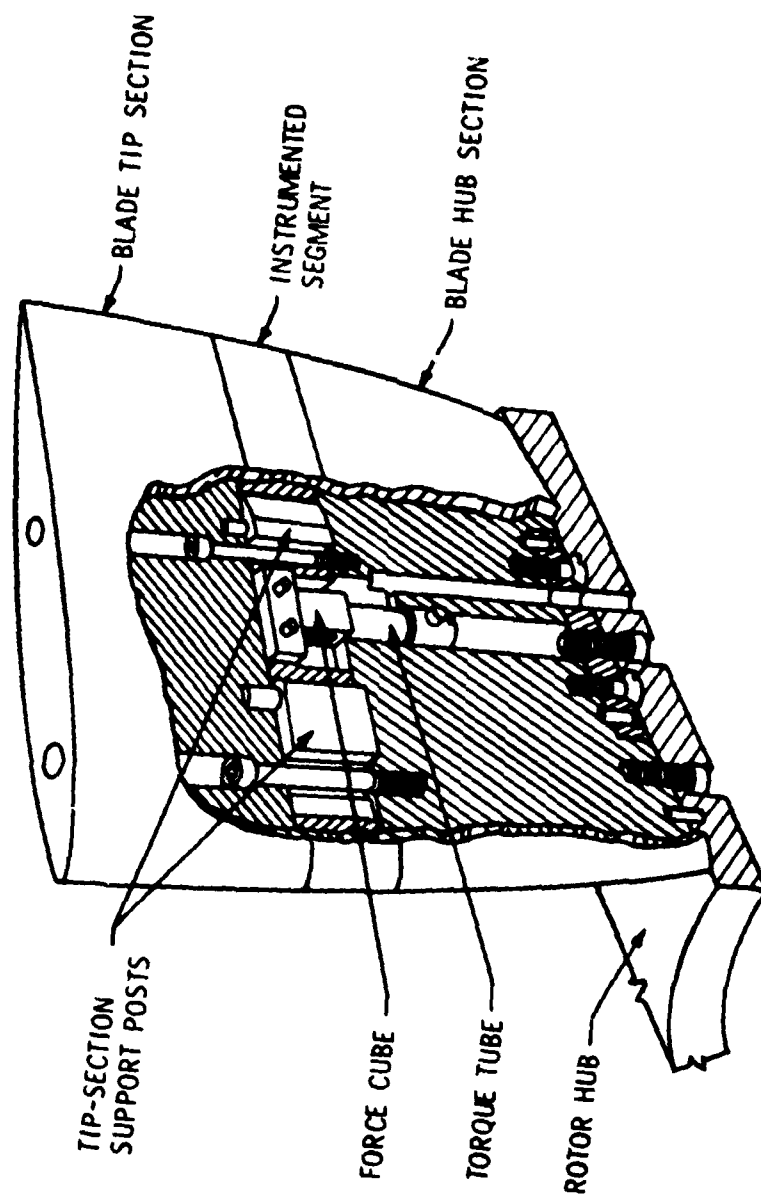
Figure 19. Instrumented Blade Schematic.

(2) The hollow 1.00-in. span instrumented segment is made of
magnesium to minimize its mass and moment of inertia.
It is mass balanced to preclude uneven displacement due
to the forces generated by rotation. It is structurally
independent of the rotor blade except for the cantilever
mount. The aluminum tip section of the blade is attached
to posts which extend outward from the hub section and
pass through slots in the 1.00-in. span instrumented seg-
ment. A maximum clearance of 0.005 in. exists between
adjacent blade and instrumented segment surfaces.

(3) Input power and signal transmission lines run from the
strain-gaged beam through the rotor hub and the hollow
drive shaft to a slip-ring unit. Lines running from
the slip-ring unit to power supplies and/or data record-
ing and analysis equipment pass through holes drilled
in one of the aft support struts.

The static response of the force and moment sensors was linear
over the full operating range with values of 0.119 volts/oz and 0.056
volts/in.-oz, respectively. Both sensors were calibrated dynamically
with excitation provided by electromagnetic shakers as shown in Figure
20. In-phase operation of the shakers produced an applied time-
dependent torque, while out-of-phase operation produced an applied
time-dependent force. The sensor response curves obtained by this
means, after applying corrections for differences between the beam/
shaker effective mass and the blade segment mass, are shown in Figure
21. In the testing performed in the research program, the maximum
fundamental frequency encountered was on the order of 130 Hz. This

Figure 20. Picture of Dynamic Calibration Apparatus.
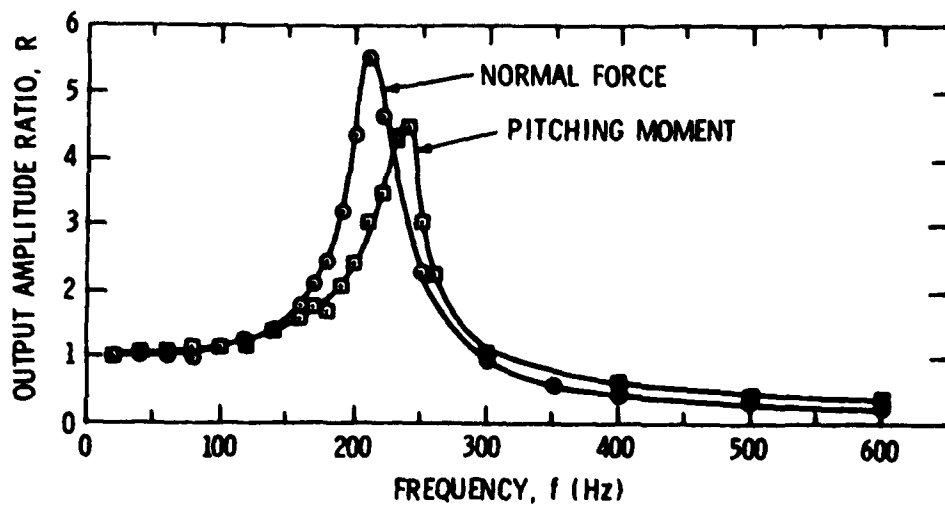
Figure 21.   Sensor Dynamic Response Characteristics.

frequency was thought to be low enough to avoid complications due to the system resonance near 200 Hz. The difference in phase between the input signal and the sensor output was recorded as part of the dynamic calibration. For frequencies below 150 Hz, the phase difference was negligible.

3.6 Unsteady Force and Moment Data Acquisition System

A block diagram of the test instrumentation is shown in Figure 22. Power to the strain gages and the unsteady signals from the strain gages were transmitted across a coin-silver slip-ring unit. A capacitor was installed in the moment gage signal transmission line to eliminate the voltage due to the steady moment induced by rotation. The fluctuating signal from the force and moment gages and the output of a protocell mounted on the rotor drive motor casing were displayed on an oscillo-scope and were simultaneously recorded on FM tape for subsequent analy-sis. The photocell signal was adjusted to appear at the instant during each rotor revolution when the point at the mid-span radius on the leading edge of the instrumented segment passed a selected circumfer-ential position. This photocell signal was used as a trigger for ensemble averaging during data analysis and in defining the phase relationship between the circumferentially nonuniform rotor inflow and the unsteady force and moment generated on the instrumented blade segment. The three recorded signals were selectively displayed on the oscilloscope for comparison with the input signal during each test to assure that the recorded signal was identical to the input signal. Prior to and after recording each set of data, calibration tones with
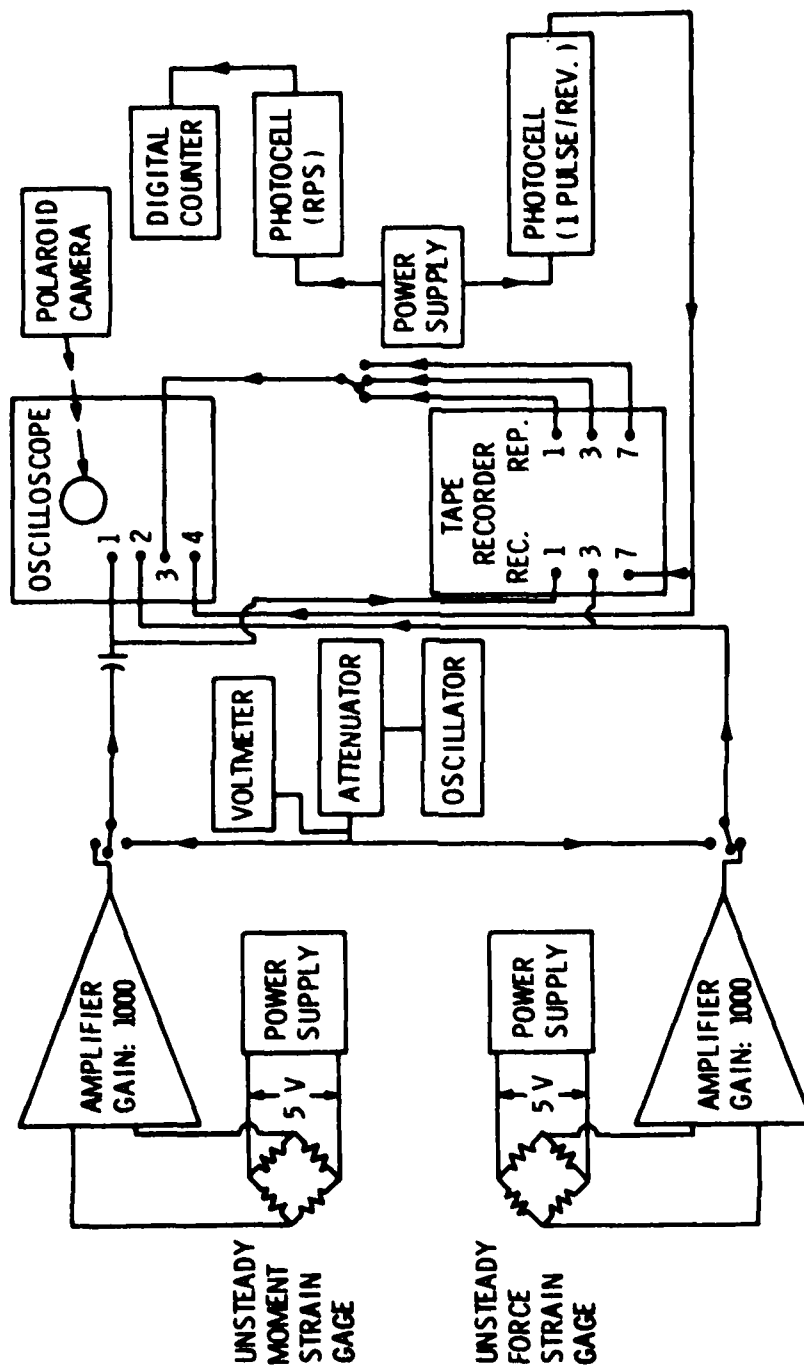
Figure 22. Unsteady Force and Moment Instrumentation Block Diagram.

preselected amplitudes were recorded on each data channel for use in monitoring the recorded signal voltage levels.

3.7 Data Analysis

A 150-sec duration record was made at each test condition of the force and moment gage output and of the output of the photocell which emitted one pulse for each revolution of the test rotor. The maximum and minimum rotor speeds used in the experimental program were 1309 and 593 RPM, respectively. As a result, the period for one rotor revolution varied from a minimum of 0.0458 to a maximum of 0.1011 sec. Thus, the total taped record contained data for a minimum of 1484 and a maximum of 3275 rotor revolutions at each test condition.

Data analysis at each test condition was based on a total of 500 samples of the taped gage output which were digitized and phase-lock averaged, using the photocell output as a trigger. Each data sample contained 512 points with a time increment between points of 0.0002 sec. The time duration of the digitizing process, 0.1024 sec, exceeded the rotor period in all cases. The portion of this averaged signal which corresponded to the time for one rotor revolution, starting with the photocell pulse at time zero, was then Fourier analyzed to define the gage output—both magnitude and phase angle—associated with the frequencies which corresponded to integer multiples of the rotor speed. The gage output at the frequency at which the gages were driven by the disturbance-generating wire grids was then reduced to force or moment coefficient form and the phase angle results were combined with the measured no-rotor disturbance flow field data to obtain the force and moment coefficient phase angle results.

The usual purpose of phase-lock averaging is to extract a periodic signal that is obscured by the presence of noise. The signals analyzed here were not of this type; however, the process was used to assure elimination of the effects of gage response to random sources of excitation, such as mechanical vibration and turbulence. Results at a number of test conditions were examined to determine how the number of samples used in the averaging process affected the final result. Results for one of the most strongly affected cases are shown in Figure 23 and Table 3. These results show that the noise present in the signals did not have a significant effect on either the magnitude or the phase of the gage output at the driven frequency.

ROTOR: $S/C = 1.353$, $\xi = 35^0$

DISTURBANCE GRID: 4 CYCLE

OPERATING CONDITION: $V = U = 56.8$ ft/sec
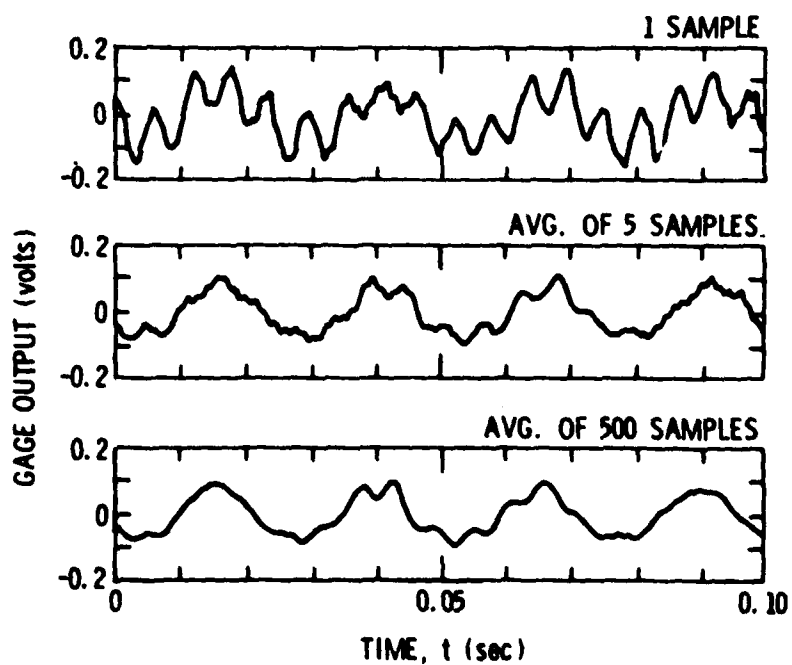
Figure 23.   Effect of Increasing Number of Samples
on Moment Gage Output Signal.

TABLE 3

EFFECT OF INCREASING NUMBER OF SAMPLES ON
FOURIER COEFFICIENTS AT THE DRIVEN FREQUENCY

ROTOR: S/C = 1.353, ξ = 35°
DISTURBANCE GRID: 4-cycle
OPERATING CONDITION: V = U = 56.8 ft/sec

Number of Samples	Amplitude (E_4) volts	Phase (ϕ_4) deg
1	0.07667	228.91
5	0.07755	226.60
10	0.07672	226.17
50	0.07764	225.44
100	0.07805	225.16
500	0.07757	225.31

CHAPTER 4

EXPERIMENTAL AND THEORETICAL RESULTS

4.1 Introduction

Experimental results obtained using the system described in Chapter
3 are presented herein in the form of unsteady normal force and pitching
moment coefficients, $\tilde{C}_N$ and $\tilde{C}_M$, the related phase angles, ϕ_F and ϕ_M, and
the nondimensionalized location of the unsteady center-of-pressure,
$\frac{x_{C.P.}}{C}$. These experimental results are compared with predictions
obtained from Equations (36) and (40) of Chapter 2 and from the theory
of Whitehead-Smith [17]. Since the results are limited to mean angles
of incidence below 9°, the difference at a given test condition between
normal force coefficient and lift force coefficient is small enough to
be neglected. Accordingly, the ordinate in the figures where force
coefficient comparisons are shown is denoted as unsteady lift force
coefficient even though the data points represent normal force coef-
ficients.

4.2 Programming of the Theoretical Solution

The computer program developed by Henderson [18] was modified and
extended as a result of the analysis presented in Chapter 2 to obtain
lift force and pitching moment coefficient predictions based on
Equations (36) and (40). In Henderson's program, the only programming
that was not straightforward was associated with evaluation of the func-
tion $G(\omega, x_c^+, S/C, \xi)$. He evaluated the integrals defined as B_1, B_2, D_1,

and D_2 [see Equation (22)] numerically since they could not be evaluated in closed form. Based on the fact that the behavior of the integrands, for all values of the other parameters, was characterized by a damped oscillation about the value zero as λ^+ increased, he argued that convergence of the integrals was assured. By adopting a convergence criterion of an increase in the magnitude of the value of the integral less than 0.001 for a one-wavelength increase in λ^+ to define the value of the integrals, he then evaluated each integral for a given value of n and constructed sums—which also were characterized by a damped, oscillatory behavior—by including the contribution due to positive and negative pairs (n = ±1, ±2, etc.) of values for the integrals combined with the contributions due to the terms containing the factor $[C_1 + C_2 - 2]$. The calculation of each sum was continued, with these complex quantities separated into real and imaginary parts, until the difference between the average value of the individual sums computed from $|n| = 3$ to $|n| = k$ differed from the average value of the individual sums computed from $|n| = 3$ to $|n| = k + 1$ by less than a factor of 0.01. Henderson's programming of this part of the solution for $G(\omega,x_c^+,S/C,\xi)$ was retained in the present analysis.

As shown in Appendix A, the term in the expression for $G(\omega,x_c^+,S/C,\xi)$ that Henderson expressed as

$$\left[\sum_{-\infty}^{-1} + \sum_{1}^{\infty}\right] e^{in\tau}\left[\frac{2i\omega e^{-i\omega}}{\pi}(A_1 + A_2 - A_3 - A_4)\right]$$

was replaced in the present analysis by its integrated value

$$\left[\sum_{-\infty}^{-1} + \sum_{1}^{\infty}\right] e^{in\tau}\left[i\omega e^{-i\omega}(E_1 + E_2)\right] \quad .$$

The convergence criterion described above based on the magnitude of the difference between successive average values of the sums was also applied to this term. This change had no effect on the computed values of the function $G(\omega, x_c^+, S/C, \xi)$, as the values computed for use in this analysis agree with Henderson's values to five decimal places. Computed values of the function $G(o, x_c^+, S/C, \xi)$ also were not affected since this term is zero when $\omega = 0$. For most cases, the value of these functions had converged for $n \leq \pm 12$. More terms were required for convergence for cases with low values of reduced frequency and for cases where the wavelength of the inlet disturbance, ℓ, was equal to the blade spacing divided by a positive integer.

Computed unsteady lift force coefficients based on Equation (36) differ from those computed by Henderson (see Appendix A) by the contribution due to the term

$$-(y_{max}^+ + i_m)G(o, x_c^+, S/C, \xi)\left[\sum_{-\infty}^{-1} + \sum_{1}^{\infty}\right]$$

$$\cdot \left[\sum_{m=1}^{\infty} (1)^{-m} J_m(\theta)\left[\left[g_c - \sqrt{g_c^2 - 1}\right]^m + \left[h_c - \sqrt{h_c^2 - 1}\right]^m\right]\right] \quad .$$

In adding this term to the computer program, the summations on m were carried out with a fixed upper value of $m = 20$. This upper limit was

selected to assure convergence of these interior sums. A preliminary examination of their behavior showed that they had converged to a fixed value good to five decimal places with values of m in the range between m = 5 and m = 10. Examination of the value of this entire term as a function of n showed that the convergence criterion adopted by Henderson for evaluation of the term containing the integrals denoted as B_1, B_2, D_1, and D_2 would not be satisfactory. In Henderson's case, large oscillations in the value of the term were restricted to values of n in the range $|n| < 3$. In this term, the oscillations were more lightly damped and the final value of the sum was much closer to the intermediate values given by terminating the summation with any positive value of n. Consequently, the value of the sum in this term was determined by taking the average of the values obtained for each individual value of n in the range from n = 20 to n = -30.

The solution for the unsteady pitching moment, Equation (40), contains two new summations on n, the number of blades. One of these summations appears as the part of the second term in the numerator of Equation (39), the equation for the function $B(\omega, x_c^+, S/C, \xi)$, which contains the expressions grouped together as K_1. The other summation appears in Equation (40) as a factor to be multiplied by $\frac{\cos\phi}{4}[i_m + y_{max}^+]$ $G(o, x_c^+, S/C, \xi)$. A detailed examination of the behavior of these summations showed that they approached a finite value in all cases while undergoing an oscillation that was more lightly damped than were the summations in the equation for the unsteady lift. As a result, the values of these summations were determined by taking the average of the values obtained for each individual value of n in the range from n = 40 to n = -50. Convergence of the interior sums on m in Equation (40)

also was slower. As a result, these summations were carried out with a
fixed upper value of $m = 40$.

The unsteady lift force and pitching moment coefficients, as
expressed by Equations (36) and (40), are complex quantities. Thus,
they can be expressed as

$$\tilde{c}_L = (\tilde{c}_L)_R + i(\tilde{c}_L)_I$$

and

$$\tilde{c}_M = (\tilde{c}_M)_R + i(\tilde{c}_M)_I \quad .$$

An alternate form for expressing these quantities, which is discussed
in detail by von Kármán and Sears [3], utilizes magnitude and phase
relationships such that

$$|\tilde{c}_L| = [(\tilde{c}_L)_R^2 + (\tilde{c}_L)_I^2]^{1/2} \quad , \quad \phi_F = \tan^{-1}\frac{(\tilde{c}_L)_I}{(\tilde{c}_L)_R}$$

and

$$|\tilde{c}_M| = [(\tilde{c}_M)_R^2 + (\tilde{c}_M)_I^2]^{1/2} \quad , \quad \phi_M = \tan^{-1}\frac{(\tilde{c}_M)_I}{(\tilde{c}_M)_R} \quad .$$

where the phase angles represent the amount by which the force or moment
vector lags the vector of the oscillating velocity w_d. These magnitude-
phase relationships have been employed in the results presented in the
remainder of this chapter.

With these definitions of the magnitude of the unsteady lift force
and pitching moment coefficients, the location of the unsteady center

of pressure, $x_{C.P.}$, measured from the leading edge of the blade and expressed as a fraction of the chord length, is given by

$$\frac{x_{C.P.}}{c} = \frac{1}{2} - \frac{|\overset{\alpha}{c}_M|}{|\overset{\alpha}{c}_r|} \quad .$$

By treating the summations in Equations (36) and (40) as outlined above, the quantities $\overset{\alpha}{c}_L$, $\overset{\alpha}{c}_M$, $|\overset{\alpha}{c}_L|$, $|\overset{\alpha}{c}_M|$, ϕ_F, ϕ_M, and $\frac{x_{C.P.}}{c}$ were computed for values of ξ, S/C, and i_m covered in the experimental program with $y^+_{max} = 0$ and $\omega = 0.2$, 0.3, 0.4, $\ldots$, 2.0, 2.1, 2.2. The results of these computations are presented in the final section of this chapter where they are compared with the measured data and with available computations based on the Whitehead-Smith theory with $i_m = y^+_{max} = 0$.

4.3 Comparison of Theoretical Predictions and Measured Data

Comparisons between experimental and theoretical force coefficients, $|\overset{\alpha}{c}_L|$ or $|\overset{\alpha}{c}_N|$, moment coefficients, $|\overset{\alpha}{c}_M|$, center-of-pressure locations, $\frac{x_{C.P.}}{c}$, force coefficient phase angles, ϕ_F, and moment coefficient phase angles, ϕ_M, are presented as Figures 24 through 38. Examination of the results at $S/C = 1.353$ and 2.029 shows that certain critical reduced frequencies exist at which the theory developed in Chapter 2 predicts the occurrence of significant changes in cascade performance. These theoretically predicted changes are substantiated, in many cases, by the experimental results. The values of reduced frequency at which these changes occur are associated with cascade inflow conditions for which the spacing between blades, S, is equal to the wavelength of the distorted inflow, ℓ, or an integer multiple of this wavelength. If k represents the integers 1, 2, 3, $\ldots$, then, for

Figure 24. Comparison of Experimental and Theoretical Unsteady Lift Force Coefficients with $y^{+}_{max} = 0$ and $\xi = 35°$.
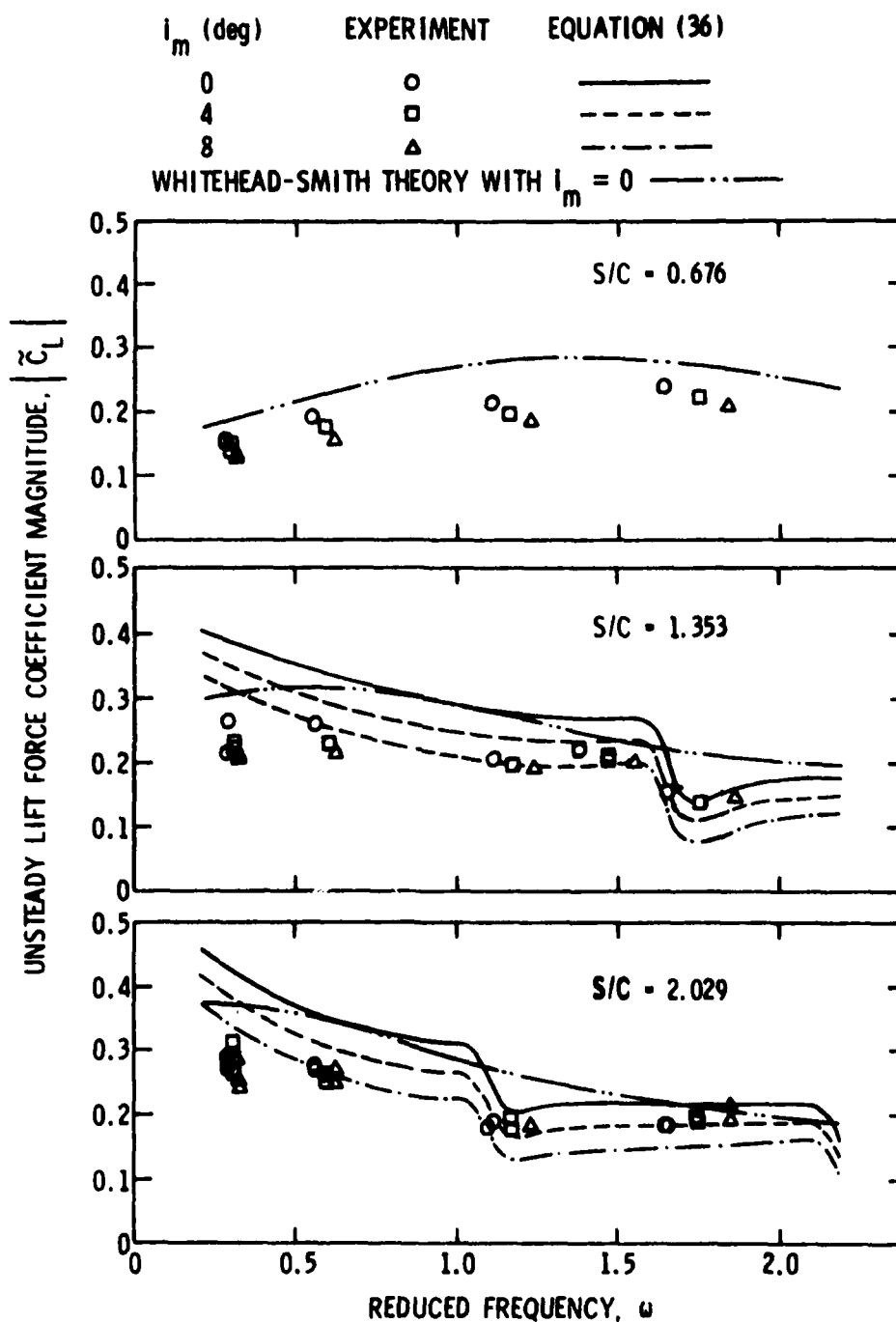
Figure 25.   Comparison of Experimental and Theoretical Unsteady
Lift Force Coefficients with $y^+_{max} = 0$ and $\xi = 45°$.
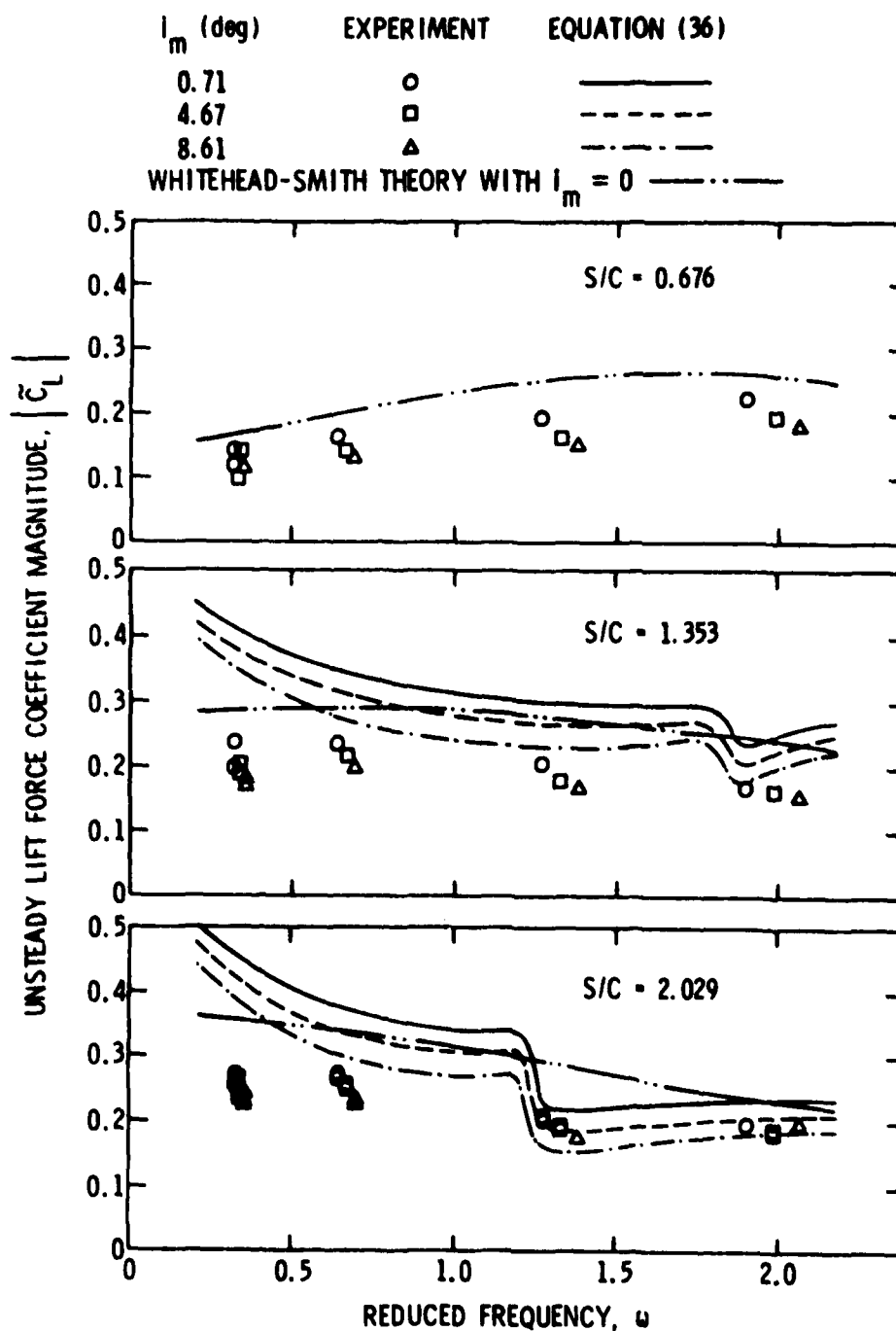
Figure 26. Comparison of Experimental and Theoretical Unsteady Lift Force Coefficients with $y^+_{max} = 0$ and $\xi = 55^\circ$.

i_m (deg)	EXPERIMENT	EQUATION (40)
0.24	O	———
2.78	□	– – –
5.03	△	–·–·–
7.01	▽	——

WHITEHEAD-SMITH THEORY WITH i_m = 0 ——·——

Figure 27. Comparison of Experimental and Theoretical Unsteady Pitching Moment Coefficients with y^+_{max} = 0 and ξ = 35°.
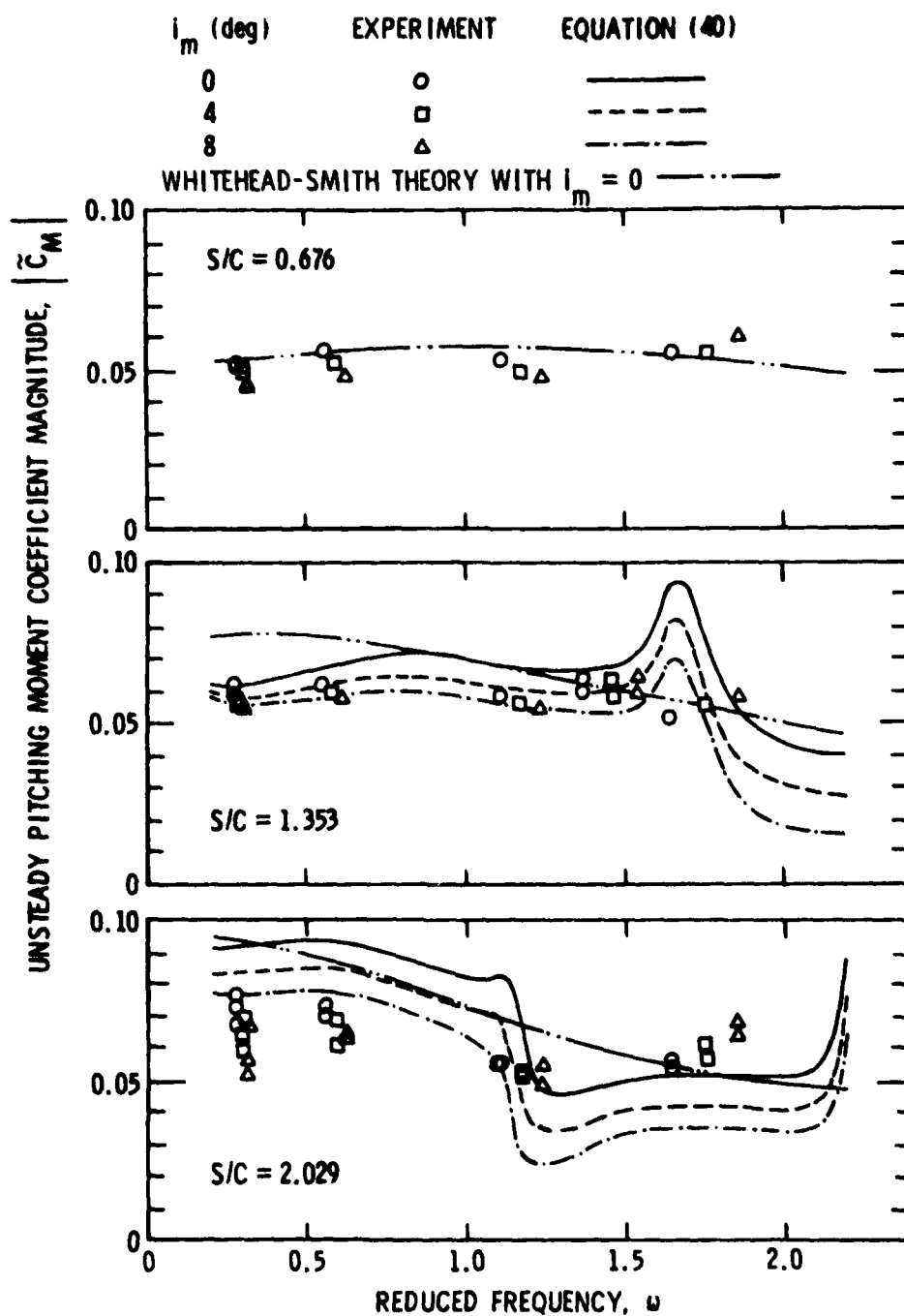
Figure 28. Comparison of Experimental and Theoretical Unsteady
Pitching Moment Coefficients with $y^+_{max} = 0$ and
$\zeta = 45°$.
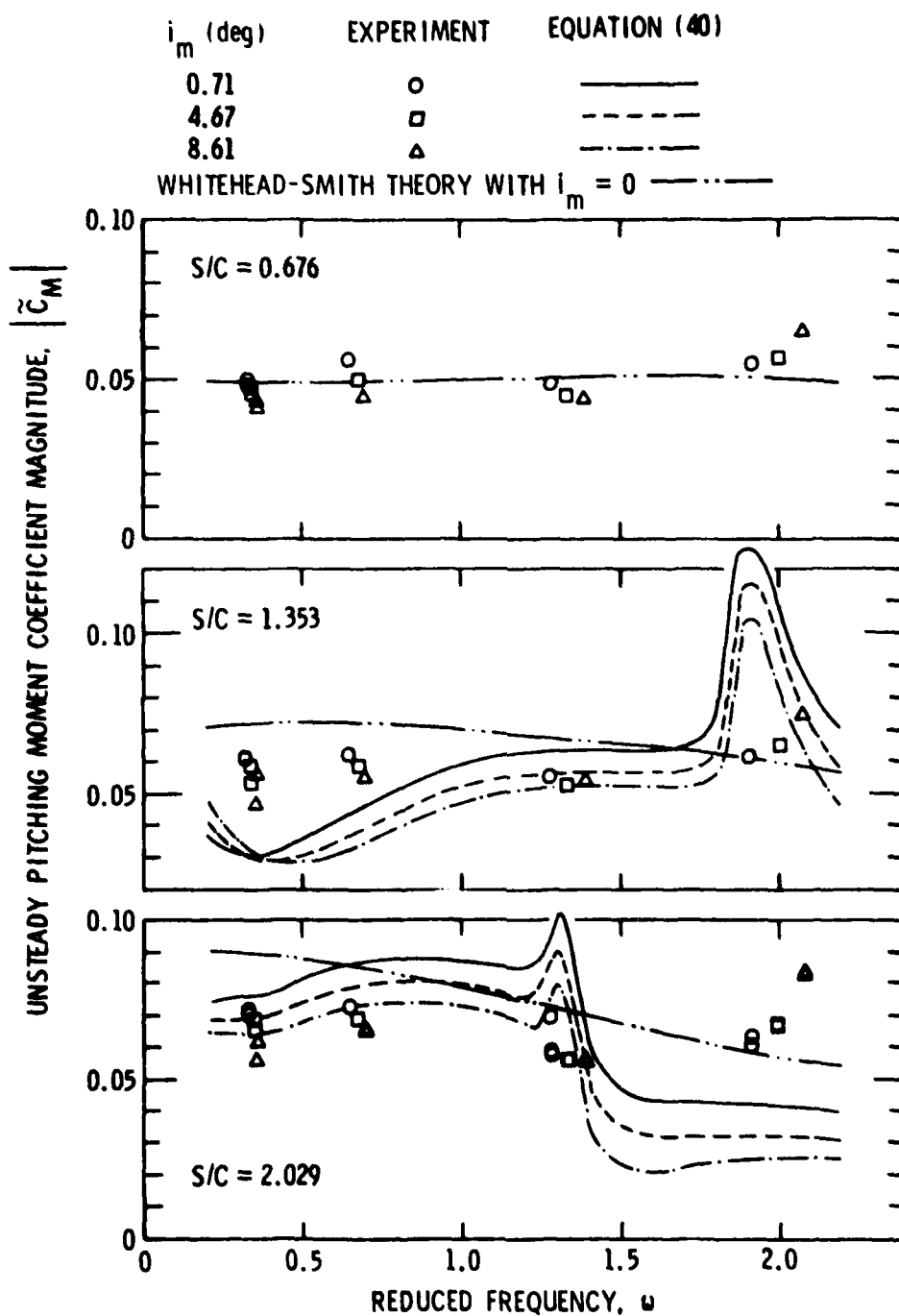
Figure 29. Comparison of Experimental and Theoretical Unsteady
Pitching Moment Coefficients with $y_{max}^+ = 0$ and
$\xi = 55°$.
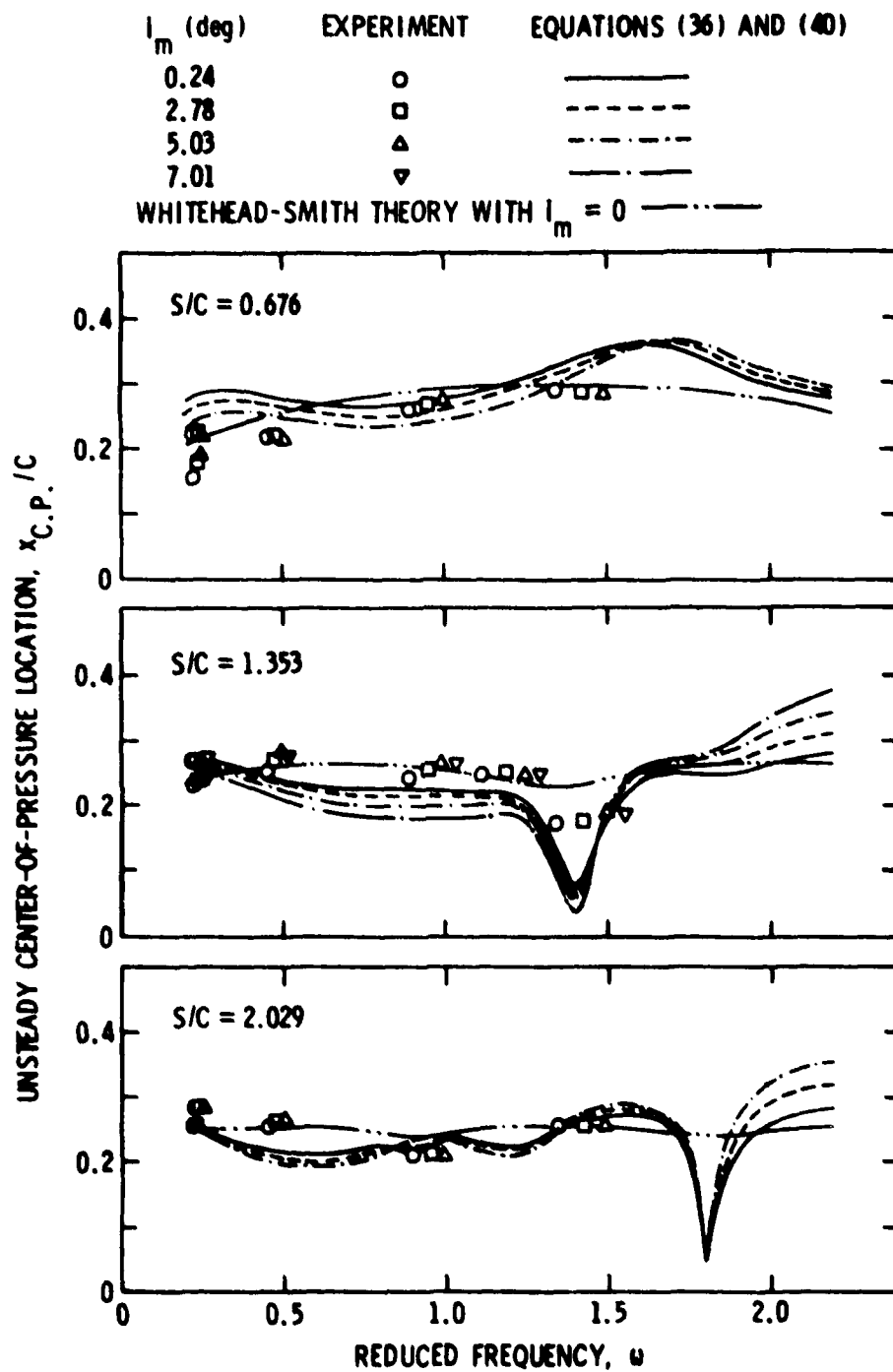
Figure 30. Comparison of Experimental and Theoretical Unsteady Center-of-Pressure Locations with $y^+_{max} = 0$ and $\xi = 35°$.
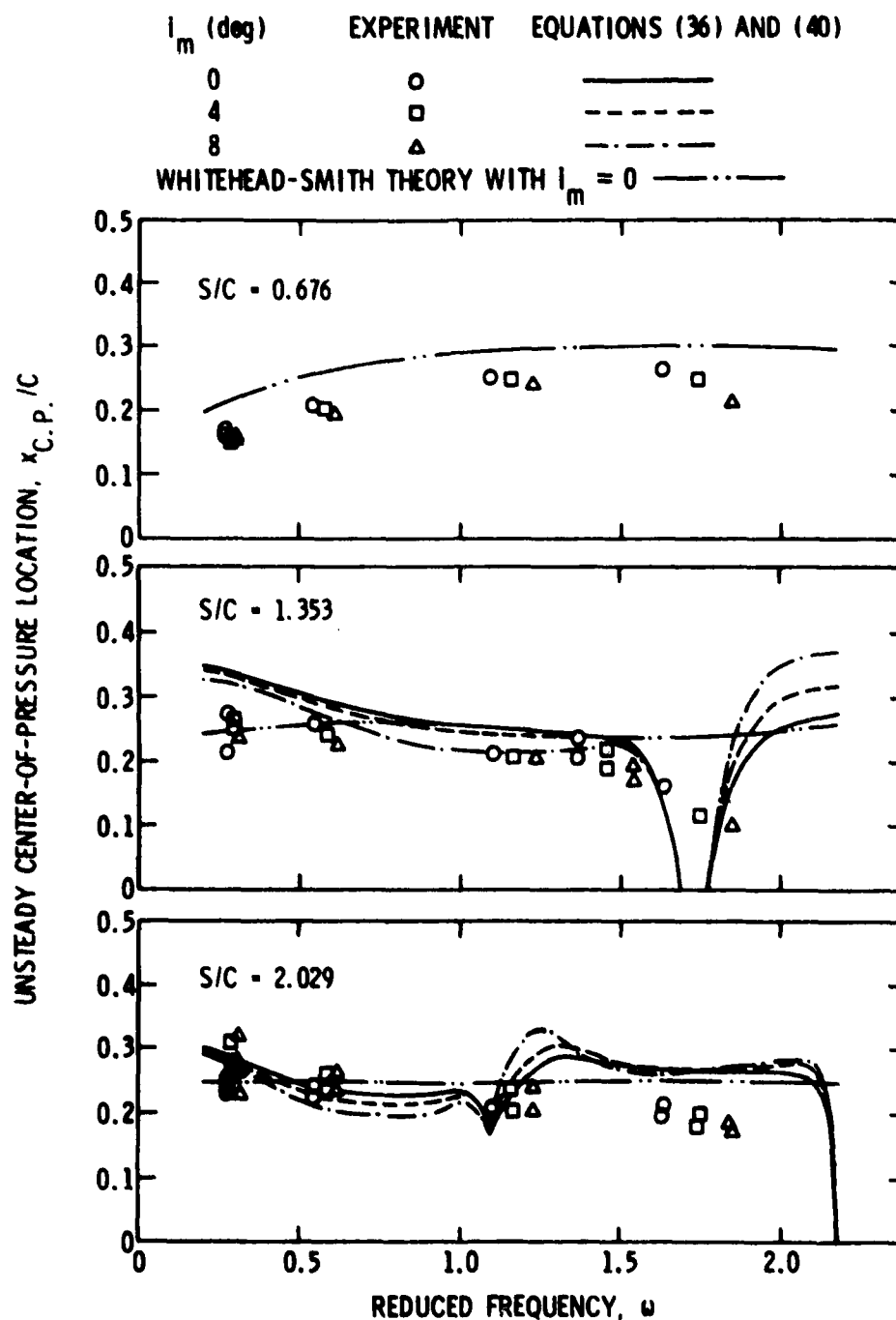
Figure 31. Comparison of Experimental and Theoretical Unsteady Center-of-Pressure Locations with $y_{max}^{+} = 0$ and $\xi = 45°$.
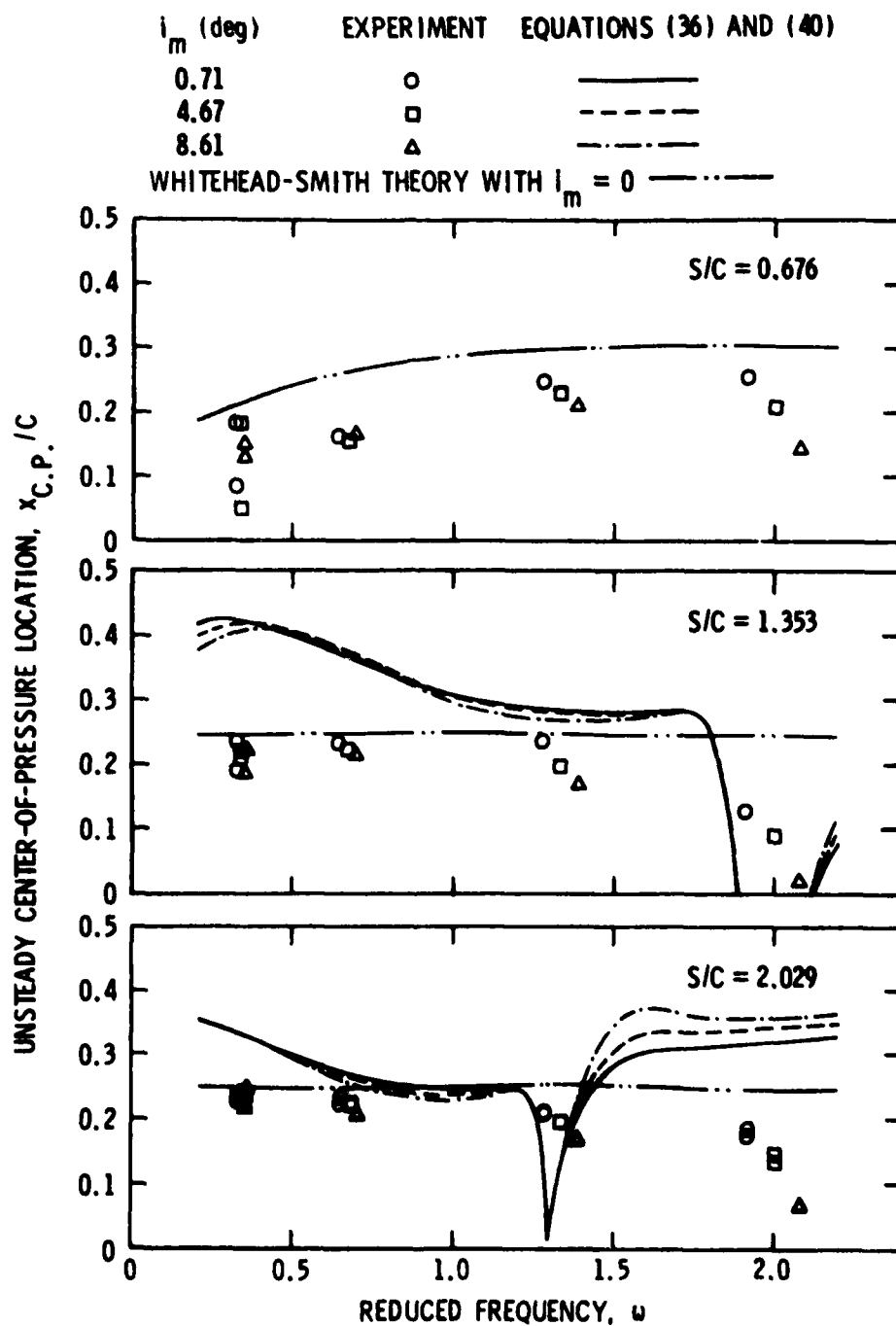
Figure 32. Comparison of Experimental and Theoretical Unsteady
Center-of-Pressure Locations with $y_{max}^+ = 0$ and
$\xi = 55^o$.
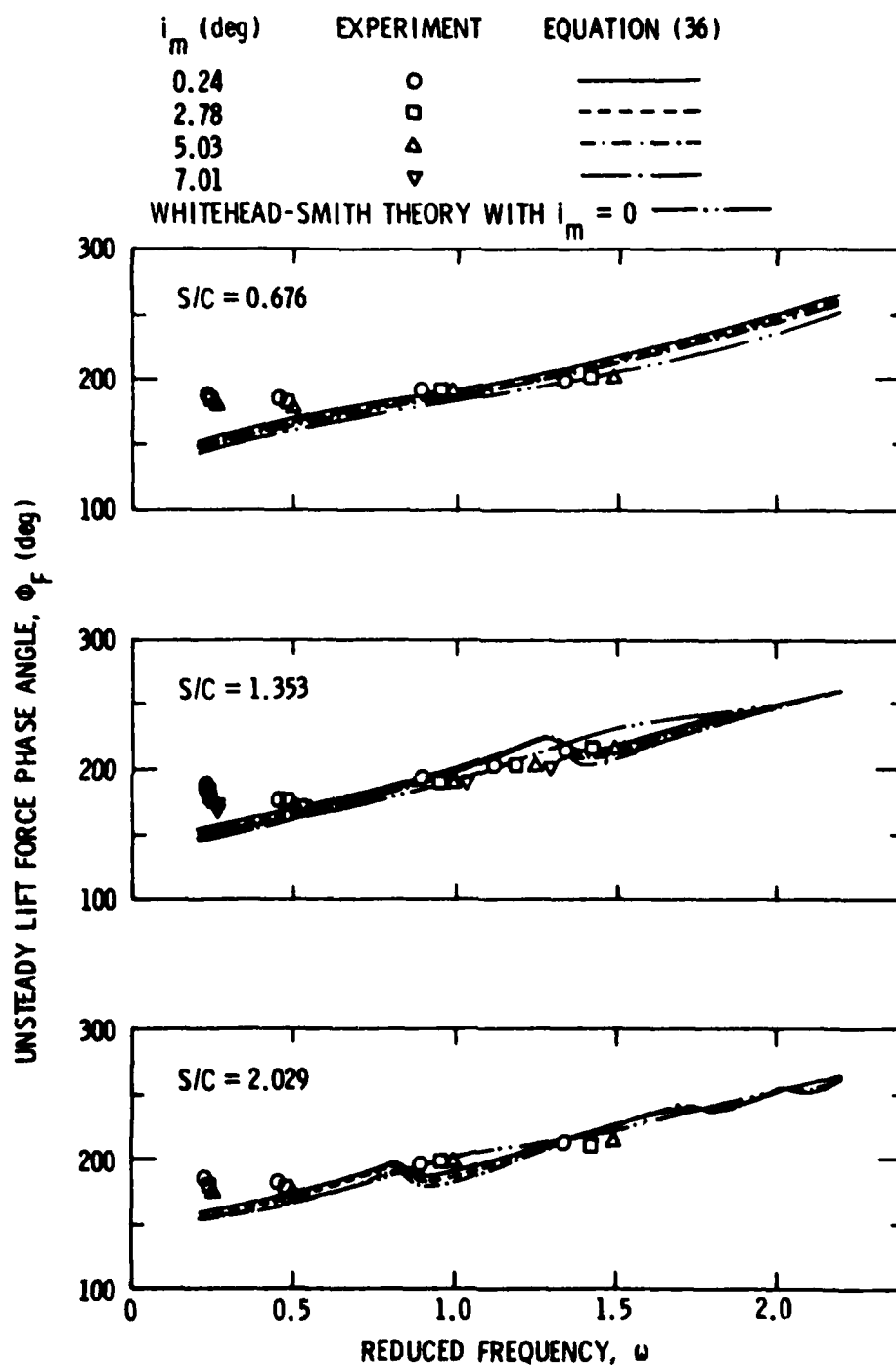
Figure 33. Comparison of Experimental and Theoretical Unsteady Lift Force Phase Angles with $y^+_{max} = 0$ and $\xi = 35^\circ$.
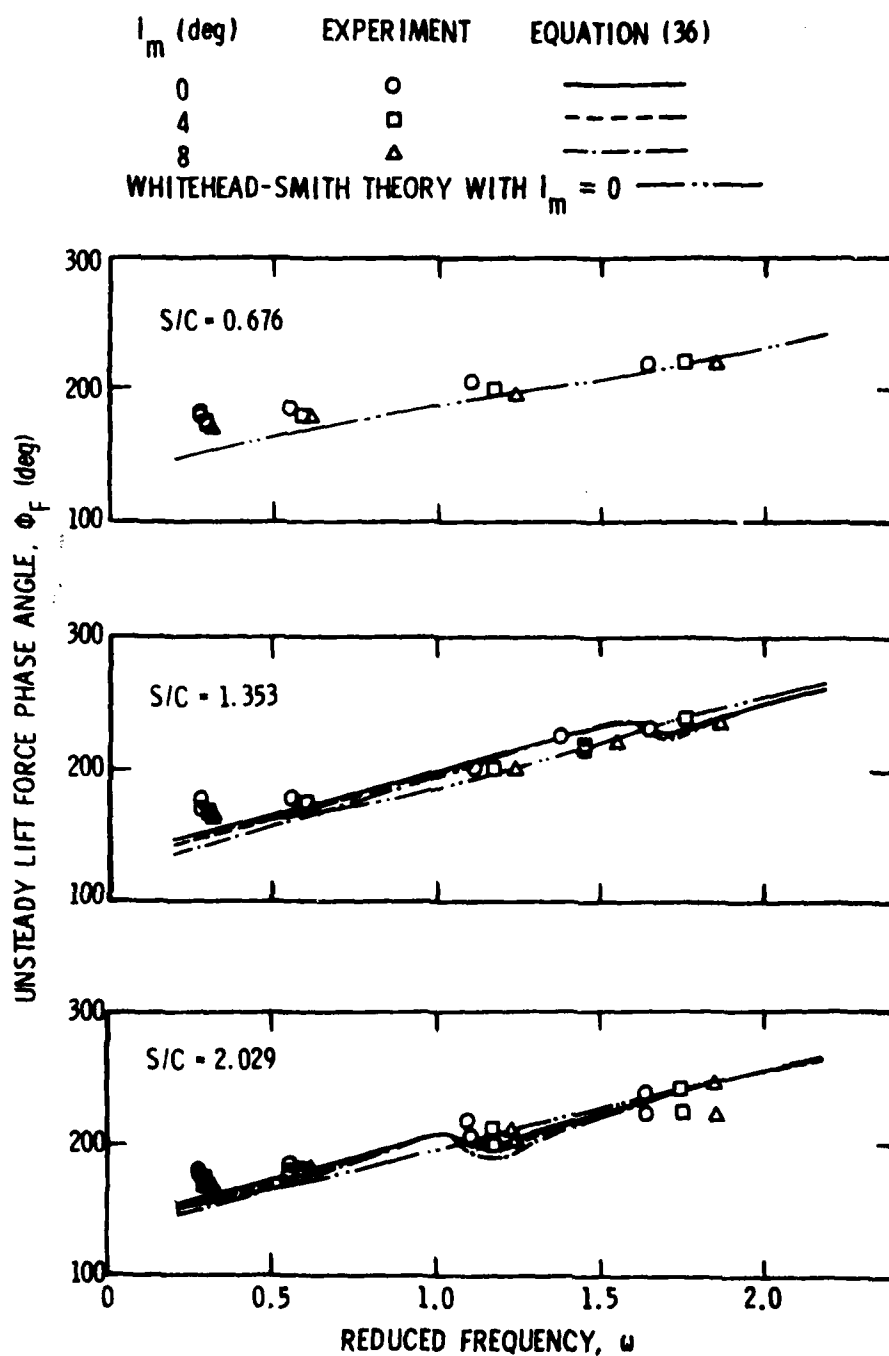
Figure 34. Comparison of Experimental and Theoretical Unsteady Lift Force Phase Angles with $y^+_{max} = 0$ and $\xi = 45°$.
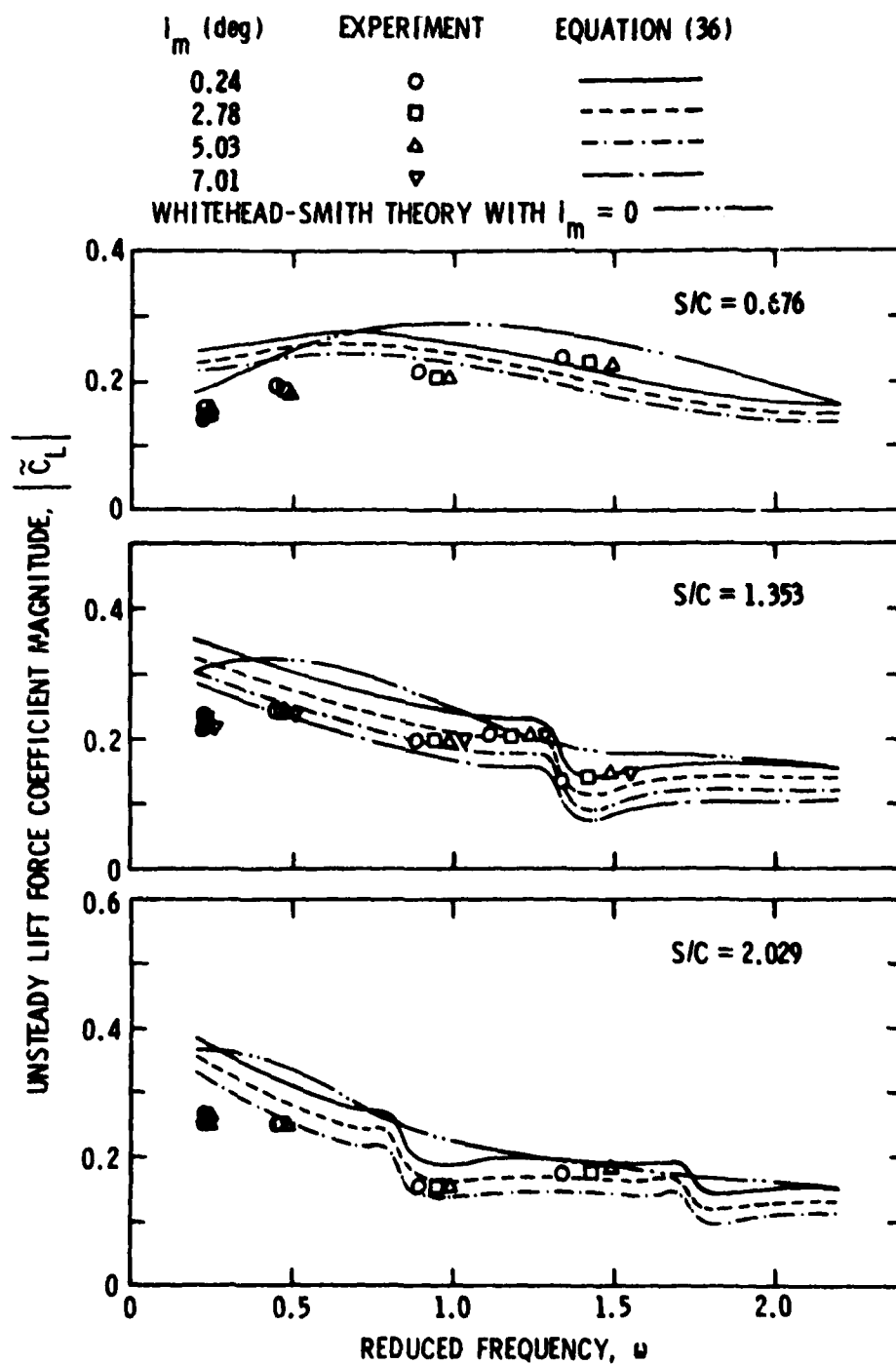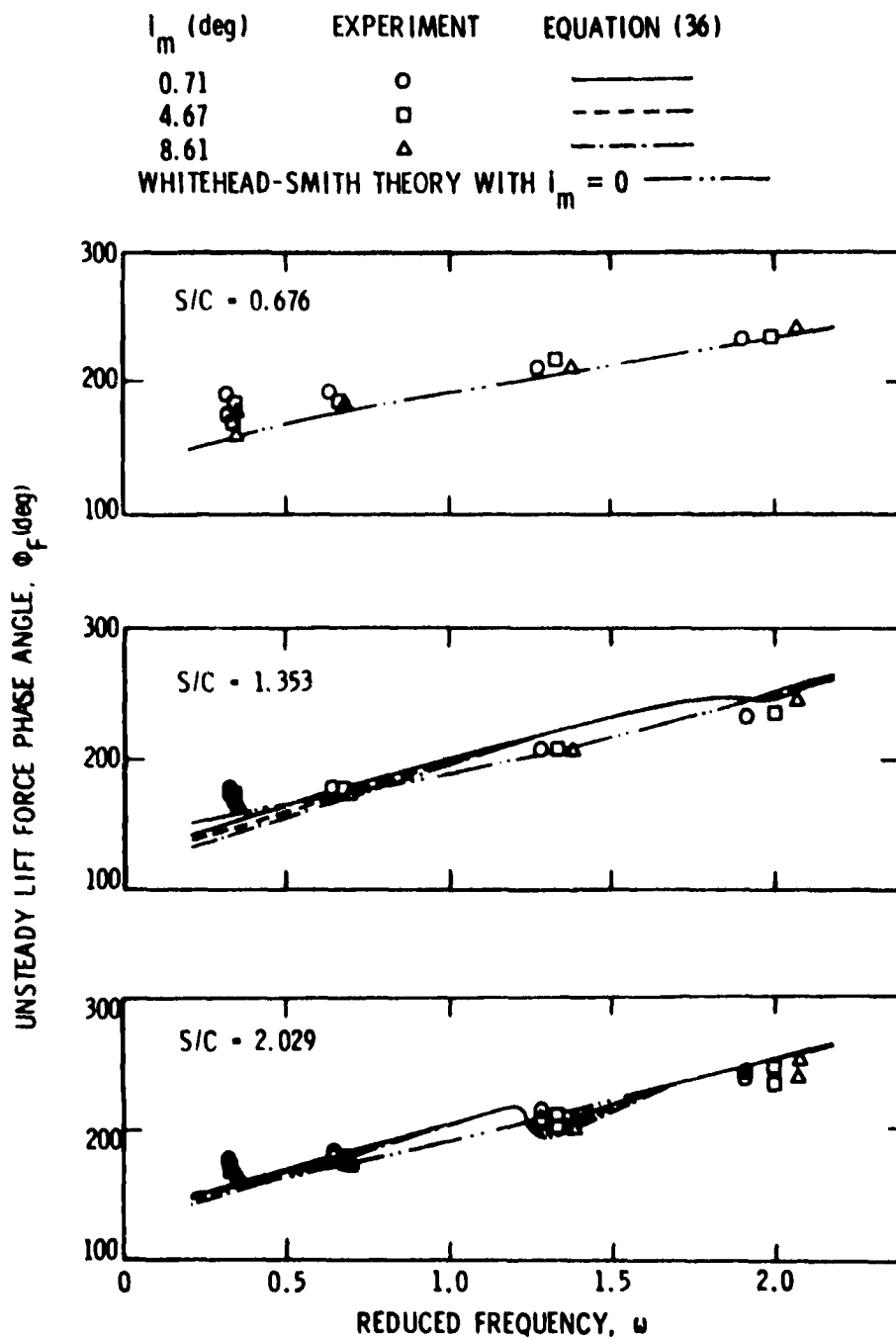
Figure 35. Comparison of Experimental and Theoretical Unsteady Lift Force Phase Angles with $y_{max}^{+} = 0$ and $\xi = 55^{\circ}$.
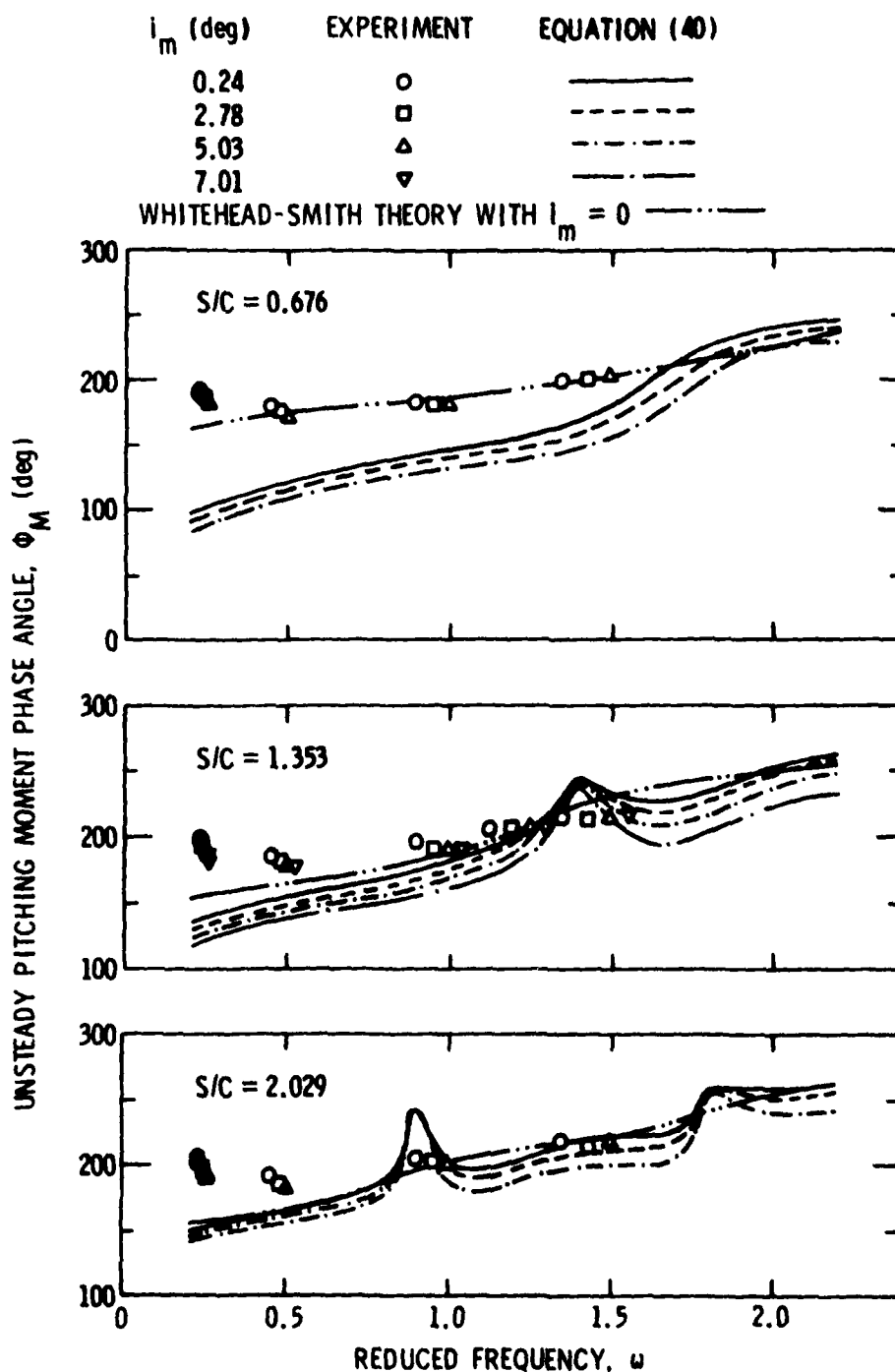
Figure 36. Comparison of Experimental and Theoretical Unsteady
Pitching Moment Phase Angles with $y^+_{max} = 0$ and
$\xi = 35^\circ$.
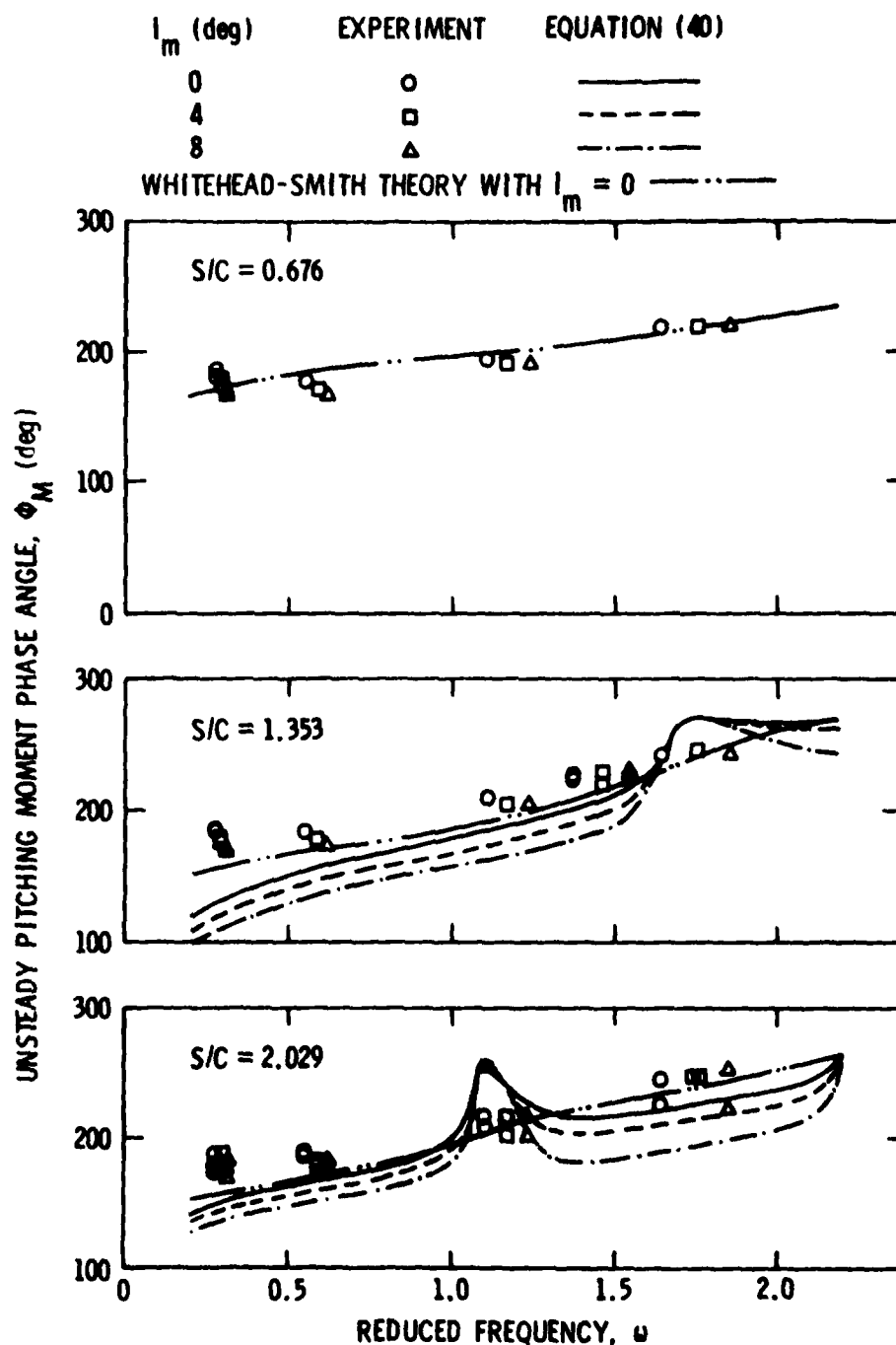
Figure 37. Comparison of Experimental and Theoretical Unsteady Pitching Moment Phase Angles with $y^+_{max} = 0$ and $\xi = 45°$.
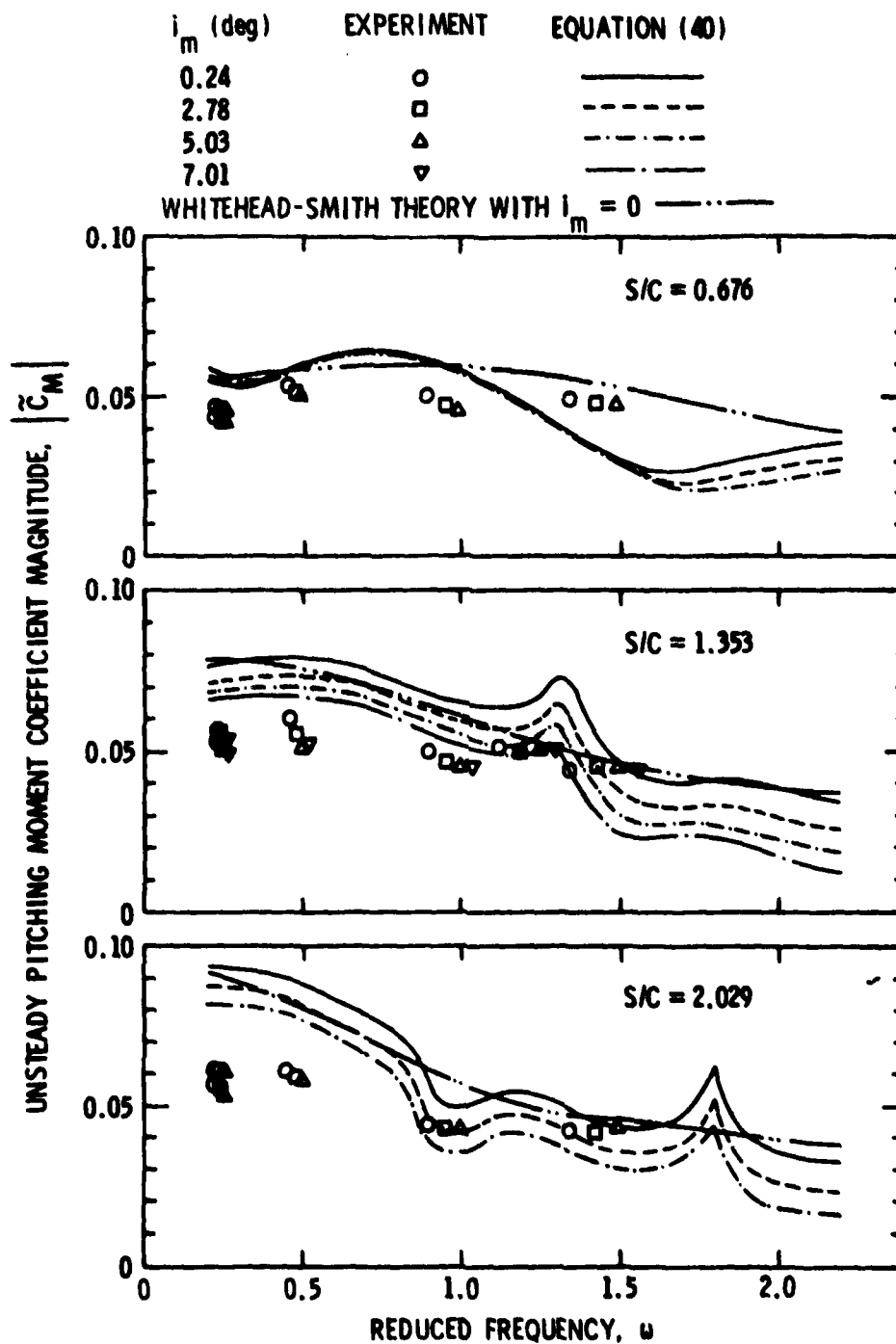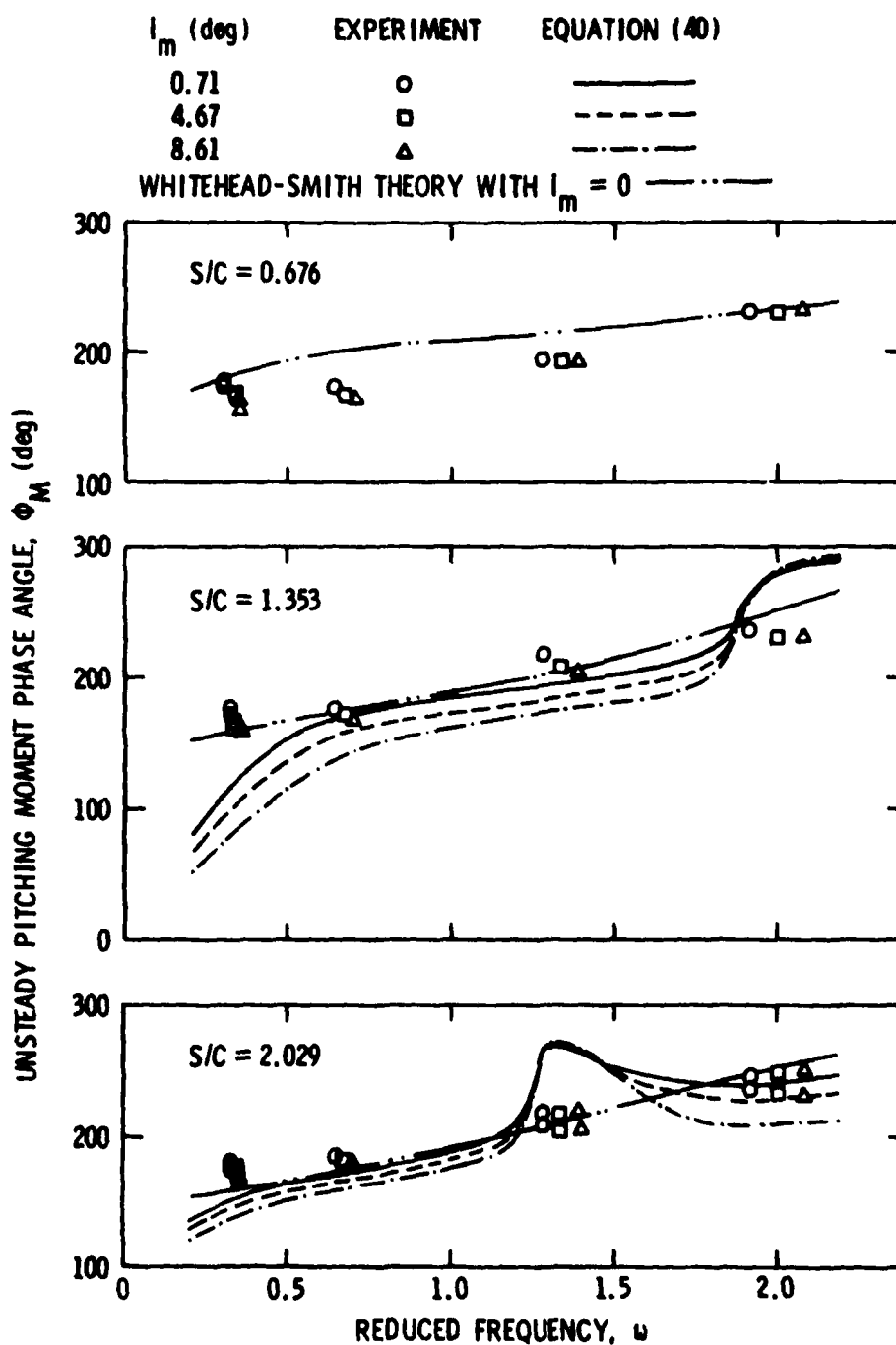
Figure 38. Comparison of Experimental and Theoretical Unsteady Pitching Moment Phase Angles with $y_{max}^{+} = 0$ and $\xi = 55^{\circ}$.

this condition, $S = k\ell$. For the case of interest here, $\alpha_m = 0$, $\mu_R = \nu$, and $\mu_I = 0$, so $\theta = \omega$, and, with $\sin\xi \approx \dfrac{U}{W_m}$, $\omega \approx \dfrac{\pi k s \sin\xi}{(S/C)}$. Values of ω computed using this relation are presented in Table 4 for $k = 1$, 2, and 3; $\xi = 35^\circ$, 45°, and 55°; and $(S/C) = 0.676$, 1.353, and 2.029.

Henderson [18] classified these critical values of ω as "resonance" points and noted that, since the computed quantities remained finite at these points, they were not associated with singularities in the solution or in the computational procedure. He also suggested a physical interpretation based on phase-angle differences as follows. A basic assumption in the analysis is that the vorticity and, as a result, the circulation on the nth blade differs from that on the reference blade only by the phase angle τ. When $\tau = -2k\pi$, the vorticity and circulation on all blades and their wakes are in-phase and their individual contributions to the unsteady response of the reference blade tend to be additive. When $\tau \neq -2k\pi$, an out-of-phase condition exists, and some cancellation of the contributions due to neighboring blades occurs.

These "resonance" conditions are well known in turbomachinery design--they correspond, for example, to cases in which an inlet guide vane blade row with a given number of blades is employed upstream of a rotor blade row having the same number of blades. Designs such as this are avoided since their performance is characterized by high levels of radiated noise and vibration. A common rule of thumb in design practice is to mismatch the number of blades employed in adjacent blade rows.

As shown in Figures 24 through 38, the Whitehead-Smith analysis does not indicate the existence of these "resonances." Henderson attributed this to the use of a limit value for the summation of the induced velocities due to all of the blades in the cascade. The limit value

TABLE 4

CRITICAL REDUCED FREQUENCIES

Stagger Angle (ξ) deg	Space-to-Chord Ratio (S/C)	Reduced Frequency (ω)		
		k = 1	k = 2	k = 3
35	0.676	2.666	5.331	7.997
35	1.353	1.332	2.664	3.995
35	2.029	0.888	1.776	2.664
45	0.676	3.286	6.572	9.858
45	1.353	1.642	3.284	4.926
45	2.029	1.095	2.190	3.285
55	0.676	3.807	7.614	11.421
55	1.353	1.902	3.804	5.706
55	2.029	1.268	2.537	3.805

is restricted to values of τ in the range $-2\pi < \tau < 0$. Thus, computations at points corresponding to $\tau = -2k\pi$ are prohibited in the Whitehead-Smith analysis.

The discussion which follows applies to the experimentally determined variation of $|\tilde{c}_L|$ with (S/C), ξ, and ω. However, with only a few exceptions, which will be noted, the observations also apply to $|\tilde{c}_M|$. As shown in Figures 24, 25, and 26, the effect of (S/C) on $|\tilde{c}_L|$ is most strongly felt through the manner in which $|\tilde{c}_L|$ varies with ω. These characteristic variations are only slightly dependent on ξ. Basically, they show a strong cascade effect in that the variation of $|\tilde{c}_L|$ with ω at (S/C) = 0.676 is characterized by low values of $|\tilde{c}_L|$ at low values of ω followed by a rise to a peak value of $|\tilde{c}_L|$ at a value of ω that increases with increasing ξ. This variation changes as (S/C) increases and, at (S/C) = 2.029, it approaches the type of variation of $|\tilde{c}_L|$ with ω that is more characteristic of an isolated airfoil. The cascade effect is still evident at (S/C) = 2.029 as shown by the slight increase in $|\tilde{c}_L|$ with an increase in ω at the two highest reduced frequencies included in the experimental program at each value of ξ. This increase in $|\tilde{c}_L|$ with an increase in ω is due in part to the fact that $|\tilde{c}_L|$ decreases at each value of ξ as ω passes through the $k = 1$ critical frequency. Clear evidence of this decrease in $|\tilde{c}_L|$ is also present at the $k = 1$ critical reduced frequency with (S/C) = 1.353.

These observations apply as well to the measured values of $|\tilde{c}_M|$— see Figures 27, 28, and 29—except for the fact that $|\tilde{c}_M|$ is practically independent of ω at (S/C) = 0.676. The effect of mean incidence angle, i_m, on $|\tilde{c}_L|$ and $|\tilde{c}_M|$ is strongest at low and high values of ω with

$\dfrac{\partial |\ddot{C}_L|}{\partial i_m}$ and $\dfrac{\partial |\ddot{C}_M|}{\partial i_m}$ negative for all values of (S/C) and ξ at low values of

ω. At high values of ω, $\dfrac{\partial |\ddot{C}_L|}{\partial i_m}$ gradually becomes less negative for all

values of (S/C) and ξ, while $\dfrac{\partial |\ddot{C}_M|}{\partial i_m}$ goes through zero and becomes more

and more strongly positive with increasing values of (S/C), ξ, and ω.

With regard to $\dfrac{x_{C.P.}}{C}$, the data points shown in Figures 30, 31, and

32 reveal a cascade effect at (S/C) = 0.676 by the rearward movement of

$\dfrac{x_{C.P.}}{C}$ with increasing ω at all values of ξ. For ξ = 35°, there is very

little effect due to changes in i_m, and the center-of-pressure moves

aft of the isolated airfoil location at the quarter-chord point as ω

increases. At ξ = 45° and 55° with $i_m \simeq 0$, $\dfrac{x_{C.P.}}{C}$ moves aft to the

quarter-chord point as ω increases, while, at the higher reduced fre-

quencies for which data are available, the effect of positive mean inci-

dence is to move the center-of-pressure forward. At (S/C) = 1.353, for

low values of i_m, $\dfrac{x_{C.P.}}{C}$ is close to the isolated airfoil position for

all values of ξ and for all values of ω except those in the neighborhood

of a critical reduced frequency. Near these frequencies, the measured

$\dfrac{x_{C.P.}}{C}$ location is forward of the location occupied at neighboring values

of ω. As ω and ξ increase, the effect of increases in i_m is to move the

center-of-pressure forward. These observations also apply to the data

at (S/C) = 2.029, except for the fact that the data points at high

values of ω for ξ = 45° and 55° define a position well forward of the

isolated airfoil location.

Phase-angle data for the lift force, ϕ_F, and pitching moment, ϕ_M,

are presented in Figures 33-35 and 36-38, respectively. These data are

essentially independent of ξ. Their dependence on (S/C) is slight. It

consists of a slight increase in the slope of the linear variation of
ϕ_F with ω, for values of ω above 0.4, with increasing values of (S/C).
At values of ω less than 0.4, the data approach a constant value of $\phi_F =$
180°. The effect of a positive change in i_m is a slight reduction in
ϕ_F; however, this effect becomes smaller as ω increases. These data do
not show a significant effect at values of ω close to the critical val-
ues listed in Table 4 as do the $|\hat{c}_L|$, $|\hat{c}_M|$, and $\frac{x_{C.P.}}{C}$ data.

Theoretical predictions based on Equations (36) and (40) of Chapter
2 and on the Whitehead-Smith theory are also shown in Figures 24 through
38. As shown in Appendix C, the theoretical model developed herein is
not valid for $\xi = 45^{\circ}$ and 55° at (S/C) = 0.676. Consequently, the data
for these cases are compared only with the Whitehead-Smith results.

As shown in Figures 24, 25, and 26, Equation (36) predicts $|\hat{c}_L|$
for $i_m = 0$ fairly accurately for $\omega > 0.8$. For $\omega < 0.8$, the predicted
$|\hat{c}_L|$ is too large, and the disagreement increases as ω decreases. The
general trend is for the theory to predict a $|\hat{c}_L|$ that is higher than
the measured value. Equation (36) does predict many of the changes
shown in the data near critical values of reduced frequency regardless
of whether they represent increases or decreases in $|\hat{c}_L|$. Throughout
the range of reduced frequencies covered by the experiments, the theo-
retical $\frac{\partial|\hat{c}_L|}{\partial i_m}$ is negative and, in general, the predicted effect due to
increasing i_m exceeds the measured effect.

Figures 27, 28, and 29 show that, in most cases, the $|\hat{c}_M|$ as pre-
dicted by Equation (40) at $i_m = 0$ also exceeds the measured values.
Except for the points for $\omega < 0.8$ with (S/C) = 1.353 and $\xi = 55^{\circ}$, the
points where the theory underpredicts the data are associated with the

relatively large changes in predicted values of $|\overset{\curlyvee}{c}_M|$ that occur at reduced frequencies near the critical values listed in Table 4. At values of $\omega < 1.0$ with $\xi = 35^{\circ}$ and $i_m = 0$, while fairly accurately predicting the results at $(S/C) = 0.676$, the theory then overpredicts the measured results to a greater and greater degree as (S/C) increases. The most accurate prediction in this reduced frequency range shifts to $(S/C) = 1.353$ at $\xi = 45^{\circ}$ and to $(S/C) = 2.029$ at $\xi = 55^{\circ}$. At higher reduced frequencies, the predicted cascade effects are reduced and, except for variations associated with reduced frequencies near critical values, the predicted performance tends to be independent of (S/C) and ξ. Equation (40) predicts negative values of $\dfrac{\partial |\overset{\curlyvee}{c}_M|}{\partial i_m}$ for all cases covered by the experiments except for the $(S/C) = 1.353$, $\xi = 55^{\circ}$ case for low values of ω. This trend is supported by the data only at low values of reduced frequency.

Curves defining the predicted center-of-pressure position for the unsteady lift are presented in Figures 30, 31, and 32. Since the ratio of $|\overset{\curlyvee}{c}_M|$ to $|\overset{\curlyvee}{c}_L|$ is used in the definition of $\dfrac{x_{C.P.}}{C}$, it is possible for the predicted $\dfrac{x_{C.P.}}{C}$ to agree with the measured value in cases where good agreement is not present between the predicted and measured values of $|\overset{\curlyvee}{c}_M|$ and $|\overset{\curlyvee}{c}_L|$. Examples of this behavior are the low reduced frequency cases for $\xi = 35^{\circ}$ with $(S/C) = 1.353$ and 2.029 and the low reduced frequency case with $\xi = 45^{\circ}$ and $(S/C) = 2.029$. The predicted and measured values for $i_m = 0$ are in good agreement, i.e., to within 5% of the chord length, for all cases covered by the experiments except for:

    (1) $\omega < 0.6$ for $\xi = 35^{\circ}$ and $(S/C) = 0.676$,

    (2) $\omega < 0.4$ for $\xi = 45^{\circ}$ and $(S/C) = 1.353$,

(3) $\omega > 1.6$ for $\xi = 45^\circ$ and $(S/C) = 2.029$,

(4) all values of ω for $\xi = 55^\circ$ and $(S/C) = 1.353$,

(5) $\omega < 0.5$ for $\xi = 55^\circ$ and $(S/C) = 2.029$, and

(6) $\omega > 1.6$ for $\xi = 55^\circ$ and $(S/C) = 2.029$.

In all of the cases noted above, except for $\omega > 1.8$ with $\xi = 55^\circ$ and $(S/C) = 1.353$, the predicted $\frac{x_{C.P.}}{C}$ position is aft of the measured position. The predicted forward center-of-pressure position for this case occurs at one of the critical reduced frequency conditions listed in Table 4. The theoretical curves show that the center-of-pressure moves forward at each of these critical reduced frequencies. In all cases where this predicted movement is significant, the measured data also show a forward $\frac{x_{C.P.}}{C}$ movement.

The predicted effect of increasing mean incidence angle, i_m, on $\frac{x_{C.P.}}{C}$ is generally not as large as in the case of $|\overset{\alpha}{C}_L|$ and $|\overset{\alpha}{C}_M|$. A significant forward shift of $\frac{x_{C.P.}}{C}$ with increasing i_m is shown by the data for all values of (S/C) for $\xi = 55^\circ$ and $\omega \approx 2.0$. The theory for $(S/C) = 2.029$ defines a much more aft $\frac{x_{C.P.}}{C}$ position and a trend due to incidence that is in the opposite direction. Examination of the high reduced frequency measured data for $\xi = 55^\circ$ shows the largest effects due to incidence and the poorest agreement with the levels and trends predicted by the theory for both $|\overset{\alpha}{C}_M|$ and $\frac{x_{C.P.}}{C}$ at $(S/C) = 1.353$ and 2.029. Theoretical predictions are not available for $(S/C) = 0.676$; however, the data for $|\overset{\alpha}{C}_M|$ at this condition show a trend due to incidence that is similar to the trend at the other values of (S/C) and is in opposition to the trend established by the lower reduced frequency data at $(S/C) = 0.676$. These differences are sufficient to arouse suspicion as to the validity of the $|\overset{\alpha}{C}_M|$ data for $\omega \approx 2.0$ with $\xi = 55^\circ$,

particularly at high values of i_m. The fundamental frequencies, f, required in the generation of these data points were among the highest of any in the entire experimental program. For $i_m = 4.67°$, $f = 110.7$ Hz, and, for $i_m = 8.61°$, $f = 130.6$ Hz. As shown in Figure 21, operation at these frequencies requires an amplitude ratio correction on the order of 10 to 30% which, since the sensor was accurately calibrated, should not have caused any loss of data accuracy. In operating the facility, the rotor inlet velocity components V and U were adjusted as ξ and i_m were changed so as to maintain a minimum Reynolds number, based on C and W_1, of 250,000. Horlock [36] has shown that large total pressure losses can be avoided in cascade testing by operating at or above this value. In the test program, $(\xi + i_m)$ changed from about 35° to about 65°. This change was accompanied by a gradual decrease in the value of V and a gradual increase in the value of U. Thus, if a loss of accuracy in the experimental data could have been caused by driving the force or moment sensors at high frequencies, it would have appeared in the data at large values of $(\xi + i_m)$. An adequate check on these data points would require repeating the experiments using a sensor designed to provide higher resonant frequencies. This dynamic performance improvement could only be achieved at the expense of reduced static sensitivity, so clearly a careful tradeoff would be required.

Figures 33, 34, and 35 show that the predicted unsteady lift force phase angle, ϕ_F, is in good agreement with the measured data at all conditions covered in the experimental program except for $\omega < 0.6$. As ω decreases, starting from $\omega \approx 0.6$, the theoretical predictions and the measured data gradually diverge until a difference of approximately 20° exists at $\omega \approx 0.2$. Theoretical results were not generated for $\omega < 0.2$

because no data were available for comparison in this range and because the computer program running time increased significantly as ω approached zero. In the limit, when $\omega = 0$, Equation (36) yields the value $\phi_F = 180°$ for $i_m = 0$, which is in agreement with the result presented by Henderson [18].

The figures also show that the predicted effects on unsteady lift force phase angle due to variations in (S/C) and i_m and due to operation at or near the critical reduced frequencies listed in Table 4 are small. The effects due to changes in stagger angle, ξ, are negligible for $35° < \xi < 55°$.

The predicted unsteady pitching moment phase angles, ϕ_M, are shown in Figures 36, 37, and 38. Examination of these results shows that agreement with the measured data is poor at low values of (S/C), at low values of ω, and at values of ω close to the critical values. In the limit, when $\omega = 0$, with $i_m = y_{max}^+ = 0$, Equation (40) reduces to

$$\left[(C_M)_{\omega = i_m = y_{max}^+ = 0}\right] = -\frac{\sin\phi}{4}\left[B(o, x_c^+, S/C, \xi) + 1\right] \quad ,$$

where

$$B(o, x_c^+, S/C, \xi) = \frac{\left[\displaystyle\sum_{-\infty}^{-1} + \sum_1^\infty\right]\left[\sqrt{g_c^2 - 1} - g_c + \sqrt{h_c^2 - 1} - h_c\right]}{\frac{1}{2}\left[\displaystyle\sum_{-\infty}^{-1} + \sum_1^\infty\right](C_1 + C_2 - 2) - 1} \quad ,$$

a positive real number. Thus, for this condition, $\phi_M = 180°$. This value is in agreement with the trend established by the experimental

results. It also indicates that the theory will predict large changes in ϕ_M due to small changes in ω for $\omega < 0.2$, a characteristic which lacks experimental support. The rapid changes in ϕ_M predicted by Equation (40) in the neighborhood of critical reduced frequencies also are not supported by the data. At fixed values of ξ, ω, and i_m, the theory predicts a slight reduction in ϕ_M with increasing (S/C). This feature is supported by the measured results as is the trend due to changes in i_m. However, the theory generally overpredicts the effect on ϕ_M due to changes in i_m.

The performance predictions based on the Whitehead-Smith model are valid only for $i_m = y_{max}^+ = 0$. Figures 24, 25, and 26 show that this model overpredicts the measured $|\tilde{C}_L|$ in all cases. However, it predicts the trends of the variation of $|\tilde{C}_L|$ with ω very well even though it does not follow closely the changes in the level of $|\tilde{C}_L|$ shown by the data in the neighborhood of critical reduced frequencies. Except for the low reduced frequency region and regions containing critical reduced frequencies, predictions based on the Whitehead-Smith theory and Equation (36) are generally close to each other.

Figures 27, 28, and 29 show that the Whitehead-Smith theory over-predicts the measured values of $|\tilde{C}_M|$ in all cases except (S/C) $= 0.676$ with $\xi = 45°$ and $55°$, which it predicts quite accurately, and $\omega \approx 2.0$ with $\xi = 55°$, where the validity of the data could be questionable. This multiple bound vortex theory also predicts the trends of the varia-tion of $|\tilde{C}_M|$ with ω quite well except for the $\omega < 0.8$ region with $\xi = 35°$ and (S/C) $= 2.029$. For all cases where low reduced frequency and criti-cal reduced frequency effects do not cause large changes in $|\tilde{C}_M|$ as

predicted by Equation (40), predicted levels of $|\overset{\alpha}{c}_M|$ as given by the two theories do not differ greatly.

The Whitehead-Smith prediction of $\dfrac{x_{C.P.}}{C}$ is quite good as shown by Figures 30, 31, and 32. In cases where the predicted and measured center-of-pressure positions do not agree closely, the predicted position is aft of the measured position. These cases are (S/C) = 0.676 with ξ = 45° and 55°, critical reduced frequency regions for (S/C) = 1.353 for all values of ξ, and the regions near $\omega \simeq 2.0$ with ξ = 55°.

The Whitehead-Smith unsteady lift force phase angle predictions, shown in Figures 33, 34, and 35, are also quite accurate except for reduced frequencies below ω = 0.4. The predictions due to the two theoretical models are essentially in agreement, with differences appearing only where the values of ϕ_F given by Equation (36) are affected by critical reduced frequency effects. Figures 36, 37, and 38 show that predictions by the Whitehead-Smith theory of ϕ_M, the unsteady pitching moment phase angle, are also in good agreement with the measured results for reduced frequencies above $\omega \simeq 0.6$. These predictions are significantly better than predictions based on Equation (40) at values of ω below $\omega \simeq 0.6$ for all values of (S/C) and ξ and for all values of ω with (S/C) = 0.676 and ξ = 35°.

The preceeding comparisons show that the theory developed herein tends to overpredict the effect on $|\overset{\alpha}{c}_L|$ and $|\overset{\alpha}{c}_M|$ due to changes in mean incidence angle and that both theories tend to overpredict the measured values of $|\overset{\alpha}{c}_L|$ and $|\overset{\alpha}{c}_M|$ at zero mean incidence. Possible reasons for these overpredictions can be traced to two main sources as noted in the following paragraphs.

First, in the theoretical models, the assumption is made that disturbance velocities proceed through the rotor with no amplitude attenuation. In recently conducted experiments, it has been demonstrated by Yocum [37] that significant attenuation of these velocities occurs upstream of the rotor, due to potential flow interactions, and that still further attenuation occurs as the distortion passes through the rotor blade row. Attenuation means a lessening of the disturbance velocity magnitude. The attenuation that occurs between flow conditions far upstream of the rotor and flow conditions at the rotor inlet is defined as the ratio of the magnitude of the dominant harmonic of the axial velocity profile as measured at the rotor inlet to the corresponding harmonic of the far upstream axial velocity profile. The term total attenuation is defined as the corresponding ratio applied to the rotor exit-to-far upstream conditions. Attenuation may be greater than one (negative attenuation) or less than one (positive attenuation). Increasing attenuation is associated with decreasing values of the velocity ratio, and, conversely, decreasing attenuation is associated with increasing values of the velocity ratio. Yocum also showed that the total attenuation increased with increasing values of i_m, ξ, and ω for values of these parameters covered in the experimental program described herein. The degree of increase in total attenuation at $\omega \simeq 1$ due to increasing i_m was greater for $\xi = 35^o$ than $\xi = 45^o$. At $\xi = 55^o$ with $\omega \simeq 1$, Yocum obtained no increase in total attenuation due to variations in i_m. Over the full range of variations in i_m, the general trend was for attenuation upstream of the rotor to decrease from a value of approximately 0.6 at $\omega \simeq 0.3$ to a value of approximately 0.7 at $\omega \simeq 1.8$. The total attenuation, on the other hand, increased from a value

of approximately 0.4 at $\omega = 0.3$ to a value of approximately 0.2 at $\omega = 1.8$. The failure of the theoretical models to account for this distortion velocity attenuation is one sure source for overprediction of the measured results. The fact that the total attenuation is slightly dependent upon i_m could also contribute to the disagreement between the measured and predicted effects due to changes in this variable.

Second, the role of fluid viscosity is neglected in the theoretical models. Due to viscosity, the wake formed downstream of each blade is characterized by a velocity defect profile. As a result, the fluid in the wake moves away from the blade at a velocity that is less than that of the surrounding stream. Thus, the assumption that the shed or trailing vorticity is transported away from the blades with the mean relative velocity W_m is not valid. Bradshaw et al. [38] have shown that a more realistic assumption would equate this transport velocity to a lower value such as $0.6 \ W_m$ or $0.7 \ W_m$. In addition, viscosity causes dissipation of the shed vorticity; thus, the assumption that the wake vorticity extends unaltered to an infinite distance downstream of each blade also is not valid. In this regard it would be more realistic to introduce a factor which would force the wake vorticity distribution to decay in some prescribed manner with increasing distance from the airfoil. An exponential decay is a reasonable choice for a first attempt.

Up to this point in this research program, no attention has been given to an evaluation of the effects of blade camber. This is because experimental data are not available for a rotor containing cambered blades. In addition, the analysis of the effects of reduced frequency has been limited to values covered in the experimental program. The results presented in Chapter 5 remedy these situations by the

presentation of results obtained using Equations (36) and (40) in the

form of plots for ξ = 35°, 45°, and 55° of $|\tilde{c}_{L_{o,o}}|$, $\dfrac{\partial|\tilde{c}_L|}{\partial i_m}$, $\dfrac{\partial|\tilde{c}_L|}{\partial y^+_{max}}$,

$|\tilde{c}_{M_{o,o}}|$, $\dfrac{\partial|\tilde{c}_M|}{\partial i_m}$, and $\dfrac{\partial|\tilde{c}_M|}{\partial y^+_{max}}$ versus ω for $0.2 \leq \omega \leq 10.0$ for 0.676 or

$1.353 \leq$ (S/C) $\leq$ 99. Here, $|\tilde{c}_{L_{o,o}}|$ and $|\tilde{c}_{M_{o,o}}|$ denote values of the

lift force and pitching moment coefficients computed for the case of

zero mean incidence angle and zero camber. These basic values are

essential for computation of the final coefficients which may be expres-

sed as

$$|\tilde{c}_L| = |\tilde{c}_{L_{o,o}}| + \frac{\partial|\tilde{c}_L|}{\partial i_m}i_m + \frac{\partial|\tilde{c}_L|}{\partial y^+_{max}}y^+_{max} \tag{45}$$

and

$$|\tilde{c}_M| = |\tilde{c}_{M_{o,o}}| + \frac{\partial|\tilde{c}_M|}{\partial i_m}i_m + \frac{\partial|\tilde{c}_M|}{\partial y^+_{max}}y^+_{max} \quad . \tag{46}$$

The plots clearly show regions where cascade effects are significant;

however, their greatest utility is perhaps in the rapid estimation of

cascade unsteady response including effects of blade camber and positive

mean incidence angle.

CHAPTER 5

THEORETICAL PREDICTIONS OF THE EFFECTS OF STAGGER ANGLE, SPACE-TO-CHORD RATIO, MEAN INCIDENCE, AND CAMBER ON THE LIFT FORCE AND PITCHING MOMENT COEFFICIENT MAGNITUDE FOR A RANGE OF VALUES OF REDUCED FREQUENCY

5.1 Introduction

Theoretical results given by Equations (36) and (40) are presented

in Figures 39 through 56 in the form of plots for $\xi = 35^{\circ}$, 45°, and 55°

of $|\hat{c}_{L_{o,o}}|$, $\dfrac{\partial|\hat{c}_L|}{\partial i_m}$, $\dfrac{\partial|\hat{c}_L|}{\partial y_{max}^+}$, $|\hat{c}_{M_{o,o}}|$, $\dfrac{\partial|\hat{c}_M|}{\partial i_m}$, and $\dfrac{\partial|\hat{c}_M|}{\partial y_{max}^+}$ versus ω for $0.2 \leq$

$\omega \leq 10.0$ with $(S/C) = 0.676$ or 1.353, 2.029, and 99. The expanded

ranges covered by the parameters ω and (S/C) are sufficient to define

regions where cascade effects are significant by comparison with iso-

lated airfoil results. A second, and perhaps more important, use for

the plots is as a means for the rapid estimation of cascade unsteady

performance as a function of ξ, ω, (S/C), i_m, and y_{max}^+.

5.2 Discussion of Results

The characteristics of each coefficient or partial derivative are

discussed separately in the following paragraphs. These paragraphs are

followed by a discussion of a more general nature. In this analysis,

the cascade results for $(S/C) = 99$ are considered to be equivalent to

isolated airfoil results.

Figures 39, 40, and 41 contain the $|\hat{c}_{L_{o,o}}|$ data. They show that,

for a given value of ω with $(S/C) = 99$, an increase in the value of ξ
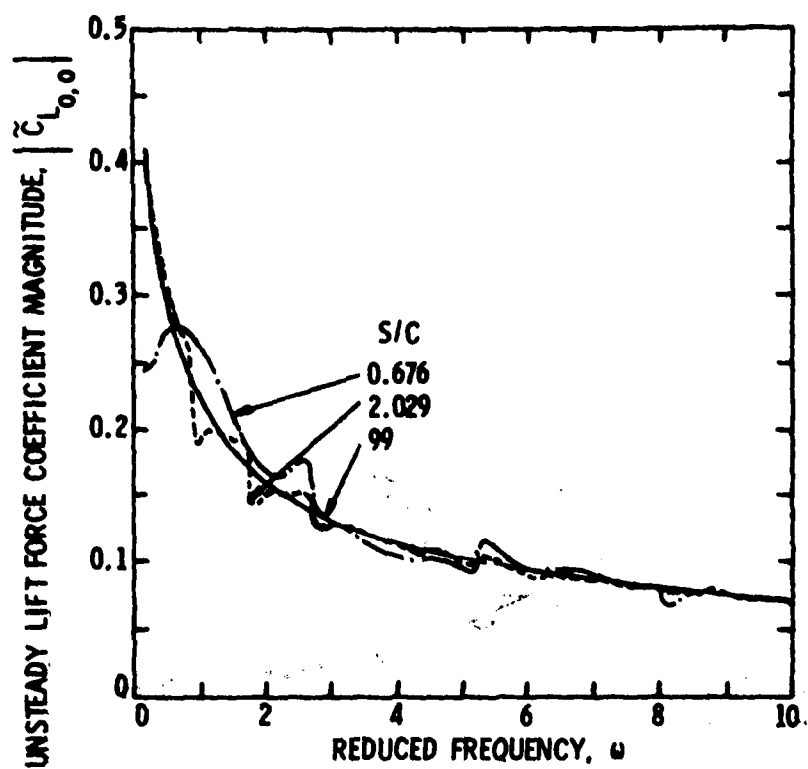
Figure 39. Unsteady Lift Force Coefficient with $i_m = y^+_{max} = 0$ and $\xi = 35^{\circ}$.
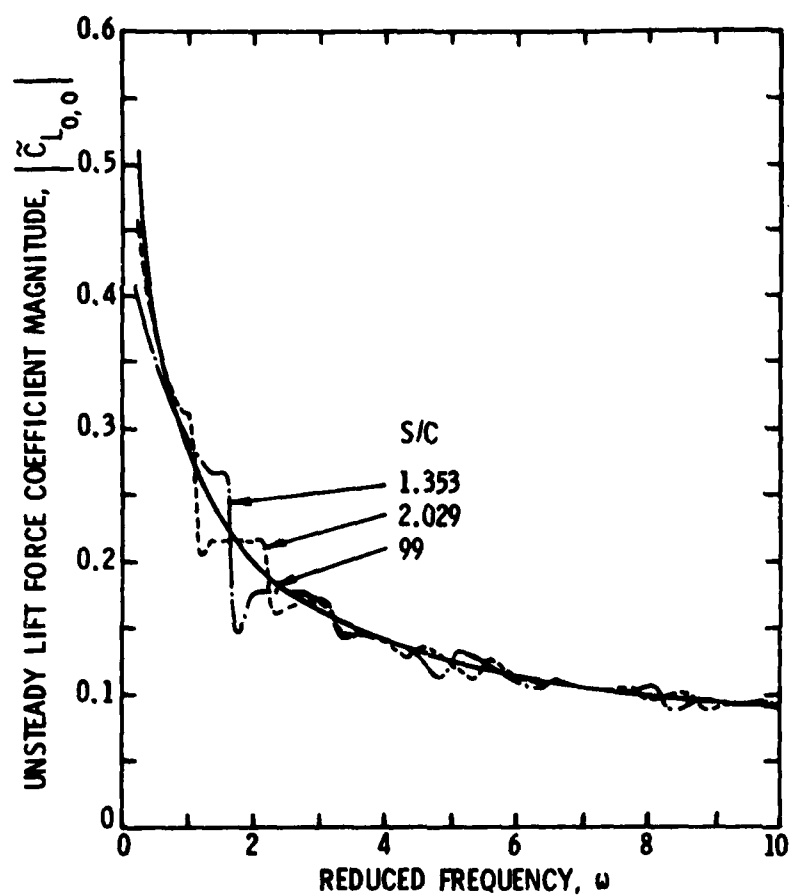
Figure 40. Unsteady Lift Force Coefficient with $i_m = y^+_{max} = 0$ and $\xi = 45°$.
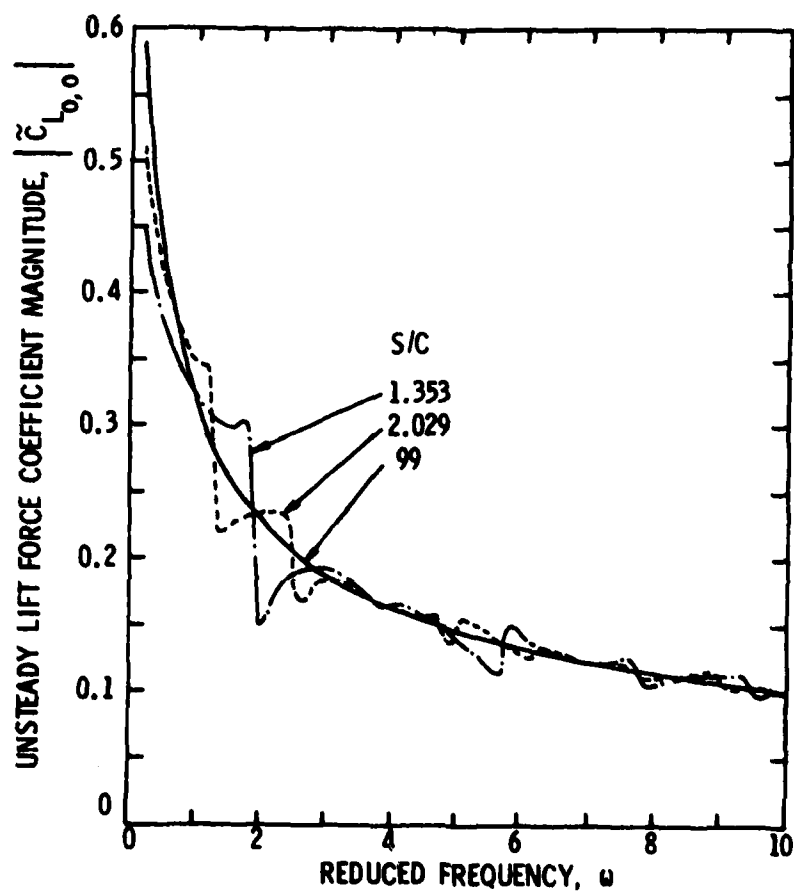
Figure 41. Unsteady Lift Force Coefficient with $i_m = y^+_{max} = 0$ and $\xi = 55°$.
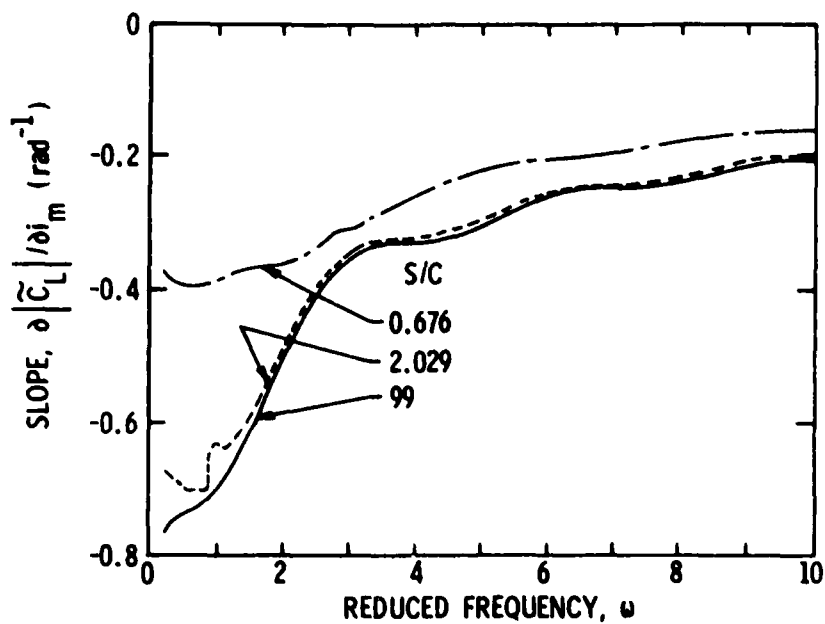
Figure 42. Partial Derivative of the Unsteady Lift Force Coefficient with Respect to Mean Incidence Angle with $y_{max}^+ = 0$ and $\xi = 35^o$.
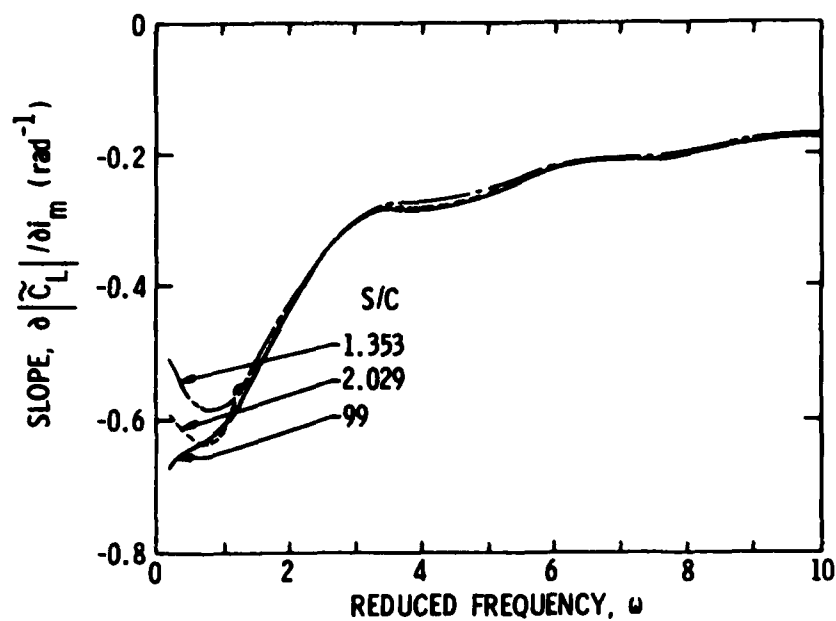
Figure 43. Partial Derivative of the Unsteady Lift Force Coefficient with Respect to Mean Incidence Angle with $y^+_{max} = 0$ and $\xi = 45^o$.
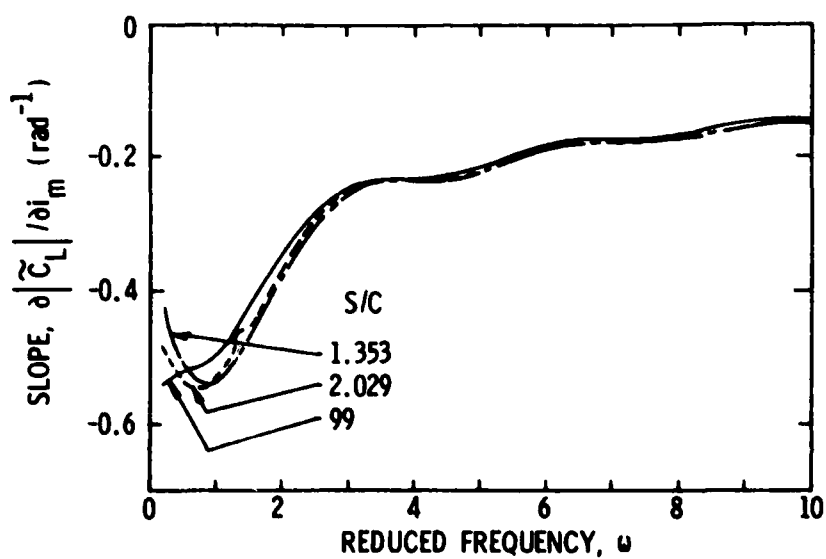
Figure 44. Partial Derivative of the Unsteady Lift Force Coefficient with Respect to Mean Incidence Angle with $y^+_{max} = 0$ and $\xi = 55^o$.

Figure 45. Partial Derivative of the Unsteady Lift Force Coefficient
with Respect to Camber with $i_m = 0$ and $\xi = 35^o$.

Figure 46. Partial Derivative of the Unsteady Lift Force Coefficient
with Respect to Camber with $i_m = 0$ and $\xi = 45^o$.

Figure 47. Partial Derivative of the Unsteady Lift Force Coefficient with Respect to Camber with $i_m = 0$ and $\xi = 55°$.
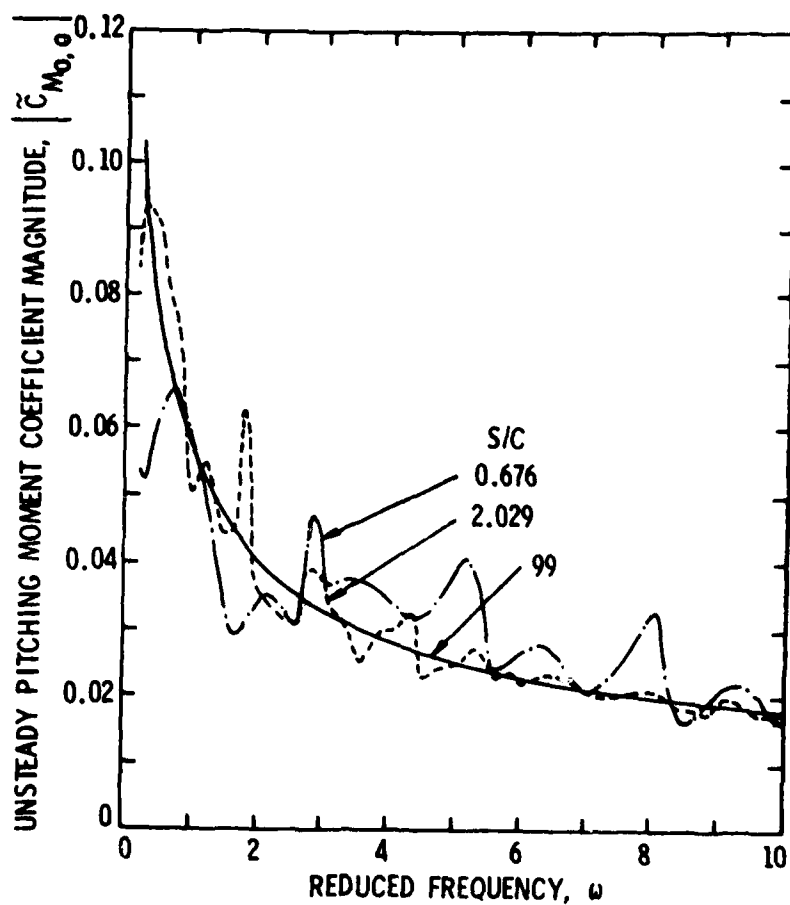
Figure 48. Unsteady Pitching Moment Coefficient with
$i_m = y_{max}^+ = 0$ and $\xi = 35^o$.
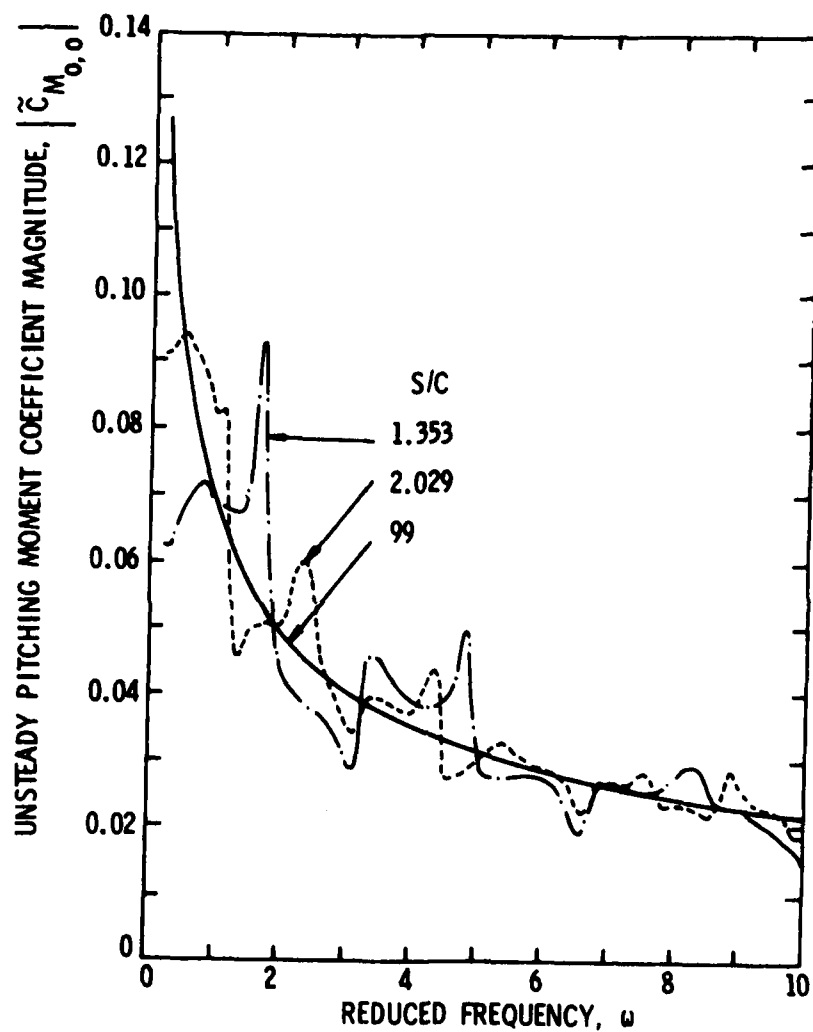
Figure 49.   Unsteady Pitching Moment Coefficient with
$i_m = y^+_{max} = 0$ and $\xi = 45^o$.
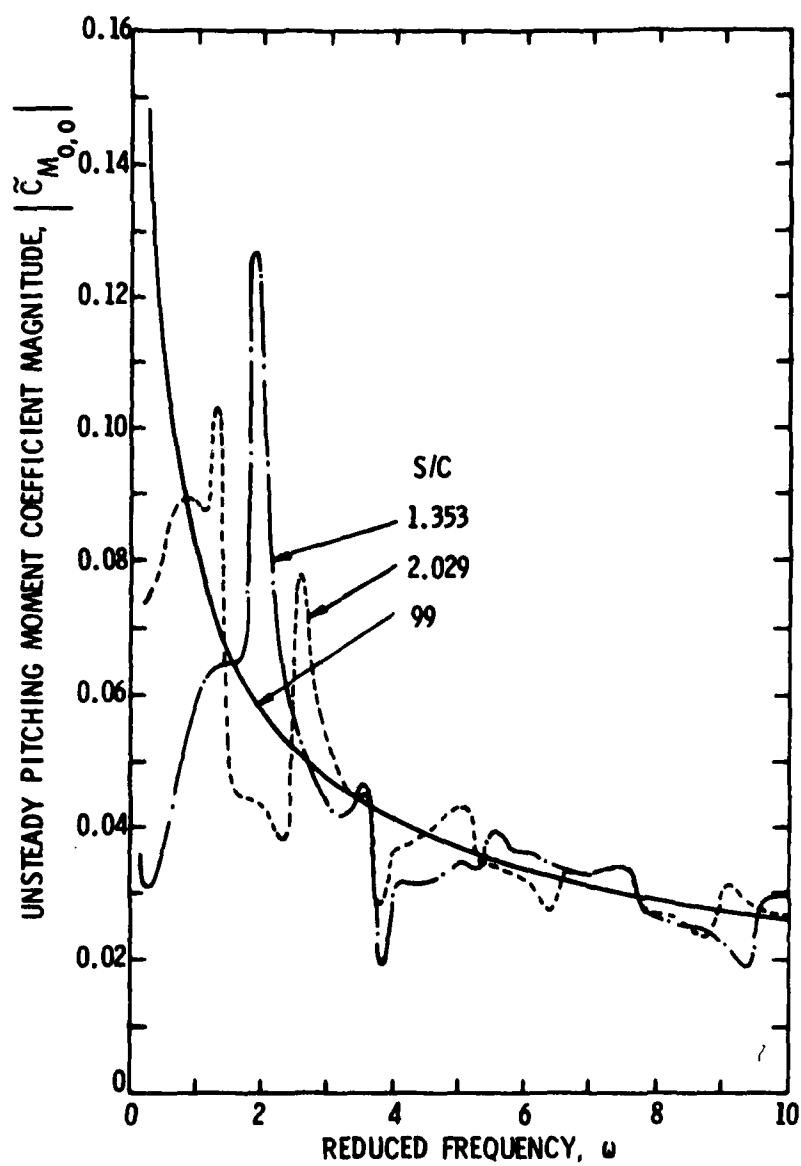
Figure 50. Unsteady Pitching Moment Coefficient with $i_m = y^+_{max} = 0$ and $\xi = 55^o$.
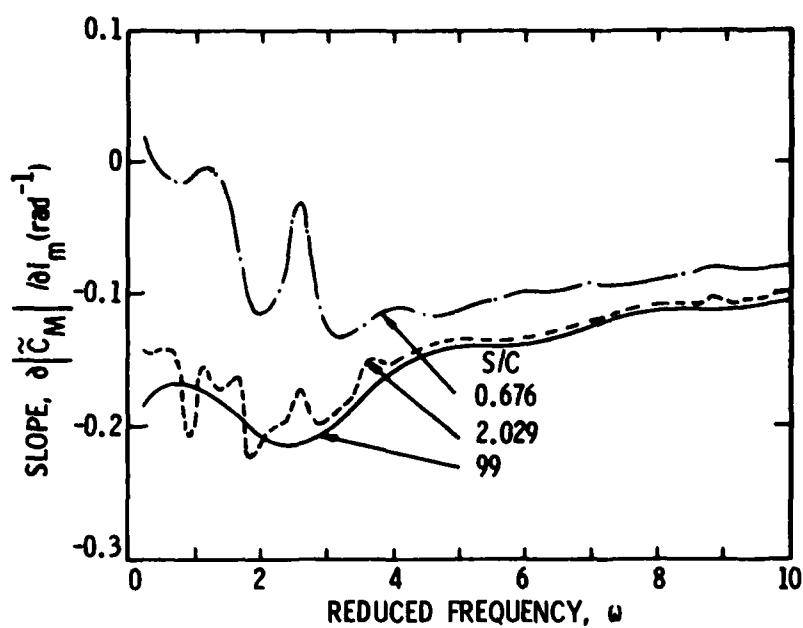
Figure 51.   Partial Derivative of the Unsteady Pitching Moment
Coefficient with Respect to Mean Incidence Angle
with $y^{+}_{max} = 0$ and $\xi = 35^{o}$.
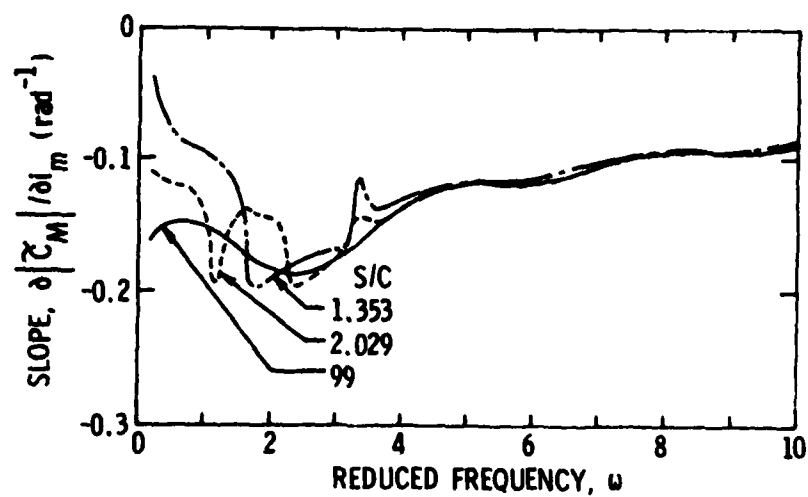
Figure 52. Partial Derivative of the Unsteady Pitching Moment
Coefficient with Respect to Mean Incidence Angle
with $y_{max}^+ = 0$ and $\xi = 45^o$.
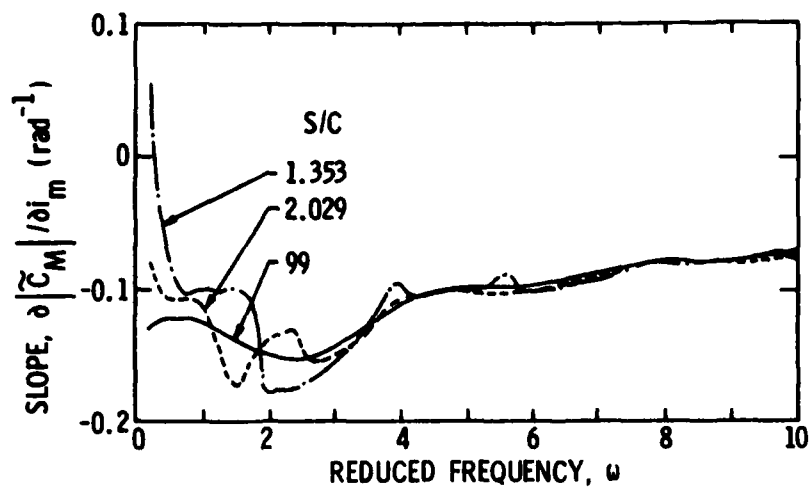
Figure 53. Partial Derivative of the Unsteady Pitching Moment
Coefficient with Respect to Mean Incidence Angle
with $y_{max}^{+} = 0$ and $\xi = 55^{o}$.
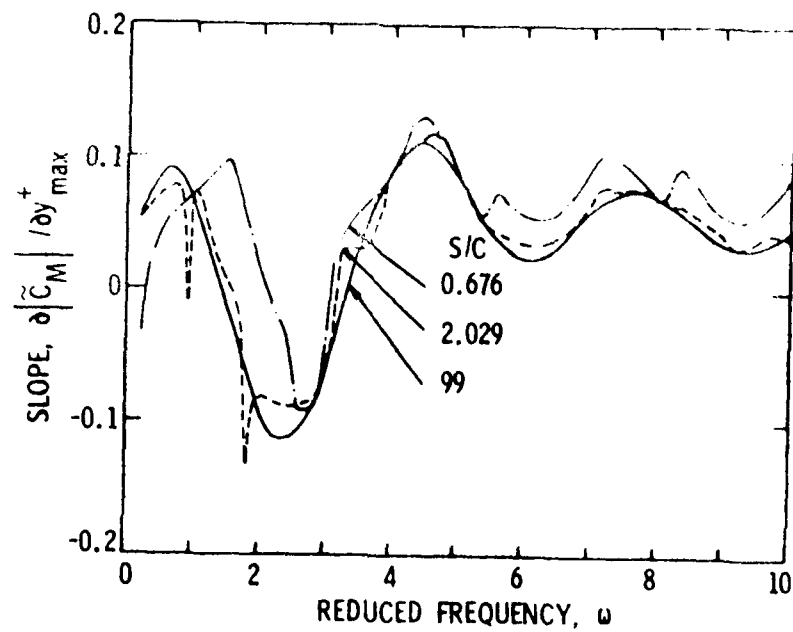
Figure 54. Partial Derivative of the Unsteady Pitching Moment Coefficient with Respect to Camber with $i_m = 0$ and $\xi = 35^\circ$.
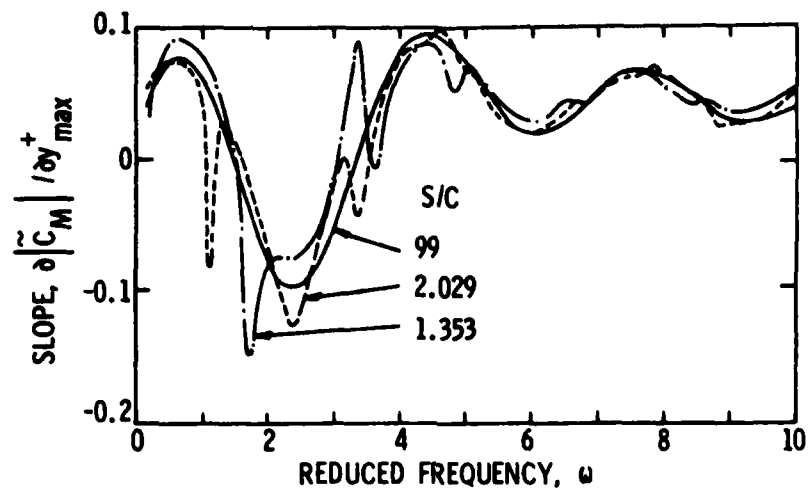
Figure 55. Partial Derivative of the Unsteady Pitching Moment
Coefficient with Respect to Camber with $i_m = 0$ and
$\xi = 45^o$.

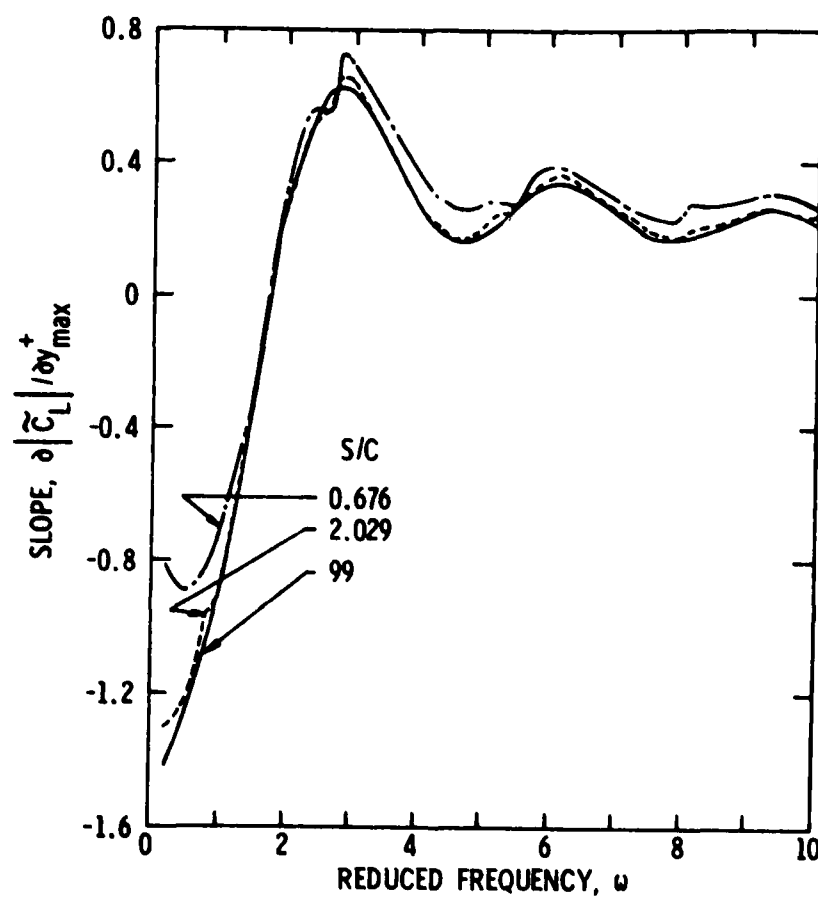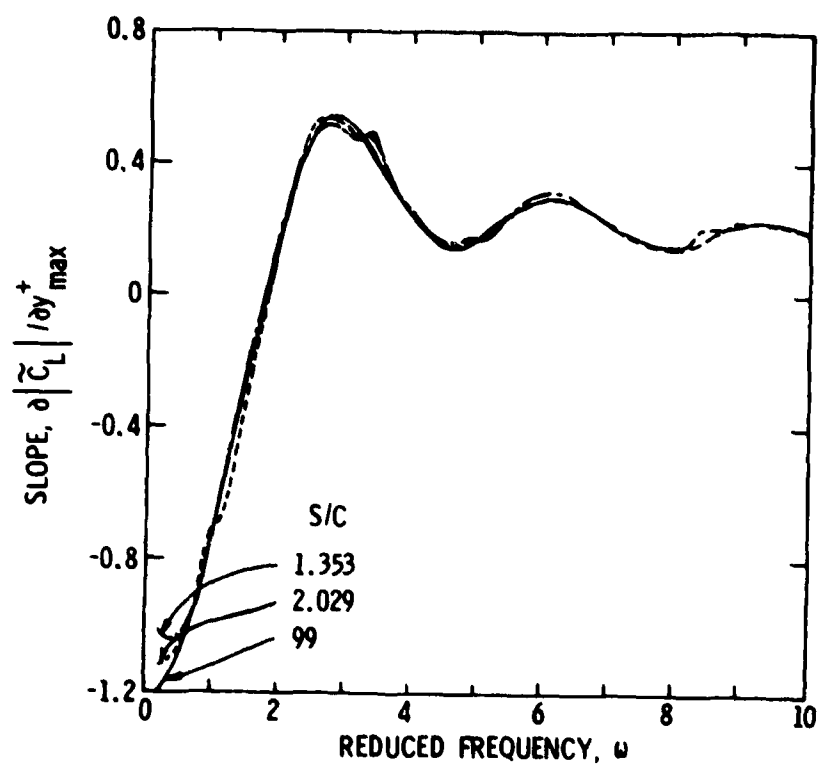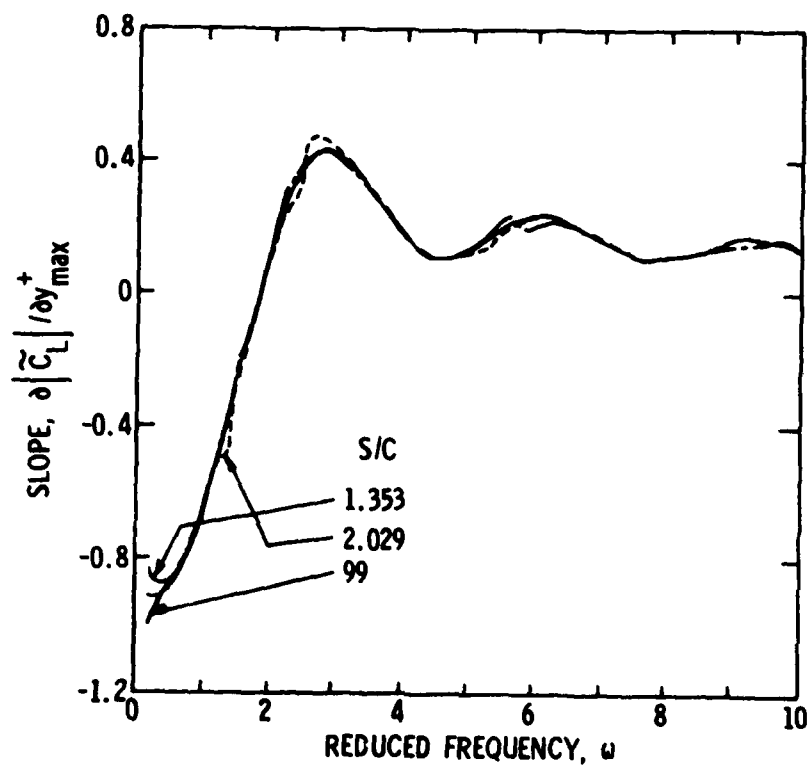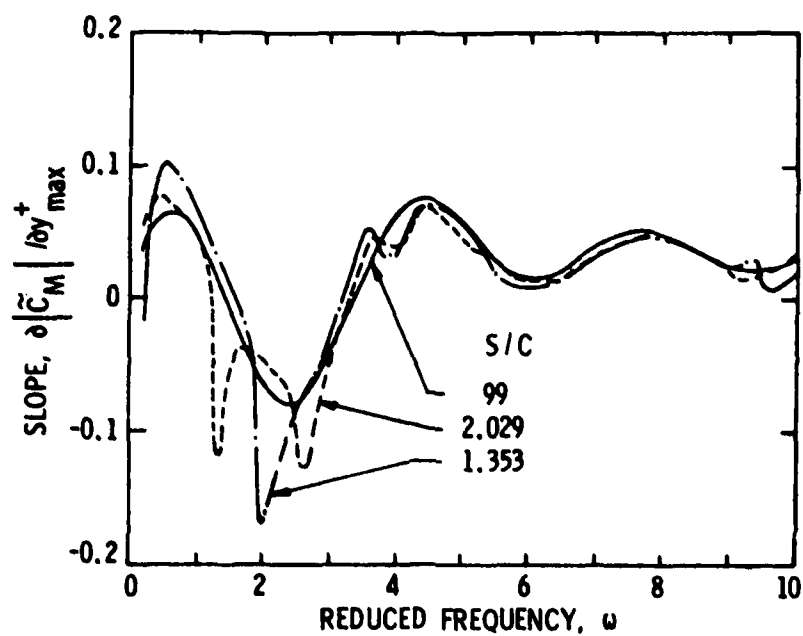Figure 56. Partial Derivative of the Unsteady Pitching Moment Coefficient with Respect to Camber with $i_m = 0$ and $\xi = 55°$.

results in an increase in $|\overset{\alpha}{C}_{L_{o,o}}|$. Cascade effects, i.e., effects due

to changes in the value of the parameter (S/C), are absent for $\omega > 4$

except for small perturbations at values of ω in the neighborhood of

critical values. Thus, for $\omega > 4$, values of $|\overset{\alpha}{C}_{L_{o,o}}|$ predicted by iso-

lated airfoil theory represent a good approximation of cascade perform-

ance.

The characteristics of the partial derivative $\dfrac{\partial|\overset{\alpha}{C}_L|}{\partial i_m}$ are shown in

Figures 42, 43, and 44. For a given value of ω with (S/C) = 99, this

partial derivative increases as ξ increases. Cascade effects are impor-

tant at low values of ξ, where $\dfrac{\partial|\overset{\alpha}{C}_L|}{\partial i_m}$ becomes significantly less negative

as (S/C) decreases from 2.029 to 0.676. At other values of (S/C) and ξ,

cascade effects are unimportant for $\omega > 2$. Values of this derivative

are negative for all values of ξ, ω, and (S/C), indicating that positive

values of mean incidence angle could be employed to reduce $|\overset{\alpha}{C}_L|$.

The results shown in Figures 45, 46, and 47 show that the partial

derivative $\dfrac{\partial|\overset{\alpha}{C}_L|}{\partial y^+_{max}}$ is practically independent of ξ. Variations in this

derivative in the neighborhood of critical values of ω are small and

cascade effects are important only for $\omega < 1$ with (S/C) < 2.029 and for

$\omega > 2.5$ with (S/C) < 2.029 and $\xi < 45^o$. The value of the derivative is

negative for $\omega < 1.7$; therefore, camber could be used to reduce $|\overset{\alpha}{C}_L|$ in

this range. For values of $\omega > 1.7$, $|\overset{\alpha}{C}_L|$ increases with increasing

camber.

The computed unsteady pitching moment coefficient results are

presented in Figures 48, 49, and 50. They show that, for a fixed value

of ω with (S/C) = 99, an increase in stagger angle, ξ, leads to an increase in $|\mathcal{C}_{M_{o,o}}|$. The results also show that cascade effects are small for $\omega > 4$, in all cases except for (S/C) < 2.029 with $\xi < 45°$, if changes in $|\mathcal{C}_{M_{o,o}}|$ at values of ω in the neighborhood of critical values are neglected. The results presented in Chapter 4 show that neglecting the predicted large changes of this type would produce both a more realistic representation of the data and better agreement with the predictions of the Whitehead-Smith theory. Such a smoothing of the theoretical predictions, if adopted, would not eliminate the cascade effects entirely.

Figures 51, 52, and 53 define the predicted effect of mean incidence angle, i_m, on $|\mathcal{C}_M|$. Again, at a given value of ω with (S/C) = 99, $\dfrac{\partial|\mathcal{C}_M|}{\partial i_m}$ increases as ξ increases. Cascade effects are important at low values of ξ, where $\dfrac{\partial|\mathcal{C}_M|}{\partial i_m}$ becomes less negative as (S/C) decreases from 2.029 to 0.676. At other values of (S/C), except for local changes at critical values of ω, cascade effects are unimportant for $\omega > 3$. The values of $\dfrac{\partial|\mathcal{C}_M|}{\partial i_m}$ are negative in all cases for $\omega > 0.5$. Therefore, for $\omega > 0.5$, positive values of mean incidence could be employed to reduce $|\mathcal{C}_M|$.

The final group of figures, Figures 54, 55, and 56, define the predicted effect of camber on $|\mathcal{C}_M|$. Just as $\dfrac{\partial|\mathcal{C}_L|}{\partial y^+_{max}}$ is practically independent of ξ, $\dfrac{\partial|\mathcal{C}_M|}{\partial y^+_{max}}$ is only slightly influenced by changes in ξ at a given value of ω with (S/C) = 99. The typical effects of critical

reduced frequency are present only at low values of ω, and for $\omega > 4$ cascade effects are unimportant except for $(S/C) < 2.029$ with $\xi < 45^{\circ}$.

Values of $\dfrac{\partial |\tilde{C}_M|}{\partial y^{+}_{max}}$ are negative for $1.5 < \omega < 3.2$, so in this region positive camber can be employed to reduce $|\tilde{C}_M|$. At values of ω outside of this region, $|\tilde{C}_M|$ increases with increases in camber.

The results presented in Figures 39 through 56, when considered as an entity, reveal a number of significant aspects regarding cascade response to distorted inflow. First, with the exception of cascades with $(S/C) < 2.029$ and $\xi < 45^{\circ}$, cascade response to distorted inflow can be adequately approximated by isolated airfoil theory for $\omega > 4$. Second, for $\omega < 1.7$, positive mean incidence and positive camber can be employed beneficially to reduce $|\tilde{C}_L|$. For $\omega > 1.7$, the effect of positive camber becomes detrimental, while the effect of positive mean incidence remains beneficial. Third, with the exception of cascades having low values of (S/C) operating at very low values of ω, positive values of mean incidence angle can be employed to reduce $|\tilde{C}_M|$. In the range $1.5 < \omega < 3.2$, positive camber can be employed to obtain a further reduction in $|\tilde{C}_M|$. Fourth, the above results show that it is only in the narrow region $1.5 < \omega < 1.7$ that both positive mean incidence and positive camber can be employed to reduce both $|\tilde{C}_L|$ and $|\tilde{C}_M|$.

CHAPTER 6

CONCLUSIONS AND RECOMMENDATIONS

The following conclusions are based on the results of a study of unsteady cascade performance using the theoretical model developed herein over an extended range of variation of the parameters (S/C) and ω. These conclusions are of particular significance with regard to the selection of cascades with minimum response during operation in a given distorted flow:

(1) To predict the unsteady performance of a given cascade containing cambered blades and operating at a nonzero mean incidence angle, the best approach at present would be to obtain zero mean incidence, zero camber results from the Whitehead-Smith theory and apply corrections for camber and incidence as defined by the theory developed herein. If the zero mean incidence, zero camber results are denoted by $|\overset{\curvearrowright}{C}_{L_{o,o}}|$ and $|\overset{\curvearrowright}{C}_{M_{o,o}}|$, then the desired results are expressed by Equations (45) and (46) as

$$|\overset{\curvearrowright}{C}_L| = |\overset{\curvearrowright}{C}_{L_{o,o}}| + \frac{\partial|\overset{\curvearrowright}{C}_L|}{\partial i_m}i_m + \frac{\partial|\overset{\curvearrowright}{C}_L|}{\partial y^+_{max}}y^+_{max}$$

and

$$|\tilde{C}_M| = |\tilde{C}_{M_{o,o}}| + \frac{\partial |\tilde{C}_M|}{\partial i_m} i_m + \frac{\partial |\tilde{C}_M|}{\partial y_{max}^+} y_{max}^+ \quad .$$

In this formulation, the partial derivatives would be obtained from Equations (36) and (40). Alternately, Equations (36) and (40) could be employed directly to compute $|\tilde{C}_L|$ and $|\tilde{C}_M|$; however, in this case, large changes in the predicted level of the coefficients at values of reduced frequency in the neighborhood of critical values should be ignored.

(2) With the exception of cascades with (S/C) < 2.029 and ξ < 45°, cascade response to distorted inflow can be adequately approximated by isolated airfoil theory for ω > 4. For cascades with (S/C) < 2.029 and ξ < 45°, the only term in Equations (45) and (46) which does not exhibit significant cascade effects is $|\tilde{C}_{L_{o,o}}|$.

(3) In the reduced frequency range where cascade effects are important for all values of the parameters (S/C) and ξ, i.e., for ω < 4, low values of $|\tilde{C}_{L_{o,o}}|$ and $|\tilde{C}_{M_{o,o}}|$ at a given value of ω are generally associated with low values of ξ. The value of the parameter (S/C) also has a significant effect on $|\tilde{C}_{L_{o,o}}|$ and $|\tilde{C}_{M_{o,o}}|$ and, for given values of ω and ξ, judicious selection of the value of (S/C) can result in significant reductions in $|\tilde{C}_{L_{o,o}}|$ and $|\tilde{C}_{M_{o,o}}|$.

(4) In addition to the effects on the basic quantities $|\tilde{C}_{L_{o,o}}|$ and $|\tilde{C}_{M_{o,o}}|$ due to variations in ω and (S/C)

END
DATE
FILMED
3-80
DDC

noted above, the final values $|\overset{\alpha}{C}_L|$ and $|\overset{\alpha}{C}_M|$ can be
reduced to still lower levels through selection of
advantageous values for mean incidence angle and maxi-
mum camber. For all values of (S/C) with $\omega < 1.7$,
positive mean incidence and positive camber can be
employed beneficially to reduce $|\overset{\alpha}{C}_L|$. For $\omega > 1.7$,
the effect of positive camber becomes detrimental
while the effect of positive mean incidence remains
beneficial. With the exception of cascades having low
values of (S/C) operating at very low values of ω,
positive values of mean incidence angle can be employed
to reduce $|\overset{\alpha}{C}_M|$. In the range $1.5 < \omega < 3.2$, positive
camber can be employed to obtain a further reduction in
$|\overset{\alpha}{C}_M|$. Thus, it is only in the narrow region $1.5 < \omega <$
1.7 that both positive mean incidence and positive cam-
ber can be employed to reduce both $|\overset{\alpha}{C}_L|$ and $|C_M|$.

(5) The information presented in Figures 39 through 56 can
be employed in the estimation of the unsteady perform-
ance of a given cascade operating in a given distorted
inflow.

The following conclusions are based on the results of the portion
of this study in which theoretical predictions of cascade performance
were compared with measured performance:

(1) The Whitehead-Smith theory, while it does not predict
the changes in performance levels substantiated by
the data in the neighborhood of critical reduced
frequencies, provides a better over-all estimate of

unsteady cascade performance at zero mean incidence
angle and zero camber than does the model developed
herein. This superior prediction capability is
thought to be due to the use in the Whitehead-Smith
model of a more detailed unsteady bound vorticity
distribution.

(2) The theory presented herein does not provide a good
prediction of unsteady cascade performance at low
values of reduced frequency, i.e., $\omega < 0.8$. In addi-
tion, the unsteady lift force coefficient predicted
by Equation (36) undergoes significant changes in level
in the neighborhood of values of reduced frequency for
which the blade-to-blade spacing is an integer multiple
of the wavelength of the distorted inflow. These level
changes also appear in the measured data. Similar
changes in level are predicted by Equation (40) for the
unsteady pitching moment coefficient; however, the
related changes in the measured data are not as pro-
nounced.

(3) For $\omega > 0.8$, in regions away from critical values of
reduced frequency, differences in performance predic-
tions by the two theoretical models are not large. In
general, both models overpredict $|\tilde{c}_L|$ and $|\tilde{c}_M|$ and
accurately predict ϕ_F and ϕ_M.

(4) The theoretical model developed herein predicts effects
due to positive values of mean incidence angle that are
generally greater than the effects shown by the measured

data. Effects due to different levels of blade camber were not evaluated experimentally; however, this theoretical model can be used in an analytical evaluation of the effects of camber on cascade unsteady performance.

(5) Two factors not included in the theoretical predictions that may be responsible for the overpredictions noted above are distortion velocity attenuation and fluid viscosity. Recently published results show that significant attenuation of the distortion velocity occurs as the flow approaches and passes through the rotor. In addition, due to viscosity, the wake vorticity is transported away from the blades at 60 to 70% of the mean flow velocity and is dissipated completely within some finite distance.

The unsteady force coefficient results can be used as input data in radiated noise studies for cases in which the wavelength of the radiated sound is much greater than the blade chord length. For these cases, the blade acts, from an acoustic standpoint, as a compact dipole source. By computing the unsteady force magnitude for equally spaced spanwise blade elements and employing the blade-to-blade phase angle relationship, an equivalent acoustic dipole source strength distribution for an entire rotor can be generated.

Recommendations for the direction of additional theoretical and experimental efforts are as follows:

(1) Modify the theoretical model developed herein to account for distortion velocity attenuation. This can be done

by using Yocum's [37] data to define the parameter μ_I in the expression for θ, the generalized reduced frequency parameter.

(2) Modify the theoretical model developed herein to account for the effects of fluid viscosity on the contribution due to the blade wakes. This can be done by reducing the wake transport velocity to a value on the order of $0.6 \, W_m$ to $0.7 \, W_m$ and introducing an exponential factor to reduce the strength of the wake vorticity as a function of distance travelled in the wake.

(3) Conduct a detailed evaluation of the magnitude of the individual terms in Equation (40), the equation for $\overset{\lambda}{C}_M$, at reduced frequencies in the neighborhood of critical values to determine which terms undergo significant magnitude changes at critical reduced frequencies and whether modifications to the convergence criteria used in the computer program are justified as a means for attempting to reduce these magnitude changes.

(4) Extend the reduced frequency range of the experimental data to $\omega = 4$, the approximate upper limit for significant cascade effects. The existing strain-gaged sensing element could be used in a new rotor having a chord length on the order of 12 in. to achieve this value of ω, since $\omega \approx \dfrac{\pi C \sin\beta_m}{\ell}$. This would permit operating the test facility at the same conditions as in the present tests while using the same

distortion-generating wire grids. An alternate approach which would permit using the present test rotor would require the design, fabrication, and calibration of a new sensing element having higher natural frequencies. This could be accomplished with some sacrifice in static sensitivity. This approach would require using additional distortion-generating wire grids having higher values of N, the number of distortion cycles per circumference. The required grids are available at present.

(5) Conduct a series of experiments employing a test rotor with cambered blades and compare the results with predictions obtained using the theoretical model modified in the manner noted above.

REFERENCES

1. Kemp, N. H., and Sears, W. R., "Aerodynamic Interference Between Moving Blade Rows," Journal of the Aeronautical Sciences, Vol. 20, No. 9, September 1953, pp. 585-597 and 612.

2. Kemp, N. H., and Sears, W. R., "The Unsteady Forces Due to Viscous Wakes in Turbomachines," Journal of the Aeronautical Sciences, Vol. 22, No. 7, July 1955, pp. 478-483.

3. von Kármán, T., and Sears, W. R., "Airfoil Theory for Non-Uniform Motion," Journal of the Aeronautical Sciences, Vol. 5, No. 10, August 1938, pp. 379-390.

4. Sears, W. R., "Some Aspects of Non-Stationary Airfoil Theory and Its Practical Application," Journal of the Aeronautical Sciences, Vol. 8, No. 3, January 1941, pp. 104-108.

5. Kemp, N. H., "On the Lift and Circulation of Airfoils in Some Unsteady-Flow Problems," Journal of the Aeronautical Sciences, Vol. 19, No. 10, October 1952, pp. 713-714.

6. Theodorsen, T., "General Theory of Aerodynamic Instability and the Mechanism of Flutter," NACA Report No. 496, 1949.

7. Meyer, R. X., "The Effect of Wakes on the Transient Pressure and Velocity Distributions in Turbomachines," Transactions of the ASME, Vol. 80, October 1958, pp. 1544-1552.

8. Küssner, H. G., "Das zweidimensionale Problem der beliebig bewegten Tragfläche unter Berücksichtigung von Partialbewegungen der Flüssigkeit," Luft. Forsch., Vol. 17, No. 11/12, 1940, pp. 355-361.

9. Yeh, H., and Eisenhuth, J. J., "The Unsteady Wake Interaction in Turbomachinery and Its Effect on Cavitation," Transactions of the ASME, Journal of Basic Engineering, Series D, Vol. 18, No. 2, June 1959, pp. 180-189.

10. Horlock, J. H., "Fluctuating Lift Forces on Airfoils Moving Through Transverse and Chordwise Gusts," Transactions of the ASME, Journal of Basic Engineering, Series D, Vol. 90, No. 4, December 1968, pp. 494-500.

11. Horlock, J. H., "Unsteady Flow in Turbomachines," Paper No. 2674 presented at the Third Australasian Conference on Hydraulics and Fluid Mechanics, Sydney, Australia, November 25-29, 1968.

12. Naumann, H., and Yeh, H., "Lift and Pressure Fluctuations of a Cambered Airfoil Under Periodic Gusts and Applications in Turbomachinery," Transactions of the ASME, Journal of Engineering for Power, Series A, Vol. 95, No. 1, January 1973, pp. 1-10.

13. Holmes, D. W., "Lift Fluctuations on Airfoils in Transverse and Streamwise Gusts," Ph.D. Dissertation, St. Johns College, Cambridge University, 1972.

14. Whitehead, D. S., "Force and Moment Coefficients for Vibrating Airfoils in Cascade," ARC R&M 3254, February 1960.

15. Mani, R., "Compressibility Effects in the Kemp-Sears Problem," NASA SP 304, Fluid Mechanics, Acoustics and Design of Turbomachinery, Part II, 1974, pp. 513-533.

16. Schorr, B., and Reddy, K. C., "Inviscid Flow through Cascades in Oscillatory and Distorted Flow," AIAA Journal, Vol. 9, No. 10, October 1971, pp. 2043-2050.

17. Smith, S. N., "Discrete Frequency Sound Generation in Axial Flow Turbomachines," University of Cambridge Department of Engineering Report CUED/A-Turbo/TR 29, 1971.

18. Henderson, R. E., "The Unsteady Response of an Axial Flow Turbomachine to an Upstream Disturbance," Ph.D. Dissertation, Churchill College, Cambridge University, 1972.

19. Hanamura, Y., "Flutter of Cascading Blade Row," Institute of Space and Aeronautical Science, University of Tokyo, Report No. 459, 1971.

20. Gutin, L., "On the Sound Field of a Rotating Propeller," Phys. Z. Sowjet, Vol. 9, 1936, pp. 57-71 (Trans. NACA Technical Memorandum No. 1195, 1948).

21. Tyler, J. M., and Sofrin, T. G., "Axial Flow Compressor Noise Studies," Trans. SAE, 1962, pp. 309-332.

22. House, M. E., "Rotor Noise," An Advanced Course in Noise and Vibration, Chapter 20, Institute of Sound and Vibration Research, University of Southampton, England, 1975.

23. Tanabe, K., and Horlock, J. H., "A Simple Method for Predicting the Performance of Cascades of Low Solidity," The Aeronautical Quarterly, Vol. 18, Part 3, August 1967, pp. 225-236.

24. Weinig, F., "Die Strömung um die Schaufeln von Turbomaschinen," J. A. Barth, 1935.

25. Bisplinghoff, R. L., Ashley, H., and Halfman, R. L., Aeroelasticity, Addison-Wesley Publishing Company, Reading, Massachusetts, 1967.

26. Reissner, E., "Effect of Finite Span on the Airload Distributions for Oscillating Wings, I - Aerodynamic Theory of Oscillating Wings of Finite Span," NACA Technical Note No. 1194, March 1947.

27. Söhngen, H., "Die Lösungen der Integralgleichung und deren Anwendung in der Tragflügeltheorie," Math. Z., Band 45, 1939, pp. 245-264.

28. Bruce, E. P., "The ARL Axial Flow Research Fan - A New Facility for Investigation of Time-Dependent Turbomachinery Flows," ASME Paper No. 74-FE-27 presented at the Joint Fluids Engineering and CSME Conference, Montreal, Quebec, Canada, May 13-15, 1974.

29. Weighardt, K. E. G., "On the Resistance of Screens," The Aeronautical Quarterly, Vol. 4, February 1953, pp. 186-192.

30. Cornell, W. G., "Losses in Flow Normal to Plane Screens," Transactions of the ASME, Vol. 80, May 1958, pp. 791-799.

31. McCarthy, J. H., "Steady Flow Past Nonuniform Wi.·e Grids," Journal of Fluid Mechanics, Vol. 19, 1964, pp. 491-512.

32. Owen, P. R., and Zienkiewicz, H. K., "The Production of Uniform Shear Flow in a Wind Tunnel," Journal of Fluid Mechanics, Vol. 2, 1957, pp. 521-531.

33. Elder, J. W., "Steady Flow Through Nonuniform Gauzes of Arbitrary Shape," Journal of Fluid Mechanics, Vol. 5, 1959, pp. 355-368.

34. Bruce, E. P., "Design and Evaluation of Screens to Produce Multi-Cycle ±20% Amplitude Sinusoidal Velocity Profiles," AIAA Paper No. 74-623 presented at the AIAA 8th Aerodynamic Testing Conference, Bethesda, Maryland, July 8-10, 1974.

35. Howell, A. R., "The Present Basis of Axial Flow Compressor Design: Part I - Cascade Theory and Performance," ARC R&M 2095, June 1942.

36. Horlock, J. H., Axial Flow Compressors, Fluid Mechanics and Thermodynamics, Robert E. Krieger Publishing Co., Inc., Box 542, Huntington, New York 11973, 1973.

37. Yocum, A. M., "The Effects of Design and Operating Variables on the Response of an Axial Flow Fan to Inlet Flow Distortions," M.S. Thesis, Department of Mechanical Engineering, The Pennsylvania State University, August 1978.

38. Bradshaw, P., Ferriss, D. H., and Johnson, R. F., "Turbulence in the Noise-Producing Region of a Circular Jet," Journal of Fluid Mechanics, Vol. 19, 1964, pp. 591-624.

39. Van Dyke, M. D., "Second-Order Subsonic Airfoil Theory Including Edge Effects," NACA Report 1274, 1956.

40. Durand, W. F., <u>Aerodynamic Theory</u>, Vol. 2, Julius Springer, Berlin, 1935.

41. Shen, I-Chung, Personal communication, April 16, 1979.

42. Goldstein, M. E., Personal communication to R. E. Henderson, February 27, 1973.

43. Henderson, R. E., and Daneshyar, H., "Theoretical Analysis of Fluctuating Lift on the Rotor of an Axial Turbomachine," ARC R&M 3684, September 1970.

44. Schenck, H., <u>Theories of Engineering Experimentation</u>, Hemisphere Publishing Corporation, Washington, 1979.

APPENDIX A

DIFFERENCES BETWEEN THE PRESENT ANALYSIS
AND HENDERSON'S ANALYSIS

The objective of this appendix is to describe the differences that exist between the theoretical analysis of unsteady lift presented in Chapter 2 and the related analysis by Henderson [18]. These differences affect the following items:

(1) the region of validity of the theoretical model,

(2) the identification of the type of blade camber line used in the model,

(3) the form of the equation which defines the cascade lift function $G(\omega, x_c^+, S/C, \xi)$, and

(4) the equation which defines the unsteady lift coefficient $\overset{\scriptstyle\sim}{C}_L$.

Each of these items is discussed in detail in the paragraphs that follow.

A thorough analysis of the region of validity of the theoretical model is presented in Appendix C. There it is shown that, for $|g_c|^2 - |h_c|^2 > 1$ and for $|g_\lambda|^2 - |h_\lambda|^2 > 1$, the limiting boundary is defined by combining results for the point locating the lumped vorticity on the n = +1 blade and results for points locating the distributed vorticity in the wake of the n = -1 blade. The two curves thus formed define lower limit values of permissible cascade space-to-chord ratio S/C as a function of the sine of the blade stagger angle ξ. In comparison with Henderson's approximate definition of the region of validity, as values of $S/C > \frac{1}{2}$ or $\sin\xi$, whichever is greater, the exact definition developed in Appendix C expands the region of validity slightly at low values of $\sin\xi$ and contracts the region of validity both at moderate and at high values of $\sin\xi$.

The equation for the blade camber line used in this analysis and in Henderson's analysis is given in Equation (26) as $y^+ = y^+_{max}\left[1 - (x^+)^2\right]$. This is the equation for a symmetrical parabolic arc rather than a circular arc as stated by Henderson. Equation (26) has been used frequently in isolated thin airfoil analyses as an approximate relation for a circular arc. Such an approximation is acceptable only for low values of y^+_{max}, i.e., $y^+_{max} \ll 0.06$.

The differences in the form of the two expressions which define the cascade lift function $G(\omega, x^+_c, S/C, \xi)$ have their origin in the analysis of the unsteady pressure distribution. In Equation (16), in the three integrals with respect to the variable λ^+ in the second and fourth terms on the right-hand side, the integrand in Henderson's formulation has the form $\Lambda(\sigma^+, k)e^{-i\omega\lambda^+}$, whereas the correct form is $\dfrac{\partial \Lambda(\sigma^+, k)}{\partial k}e^{-i\omega\lambda^+}$, where k represents λ^+, g_λ, or h_λ. This is a typographical error, since the terms that would have been affected subsequently in Henderson's expression for the unsteady distribution of the pressure difference are correct as he presented them. Another difference in form exists with respect to the fifth term on the right-hand side of Equation (18). This term is

$$\frac{i\omega\Delta e^{-i\omega}}{\pi}\left[\sum_{-\infty}^{-1} + \sum_{1}^{\infty}\right] e^{in\tau}\left[\Lambda(\sigma^+, g_c) + \Lambda(\sigma^+, h_c) - \Lambda(\sigma^+, g_1) - \right.$$

$$\left. \Lambda(\sigma^+, h_1)\right] \quad .$$

Its form is easily verified by examination of Equations (17) and (15). The corresponding term in Henderson's derivation was expressed as

$$
- \frac{2i\Delta\omega e^{-i\omega}}{\pi} \left[\sum_{-\infty}^{-1} + \sum_{1}^{\infty} \right] e^{in\tau} \left[\frac{\partial A_1}{\partial\sigma+} + \frac{\partial A_2}{\partial\sigma+} - \frac{\partial A_3}{\partial\sigma+} - \frac{\partial A_4}{\partial\sigma+} \right] \quad ,
$$

where

$$
A_1 = \int_{-1}^{1} \tan^{-1} \left\{ \sqrt{\frac{(1 - \sigma^+)(\frac{n}{ib} - 2)}{(1 + \sigma^+)(\frac{n}{ib})}} \right\} d\sigma^+ \quad ,
$$

$$
A_2 = \int_{-1}^{1} \tan^{-1} \left\{ \sqrt{\frac{(1 - \sigma^+)(\frac{n}{ia} + 2)}{(1 + \sigma^+)(\frac{n}{ia})}} \right\} d\sigma^+ \quad ,
$$

$$
A_3 = \int_{-1}^{1} \tan^{-1} \left\{ \sqrt{\frac{(1 - \sigma^+)(x_c^+ + 1 - \frac{n}{ib})}{(1 + \sigma^+)(x_c^+ - 1 - \frac{n}{ib})}} \right\} d\sigma^+ \quad ,
$$

and

$$
A_4 = \int_{-1}^{1} \tan^{-1} \left\{ \sqrt{\frac{(1 - \sigma^+)(x_c^+ + 1 + \frac{n}{ia})}{(1 + \sigma^+)(x_c^+ - 1 + \frac{n}{ia})}} \right\} d\sigma^+ \quad .
$$

It is clear that since A_1, A_2, A_3, and A_4 are definite integrals with respect to the variable σ^+, their partial derivatives with respect to σ^+ are zero. Thus, the entire term, in Henderson's formulation, should have been set equal to zero. The fact that the notation $\frac{\partial A_1}{\partial\sigma+}$, $\frac{\partial A_2}{\partial\sigma+}$, etc., was erroneous and was not followed in a rigorous sense becomes evident upon examination of Henderson's equation for $G(\omega, x_c^+, S/C, \xi)$. The term

in question appears in the numerator of the second term on the right-hand side. It was presented correctly as

$$\left[\sum_{-\infty}^{-1} + \sum_{1}^{\infty}\right] e^{in\tau} \left[\frac{2i\omega e^{-i\omega}}{\pi}(A_1 + A_2 - A_3 - A_4)\right] \quad .$$

The corresponding term in Equation (22) is

$$\left[\sum_{-\infty}^{-1} + \sum_{1}^{\infty}\right] e^{in\tau} [i\omega e^{-i\omega}(\sqrt{g_c^2 - 1} - g_c - \sqrt{g_1^2 - 1} + g_1 +$$

$$\sqrt{h_c^2 - 1} - h_c - \sqrt{h_1^2 - 1} + h_1)] \quad ,$$

which is the integrated form of Henderson's expression.

The remaining difference in the two analyses concerns the final equation for the unsteady lift. This difference concerns the expression

$$\left[(C_1 + C_2 - 2)J_o(\theta) - 2 \sum_{m=1}^{\infty} (1)^{-m}J_m(\theta)[(g_c - \sqrt{g_c^2 - 1})^m +\right.$$

$$\left.(h_c - \sqrt{h_c^2 - 1})^m]\right] \quad ,$$

which appears in one term on the right-hand side of Equation (36). In Henderson's analysis, he retained only the $m = 1$ term in this expression, arguing that the remaining terms were of higher order and were, as a result, negligible. Since this conclusion is not obvious, the

summations on m were retained throughout the analysis presented in Chapter 2. If $m = 1$, the term in question is

$$(C_1 + C_2 - 2)J_o(\theta) + 2iJ_1(\theta)\left[g_c - \sqrt{g_c^2 - 1} + h_c - \sqrt{h_c^2 - 1}\right] \quad .$$

Henderson's expression for the same term is

$$(C_1 + C_2)J_o(\theta) - 2 - 2J_1(\theta)\left[g_c^2(g_c - \sqrt{g_c^2 - 1} + h_c^2(h_c - \sqrt{h_c^2 - 1}\right] \quad ,$$

which contains a number of typographical errors. In Henderson's predictions of unsteady lift coefficient, the effect due to the part of the above term given by

$$2iJ_1(\theta)\left[g_c - \sqrt{g_c^2 - 1} + h_c - \sqrt{h_c^2 - 1}\right]$$

was not included since, when he programmed his solution, this term was dropped. Thus, predictions of unsteady lift coefficient presented in Chapters 4 and 5 differ from Henderson's predictions for corresponding cases at nonzero values of mean incidence and blade camber.

APPENDIX B

ALTERNATE EXPRESSIONS FOR THE CASCADE
INFLUENCE FUNCTIONS

In Equations (5), the terms which involve cascade parameters are

$$A = \frac{e^{in\tau} n \cos\xi}{\left[\frac{x_n - x_p}{S} + n\sin\xi\right]^2 + \left[n\cos\xi\right]^2}$$

and

$$B = \frac{e^{in\tau}\left[\frac{x_n - x_p}{S} + n\sin\xi\right]}{\left[\frac{x_n - x_p}{S} + n\sin\xi\right]^2 + \left[n\cos\xi\right]^2} \quad .$$

An approach has been developed by Whitehead [14] in which these expressions are rewritten as

$$A = \frac{1}{2}\{e^{-i\xi}F(\chi) + e^{i\xi}F(\bar{\chi})\}$$

and

$$B = -\frac{1}{2i}\{e^{-i\xi}F(\chi) - e^{i\xi}F(\bar{\chi})\} \quad ,$$

where $\chi = ize^{-i\xi}$, $\bar{\chi} = -ize^{i\xi}$, $z = \frac{x_n - x_p}{S}$, and $F(\chi) = \frac{e^{in\tau}}{\chi + n}$. If $\Theta(\chi)$ and $\Phi(\chi)$ are defined as

$$\Theta(\chi) = e^{-i\xi}F(\chi) + e^{i\xi}F(\bar{\chi})$$

and

$$\Phi(\chi) = e^{-i\xi}F(\chi) - e^{i\xi}F(\bar{\chi}) \quad ,$$

then

$$A = \frac{1}{2}\Theta(\chi)$$

and

$$B = -\frac{1}{2i}\Phi(\chi) \quad .$$

In the text, the coordinate transformation

$$x^+ = \frac{2x}{C} - 1 \quad , \quad y^+ = \frac{2y}{C}$$

is introduced. In the transformed nondimensional system,

$$z^+ = \left[\frac{x_n^+ - s_p^+}{2} \right] \left[\frac{S}{C} \right]$$

and

$$\chi = iz^+ e^{-i\xi} \quad .$$

Then,

$$A^+ = \frac{1}{2}\Theta(\chi^+)$$

and

$$B^+ = -\frac{1}{2i}\Phi(\chi^+) \quad .$$

The expression for $\Phi(\chi^+)$ can be written as

$$\phi(\chi^+) = e^{in\tau} \left[\frac{e^{-i\xi}}{i(x_n^+ - x_p^+)\frac{Ce^{-i\xi}}{2S}} + \frac{e^{i\xi}}{i(x_n^+ - x_p^+)\frac{Ce^{i\xi}}{2S} - n} \right]$$

$$= (\frac{2S}{iC})e^{in\tau} \left[\frac{1}{g_n - x_p^+} + \frac{1}{h_n - x_p^+} \right] \quad ,$$

where $g_n = x_n^+ + \frac{n}{ia}$, $h_n = x_n^+ - \frac{n}{ib}$, $a = \frac{Ce^{-i\xi}}{2S}$, and $b = \frac{Ce^{i\xi}}{2S}$.

By a similar analysis,

$$\Theta(\chi^+) = (\frac{2S}{iC})e^{in\tau} \left[\frac{1}{g_n - x_p^+} - \frac{1}{h_n - x_p^+} \right] \quad .$$

APPENDIX C

THEORETICAL MODEL REGION OF VALIDITY

In solving for the vorticity distribution on the reference blade, values must be specified for integrals of the form

$$\int_{-1}^{1} \sqrt{\frac{1+k}{1-k}} \frac{dk}{j-k} \quad,$$

where j can represent any of the parameters g_c, h_c, g_λ, h_λ. The value of the integral depends upon the magnitude of j, for if $|j|^2 \le 1$, the Cauchy principal value must be taken with the result

$$\oint_{-1}^{1} \sqrt{\frac{1+k}{1-k}} \frac{dk}{j-k} = -\pi \quad,$$

while if $|j|^2 > 1$, the result is

$$\int_{-1}^{1} \sqrt{\frac{1+k}{1-k}} \frac{dk}{j-k} = -\pi \left[1 - \sqrt{\frac{j+1}{j-1}} \right] \quad.$$

Consequently, an analysis of the expressions for the square of the magnitude of the quantities g_c, h_c, g_λ, and h_λ must be conducted.

Consider first the parameters g_c and h_c, the parameters that locate points where vorticity has been lumped on the neighboring blades. With $g_c = x_c^+ + \frac{n}{ia}$, $h_c = x_c^+ - \frac{n}{ib}$, $x_c^+ = \frac{2x_c}{C} - 1$, $x_c = \frac{C}{4}$, $a = \frac{Ce^{-i\xi}}{2S}$, and $b = \frac{Ce^{i\xi}}{2S}$, it follows that

$$g_c = \left[2n(\frac{S}{C})\sin\xi - \frac{1}{2} \right] - i \left[2n(\frac{S}{C})\cos\xi \right]$$

and

$$h_c = \left[2n(\tfrac{S}{C})\sin\xi - \tfrac{1}{2} \right] + i \left[2n(\tfrac{S}{C})\cos\xi \right] \quad .$$

Since h_c is the complex conjugate of g_c,

$$|g_c|^2 = |h_c|^2 = \tfrac{1}{4} - 2n(\tfrac{S}{C})\sin\xi + 4n^2(\tfrac{S}{C})^2 \quad .$$

The boundary between regions on a plot of $\frac{S}{C}$ versus $\sin\xi$ for which $|g_c|^2 = |h_c|^2 \leq 1$ and $|g_c|^2 = |h_c|^2 > 1$ is defined by the relation $|g_c|^2 = |h_c|^2 = 1$. For this condition,

$$(\tfrac{S}{C}) = \tfrac{1}{4n}\left[\pm\sin\xi + \sqrt{\sin^2\xi + 3}\right] \quad ,$$

where the plus sign applies if $n = 1, 2, 3, \ldots$, and the minus sign applies if $n = -1, -2, -3, \ldots$. Boundary limits defined by assigning successive values of n and solving the above expression for $\frac{S}{C}$ as a function of $\sin\xi$ are shown in Figure C1. For any value of n, in the region above the curve for that n, $|g_c|^2 = |h_c|^2 > 1$. The $n = +1$ case is the limiting case. Consequently, to the extent that g_c and h_c control the over-all situation, the theoretical model is valid for combinations of values of $\frac{S}{C}$ and $\sin\xi$ lying above the $n = +1$ line in Figure C1.

The wake parameters g_λ and h_λ also affect the region of validity of the model. With $g_\lambda = \lambda^+ + \frac{n}{ia}$, $h_\lambda = \lambda^+ - \frac{n}{ib}$, and $\lambda^+ > 1$,

$$g_\lambda = \left[2n(\tfrac{S}{C})\sin\xi + \lambda^+ \right] - i \left[2n(\tfrac{S}{C})\cos\xi \right]$$

and
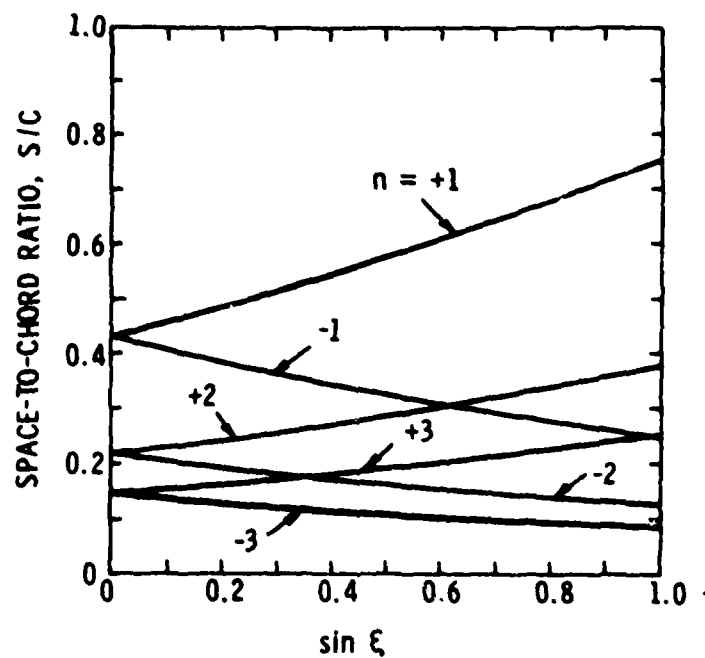
Figure C1. Effect of Neighboring Blade Number on the
Region of Validity of the Theoretical
Model.

$$h_\lambda = \left[2n(\tfrac{S}{C})\sin\xi + \lambda^+ \right] + i \left[2n(\tfrac{S}{C})\cos\xi \right] \quad .$$

From these relations,

$$|g_\lambda|^2 = |h_\lambda|^2 = (\lambda^+)^2 + 4\lambda^+ n(\tfrac{S}{C})\sin\xi + 4n^2(\tfrac{S}{C})^2 \quad .$$

Examination of this relation shows immediately that $|g_\lambda|^2 = |h_\lambda|^2 > 1$ for all positive values of n since $\lambda^+ > 1$, and $\frac{S}{C}$ and $\sin\xi$ are always positive quantities. To examine this relation for negative values of n, it is advantageous to set $|g_\lambda|^2 = |h_\lambda|^2 = 1$ and solve the resulting expression for $\sin\xi$ as a function of λ^+, n, and $\frac{S}{C}$. The result is

$$\sin\xi = \frac{1 - (\lambda^+)^2 - 4n^2(\tfrac{S}{C})^2}{4\lambda^+ n(\tfrac{S}{C})} \quad .$$

With n = -1, this relation defines the boundary shown in Figure C2. Here, each value of λ^+ defines a line which separates a region, in the plot of $\frac{S}{C}$ versus $\sin\xi$, where $|g_\lambda|^2 = |h_\lambda|^2 > 1$ from a region where $|g_\lambda|^2 = |h_\lambda|^2 \le 1$. For all values of λ^+, $|g_\lambda|^2 = |h_\lambda|^2 > 1$ in the region above the envelope of the λ^+ curves. Setting n = -2 and repeating this procedure defines the larger region of validity for the theoretical model shown in Figure C3. Setting n = -3, -4, -5, ..., in turn defines successively larger regions of validity. Thus, for the quantities g_λ and h_λ, which locate points in the wakes of neighboring blades, n = -1 is the limiting case.

The over-all region of validity of the theoretical model is defined by combining the results for the n = +1 case from the analysis of g_c and h_c, and the results for the n = -1 case from the analysis of g_λ and h_λ.
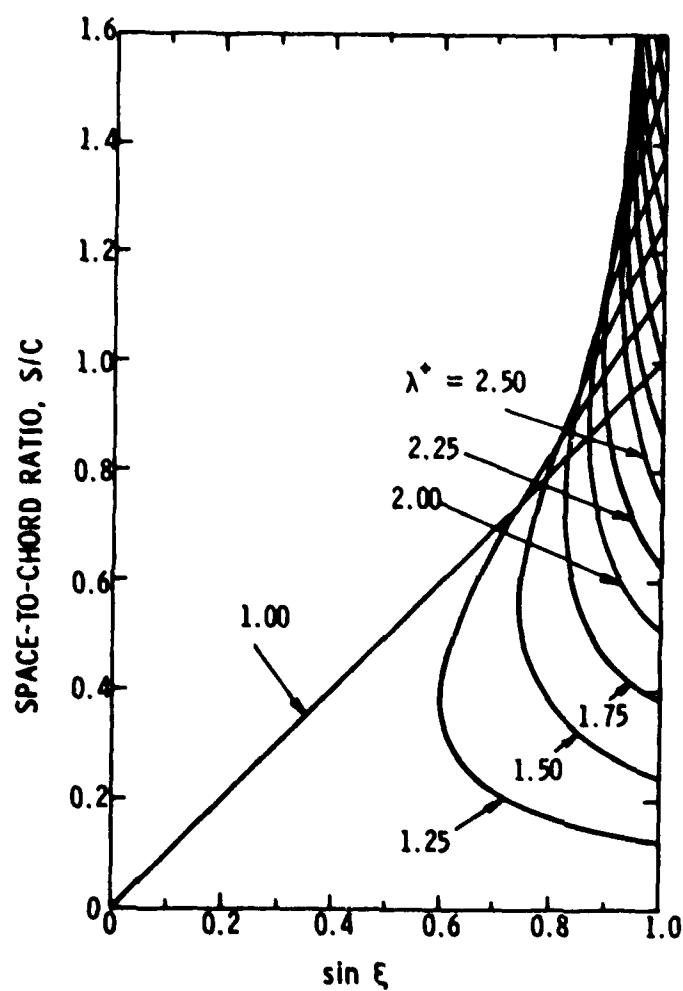
Figure C2. Effect of Position in the Wake of the n = -1 Blade on the Region of Validity of the Theoretical Model.
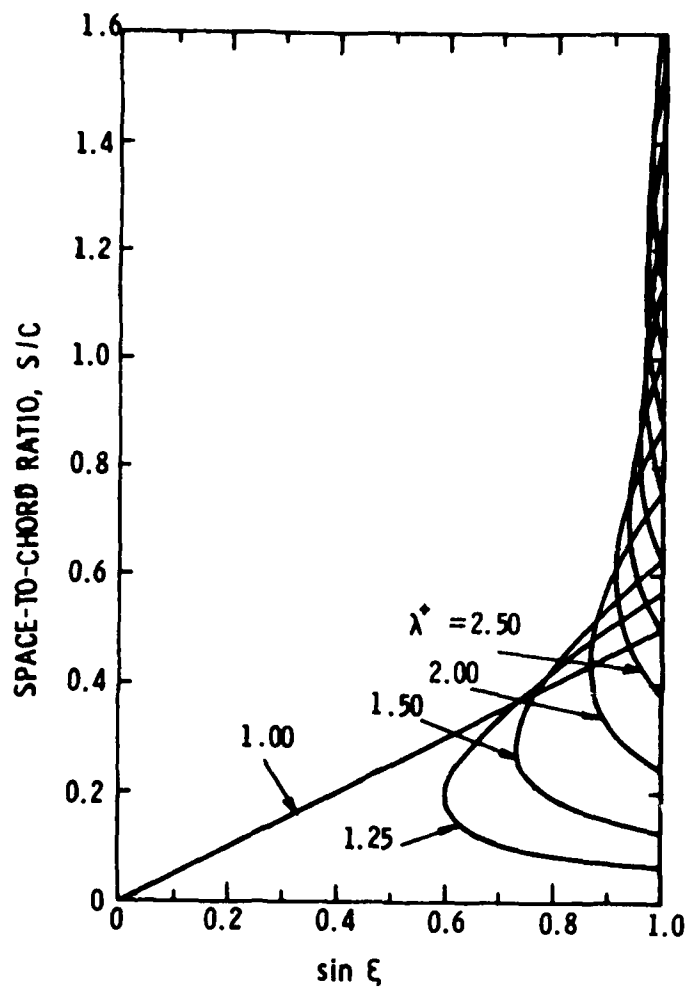
Figure C3. Effect of Position in the Wake of the n = -2
Blade on the Region of Validity of the
Theoretical Model.

This region is shown as a shaded area in Figure C4. Also shown in Figure C4 is the approximate region of validity defined by Henderson [18] as values of $\frac{S}{C} > \frac{1}{2}$ or $\sin\xi$, depending upon which is larger. With respect to Henderson's approximate definition, the present exact definition expands the region of validity slightly at low values of $\sin\xi$ and contracts the region of validity both at moderate and at high values of $\sin\xi$.
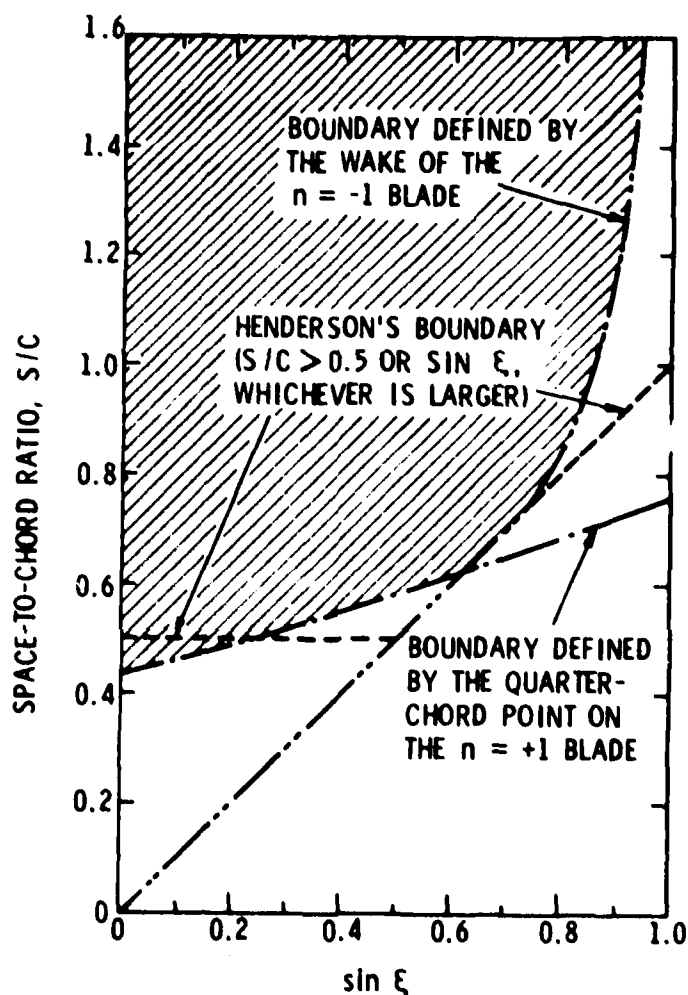
Figure C4. Region of Validity (Crosshatched) of the
            Theoretical Model Defined by Considering
            Points on Neighboring Blades and in the
            Wakes of Neighboring Blades.

APPENDIX D

TABULATION OF INTEGRALS AND THEIR VALUES

The equations presented herein consist of integrals and their values. Solutions for these integrals are required in the development of the unsteady cascade theory of Chapter 2. Restrictions upon the region of validity of the solutions are listed, where appropraite, as are references for those equations obtained from previous work.

1. $\displaystyle\oint_{-1}^{1} \sqrt{\frac{1+k}{1-k}}\,\frac{dk}{j-k} = -\pi$ for $|j|^2 \leq 1$

  Van Dyke [39]

2. $\displaystyle\int_{-1}^{1} \sqrt{\frac{1+k}{1-k}}\,\frac{dk}{j-k} = -\pi\left[1 - \sqrt{\frac{j+1}{j-1}}\right]$ for $|j|^2 > 1$

  Henderson [18]

3. $\displaystyle\oint_{-1}^{1} \sqrt{\frac{1-k}{1+k}}\,\frac{dk}{j-k} = \pi$ for $|j|^2 \leq 1$

  Van Dyke [39]

4. $\displaystyle\int_{-1}^{1} \sqrt{\frac{1-k}{1+k}}\,\frac{dk}{j-k} = \pi\left[1 - \sqrt{\frac{j-1}{j+1}}\right]$ for $|j|^2 > 1$

5. $\displaystyle\int_{1}^{\infty} \left[\sqrt{\frac{k+1}{k-1}} - 1\right] e^{-i\omega k}dk = -\frac{\pi}{2}\left[H_1^{(2)}(\omega) + iH_0^{(2)}(\omega)\right] - \frac{e^{-i\omega}}{i\omega}$

  Durand [40]

6. $\displaystyle\oint_{-1}^{\sigma} \sqrt{\frac{1-k}{1+k}}\,\frac{dk}{j-k} = \frac{\pi}{2} + \sin^{-1}\sigma + \sqrt{\frac{1-j}{1+j}}\,\Omega(\sigma,j)$ for $|j|^2 \le 1$,

where $\Omega(\sigma,j) = \dfrac{1}{2}\ln\left[\dfrac{1 - \sigma j + \sqrt{1-j^2}\,\sqrt{1-\sigma^2}}{1 - \sigma j - \sqrt{1-j^2}\,\sqrt{1-\sigma^2}}\right]$

Reissner [26]

7. $\displaystyle\int_{-1}^{\sigma} \sqrt{\frac{1-k}{1+k}}\,\frac{dk}{j-k} = \frac{\pi}{2} + \sin^{-1}\sigma + \sqrt{\frac{j-1}{j+1}}\,\Lambda(\sigma,j)$ for $|j|^2 > 1$,

where $\Lambda(\sigma,j) = 2\tan^{-1}\left[\sqrt{\left[\dfrac{1-\sigma}{1+\sigma}\right]\left[\dfrac{j+1}{j-1}\right]}\right] - \pi$

Reissner [26]

8. $\displaystyle\int_{1}^{\infty}\left[\Lambda(\sigma,k) + \frac{\pi}{2} + \sin^{-1}\sigma\right]e^{-i\omega k}dk = \frac{e^{-i\omega}}{i\omega}\left[\frac{\pi}{2} + \sin^{-1}\sigma\right]$

$$+ \frac{1}{i\omega}\int_{1}^{\infty}\frac{\partial\Lambda(\sigma,k)}{\partial k}e^{-i\omega k}dk$$

for $k = \lambda^{+}$

9. $\int\limits_{1}^{\infty} \left[\Lambda(\sigma,k_\lambda) + \frac{\pi}{2} + \sin^{-1}\sigma \right] e^{-i\omega k}dk = \frac{e^{-i\omega}}{i\omega} \left[\Lambda(\sigma,k_1) + \frac{\pi}{2} + \sin^{-1}\sigma \right]$

$$+ \frac{1}{i\omega} \int\limits_{1}^{\infty} \frac{\partial\Lambda(\sigma,k_\lambda)}{\partial k_\lambda} e^{-i\omega k}dk$$

for $k = \lambda^+$, $k_\lambda = g_\lambda$, and $k_1 = g_1$ or for $k = \lambda^+$, $k_\lambda = h_\lambda$, and

$k_1 = h_1$

Shen [41]

10. $\int\limits_{1}^{\infty} \frac{e^{-i\omega k}}{\sqrt{k^2 - 1}}dk = - \left[\frac{i\pi}{2} \right] H_o^{(2)}(\omega)$ \qquad Durand [40]

11. $\int\limits_{-1}^{1} \sqrt{\frac{1 - k}{1 + k}}dk = \pi$ \qquad Henderson [18]

12. $\int\limits_{-1}^{1} \sqrt{\frac{1 + k}{1 - k}} \frac{kdk}{j - k} = -\pi(1 + j)$ for $|j|^2 \leq 1$

13. $\int\limits_{-1}^{1} \sqrt{\frac{1 + k}{1 - k}} \frac{kdk}{j - k} = -\pi \left[1 + j - j \sqrt{\frac{j + 1}{j - 1}} \right]$ for $|j|^2 > 1$

14. $\displaystyle\int_{-1}^{1} \Omega(\sigma,k)d\sigma = \pi\sqrt{1-k^2}$ for $|k|^2 \leq 1$ Henderson [18]

15. $\displaystyle\int_{-1}^{1} \Lambda(\sigma,k)d\sigma = -\pi\left[1 + \sqrt{\frac{k-1}{k+1}} - k + k\sqrt{\frac{k-1}{k+1}}\right]$ for $|k|^2 > 1$

16. $\displaystyle\oint_{-1}^{1} \frac{dk}{\sqrt{1-k^2}\,(j-k)} = 0$ for $|j|^2 \leq 1$ Van Dyke [39]

17. $\displaystyle\oint_{-1}^{1} \frac{kdk}{\sqrt{1-k^2}\,(j-k)} = -\pi$ for $|j|^2 \leq 1$ Van Dyke [39]

18. $\displaystyle\oint_{-1}^{1} \frac{k^2dk}{\sqrt{1-k^2}\,(j-k)} = -\pi j$ for $|j|^2 \leq 1$ Van Dyke [39]

19. $\displaystyle\int_{-1}^{1} \sqrt{\frac{1+k}{1-k}}dk = \pi$

20. $\displaystyle\int_{-1}^{1} \sqrt{\frac{1+k}{1-k}}kdk = \frac{\pi}{2}$ Henderson [18]

21. $\displaystyle\int_{-1}^{1} \sqrt{\frac{1-k}{1+k}}e^{-i\theta k}dk = \pi\left[J_o(\theta) + iJ_1(\theta)\right]$ Henderson [18]

22. $\displaystyle\int_{-1}^{1} \sqrt{\frac{1-k}{1+k}}\, k e^{-i\theta k}\, dk = \frac{\pi}{2}\left[J_2(\theta) - J_0(\theta) - 2iJ_1(\theta)\right]$ Henderson [18]

23. $\displaystyle\int_{-1}^{1} \sqrt{\frac{1-k}{1+k}}\, \frac{e^{-i\theta k}}{j-k}\, dk = \pi\left[J_0(\theta)\left[1 - \sqrt{\frac{j-1}{j+1}}\right] - 2\sqrt{\frac{j-1}{j+1}}\right.$

$$\left. \cdot \sum_{m=1}^{\infty} (i)^{-m}\left[j - \sqrt{j^2 - 1}\right]^m J_m(\theta) \right]$$

for $|j|^2 > 1$ Goldstein [42]

24. $\displaystyle\int_{-1}^{1} \sqrt{\frac{1+k}{1-k}}\, e^{-i\theta k}\, dk = \pi\left[J_0(\theta) - iJ_1(\theta)\right]$ Reissner [26]

25. $\displaystyle\int_{-1}^{1} \sqrt{\frac{1+k}{1-k}}\, k e^{-i\theta k}\, dk = \frac{\pi}{2}\left[J_0(\theta) - J_2(\theta) - 2iJ_1(\theta)\right]$ Henderson [18]

26. $\displaystyle\int_{-1}^{1} \sqrt{1-k^2}\, e^{-i\theta k}\, dk = \left[\frac{\pi}{\theta}\right] J_1(\theta)$

27. $\displaystyle\int_{-1}^{1} \sqrt{1 - k^2}\; ke^{-i\theta k}dk = -\left[\frac{i\pi}{\theta}\right] J_2(\theta)$

28. $\displaystyle\oint_{-1}^{1} \sqrt{\frac{1 - k}{1 + k}}\; \frac{kdk}{j - k} = -\pi(1 - j) \quad \text{for } |j|^2 \le 1$

29. $\displaystyle\int_{-1}^{1} \sqrt{\frac{1 - k}{1 + k}}\; \frac{kdk}{j - k} = -\pi\left[1 - j + j\sqrt{\frac{j - 1}{j + 1}}\right] \quad \text{for } |j|^2 > 1$

30. $\displaystyle\oint_{-1}^{1} \sqrt{\frac{1 + k}{1 - k}}\; \frac{k^2 dk}{j - k} = -\pi\left[\frac{1}{2} + j + j^2\right] \quad \text{for } |j|^2 \le 1$

31. $\displaystyle\int_{-1}^{1} \sqrt{\frac{1 + k}{1 - k}}\; \frac{k^2 dk}{j - k} = -\pi\left[\frac{1}{2} + j + j^2 - j^2\sqrt{\frac{j + 1}{j - 1}}\right] \quad \text{for } |j|^2 > 1$

32. $\displaystyle\int_{-1}^{1} \Omega(\sigma,k)\sigma d\sigma = \frac{\pi}{2}(k)\sqrt{1 - k^2} \quad \text{for } |k|^2 \le 1$

33. $\displaystyle\int_{-1}^{1} \Lambda(\sigma,k)\sigma d\sigma = \frac{\pi}{2}[k^2 - 1 - k\sqrt{k^2 - 1}] \quad \text{for } |k|^2 > 1$

34. $$\int_{-1}^{1} \sqrt{\frac{1-k}{1+k}}\, \frac{ke^{-i\theta k}}{j-k}\, dk = \pi \left[J_0(\theta) \left[j - 1 - j\sqrt{\frac{j-1}{j+1}}\,\right] - iJ_1(\theta) \right.$$

$$- 2j\sqrt{\frac{j-1}{j+1}}\sum_{m=1}^{\infty} (i)^{-m}$$

$$\left. \cdot\, [\,j - \sqrt{j^2-1}\,]^m J_m(\theta) \right]$$

for $|j|^2 > 1$

35. $$\int_{-1}^{1} \sqrt{1-k^2}\, k^2 e^{-i\theta k}\, dk = \frac{\pi}{\theta}\left[J_1(\theta) - \left[\frac{3}{\theta}\right] J_2(\theta)\right]$$

APPENDIX E

UNSTEADY LIFT EQUATION FOR THE CASE OF INFINITE SPACING

The general equation for the unsteady lift coefficient for a blade in a cascade of symmetrical parabolic arc blades operating at a nonzero mean angle of incidence in a velocity field that contains both transverse and chordwise disturbance velocities is presented as Equation (36) in Chapter 2. The objective of this appendix is to show that when the spacing between blades becomes infinite this equation reduces to the well-known solution for an isolated airfoil.

First consider the function $G(\omega, x_c^+, S/C, \xi)$ defined by Equation (22) of Chapter 2. Henderson and Daneshyar [43] have shown that $\lim_{S\to\infty} B_1 = \lim_{S\to\infty} B_2 = \lim_{S\to\infty} D_1 = \lim_{S\to\infty} D_2 = 0$ and $\lim_{S\to\infty} C_1 = \lim_{S\to\infty} C_2 = 1$. To determine the limiting value of E_1 and E_2, express E_1 in the form

$$E_1 = \left[g_c \left[\sqrt{\frac{g_c + 1}{g_c - 1}} - 1 \right] - \sqrt{\frac{g_c + 1}{g_c - 1}} \right]$$

$$- \left[g_1 \left[\sqrt{\frac{g_1 + 1}{g_1 - 1}} - 1 \right] - \sqrt{\frac{g_1 + 1}{g_1 - 1}} \right]$$

from which

$$\lim_{S\to\infty} E_1 = \lim_{S\to\infty} \left[g_c \left[\sqrt{\frac{g_c + 1}{g_c - 1}} - 1 \right] \right]$$

$$- 1 - \lim_{S\to\infty} \left[g_1 \left[\sqrt{\frac{g_1 + 1}{g_1 - 1}} - 1 \right] \right] + 1 \quad ,$$

since, by analogy with Henderson and Daneshyar's result that

$$\lim_{S\to\infty} C_1 = \lim_{S\to\infty} \sqrt{\frac{g_c + 1}{g_1 - 1}} = 1 \quad , \qquad \lim_{S\to\infty} \sqrt{\frac{g_1 + 1}{g_1 - 1}} = 1 \quad .$$

To determine the limiting value of the term $g_c \left[\sqrt{\dfrac{g_c + 1}{g_c - 1}} - 1 \right]$, express g_c as $g_c = x_c^+ - iSk$, where $k = \left[\dfrac{2n}{C} \right] e^{i\xi}$. Then,

$$\lim_{S \to \infty} \left[g_c \left[\sqrt{\frac{g_c + 1}{g_c - 1}} - 1 \right] \right] = \lim_{S \to \infty} \left\{ \frac{\sqrt{\dfrac{\dfrac{x_c^+ + 1}{S} - ik}{\dfrac{x_c^+ - 1}{S} - ik}} - 1}{\dfrac{1}{x_c^+ - iSk}} \right\}$$

$$= \frac{0}{0} \quad ,$$

an indeterminate form. Applying L'Hospital's rule with

$$\frac{\partial}{\partial S} \left[\sqrt{\frac{g_c + 1}{g_c - 1}} - 1 \right] = - \sqrt{\frac{g_c - 1}{g_c + 1}} \frac{\dfrac{\partial g_c}{\partial S}}{(g_c - 1)^2}$$

and

$$\frac{\partial}{\partial S} \left[\frac{1}{g_c} \right] = - \frac{\dfrac{\partial g_c}{\partial S}}{(g_c)^2}$$

leads to

$$\lim_{S\to\infty}\left[g_c\left[\sqrt{\frac{g_c+1}{g_c-1}}-1\right]\right] = \lim_{S\to\infty}\left\{\sqrt{\frac{\dfrac{x_c^+-1}{S}-ik}{\dfrac{x_c^++1}{S}-ik}}\right.$$

$$\left.\cdot\frac{\left[\dfrac{x_c^+}{S}-ik\right]^2}{\left[\dfrac{x_c^+-1}{S}-ik\right]^2}\right\}$$

$$= 1 \quad.$$

By analogy with this result, $\lim_{S\to\infty}\left[g_1\left[\sqrt{\dfrac{g_1+1}{g_1-1}}-1\right]\right] = 1$. Thus, $\lim_{S\to\infty} E_1 = 0$, and a completely similar analysis shows that $\lim_{S\to\infty} E_2 = 0$. Consequently, in the limit when $S = \infty$,

$$G(\omega,x_c^+,\infty,\xi) = 1 + \frac{\pi\omega H_o^{(2)}(\omega)}{i\pi\omega\left[H_1^{(2)}(\omega) + iH_o^{(2)}(\omega)\right]}$$

$$= C(\omega) \quad.$$

Now consider the terms inside the double summation in Equation (36). Clearly, since $\lim_{S\to\infty} C_1 = \lim_{S\to\infty} C_2 = 1$, the term $C_1 + C_2 - 2 = 0$ when $S = \infty$. The remaining term contains the sum $\left[g_c - \sqrt{g_c^2-1}\right]^m + \left[h_c - \sqrt{h_c^2-1}\right]^m$ where $m = 1, 2, 3, \ldots$. From the results presented above,

$$\lim_{S \to \infty}\left[g_c - \sqrt{g_c^2 - 1}\right] = \lim_{S \to \infty}\left[g_c\left[\sqrt{\frac{g_c + 1}{g_c - 1}} - 1\right] - \sqrt{\frac{g_c + 1}{g_c - 1}}\right]$$

$$= 0 \quad .$$

By analogy, $\lim_{S \to \infty}\left[h_c - \sqrt{h_c^2 - 1}\right] = 0$. With these results, the entire term inside the double summation is equal to zero when $S = \infty$.

With these results, Equation (36) of Chapter 2 reduces to

$$C_L = -\cos\phi\left[y_{max}^+\left[\left[1 + \frac{2\omega}{\theta}\right]J_2(\theta) + J_0(\theta)\right.\right.$$

$$\left.+ C(\omega)\left[J_0(\theta) - J_2(\theta) - 2iJ_1(\theta)\right]\right]$$

$$\left.+ i_m\left[J_0(\theta) + iJ_1(\theta)\right]\right] - \sin\phi\left[C(\omega)\left[J_0(\theta) - iJ_1(\theta)\right]\right.$$

$$\left.+ \left[\frac{i\omega}{\theta}\right]J_1(\theta)\right] \quad .$$

Henderson and Daneshyar [43] have shown that this equation is equivalent to the equation presented by Horlock [11] for the unsteady lift of an isolated airfoil.

APPENDIX F

VALUE OF THE FUNCTION $B(\omega, x_c^+, S/C, \xi)$ FOR
THE CASE OF INFINITE SPACING

The objective of this appendix is to define the value of the function $B(\omega, x_c^+, S/C, \xi)$ when the spacing between blades in the cascade becomes infinite. With $B(\omega, x_c^+, S/C, \xi)$ given by Equation (39) of Chapter 2 and with the results $\lim_{S\to\infty} B_1 = \lim_{S\to\infty} B_2 = \lim_{S\to\infty} D_1 = \lim_{S\to\infty} D_2 = \lim_{S\to\infty} g_c(C_1 - 1) - C_1 = \lim_{S\to\infty} h_c(C_2 - 1) - C_2 = 0$ and $\lim_{S\to\infty} C_1 = \lim_{S\to\infty} C_2 = 1$ from Appendix E, it is clear that the function $B(\omega, x_c^+, S/C, \xi)$ reduces to

$$B(\omega, x_c^+, \infty, \xi) = C(\omega) - 1$$

if it can be shown that $\lim_{S\to\infty} F_1 + F_2 = 0$.

Rewrite the expression for F_1 as

$$F_1 = g_c \left[\sqrt{\frac{g_c + 1}{g_c - 1}} - g_c \left[\sqrt{\frac{g_c + 1}{g_c - 1}} - 1 \right] \right]$$

$$- g_1 \left[\sqrt{\frac{g_1 + 1}{g_1 - 1}} - g_1 \left[\sqrt{\frac{g_1 + 1}{g_1 - 1}} - 1 \right] \right] ,$$

express g_c as $g_c = x_c^+ - iSk$, where $k = \left[\frac{2n}{C} \right] e^{i\xi}$, and consider the term in F_1 that is dependent upon g_c. Then,

$$\lim_{S \to \infty} g_c \left[\sqrt{\frac{g_c + 1}{g_c - 1}} - g_c \left[\sqrt{\frac{g_c + 1}{g_c - 1}} - 1 \right] \right]$$

$$= \lim_{S \to \infty} \left\{ \frac{\sqrt{\dfrac{\dfrac{x_c^+ + 1}{S} - ik}{\dfrac{x_c^+ - 1}{S} - ik}} - (x_c^+ - iSk) \sqrt{\dfrac{\dfrac{x_c^+ + 1}{S} - ik}{\dfrac{x_c^+ - 1}{S} - ik} - 1}}{\dfrac{1}{x_c^+ - iSk}} \right\}$$

$$= \frac{1 - (\infty)(0)}{0} \quad ,$$

an indeterminate form. Applying L'Hospital's rule with

$$\frac{\partial}{\partial S} \left[\sqrt{\frac{g_c + 1}{g_c - 1}} - g_c \left[\sqrt{\frac{g_c + 1}{g_c - 1}} - 1 \right] \right] = - \sqrt{\frac{g_c - 1}{g_c + 1}} \frac{\dfrac{\partial g_c}{\partial S}}{(g_c - 1)^2}$$

$$- \left[\sqrt{\frac{g_c + 1}{g_c - 1}} - 1 \right] \frac{\partial g_c}{\partial S}$$

$$+ g_c \sqrt{\frac{g_c - 1}{g_c + 1}} \frac{\dfrac{\partial g_c}{\partial S}}{(g_c - 1)^2}$$

and

$$\frac{\partial}{\partial S} \left[\frac{1}{g_c} \right] = - \frac{\dfrac{\partial g_c}{\partial S}}{(g_c)^2}$$

leads to

$$\lim_{S \to \infty} g_c \left[\sqrt{\frac{g_c + 1}{g_c - 1}} - g_c \left[\sqrt{\frac{g_c + 1}{g_c - 1}} - 1 \right] \right]$$

$$= \lim_{S \to \infty} \left[[1 - g_c] \left[\sqrt{\frac{g_c - 1}{g_c + 1}} \frac{g_c^2}{(g_c - 1)^2} \right] \right.$$

$$\left. + g_c \left[g_c \left[\sqrt{\frac{g_c + 1}{g_c - 1}} - 1 \right] \right] \right]$$

$$= 1 - g_c + g_c$$

$$= 1$$

since $\lim\limits_{S \to \infty} \left[\sqrt{\dfrac{g_c - 1}{g_c + 1}} \dfrac{g_c^2}{(g_c - 1)^2} \right] = 1$ and $\lim\limits_{S \to \infty} \left[g_c \left[\sqrt{\dfrac{g_c + 1}{g_c - 1}} - 1 \right] \right]$

$= 1$ from Appendix E.

By analogy with this result, it follows that

$$\lim_{S \to \infty} g_1 \left[\sqrt{\frac{g_1 + 1}{g_1 - 1}} - g_1 \left[\sqrt{\frac{g_1 + 1}{g_1 - 1}} - 1 \right] \right] = 1 \quad ,$$

$$\lim_{S \to \infty} h_c \left[\sqrt{\frac{h_c + 1}{h_c - 1}} - h_c \left[\sqrt{\frac{h_c + 1}{h_c - 1}} - 1 \right] \right] = 1 \quad ,$$

and

$$\lim_{S \to \infty} h_1 \left[\sqrt{\frac{h_1 + 1}{h_1 - 1}} - h_1 \left[\sqrt{\frac{h_1 + 1}{h_1 - 1}} - 1 \right] \right] = 1 \quad .$$

Thus, in the limit when $S = \infty$, $F_1 = F_2 = 0$ and $B(\omega, x_c^+, \infty, \xi) = C(\omega) - 1$.

APPENDIX G

UNSTEADY PITCHING MOMENT EQUATION FOR
THE CASE OF INFINITE SPACING

The general equation for the unsteady pitching moment coefficient for a blade in a cascade of symmetrical parabolic blades operating at a nonzero mean of angle of incidence in a velocity field that contains both transverse and chordwise disturbance velocities is presented as Equation (40) in Chapter 2. The objective of this appendix is to show that when the spacing between blades becomes infinite this equation reduces to the solution for an isolated airfoil.

In Appendix E, an analysis is presented which shows that in the limit when $S = \infty$, the function $B(\omega, x_c^+, S/C, \xi)$ reduces to the value $B(\omega, x_c^+, \infty, \xi) = C(\omega) - 1$.

Consider the terms in Equation (40) that are inside the bracket that are summed over integer values of n from $n = -\infty$ to $n = -1$ and from $n = 1$ to $n = \infty$. Results presented in Appendix E, when applied to the term $[g_c(C_1 - 1) - C_1 + h_c(C_2 - 1) - C_2]$ show that $\lim\limits_{S \to \infty}[g_c(C_1 - 1) - C_1 + h_c(C_2 - 1) - C_2] = 0$. Now consider only the part of the remaining terms that contains the parameter g_c. With $g_c = x_c^+ - iSk$, where $k = \left[\dfrac{2n}{C}\right] e^{i\xi}$,

$$\lim_{S \to \infty}\left[-i\sqrt{\frac{g_c + 1}{g_c - 1}}\, J_1(\theta) - 2g_c \sum_{m=1}^{\infty} (1)^{-m} \cdot [g_c - \sqrt{g_c^2 - 1}]^m J_m(\theta)\right] = -i(1)J_1(\theta) - 2(\infty)(0) \quad,$$

since, from Appendix E, $\lim\limits_{S \to \infty}\sqrt{\dfrac{g_c + 1}{g_c - 1}} = 1$ and $\lim\limits_{S \to \infty}[g_c - \sqrt{g_c^2 - 1}] = 0$ and $\lim\limits_{S \to \infty} g_c = \infty$. The form of the limiting value above is indeterminate.
Applying L'Hospital's rule with

$$\frac{\partial}{\partial S} \sqrt{\frac{g_c + 1}{g_c - 1}} = - \sqrt{\frac{g_c - 1}{g_c + 1}} \frac{\frac{\partial g_c}{\partial S}}{(g_c - 1)^2}$$

and

$$\frac{\partial}{\partial S} \left[g_c \sum_{m=1}^{\infty} (i)^{-m} [g_c - \sqrt{g_c^2 - 1}]^m J_m(\theta) \right]$$

$$= \frac{\partial g_c}{\partial S} \left[\sum_{m=1}^{\infty} (i)^{-m} [g_c - \sqrt{g_c^2 - 1}]^m J_m(\theta) \right.$$

$$+ \left[\frac{g_c \sqrt{g_c^2 - 1} - g_c^2}{\sqrt{g_c^2 - 1}} \right] \sum_{m=1}^{\infty} m(i)^{-m}$$

$$\left. \cdot [g_c - \sqrt{g_c^2 - 1}]^{m-1} J_m(\theta) \right]$$

leads to

$$\lim_{S \to \infty} \left[-i \sqrt{\frac{g_c + 1}{g_c - 1}} J_1(\theta) - 2g_c \sum_{m=1}^{\infty} (i)^{-m} \left[g_c - \sqrt{g_c^2 - 1} \right]^m J_m(\theta) \right]$$

$$= -ik \lim_{S \to \infty} \left[\frac{1}{(g_c - 1)^2} \sqrt{\frac{g_c - 1}{g_c + 1}} J_1(\theta) \right.$$

$$- 2 \sum_{m=1}^{\infty} (i)^{-m} \left[g_c - \sqrt{g_c^2 - 1} \right]^m J_m(\theta)$$

$$+ 2 \left[\frac{g_c^2 - g_c \sqrt{g_c^2 - 1}}{\sqrt{g_c^2 - 1}} \right] \sum_{m=1}^{\infty} m(i)^{-m}$$

$$\left. \cdot \left[g_c - \sqrt{g_c^2 - 1} \right]^{m-1} J_m(\theta) \right]$$

$$= -ik \left[\frac{1}{(\infty)^2} (1) J_1(\theta) - 2(0) + 2\frac{(1)}{(\infty)}(0) \right]$$

$$= 0$$

since

$$\lim_{S \to \infty} \sqrt{\frac{g_c - 1}{g_c + 1}} = \lim_{S \to \infty} \sqrt{\frac{\dfrac{x_c^+ - 1}{S} - ik}{\dfrac{x_c^+ + 1}{S} - ik}}$$

$$= 1$$

and from Appendix F, $\lim\limits_{S \to \infty}\left[g_c^2 - g_c \sqrt{g_c^2 - 1}\right] = 1$. By a similar analysis, it follows that

$$\lim_{S \to \infty}\left[-1 \sqrt{\frac{h_c + 1}{h_c - 1}}\, J_1(\theta) - 2h_c \sum_{m=1}^{\infty} (i)^{-m} \right.$$

$$\left. \cdot \left[h_c - \sqrt{h_c^2 - 1}\right]^m J_m(\theta) \right] = 0 \quad .$$

Thus, in the limit, when $S = \infty$, the entire term in Equation (40) inside the bracket affected by the double summation vanishes. Thus, the equation for the unsteady pitching moment on an isolated airfoil, defined by the limiting value of the cascade pitching moment equation, is

$$\zeta_M = \frac{\cos\phi}{4}\left[-i_m J_0(\theta) + 2i\left[\left[\frac{\omega}{\theta}\right] y_{max}^+ - i_m\right] J_1(\theta) \right.$$

$$+ \left[i_m - \frac{6i\omega y_{max}^+}{\theta^2} \right] J_2(\theta) - y_{max}^+ [C(\omega) - 1]\left[J_0(\theta) - 2iJ_1(\theta)\right.$$

$$\left. - J_2(\theta)\right]\right] - \frac{\sin\phi}{4}\left[\left[\frac{2}{\theta}\right] J_1(\theta) - \left[\frac{\omega}{\theta}\right] J_2(\theta) \right.$$

$$+ \left[C(\omega) - 1\right]\left[J_0(\theta) - iJ_1(\theta)\right]\right] \quad .$$

For the case of zero camber, this equation reduces to

$$\mathcal{C}_m = -\frac{i_m \cos\phi}{4}[J_0(\theta) + 2iJ_1(\theta) - J_2(\theta)] - \frac{\sin\phi}{4}\left[\left[\frac{2}{\theta}\right]J_1(\theta)\right.$$

$$\left. - \left[\frac{\omega}{\theta}\right]J_2(\theta) + [C(\omega) - 1][J_0(\theta) - iJ_1(\theta)]\right] \quad .$$

If the disturbance velocity is convected with the mean relative velocity, $\theta = \omega$, and the above equation becomes

$$\mathcal{C}_M = -\frac{i_m \cos\phi}{4}[J_0(\omega) + 2iJ_1(\omega) - J_2(\omega)]$$

$$- \frac{\sin\phi}{4}\left[\left[\frac{2}{\omega}\right]J_1(\omega) - J_2(\omega) + [C(\omega) - 1][J_0(\omega) - iJ_1(\omega)]\right] \quad .$$

Holmes [13] has presented an expression for the unsteady pitching moment of an uncambered isolated airfoil by combining Sears' [4] result for a transverse disturbance velocity and Horlock's [10] result for a chordwise disturbance velocity. His result, when differences in sign conventions and nomenclature are accounted for, is identical to the result presented above except for the fact that he retained the Sears function $S(\omega)$ in the $\sin\phi$ term. Holmes' expression, when written in the nomenclature used herein, is

$$C_M = -\frac{i_m \cos\phi}{4}[J_0(\omega) + 2iJ_1(\omega) - J_2(\omega)] - \frac{\sin\phi}{4}[S(\omega)] \quad .$$

To show that

$$\left[\frac{2}{\omega}\right]J_1(\omega) - J_2(\omega) + [C(\omega) - 1][J_0(\omega) - iJ_1(\omega)] = S(\omega) \quad ,$$

it is convenient to recall the relations

$$\left[\frac{2}{\omega}\right] J_1(\omega) - J_2(\omega) = J_0(\omega)$$

and

$$C(\omega) - 1 = \frac{H_0^{(2)}(\omega)}{i\left[H_1^{(2)}(\omega) + iH_0^{(2)}(\omega)\right]} \quad .$$

Inserting these relations into the left-hand side of the above expression and simplifying the result leads to the expression

$$\frac{J_0(\omega)H_1^{(2)}(\omega) - J_1(\omega)H_0^{(2)}(\omega)}{H_1^{(2)}(\omega) + iH_0^{(2)}(\omega)} = S(\omega) \quad .$$

With $H_0^{(2)}(\omega) = J_0(\omega) - iY_0(\omega)$ and $H_1^{(2)}(\omega) = J_1(\omega) - iY_1(\omega)$, this becomes

$$\frac{i\left[J_1(\omega)Y_0(\omega) - J_0(\omega)Y_1(\omega)\right]}{\left[J_1(\omega) - iY_1(\omega)\right] + i\left[J_0(\omega) - iY_0(\omega)\right]} = S(\omega) \quad .$$

Operating on this expression using the relations

$$K_0(i\omega) = -\frac{i\pi}{2}\left[J_0(\omega) - iY_0(\omega)\right]$$

and

$$K_1(i\omega) = -\frac{\pi}{2}\left[J_1(\omega) - iY_1(\omega)\right]$$

leads to the relation

$$\frac{J_o(\omega)K_1(i\omega) + iJ_1(\omega)K_o(i\omega)}{K_1(i\omega) + K_o(i\omega)} = S(\omega) \qquad .$$

This is the form given originally by Sears [4].

APPENDIX H

ANALYSIS OF EXPERIMENTAL ERROR

The objective of this appendix is to present the results of an analysis of the percent error associated with measured values of the quantities $|\overset{\scriptscriptstyle\lambda}{C}_L|$, $|\overset{\scriptscriptstyle\lambda}{C}_M|$, ϕ_F, and ϕ_M. The method presented by Schenck [44] was used. This method defines the percentage of the correct reading represented by the standard deviation for a quantity which is functionally dependent upon combinations of products, quotients, or sums of other measured quantities. The data set for each of the other measured quantities is assumed to possess a Gaussian distribution (i.e., small skew) and to contain statistically independent readings.

The error associated with determination of the quantities $|\overset{\scriptscriptstyle\lambda}{C}_L|$ and $|\overset{\scriptscriptstyle\lambda}{C}_M|$ is dependent upon the error in determination of $\overset{\scriptscriptstyle\lambda}{L}$, $\overset{\scriptscriptstyle\wedge}{M}$, W_m, w_d, and C. With functional relations defined by

$$|\overset{\scriptscriptstyle\lambda}{C}_L| = k \left[\frac{\overset{\scriptscriptstyle\lambda}{L}}{W_m w_d C} \right]$$

and

$$|\overset{\scriptscriptstyle\lambda}{C}_M| = k \left[\frac{\overset{\scriptscriptstyle\wedge}{M}}{W_m w_d C^2} \right] \quad ,$$

where k is a constant of proportionality, the percent error in determination of each quantity is given by

$$\% \ |\overset{\scriptscriptstyle\lambda}{C}_L| = 100 \left[\left[\frac{\sigma_{\overset{\scriptscriptstyle\lambda}{L}}}{\overline{\overset{\scriptscriptstyle\lambda}{L}}} \right]^2 + \left[\frac{\sigma_{W_m}}{\overline{W}_m} \right]^2 + \left[\frac{\sigma_{w_d}}{\overline{w}_d} \right]^2 + \left[\frac{\sigma_C}{\overline{C}} \right]^2 \right]^{1/2}$$

and

$$\% \ |\overset{\curvearrowright}{\alpha}_M| \ = \ 100 \left[\left[\frac{\sigma_{\overset{\curvearrowright}{M}}}{\overline{\overset{\curvearrowright}{M}}} \right]^2 + \left[\frac{\sigma_{W_m}}{\overline{W}_m} \right]^2 + \left[\frac{\sigma_{w_d}}{\overline{W}_d} \right]^2 + 2 \left[\frac{\sigma_C}{\overline{C}} \right]^2 \right]^{1/2} \quad ,$$

where σ is the standard deviation for each data sample and the overbar denotes the sample mean value.

The error associated with determination of the phase angles ϕ_F and ϕ_M is dependent upon the error in determination of the angular position of the distortion flow field relative to the facility outer casing, ϕ_j, and the error in determination of the angular position of the sensor output signal relative to the facility outer casing, $\phi_{\overset{\curvearrowright}{F}}$ or $\phi_{\overset{\curvearrowright}{M}}$. The appropriate functional relations are

$$\phi_F = \phi_j + \phi_{\overset{\curvearrowright}{F}}$$

and

$$\phi_M = \phi_j + \phi_{\overset{\curvearrowright}{M}} \quad .$$

The related expressions for the percent error are

$$\% \ \phi_F \ = \ 100 \left[\left[\frac{\sigma_{\phi_j}}{\overline{\phi}_j} \right]^2 + \left[\frac{\sigma_{\overset{\curvearrowright}{F}}}{\overline{\phi}_{\overset{\curvearrowright}{F}}} \right]^2 \right]^{1/2}$$

and

$$\% \ \phi_M \ = \ 100 \left[\left[\frac{\sigma_{\phi_j}}{\overline{\phi}_j} \right]^2 + \left[\frac{\sigma_{\overset{\curvearrowright}{M}}}{\overline{\phi}_{\overset{\curvearrowright}{M}}} \right]^2 \right]^{1/2} \quad .$$

These relations were applied to the portion of the measured data
for which repeated evaluations were made at identical test conditions.
All of the data points for tests in which the one-cycle distortion-
generating grid was used were included in this analysis. In addition,
the data points for the five-cycle distortion-generating wire grid with
$(S/C) = 1.353$ and $\xi = 45°$ were included. In total, this data sample
represented approximately 40% of the entire data set. The results were

$$\% \ |\hat{c}_L| = 5.7 \quad ,$$

$$\% \ |\hat{c}_M| = 6.4 \quad ,$$

$$\% \ \phi_F = 2.1 \quad ,$$

and

$$\% \ \phi_M = 2.3 \quad .$$

These results indicate that the experimental portion of this study was
completed with acceptable accuracy. They also reflect the greater dif-
ficulty associated with accurate measurement of the pitching moment.
This result was expected since the sensor pitching moment static sen-
sitivity was less than the normal force static sensitivity.

From a statistical point of view, the results presented above
represent an error estimate of less than desirable confidence because
of the small number of data points available at each test condition.
At 30 test conditions, only two data points were available for analysis,
and, at three test conditions, only four data points were available for

analysis. For a statistically adequate evaluation of percent error, a total of at least seven data points should be included at each test condition.

The post-test analysis presented above also represents the least desirable form for application of Schenck's probable error method. A more useful application is in the planning stage of an experiment. By applying the ideas presented above to the sensing, transmitting, recording, and analyzing elements in the chain of operations that leads to specification of each measured quantity, it is possible to detect instruments or operations which have a dominant influence on the probable error level for an entire experiment. Upon detection, these instruments or operations can be modified, prior to recording a single data point, to reduce the probable error level. As an example, consider the instrumentation block diagram presented in Figure 22. Application of Schenck's method would require a pretest determination of the lift and moment gage output signals due to repeated application of known loads; a pretest determination of the slip-ring output signals for repeated, known input signals; and a pretest determination of the tape recorder output for repeated, known input signals. Additional steps in the chain of operations not shown in Figure 22 are associated with digitizing, phase-lock averaging, and Fourier analyzing the tape recorded signal. After evaluating the percent error associated with each of these analysis operations, an anticipated over-all percent error could be obtained by summing the results for each operation. This pre-test evaluation, by its nature, would also yield information on the probable error distribution; thus, limiting operations could be identified and modified before initiating the test program.

DISTRIBUTION LIST FOR ARL UNCLASSIFIED TM 79-149 by E. P. Bruce dated 14 August 1979.

Commander
Naval Sea Systems Command
Department of the Navy
Washington, DC 20362
Attn: Library,
       Code NSEA 09G32
(copies 1 and 2)

Naval Sea Systems Command
Attn: Code NSEA 0342
(copies 3 and 4)

Naval Sea Systems Command
Attn: T. E. Peirce,
       Code NSEA 63R3
(copy no. 5)

Naval Sea Systems Command
Attn: A. R. Paladino,
       Code NSEA 05H1
(copy no. 6)

Naval Sea Systems Command
Attn: F. Peterson,
       Code NSEA 52P
(copy no. 7)

Defense Technical Information Center
5010 Duke Street
Cameron Station
Alexandria, VA 22314
(copies 8 through 19)

Commanding Officer
Naval Underwater Systems Center
Newport, RI 02840
Attn: Library,
       Code 54
(copy no. 20)

Commanding Officer
Naval Ocean Systems Center
San Diego, CA 92152
Attn: D. Nelson,
       Code 6342
(copy no. 21)

Naval Ocean Systems Center
Attn: M. Reischman,
       Code 2542
(copy no. 22)

Naval Ocean Systems Center
Attn: Library
(copy no. 23)

Commanding Officer & Director
David W. Taylor Naval Ship R&D Center
Department of the Navy
Bethesda, MD 20084
Attn: W. B. Morgan,
       Code 154
(copy no. 24)

David W. Taylor Naval Ship R&D Center
Attn: R. Cumming,
       Code 1544
(copy no. 25)

David W. Taylor Naval Ship R&D Center
Attn: J. McCarthy,
       Code 1552
(copy no. 26)

David W. Taylor Naval Ship R&D Center
Attn: M. Sevik,
       Code 19
(copy no. 27)

David W. Taylor Naval Ship R&D Center
Attn: W. K. Blake,
       Code 1942
(copy no. 28)

Commanding Officer & Director
David W. Taylor Naval Ship R&D Center
Department of the Navy
Annapolis Laboratory
Annapolis, MD 21402
Attn: J. G. Stricker,
       Code 2721
(copy no. 29)

Commander
Naval Surface Weapon Center
Silver Spring, MD 20910
Attn: Library
(copy no. 30)

DISTRIBUTION LIST FOR ARL UNCLASSIFIED TM 79-149 by E. P. Bruce dated 14 August 1979.

Air Force Office of Scientific Research
Bolling Air Force Base, Building 410
Washington, DC 20332
Attn: Dr. Joseph F. Masi
(copy no. 31)

Air For Aero Propulsion Laboratory
Wright-Patterson AFB, OH 45433
Attn: AFAPL/TBC
      Dr. Kervyn Mach
(copy no. 32)

Naval Postgraduate School
Department of Aeronautics, Code 57
Monterey, CA 93940
Attn: Dr. Allen E. Fuhs
(copy no. 33)

Office of Naval Research Branch Office
1030 East Green Street
Pasadena, CA 91106
Attn: Dr. Rudolph J. Marcus
(copy no. 34)

Office of Naval Research Branch Office
536 South Clark Street
Chicago, IL 60605
Attn: Commander
(copy no. 35)

Office of Naval Research Branch Office
495 Summer Street
Boston, MA 02210
Attn: Commander
(copy no. 36)

Office of Naval Research
Power Branch
Department of the Navy
Arlington, VA 22217
Attn: Mr. J. R. Patton
(copy no. 37)

Office of Naval Research
Fluid Dynamics Branch, Code 438
Department of the Navy
Washington, DC 22217
Attn: Mr. Morton Cooper
(copy no. 38)

Naval Ship Research and Development Center
Annapolis Division
Annapolis, MD 21402
Attn: Library,
      Code A214
(copy no. 39)

General Electric Company
AEG Technical Information Center
Mail Drop N-32, Building 700
Cincinnati, OH 45215
Attn: J. J. Brady
(copy no. 40)

General Electric Company
SPO-Bldg., 174AE
1000 Western Avenue
West Lynn, MA 01910
Attn: Mr. W. Bruce Gist
(copy no. 41)

General Motors Corporation
Detroit Diesel Allison Division
P. O. Box 894
Indianapolis, IN 46206
Attn: Mr. P. C. Tram
(copy no. 42)

Pratt and Whitney Aircraft
Project Engineer, Advanced
Military System
Engineering Department - 2B
East Hartford, CT 06108
Attn: Mr. Donald S. Rudolph
(copy no. 43)

Pratt and Whitney Aircraft
Florida Research and Development Company
P. O. Box 2691
West Palm Beach, FL 33402
Attn: Mr. William R. Alley
      Chief of Applied Research
(copy no. 44)

Teledyne CAE
1330 Laskey Road
Toledo, OH 43601
Attn: Technical Library
(copy no. 45)

DISTRIBUTION LIST FOR ARL UNCLASSIFIED TM 79-149 by E. P. Bruce dated 14 August 1979.

United Technologies Research Center
400 Main Street
East Hartford, CT 06108
Attn: Librarian
(copy no. 46)

United Technologies Research Center
Attn: Mr. Franklin O. Carta
(copy no. 47)

Case Western Reserve University
Division of Fluid Thermal and
Aerospace Sciences
Cleveland, OH 44106
Attn: Professor Eli Reshotko
(copy no. 48)

George Washington University
Dept. of Civil, Mechanical, and
Environmental Engineering
Washington, DC 20052
Attn: Dr. Robert Goulard
(copy no. 49)

Massachusetts Institute of Technology
Room 33-207
Cambridge, MA 02139
Attn: Dr. Jack L. Kerrebrock
(copy no. 50)

Massachusetts Institute of Technology
77 Massachusetts Avenue
Cambridge, MA 02139
Attn: Dr. E. M. Greitzer
(copy no. 51)

Stevens Institute of Technology
Department of Mechanical Engineering
Castle Point Station
Hoboken, NJ 07030
Attn: Professor F. Sisto
(copy no. 52)

ONERA
Energie and Propulsion
29 Avenue de la Division Leclure
92 Chatillon sous Bagneux, FRANCE
Attn: Mr. J. Fabri
(copy no. 53)

Southern Methodist University
Thermal and Fluid Sciences Center
Institute of Technology
Dallas, TX 75275
Attn: Dr. Roger L. Simpson
(copy no. 54)

Stanford University
Mechanical Engineering Department
Stanford, CA 94305
Attn: Dr. S. J. Kline/Dr. James P. Johnston
(copy no. 55)

University of Michigan
Department of Aerospace Engineering
Ann Arbor, MI 48105
Attn: Dr. T. C. Adamson, Jr.
(copy no. 56)

Virginia Polytechnic Institute and State
University
Mechanical Engineering Department
Blacksburg, VA 24601
Attn: Dr. Walter F. O'Brien, Jr.
(copy no. 57)

Virginia Polytechnic Institute and State
University
ME Dept.
Attn: Dr. Hal. L. Moses
(copy no. 58)

Purdue University
School of Aeronautics and Astronautics
Grissom Hall
West Lafayette, IN 47907
Attn: Library
(copy no. 59)

Purdue University
School of Mechanical Engineering
Mechanical Engineering Building
Attn: Library
(copy no. 60)

Purdue University
Chaffee Hall
Attn: Dr. S. N. B. Murthy
(copy no. 61)

DISTRIBUTION LIST FOR ARL UNCLASSIFIED TM 79-149 by E. P. Bruce dated 14 August 1979.

Purdue University
Attn: Dr. S. Fleeter
(copy no. 62)

University of Salford
Salford, M5 4WT
ENGLAND
Attn: Dr. John H. Horlock
      Vice Chancellor
(copy no. 63)

Netherlands Ship Model Basin
P. O. Box 28
6700 AA Wageningen
THE NETHERLANDS
Attn: Dr. P. van Oossanen
(copy no. 64)

Mut-Munchen Gmblt
8 Munchen 50
Postfach 50 06 40
GERMANY
Attn: Dr. Hans Mokelke
(copy no. 65)

Forschungsbeauftrager für Hydroakustik
8012 Ottobrunn B Munchen
Waldparkstr. 41
Munich
GERMANY
Attn: Dr. rer. nat. Horst Merbt
(copy no. 66)

Admiralty Marine Technology Establishment
Teddington, Middlesex
ENGLAND
Attn: Dr. Allen Moore
(copy no. 67)

Whittle Turbomachine Laboratory
Madingley Road
Cambridge
ENGLAND
Attn: Dr. D. S. Whitehead
(copy no. 68)

Whittle Turbomachine Laboratory
Attn: Library
(copy no. 69)

Von-Karman Institute for Fluid Dynamics
Turbomachinery Laboratory
Rhode-Saint-Genese
BELGIUM
Attn: Library
(copy no. 70)

Turbine Research Department
Rolls Royce Ltd.
P. O. Box 31
Derby
ENGLAND
Attn: Dr. D. S. Thompson
(copy no. 71)

NASA Lewis Research Center
21000 Brookpark Road
Cleveland, OH 44135
Attn: J. Adamczyk,
      MS 5-9
(copy no. 72)

NASA Lewis Research Center
Attn: M. J. Hartman,
      MS 5-9
(copy no. 73)

NASA Lewis Research Center
Attn: Dr. M. Goldstein
(copy no. 74)

NASA Lewis Research Center
Attn: W. M. McNally,
      MS 5-9
(copy no. 75)

Cranfield Institute of Technology
School of Mechanical Engineering
Cranfield, Bedford MK430AL
ENGLAND
Attn: Professor R. E. Peacock
(copy no. 76)

Iowa State University
Mechanical Engineering Department
Ames, IA 50010
Attn: Dr. T. H. Okiishi
(copy no. 77)

NASA Ames Research Center
Moffett Field, CA 94085
Attn: Dr. S. Bodapati,
      MA 227-9
(copy no. 78)

Allis-Chalmers Corporation
Hydro-Turbine Division
Box 712
York, PA 17405
Attn: R. K. Fisher
(copy no. 79)

Commander
David W. Taylor Naval Ship R&D Center
Department of the Navy
Bethesda, MD 20084
Attn: R. J. Boswell
(copy no. 80)

NSW Institute of Technology
School of Mechanical Engineering
Broadway
Sidney
AUSTRALIA
Attn: Professor J. P. Gostelow
(copy no. 81)

U. S. Naval Air Propulsion Center
1440 Parkway Avenue
Trenton, NJ 08628
Attn: Donald Brunda
(copy no. 82)

Naval Post Graduate School
Department of Aeronautics
Monterey, CA 93940
Attn: Dr. M. F. Platzer
(copy no. 83)

University of Arizona
Department of Aerospace and Mechanical
Engineering, Bldg. 16
Tucson, AZ 85721
Attn: Dr. William Sears
(copy no. 84)

Institute for Turbomachines
Technical University
Templergraben 55
D-5100 Aachen
Federal Republic of Germany
Attn: Dr. H. Gallus
(copy no. 85)

HSVA Gmblt
Bramfelder Strasse 164
200 Hamburg 60
Postfach 600 929
Federal Republic of Germany
Attn: Dr. E. Weitendorf
(copy no. 86)

J. M. Voith Gmblt
Hydraulic Department
Postfach 1940
D-7920 Heidenheim
Federal Republic of Germany
Attn: Mr. Eichler
(copy no. 87)

Notre Dame University
Notre Dame, IN 46556
Attn: Dr. H. Atassi
(copy no. 88)

Applied Research Laboratory
The Pennsylvania State University
P. O. Box 30
State College, PA 16801
Attn: J. J. Eisenhuth
(copy no. 89)

Applied Research Laboratory
Attn: R. E. Henderson
(copy no. 90)

DISTRIBUTION LIST FOR ARL UNCLASSIFIED TM 79-149 by E. P. Bruce dated 14 August 1979.

Applied Research Laboratory
Attn: D. E. Thompson
(copy no. 91)

Applied Research Laboratory
Attn: F. S. Archibald
(copy no. 92)

Applied Research Laboratory
Attn: A. M. Yocum
(copy no. 93)

Applied Research Laboratory
Attn: M. W. McBride
(copy no. 94)

Applied Research Laboratory
Attn: J. R. Ross
(copy no. 95

Applied Research Laboratory
Attn: A. L. Treaster
(copy no. 96)

Applied Research Laboratory
Attn: W. S. Gearhart
(copy no. 97)

Applied Research Laboratory
Attn: B. R. Parkin
(copy no. 98)